UNIVERSITY OF SOUTHAMPTON

FACULTY OF PHYSICAL SCIENCES AND ENGINEERING

Optoelectronics Research Centre

Functionalised Optical Fibre Devices with Embedded Electrodes for Nonlinear Photonics

by

Francesco De Lucia

A thesis submitted for the degree of Doctor of Philosophy

October 2017

Declaration of Authorship

I, FRANCESCO DE LUCIA, declare that this thesis titled, 'FUNCTIONALISED OPTICAL FIBRE DEVICES WITH EMBEDDED ELECTRODES FOR NON-LINEAR PHOTONICS' and the work presented in it are my own. I confirm that:

- This work was done wholly or mainly while in candidature for a research degree at this University.
- Where any part of this thesis has previously been submitted for a degree or any other qualification at this University or any other institution, this has been clearly stated.
- Where I have consulted the published work of others, this is always clearly attributed.
- Where I have quoted from the work of others, the source is always given. With the exception of such quotations, this thesis is entirely my own work.
- I have acknowledged all main sources of help.
- Where the thesis is based on work done by myself jointly with others, I have made clear exactly what was done by others and what I have contributed myself.

Signed: ______________________________

Date: ______________________________

“The true measure of a man is not his intelligence or how high he rises in this freak establishment. No, the true measure of a man is this: how quickly can he respond to the needs of others and how much of himself he can give.”

P. K. DICK

UNIVERSITY OF SOUTHAMPTON

Abstract

FACULTY OF PHYSICAL SCIENCES AND ENGINEERING
Optoelectronics Research Centre

Doctor of Philosophy

by Francesco De Lucia

In this thesis are reported progresses in the development of a technique known as thermal poling of silica fibres, which allows for the creation of an effective second order nonlinearity in materials, such as glasses, which naturally lack any second order susceptibility. The main part of the thesis work was devoted to the exploration of new experimental methods as well as numerical simulations to overcome some of the apparently intrinsic limits shown by the thermal poling technique so far, such as for example the length of the nonlinear devices and the complexity of the geometrical structure of microstructured optical fibres, both solid and hollow-core. A new poling method, based on electrostatic induction, was developed and numerically modelled which allows for poling an optical fibre without any physical contact between the source of the electric potential and the electrode embedded into the fibre. Furthermore different kinds of materials (both metallic and non-metallic) have been used to create the embedded electrodes, and in particular a new method for poling metre-long optical fibres by means of aqueous solutions used as electrodes was developed. Using together both the induction poling method with liquid embedded electrodes could allow for poling metre-long fibres and microstructured fibres of very complex geometry which could raise the second harmonic efficiency up to a value of four order of magnitude higher than the one obtained in common step-index doped fibres. Part of this thesis was dedicated to the functionalisation of different kinds of silica fibres (including microstructured hollow core fibres) by means of deposition of thin layers of semiconductors (such as silicon, germanium or zinc selenide), with the aim of exploiting their intrinsic nonlinearities to increase the whole effective second order nonlinearity of an all-fibre nonlinear device.

Acknowledgements

I would like to start my list of thanks with my supervisor dr. **Pier Sazio**, who definitely represented to me, besides a very supportive and helpful guide, a continuous stimulus to improve myself and to believe into the possibility of reaching the best possible results in my research project. I recognize his support not as something due but as something special. After him, my grateful thank goes to dr. **Costantino Corbari**, a gentleman who inspired me with his enthusiasm and had the courage of transferring to me some skills very helpful for my work and my second supervisor dr. **Noel Healy** for his patient help into some experimental issues. Warm thanks go also to dr. **Sakellaris Mailis** and dr. **Walter Belardi**, who, besides their fundamental role of senior colleagues, represented for me a reference in speeches related not only to Physics but also to anything else, from politics to history, from philosophy to literature, from music to cinema. I consider them above all two friends. A sincere thank goes of course to all the people inside the ORC who sought to involve me in their work and who became fantastic collaborators, namely prof. **Gilberto Brambilla**, prof. **Peter Smith**, and dr. **James Gates**, who surprised me with their enthusiastic support and their interest in my work. Furthermore I would like to thank all the other people I worked with during these years, people who demonstrated to have the patience to work with me and so even just for this thing deserve my gratitude, namely **Imran Abdul Khudus**, **Ding Huang**, **Fariza Suhailin**, **Yun Wang**, **Li Shen**, **Adam Lewis**, **Andrea Ravagli**, dr. **Martynas Beresna**, dr. **Joris Lousteau**, dr. **Kevin Huang**, dr. **Vassili Savinov**, dr. **Eric Numkam Fokoua** and **Rex Bannerman**. A particular thank goes to prof. **Peter Kazansky**, who allowed me to use his facilities and who inspired me with his first-hand stories about the early times of thermal poling, to prof. **Walter Margulis**, dr. **Olexandre Tarasenko**, dr. **Marco Petrovich**, dr. **Tom Bradley**, prof. **Jayanta Sahu** for the fibers they provided me along my PhD path. A very warm thank goes to all the guys of the University of Auckland (NZ), in particular to the head of the group prof. **Stephane Coen**, to prof. **Stuart Murdoch**, dr. **Miro Erkintalo** and to dr. **Francois Leo**, who, as rarely it happens, became a good friend besides being a great colleague. Apart from being fantastic colleagues, they hosted me with great friendliness and made me feel at home. Many thanks to all the colleagues of the group of prof. **John Badding** in Pennsilvania University (US), namely **Steve**, **Mike**, **Subhasis** and **Derek**. Great and warm thanks to all the people I met here in Southampton who

became good friends and made my time here pleasant and this place familiar, in particular to **Rokas Drevinskas**, **Arish Achar Vasant**, **Ausra Cerkauskaite**, **Medya Fouad Namiq**, **Magdalena Miszcsak**, **Magdalena Wrobel**, **Radan Slavik**, **Rand Ismael**, **Ilaria Sanzari** and all the **Comida**'s friends. Last but not least my grateful thank goes to **Chiara**, patient, sweet, supportive, lovely, and to my best friends who, even not physically close to me, were in my hearth and in my mind all the time, in particular to **Dario**, always present in my lonely moments, **Mario**, companion of infinite and overnight discussions, **Michele**, who can be defined an old friend, **Harry**, **Lux**, **Cinzia**, **Marilù** and **Marcello**. My infinite gratitude to my all family and mainly to my parents, who never prevented me from following my crazy ideas. I hope you do not regret that too much. That is my life, but it has been possible even thanks to you.

Contents

List of Figures

List of Tables

Abbreviations

TIR	**T**otal **I**nternal **R**eflection
SHG	**S**econd **H**armonic **G**eneration
SFG	**S**um **F**requency **G**eneration
DFG	**D**ifference **F**requency **G**eneration
OR	**O**ptical **R**ectification
OPO	**O**ptical **P**arametric **O**scillation
PCF	**P**hotonic **C**rystal **F**ibre
HPCVD	**H**igh **P**ressure **C**hemical **V**apour **D**eposition
QPM	**Q**uasi **P**hase **M**atching
SMF	**S**ingle **M**ode **F**ibre
TEM	**T**ransverse **E**lectro **M**agnetic
MOF	**M**icrostructured **O**ptical **F**ibre
PBG	**P**hotonic **B**and **G**ap
FSM	**F**undamental **S**pace-filling **M**ode
HC-PCF	**H**ollow **C**ore **P**hotonic **C**rystal **F**ibre
FP	**F**abry **P**erot
NC-HCF	**N**egative **C**urvature **H**ollow **C**ore **F**ibre
SVEA	**S**lowly **V**arying **E**nvelope **A**pproximation
PPM	**P**erfect **P**hase **M**atching
BPM	**B**irefringent **P**hase **M**atching
PPSF	**P**eriodically **P**oled **S**ilica **F**ibre
SPDC	**S**pontaneous **P**arametric **D**own **C**onversion
SH	**S**econd **H**armonic
EFISH	**E**lectric **F**ield **I**nduced **S**econd **H**armonic

HF	**H**ydrogen **F**luoride
DI	**D**e **I**onized
AFM	**A**tomic **F**orce **M**icroscope
THF	**T**hree **H**ole **F**ibre
OD	**O**uter **D**iameter
MCM	**M**odified **C**amara **M**odel
SON	**S**econd **O**rder **N**onlinearity
STP	**S**tandard **T**emperature and **P**ressure
OPG	**O**ptical **P**arametric **G**enerator
OSA	**O**ptical **S**pectrum **A**nalyzer
FWM	**F**our **W**ave **M**ixing
OMF	**O**ptical **M**icro **F**ibre
FF	**F**undamental **F**requency
TH	**T**hird **H**armonic
FH	**F**ourth **H**armonic
MOPA	**M**aster **O**scillator **P**ower **A**mplifier
EOM	**E**lectro **O**ptic **M**odulator
AOM	**A**cousto **O**ptic **M**odulator
ASE	**A**mplified **S**pontaneous **E**mission
OSNR	**O**ptical **S**ignal **N**oise **R**atio
FHG	**F**ourth **H**armonic **G**eneration
THG	**T**hird **H**armonic **G**eneration
5HG	**F**ifth **H**armonic **G**eneration
PMD	**P**hase **M**atching **D**iameter
MI	**M**odulation **I**nstability
OCT	**O**ptical **C**oherence **T**omography
CSHG	**C**avity **S**econd **H**armonic **G**eneration
TON	**T**hird **O**rder **N**onlinearity
ARF	**A**nti **R**esonant **F**ibre
CM-ARF	**C**omposite **M**aterial **A**nti **R**esonant **F**ibre
SEM	**S**canning **E**lectron **M**icroscope

Symbols

$\chi^{(i)}$	i^{th} order susceptibility tensor
$\chi^{(2)}_{eff}$	Effective second order susceptibility
n	Refractive index
NA	Numerical aperture
$\boldsymbol{k}$	Wavevector
β	Propagation constant
n_{eff}	Effective refractive index
V	Normalized frequency parameter V
ω	Angular frequency
ϵ_0	Free space permittivity
$\boldsymbol{P}$	Polarization vector
$\boldsymbol{E}$	Electric field vector
$\boldsymbol{D}$	Electric displacement vector
$\boldsymbol{B}$	Magnetic induction field vector
$\boldsymbol{H}$	Magnetic field vector
$\boldsymbol{M}$	Magnetization vector
μ_0	Free space permeability
c	Free space light speed
$\boldsymbol{\epsilon^{(1)}}$	Dielectric tensor
$\epsilon^{(1)}$	Relative permittivity of a medium
$\boldsymbol{P^{(1)}}$	Linear term of polarization vector
$\boldsymbol{P^{(NL)}}$	Nonlinear term of polarization vector
$d^{(i)}$	i^{th} order nonlinear mixing tensor

Δk	Momentum mismatch
I	Optical intensity
L_c	Coherence length
A_{OVL}	Area overlap
η_{SH}	Second harmonic efficiency
$\Delta\lambda$	Bandwidth
GVM	Group velocity mismatch
v_g	Group velocity
E_{dc}	Frozen-in dc electric field
p_i	Istantaneous concentration of impurity charges
$p_{0,i}$	Initial concentration of impurity charges
μ_i	Mobility of impurity charges
e	Electron charge
D_i	Diffusion constant of the i^{th} species
V_{app}	Electric potential applied to electrodes during thermal poling
Λ_{QPM}	First order QPM period
λ_{QPM}	QPM pump wavelength
α	Attenuation of a fibre

To my grandparents, who gave the kick start of the whole story…

Chapter 1

Introduction

1.1 Overview

Although the concept of "total internal reflection"(TIR) was known since 1854 [1] and the first glass optical fibres were realized in the 1920s [2, 3], it was only in the 1970s that optical fibres started to become what they had promised to be in the previous fifty years, namely reliable waveguides to transmit information, thanks mainly to the work of Kapron *et al.* [4], who realized for the first time single-mode waveguides characterized by reasonably low intrinsic transmission losses (7 dB/km). Since then the performances of optical fibres, in terms of transmission losses, became better and better, making them finally competitive and allowing them to transfom the telecommunication world. Nowadays indeed it is possible to dope optical fibres with erbium to obtain optical amplifiers, or with ytterbium or neodymium to get fibre lasers, or integrate Bragg gratings mirrors and filters into them. Their enormous global deployment is mainly for passive photon-based data transport rather than a platform for nonlinear photonic devices (such as for example frequency converted laser sources, beam modulators and switches, optical sensors, etc.). Nonlinear optics is the study of how intense light interacts with matter. The optical response of a material usually scales linearly with the amplitude of the electric field. At high powers, however, the material properties can change more rapidly. This leads to nonlinear effects including self-focusing, solitons and high-harmonic generation [5]. In "nonlinear regime" the optical properties of the matter, such as for example the refractive index, start to depend on the intensity and on other properties of the light [6], the light waves can interact among them and the superposition principle is violated [7]. The early experimental observations of phenomena related to the topic defined as “nonlinear optics” were realized in 1961 by Franken *et al.*, who generated second harmonic (at ≈ 347.2 nm) by projecting an intense beam of light at a wavelength of 694.3 nm through a crystalline quartz [8]. Since then diverse nonlinear phenomena were observed, which could be catalogued according to the i^{th} order susceptibility tensor $\chi^{(i)}$ considered. If we consider the second order susceptibility $\chi^{(2)}$, the main nonlinear effects which could be observed are second harmonic generation (SHG), sum frequency generation (SFG), difference frequency generation (DFG), optical rectification (OR) and optical parametric oscillation (OPO) [9]. Unfortunately not all the materials possess an intrinsic $\chi^{(2)}$. For example centrosymmetric materials, such as the glasses, lack any quadratic nonlinearity in dipole approximation. This means that conventional step index optical fibres, in particular the ones made of silica (SiO_2), cannot be used to generate second order related nonlinear effects [6].

However there exists a method, called thermal poling, invented in 1991 by Myers *et al.* [10], to generate an effective second order susceptibility $\chi^{(2)}_{eff}$ in glasses. The method allows a permanent second order nonlinearity to be induced in a medium which is poled via the application of a static electric field, while it is heated up to a temperature whereby alkali impurity ions inside the material have a non-negligible diffusion and drift mobility. Although in the last 25 years there have been considerable developments in this area, the thermal poling technique to realize all-fibre nonlinear devices is still a relatively immature technology. As an example, the typical method of creating electrodes inside optical fibre devices relied on the manual insertion of thin tungsten wires inside capillary channels within the fibre structure [11], which is clearly not scalable in terms of manufacturability. Some improvements to the technique came from the introduction of molten metal alloys used as electrodes embedded into the fibre [12] and from the removal of the cathode from the electrical configuration of the setup used to pole the fibre [13]. Despite these improvements, there still remain some issues relating to the removal of the electrodes after poling or even just the need to physically contact them to deliver the electric potential essential for the thermal poling. To date, these issues have prevented the silica fibre poling technique from fulfilling its potential as a robust, widely utilised technology for quadratic frequency conversion.

1.2 Motivation and aim

Nowadays most quadratic nonlinear devices are based on a standard scheme which considers the interaction between intense light waves and materials characterized by intrinsic second order susceptibility. The most used in frequency doubling processes are nonlinear crystals such as for example lithium triborate (LBO) or beta-barium borate (BBO) while in electro-optic modulation experiments the most used is lithium niobate ($LiNbO_3$). This conventional scheme to generate second order nonlinear phenomena is however affected by many drawbacks which are unavoidable, such as for example thermal instabilities of nonlinear crystals if illuminated by very powerful laser radiations [14, 15], relatively short interaction lengths between light waves involved in the nonlinear process, high costs, low damage thresholds. Furthermore it is worth considering the fact that the light waves are subject to coupling losses due to the presence of air/nonlinear crystal interfaces as well as the onerous requirement for continuous optical alignment necessary in free-space optical setups. Most of the reported drawbacks could be almost completely overcome by realizing an all-fibre nonlinear device, where the light waves could not only be delivered with very low losses but also generate second order nonlinear processes. This is the main reason why investigating possible improvements of the thermal poling technique could be of significant scientific and technological importance.

The main aim of this thesis work is therefore the realization of an efficient all-fibre nonlinear photonic device. A number of ways have been explored to meet this target. Firstly it was explored the possibility of developing the thermal poling technique in order to make it suitable for poling any kind of optical fibre, from conventional step index fibres to the more complex photonic crystal fibres (PCFs) [16, 17]. Another path explored was the functionalisation of optical fibres by the exploitation of materials already possessing some kind of intrinsic nonlinearity (such as for example semiconductors or 2D materials [18, 19], which can be deposited inside or adjacent to the fibre core via two different techniques such as high pressure chemical vapour deposition (HPCVD) [20] and thermal decomposition (TD) of liquid precursors [21, 22].

Besides the functionalisation of optical fibres, a considerable part of the work was dedicated to the characterization of the second order nonlinearity eventually induced in each device. The main method exploited was the nonlinear characterization of SHG phenomena produced in periodically poled optical fibres [23] with the aim of evaluating the effective second order susceptibility $\chi^{(2)}_{eff}$ induced. Another objective of this thesis was the exploration of possible applications of long and efficient nonlinear photonic devices, which, apart from the already cited frequency doubler devices, includes sources of polarization-entangled photon pairs [24], electro-optic modulators and switches [25], or purely quadratic ring resonators for frequency comb sources [26]. The final target is demonstrating that the experimental methods developed during this thesis work can be considered part of an integrated technological platform which could be used for poling any optical fibre geometry and for enlarging the application field of all-fibre long and efficient nonlinear photonic devices.

1.3 Outline

The second chapter of the thesis, after a brief introduction about the guidance mechanisms of step-index optical fibres and PCFs, offers a theoretical background about parametric interactions in media possessing a non zero second order susceptibility tensor $\chi^{(2)}$ and in particular focuses on SHG. Furthermore the concepts of phase-matching and quasi phase-matching (QPM) are explained in detail. An historical perspective and a theoretical introduction about the thermal poling technique of both silica bulk glasses and optical fibres are also included. The state-of-art of thermal poling is then presented in order to place the innovations detailed in this thesis into context.

The third chapter is focused on the presentation of the new poling technique defined as "thermal poling by electrostatic induction". A theoretical model, developed in $COMSOL^{TM}$ Multiphysics (a finite element analysis, solver and simulation software package for various physics and engineering applications, especially coupled phenomena), has been also presented which explains how the space-charge region (sign of a successful poling of a silica fibre) evolves in time.

In the fourth chapter the idea of replacing solid or molten alloy electrodes with metallic and non-metallic liquids is presented. All the different solutions studied are explained in detail, together with their technical issues, their advantages and drawbacks.

The fifth chapter deals with the exploitation of the two techniques developed and discussed in the two previous chapters, namely the induction poling and the use of liquid electrodes with the aim of creating an all-fibre device for frequency doubling. The chapter presents the experimental setups for poling long fibres and the method for periodical UV erasure of the nonlinearity induced [27] to create a quasi-phase matching (QPM) condition [28]. An accurate description of the motivation for developing a method for the removal of the liquid electrodes after the poling experiments is also reported. The chapter describes the setup and method for the characterization of the second order nonlinearity induced and for the estimation of effective second order susceptibility $\chi^{(2)}_{eff}$. A presentation of the main applications of these periodically poled long devices closes the chapter.

The sixth chapter details the second topic investigated during my research programme, namely the functionalisation of novel optical fibre geometries (typically solid and hollow-core photonic crystal fibres (PCFs)). This was explored via the integration of semiconductors within the fibre microstructure, as these materials already possess high intrinsic second or third order optical nonlinearities which could significantly augment the overall nonlinear fibre device performance. The methodology used for semiconductor growth and deposition within the optical fibre templates is also described.

The seventh chapter recaps the main results obtained in this thesis work and presents a future perspective related to the further developments of the methods presented in this thesis work.

Chapter 2

Background

2.1 Optical fibres

An optical fibre is a dielectric waveguide characterized by a cylindrical symmetry which is usually made of silica or non-silica glass. The working principle of an optical fibre is the "total internal reflection " (TIR), an effect already known in the first half of the 19^{th} century, which requires that a "core"of refractive index n_{co} is surrounded by a cladding layer characterized by a refractive index $n_{cl} < n_{co}$. An optical ray is guided into the fibre core if its angle of incidence on the interface core/cladding is bigger than a critical angle $\theta_c = \sin^{-1}(n_{cl}/n_{co})$.

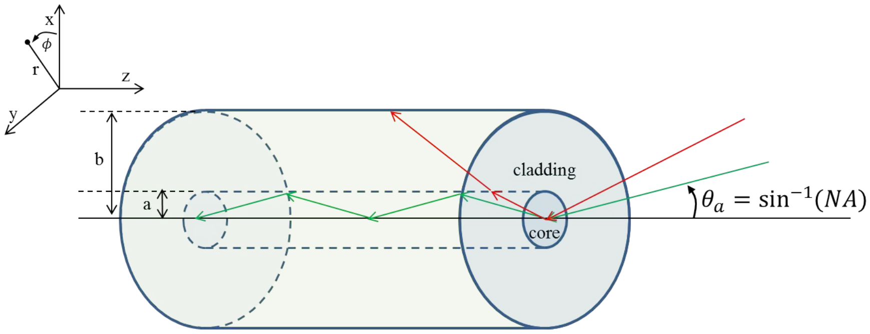

FIGURE 2.1: General schematic of an optical fibre. The green arrow represents the light wave guided into the fibre's core according to the TIR principle. The quantity θ_a represents the maximum angle beyond which a light wave is not guided (red arrow) and is called acceptance angle. "a" and "b" are respectively the core radius and the cladding radius.

Furthermore an optical ray coming from the air and entering the fibre core, is guided only if its angle of incidence on the interface air/core θ is smaller than an angle θ_a, called acceptance angle, defined by the equation $\sin(\theta_a) = \sqrt{n_{co}^2 - n_{cl}^2} = NA$, where NA is called numerical aperture of the optical fibre and is considered an important parameter. Fig. 2.1 shows the conventional schematic of an optical fibre and illustrates the concept of acceptance angle [7].

2.1.1 Step-index fibres

The conventional optical fibres used in optical communication systems are step-index single-mode fibres (SMFs). Their guidance mechanism is the already discussed TIR due to the refractive index difference between core and cladding, which allows for guiding a light wave into the fibre core. Usually both the core and the cladding are made of pure silica and the slight difference in the refractive index is obtained by means of a doping process into the fibre core of other species such as for example germanium (Ge), titanium (Ti) and boron (Bo).

If we consider a monochromatic light wave propagating into an optical fibre, its electric and magnetic field components have to fulfill the Helmholtz equation, $\nabla^2 U + n^2 k_0^2 U = 0$, where U represents the propagation mode of both the electric and magnetic fields of the light wave we are considering, n is the refractive index of the core or of the cladding and $k_0 = 2\pi/\lambda_0$ is the wavenumber of the monochromatic radiation (of wavelength λ_0) traveling into the fibre. For the sake of simplicity it is possible to assume that the cladding radius “b”is infinite because the propagation mode is confined into the core. In a cylindrical coordinate system r, ϕ and z (see Fig. 2.1) the Helmholtz equation will be expressed by [7]:

$$\frac{\partial^2 U}{\partial r^2} + \frac{1}{r}\frac{\partial U}{\partial r} + \frac{1}{r^2}\frac{\partial^2 U}{\partial \phi^2} + \frac{\partial^2 U}{\partial z^2} + n^2 k_0^2 U = 0 \tag{2.1}$$

Assuming that the light waves travel along the z direction with a propagation constant β and that U is a periodic function of the angle ϕ (of period 2π), the complex amplitude U which is solution of the Helmholtz equation (2.1), will be expressed by:

$$U(r, \phi, z) = u(r) e^{(-jl\phi)} e^{(-j\beta z)}, \qquad l = 0, \pm 1, \pm 2...., \tag{2.2}$$

Substituting the expression (2.2) in the equation (2.1), we obtain:

$$\frac{\mathrm{d}^2 u}{\mathrm{d}r^2} + \frac{1}{r}\frac{\mathrm{d}u}{\mathrm{d}r} + \left(n^2 k_0^2 - \beta^2 - \frac{l^2}{r^2}\right) u = 0 \tag{2.3}$$

So, a light wave is guided if $n_{cl}k_0 < \beta = n_{eff}k_0 < n_{co}k_0$, where n_{eff} is the effective refractive index of the guided mode. The meaning of n_{eff} can be easily understood from Fig. 2.2, where a guided mode is shown propagating through a waveguide. Due to the increased path length, the light propagates down the waveguide more slowly than it otherwise would. This means that the mode can be considered as having an effective refractive index given by $n_{eff} = n_{co}cos(\psi) = n_{co}sin(\theta)$. In the case $\theta = \pi/2$, $n_{eff} = n_{co}$, and when $\theta = \theta_c$, $n_{eff} = n_{cl}$. In other words $n_{cl} < n_{eff} < n_{co}$ [29].

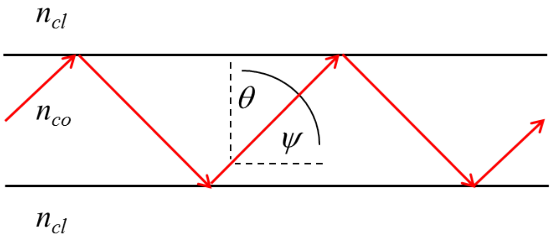

FIGURE 2.2: Mode guided by step index waveguide. The beam propagates at an angle ψ to the z axis and so has an incidence angle θ with the boundary. The core and cladding have refractive indices n_{co} and n_{cl} respectively.

At this point, introducing in equation (2.3) two new quantities [29]:

$$V = k_0\, a\, NA = \frac{2\pi}{\lambda_0}\, a\, NA \tag{2.4}$$

and

$$b = \frac{\beta^2 - n_{cl}^2 k_0^2}{n_{co}^2 k_0^2 - n_{cl}^2 k_0^2} = \frac{n_{eff}^2 - n_{cl}^2}{n_{co}^2 - n_{cl}^2} \tag{2.5}$$

respectively defined as the normalized frequency parameter V and the generalized propagation constant b, we obtain two distinguished differential equations in the core and in the cladding:

$$\frac{\mathrm{d}^2 u}{\mathrm{d}r^2} + \frac{1}{r}\frac{\mathrm{d}u}{\mathrm{d}r} + \left(\frac{V^2(1-b)}{a^2} - \frac{l^2}{r^2}\right) u = 0, \qquad r < a\,(core) \tag{2.6}$$

and

$$\frac{\mathrm{d}^2u}{\mathrm{d}r^2}+\frac{1}{r}\frac{\mathrm{d}u}{\mathrm{d}r}-\left(\frac{V^2b}{a^2}+\frac{l^2}{r^2}\right)u=0, \qquad r>a\,(cladding) \tag{2.7}$$

The two equations (2.6) and (2.7) have the family of Bessel functions as solutions:

$$u(r)\propto\begin{cases} J_l\left(\frac{V\sqrt{1-b}}{a}r\right), & r<a\,(core)\\ K_l\left(\frac{V\sqrt{b}}{a}r\right), & r>a\,(cladding)\end{cases} \tag{2.8}$$

where $J_l(x)$ are the Bessel functions of the first kind and order l and $K_l(x)$ are the modified Bessel functions of the second kind and order l [7]. By means of the Maxwell's equations and choosing the proper boundary conditions, it is possible to find the electric and magnetic field components [29].

Most of the step-index fibres are weakly guiding (i.e. $\Delta n=(n_{co}-n_{cl})\ll 1$) and the guided rays are paraxial (basically parallel to the fibre's axis). In other words the longitudinal components of both the electric and the magnetic field are negligible and then the guided waves can be considered approximately transverse electromagnetic (TEM). Furthermore the boundary conditions of the transverse components of the fields are the continuity of $u(r)$ and of its first derivative in correspondence of the core/cladding interface ($r=a$) in the equation (2.8). These last conditions can be translated into a "characteristic equation"satisfied by V and b:

$$V\sqrt{1-b}\frac{J_l'(V\sqrt{1-b})}{J_l(V\sqrt{1-b})}=V\sqrt{b}\frac{K_l'(V\sqrt{b})}{K_l(V\sqrt{b})} \tag{2.9}$$

where J_l' and K_l' are the first derivatives of the Bessel functions [7]. The derivatives J_l' and K_l' of the Bessel functions satisfy the following identities:

$$\begin{aligned} J_l'(x)&=\pm J_{l\mp1}(x)\mp l\frac{J_l(x)}{x}\\ K_l'(x)&=-K_{l\mp1}(x)\mp l\frac{K_l(x)}{x}\end{aligned} \tag{2.10}$$

Using the identities (2.10), the equation (2.9) can be re-written in the following form:

$$V\sqrt{1-b}\frac{J_{l\pm1}(V\sqrt{1-b})}{J_l(V\sqrt{1-b})} \mp V\sqrt{b}\frac{K_{l\pm1}(V\sqrt{b})}{K_l(V\sqrt{b})} = 0 \tag{2.11}$$

The characteristic equation (2.11) can be solved numerically [29]. If V and l are fixed, it is possible to find none, one or more than one solution for b, generating discrete propagation constants β_{lm}, with $m = 1, 2, ...$ Each existing solution represents a linearly polarized mode LP_{lm} with l describing the azimuthal mode and m defining the radial distribution of the transverse mode. When $V < 2.405$ all the modes are cut off apart from the mode LP_{01} and the fibre is said to be single-mode. When $V > 2.405$ the fibre is said to be multimodal.

It is possible to define even the ratio between the power associated to the mode which propagates into the core and the total power of the radiation delivered into the fibre, as [29]:

$$\Gamma = \frac{P_{co}}{P_{co}+P_{cl}} = 1-(1-b)\left[1-\frac{K_l^2(V\sqrt{b})}{K_{l+1}(V\sqrt{b})K_{l-1}(V\sqrt{b})}\right] \tag{2.12}$$

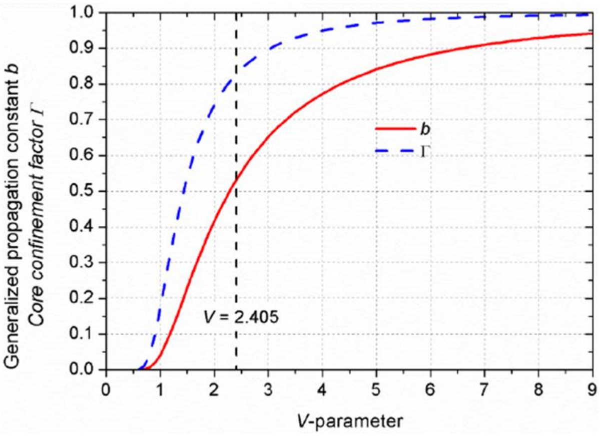

FIGURE 2.3: Γ and b vs. V-parameter for the LP_{01} mode in a weakly-guiding step-index fibre.

In Fig. 2.3 are reported the curves of Γ and b vs. V for the fundamental mode LP_{01} in a step-index fibre, where it is possible to clearly see that the power of the radiation is more confined into the core when the V-parameter increases.

2.1.2 Photonic crystal fibres

Photonic crystal fibres (PCFs), also called microstructured optical fibres (MOFs), represent a new generation of optical fibres which is gaining day by day always more relevance in optical fibre communication systems. A photonic crystal is a periodic transverse wavelength-scale lattice (also defined microstructure) of microscopic holes created into the cladding glass [30, 31]. The principal motivation to develop different kind of optical fibres was due to two main limitations typical of step-index SMFs, namely the small value of the normalized core-cladding refractive index difference $\Delta = (n_{co} - n_{cl})/n_{cl}$, which causes non negligible bend losses and limits the degree of manipulation of the group velocity dispersion (GVD) and birefringence, and the TIR principle, which could not allow for guiding light into a hollow core (with the aim, for example, of removing the issues related to the nonlinearities due to the glass) [31]. The original idea behind the PCF was to trap light into a 2D photonic crystal made of microscopic capillaries running along the entire fibre length. If this microstructure is properly designed, it would allow for guiding light via a photonic bandgap (PBG) effect, described by Knight *et al.* in 1998 [32] and by Cregan *et al.* in 1999 [33].

The first attempt to realize a PCF was made in 1996 by Knight *et al.*, who created a fibre consisting of an undoped fused silica core surrounded by a cladding constiting of a two-dimensional photonic crystal made of silica with air holes running along the length of the fibre. The holes were arranged in a hexagonal honeycomb pattern across the cross-section [16] (see Fig. 2.4). Nevertheless even if this type of fibre could resemble a PCF, it actually guides light due to a modified TIR mechanism, characterized by an average refractive index of the cladding smaller than the one of the core, because of the presence of the holes in the cladding. The relevant parameters to define the guidance properties of this fibre are the diameter “d” of each hole and the distance between the centres of each couple of consecutive holes (defined as “pitch” and labeled by “Λ”). In this case it is possible to define an effective V-parameter, as $V_{eff} = (2\pi\Lambda/\lambda)\sqrt{n_{co}^2 - n_{eff}^2}$, where $n_{eff} = \beta_{FSM}/k$. β_{FSM} is the propagation constant of the fundamental space-filling mode (FSM), that is the fundamental mode of the infinite photonic crystal cladding if the core is absent. In other words, β_{FSM} is the maximum value of β allowed in the cladding. Even if it is not possible to translate straightforwardly the single mode condition $V < 2.405$ to the effective V-parameter, it is possible to say that adjusting the values of the diameter “d ” and the pitch “Λ” of the central microstructure, it is always possible to find a condition $V_{eff} < V_{cutoff}$, thus making the fibre "endlessly single-mode" [17].

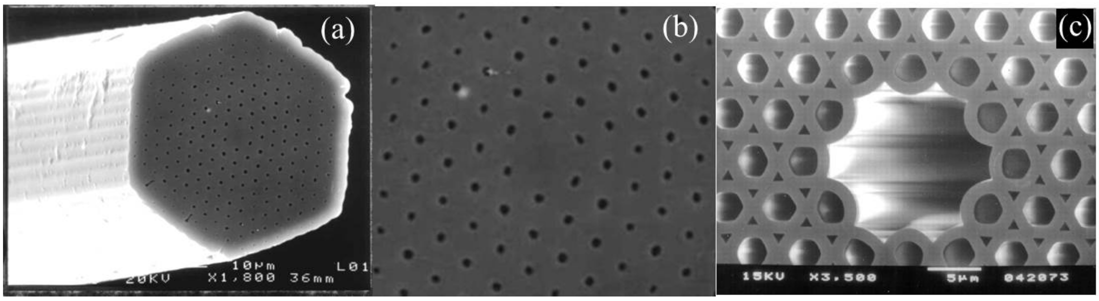

FIGURE 2.4: Scanning electron micrographs of two different kind of PCFs. (a) shows the structure of the first working PCF, with its solid core surrounded by an air-channels microstructure [16]; (b) is a detail of the same PCF reported in (a); (c) represents the first hollow-core PCF [33].

The second type of PCF, the hollow-core PCF (HC-PCF), realized for the first time in 1999 by Cregan *et al.* [33], is instead characterized by a different mechanism of guidance, defined photonic band gap (PBG) and described for the first time by Yablonovitch in 1993 [34].

In the HC-PCF realized by Cregan *et al.* the central core is replaced by a large air hole (see Fig. 2.4). It is worth noting that the wavevector component along the waveguide, known as the propagation constant β, determines whether light propagates or is evanescent in any part of the guide. If $\beta < kn$, the light propagates at an angle ψ to the axis in a material of index n, where $\beta = kncos(\psi)$ and k is the vacuum wave constant (see Fig. 2.2). If $\beta > kn$, ψ is imaginary and the light is evanescent. In a conventional TIR guidance mechanism the index n_1 of the core is bigger than the cladding index n_2 and there is a range of values of β where light propagates in the core and is evanescent in the cladding (see Fig. 2.5(A)). In contrast, light can be confined between two multilayer dielectric stacks in a core of arbitrary refractive index [35], if the stacks have a PBG for a range of β at a given optical frequency. It is important highlighting that, if we consider the photonic crystal as a dielectric structure characterized by a periodic variation of the refractive index, and we define as photonic stop band the region of frequencies and directions where light cannot propagate for any state of polarization, we could say that the photonic crystal possesses a photonic band gap if the stop band persists for all the frequencies and the directions [34–36].

Cregan *et al.* identify two possible regimes of PBG guidance, according to the value of β [33]. In the first regime (represented in Fig. 2.5(B)) light propagates ($\beta < kn_1$) in the layers of high index n_1 but is evanescent ($\beta > kn_2$) in the layers of low index n_2. The high-index layers, individually considered, act as TIR waveguides, supporting bound modes at specific values of $\beta = \beta_m$. Resonant tunneling between adjacent high-index layers makes light leak through them, provided β lies within the pass bands that open up around each β_m. The widths of the pass bands depend on the strength of coupling between the layers. Between the pass bands lie band gaps; if a high-index core layer with a different (maybe smaller) width supports a mode with β inside a band gap, it is not resonant with the other layers and light leakage by tunneling is prohibited. The mode is thus strictly guided by the frustrated tunneling form of PBG. This guidance mechanism is the one which the PCF realized by Knight *et al.* in 1998 is based on [32].

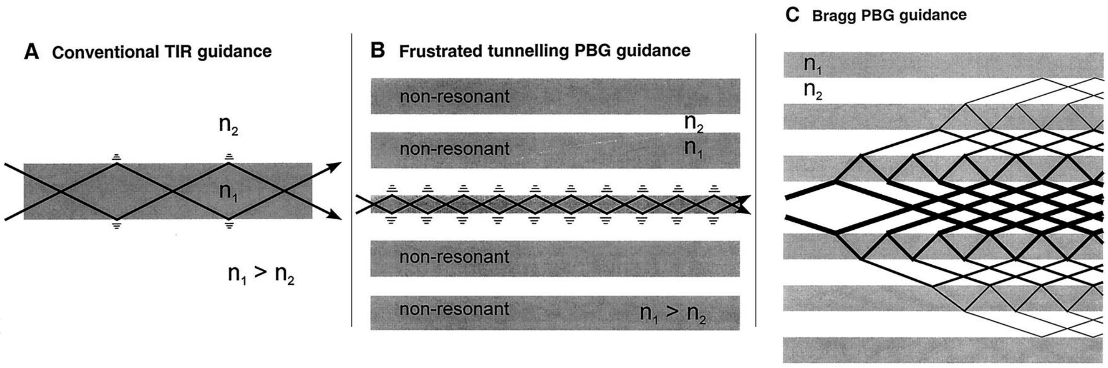

FIGURE 2.5: Different guidance mechanisms: (A) total internal reflection (TIR); (B) PBG mechanism due to frustrated tunneling: the cladding layers of dielectric material are out of resonance with the core of the fibre in such a way the tunneling to produce leakage of the mode is inhibited and the light is strongly guided; (C) guidance mechanism is produced when the light propagates in all the layers of the stack for Bragg scattering mechanism [33].

In the second regime of PBG guidance (represented in Fig. 2.5(C)), light can propagate in all layers ($\beta < kn_2$). Band gaps occur at the Bragg condition as a result of multiple scattering and interference, producing this second form of PBG guidance, which is therefore mainly governed by the periodicity of the microstructured cladding. Cregan *et al.* meausured the transmission spectra through the air core of lengths of fibre by means of an optical spectrum analyzer, illuminating them with white light (using a tungsten halogen lamp). The spectral dependence of the waveguiding in the air hole demonstrated that several well-defined bands of transmission are present, covering the whole visible spectrum and extending into the infrared [33]. After this first characterization made by using broadband light, they identified some wavelengths guided and so excited the fibre by using those wavelengths generated by some laser sources. The laser light guided in the air core formed a stable, smoothly varying, single-lobed pattern in the far field, which demonstrates the possibility of a single-mode guidance of this kind of fibre at particular wavelengths.

In a work of 2002 Litchinitser *et al.* analyzed the mechanism of guidance based on the Bragg reflections off high- and low-index periodic layers in the cladding of HC-PCFs and demonstrated that if the lattice constant of the PBG waveguide is larger than the optical wavelength and the index contrast ($\Delta = n_1 - n_2$) is high, the spectral characteristics of the waveguide can be governed by the thickness of the first high-index layer rather than the lattice constant [37]. Furthermore they demonstrated that the spectral properties of such PBG optical waveguides can be described analytically by using the so-called antiresonant reflecting optical waveguide (Arrow) model, introduced originally by Duguay *et al.* for planar waveguides [38]. The working principle of the Arrow waveguide can be explained by looking at the Fig. 2.6, which shows two different wavelengths propagating in the core of a waveguide formed by a low-index core surrounded by two high- and low-index cladding layers. The wavelengths corresponding to the minima of the transmission coefficient are defined resonant, while the wavelengths corresponding to high transmission parts of the spectrum are called antiresonant. This definition is due to the fact that high transmission originates from the antiresonant nature of the individual cladding layers with respect to the transverse propagation constant. Each layer can be considered a Fabry-Perot-(FP-) like resonator. Narrowband resonances of this FP resonator correspond to transmission minima for the light propagating in the core, or resonant wavelengths of the low-index core waveguide. Wide antiresonances of the FP resonator (wavelengths experiencing low leakage as a result of destructive interference in the FP resonator) correspond to a high transmission coefficient for the low-index core waveguide. The lower plot in Fig. 2.6 shows the transmission spectrum of this waveguide.

In 2004 a solid-core PBG fibre where light was guided in a low-index core region because of the antiresonances of the high-index strands in the fibre cladding was realized for the first time by Luan *et al.* [39] and one year later all-solid PBG fibre characterized by a low-loss region at 1550 nm was realized by Bouwmans *et al.* [40].

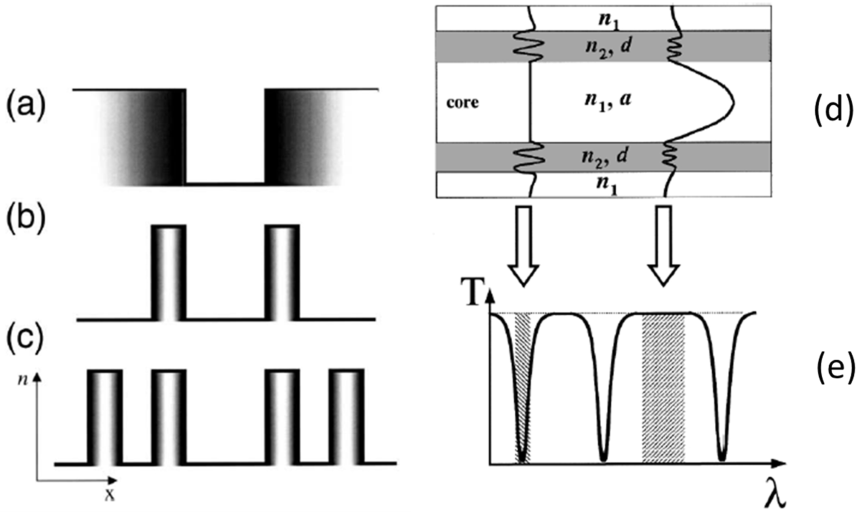

FIGURE 2.6: (a) shows the schematic of a hollow waveguide where a low-index core is surrounded by a high-index cladding; (b) and (c) show respectively a one-layer and two-layers Arrow structure; (d) represents the Arrow structure with its (e) transmission spectrum [37].

In 2011 another waveguide regime in HC-PCFs was identified by Pryamikov *et al.*, who demonstrated both theoretically and experimentally the possibility of guiding light with low losses inside a broad band spectral range (from the visible region to the mid-infrared region) by exploiting a different geometry of the microstructured cladding of the hollow-core fibre called “negative curvature” [41]. In this kind of fibres the cladding consists of a single row of silica capillaries mounted on the inner periphery of the fibres internal diameter, giving a negative curvature aspect to the core boundary (see Fig. 2.7). The guidance mechanism can be still considered as the antiresonant reflecting optical waveguide already introduced earlier. The guidance in these negative curvature PCFs is characterized by low losses despite the intrinsic non-negligible losses of the glass which each capillary of the microstructure is made of. It seems reasonable that these negative curvature PCFs could be exploited largely for the transmission of high power infrared laser radiation. A big effort is being undertaken recently to enlarge the spectral bandwidth of these fibres, in particular towards the UV region.

The potential practical advantages of a single-mode vacuum guide are enormous. It is easy to couple light into the core, because the phase is constant across the air core (giving a Gaussian-like intensity profile). Fresnel reflections, which are a problem in fibre devices where light is extracted from a fibre and then re-injected after modulation or amplification, will be extremely small in the vacuum-guided fibre, because the refractive index discontinuity between the outside world and

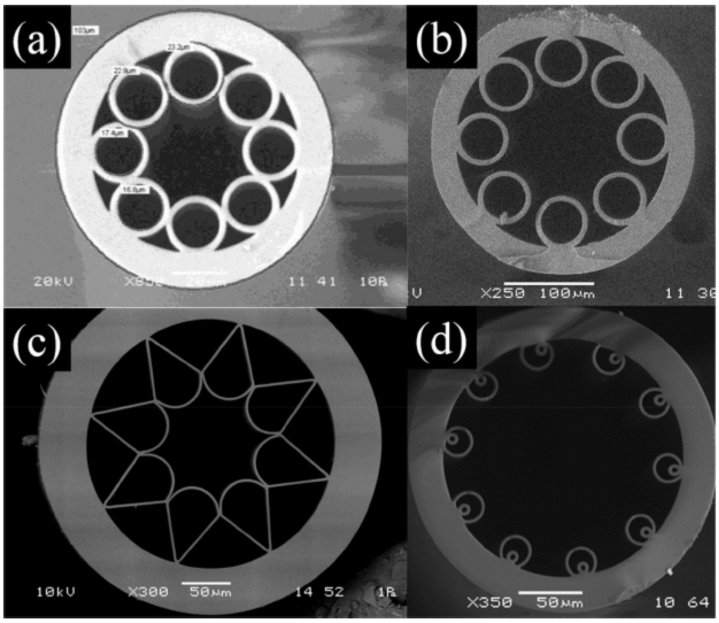

FIGURE 2.7: *SEM* pictures of different examples of negative curvature hollow-core fibres (NC-HCFs) (a) NC-HCF with touching silica capillaries; (b) NC-HCF with non-touching silica capillaries; (c) NC-HCF made of silica with ice-cream-cone shape capillaries cladding; (d) NC-HCF with non-touching silica capillaries and extra capillaries added to reduce the coupling between the core and the cladding modes [42].

the fibre mode can be tiny. Another advantage over other optical fibres is that the performance is much less limited by the interaction (absorptive or nonlinear) between the guided light and the material forming the fibre core. This will allow transmission of wavelengths and power levels not possible in conventional fibres, and will lead to greatly increased threshold powers for stimulated Raman, Brillouin effects. On the other hand, if the hollow core is deliberately filled with a gas, vapour, or low-index liquid, very strong interactions are possible with the light in the guided mode. This may prove useful for gas sensing and monitoring, for the generation of multiple optical wavelengths by nonlinear processes, and more generally in enhanced nonlinear optics. The narrow-band performance of the fibre suggests that it might be useful as a spectral filtering device. The ability to form a single transverse mode in a tube of vacuum offers possibilities in the fields of atom guiding and laser delivery of small particles [33].

2.2 Nonlinearities in optical fibres

Optics deals with all the phenomena which occur when light interacts with matter, and, according to the intensity of the interacting light and the response of the material media involved into the interaction, it can be distinguished in linear and nonlinear optics. At relatively low intensities the interaction of light with matter is characterized mainly by phenomena such as absorption and refraction of the light which crosses the medium, different wavelengths cannot interact each others (the superposition principle is valid) and the optical properties of the medium do not depend on the intensity of the interacting light. When the light intensity reaches higher values, it can happen that the properties of the medium start to depend on the light intensity and various optical waves could interact each others violating the superposition principle. This second case is the realm of nonlinear optics [6].

If we consider the medium where light propagates as a collection of particles, namely ions and electrons, applying an electric field causes a displacement of the two different kinds of charges towards two opposite directions and, if the medium is a dielectric (electrons and ions are bound in such a way the charges can only slightly move with respect to their equilibrium position), this displacement creates a collection of induced electric-dipole moments, or in other words a polarization of the medium. Because light is an electromagnetic field which oscillates at a certain frequency, also the induced dipoles will oscillate and their motion will be governed by the equation of the mechanical oscillator, which, in case of dipoles all oscillating in the same direction x, is [6]:

$$m\left[\frac{\mathrm{d}^2x}{\mathrm{d}t^2}+2\Gamma\frac{\mathrm{d}x}{\mathrm{d}t}+\Omega^2x-(\xi^{(2)}x^2+\xi^{(3)}x^3+....)\right]=-eE(t) \tag{2.13}$$

where x is the displacement from the mean position, Ω is called resonance frequency, Γ is the damping constant, the term $-eE(t)$ represents the electric force acting on each electron and the terms $\xi^{(2)}x^2$, $\xi^{(3)}x^3$, etc. are the anharmonic terms of the oscillation. If the equation (2.13) is solved ignoring the anharmonic terms of the oscillation, it is easy to obtain a relationship which expresses the linear dependence of the polarization vector on the electric field. In the case of linear dependence the polarization oscillates at the same frequency of the electric field and the behaviour of the medium is linear. Nevertheless this picture is valid only when the displacements x from the mean positions are small, while, if they become bigger, the approximation of linear behaviour is not anymore valid, and in the equation (2.13) it is necessary to consider even the anharmonic terms. In Fig. 2.8 it is possible to visualize the difference between linear and nonlinear behaviour of a dieletric medium when interacts with a light wave. In particular a spectral analysis of the case (b) of Fig. 2.8 will show in the polarization the presence, besides the linear term oscillating at the frequency of the incoming electric field ω, of nonlinear terms oscillating at harmonic frequencies 2ω, 3ω, ... and even a not oscillating term (dc component). Because an electric-dipole oscillating emits a radiation field at the frequency of oscillation, the different components of the polarization vector oscillating at different frequencies will emit radiation at those particular frequencies. Assuming the anharmonic terms are small if compared to the harmonic one, it is possible to solve the equation (2.13) to successive orders of approximation expressing x as a power series and consequently the polarization P can be expressed as a Taylor series expansion [6]:

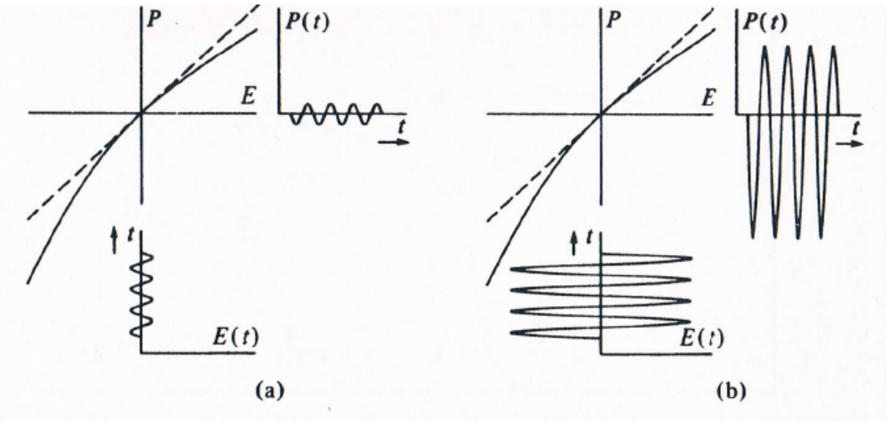

FIGURE 2.8: The effect of linear and nonlinear dependence of the polarization on the electric field is presented. (a) for small applied electric field P is linear, while for higher electric field P goes far apart from linearity and transforms the electric field in nonlinear way [6].

$$P = \epsilon_0(\chi^{(1)}E + \chi^{(2)}E^2 + \chi^{(3)}E^3 + ...) \tag{2.14}$$

where ϵ_0 is the permittivity of free space, $\chi^{(1)}$ is the linear electric susceptibility of the medium, and $\chi^{(2)}, \chi^{(3)}$.... are the nonlinear electric susceptibilities of the medium of first, second, etc order. It is worth highlighting that the equation (2.14) is expressed in scalar approximation, which is valid only in the simplest case of a medium lossless and dispersionless. In the most general case of a medium with losses and dispersion, the electric field $\boldsymbol{E}$ and the polarization $\boldsymbol{P}$ become vectors and the susceptibilities tensors of rank $(i + 1)$, where i is the order of the susceptibility $\chi^{(i)}$.

2.2.1 The wave equation for nonlinear optical media

In order to obtain the wave equation which describes the propagation of light waves through nonlinear media, we start from the Maxwell's equations, which, in a space without free charges and currents, can be written in the SI units as:

$$\boldsymbol{\nabla} \cdot \boldsymbol{D} = 0 \tag{2.15}$$

$$\boldsymbol{\nabla} \cdot \boldsymbol{B} = 0 \tag{2.16}$$

$$\boldsymbol{\nabla} \times \boldsymbol{E} = -\frac{\partial \boldsymbol{B}}{\partial t} \tag{2.17}$$

$$\boldsymbol{\nabla} \times \boldsymbol{H} = \frac{\partial \boldsymbol{D}}{\partial t} \tag{2.18}$$

where $\boldsymbol{\nabla}$ is the vector operator *nabla*, $\boldsymbol{D} = \epsilon_0 \boldsymbol{E} + \boldsymbol{P}$ is the electric displacement, $\boldsymbol{B} = \mu_0 \boldsymbol{H} + \boldsymbol{M}$ is the magnetic induction field, μ_0 is the free space permeability, $\boldsymbol{H}$ is the magnetic field, $\boldsymbol{M}$ is the magnetization (which can be neglected if we consider a non-magnetic medium) and the electric field vector $\boldsymbol{E}$ can be expressed as superposition of monochromatic waves [9]:

$$\boldsymbol{E}(\boldsymbol{r}, t) = {\sum_n}' \boldsymbol{E}_n(\boldsymbol{r}) e^{-i\omega_n t} + c.c. = {\sum_n}' \boldsymbol{A}_n e^{i(\boldsymbol{k}_n \cdot \boldsymbol{r} - \omega_n t)} + c.c. \tag{2.19}$$

where $\boldsymbol{E}_n$, $\boldsymbol{A_n}$ and $\boldsymbol{k}_n$ are respectively the electric field vector, the spatially slowly varying field amplitude and the propagation vector of the n^{th} frequency. The summation is performed over the positive frequencies only. If we express the field amplitudes using the alternative notation $\boldsymbol{E}_n = \boldsymbol{E}(\omega_n)$ and $\boldsymbol{A}_n = \boldsymbol{A}(\omega_n)$ and consider that $\boldsymbol{E}(-\omega_n) = \boldsymbol{E}(\omega_n)^*$ and $\boldsymbol{A}(-\omega_n) = \boldsymbol{A}(\omega_n)^*$ (where the sign * represents the complex conjugate), it is possible to write:

$$\boldsymbol{E}(\boldsymbol{r}, t) = \sum_n \boldsymbol{E}(\omega_n) e^{-i\omega_n t} = \sum_n \boldsymbol{A}(\omega_n) e^{i(\boldsymbol{k}_n \cdot \boldsymbol{r} - \omega_n t)} \tag{2.20}$$

where the summation is now performed over both positive and negative frequencies. According to the definition of electric field:

$$\boldsymbol{E}(\boldsymbol{r}, t) = \mathcal{E} cos(\boldsymbol{k} \cdot \boldsymbol{r} - \omega t) \tag{2.21}$$

it is possible to write a relationship between the spatially slowly varying field amplitude and the physical field amplitude $\mathcal{E}$ [9]:

$$\boldsymbol{A}(\omega) = \boldsymbol{A}(-\omega) = \frac{1}{2}\mathcal{E} \tag{2.22}$$

Using a similar notation to that of the equation (2.20) it is possible to write the expression of $\boldsymbol{P}$:

$$\boldsymbol{P}(\boldsymbol{r}, t) = \sum_n \boldsymbol{P}(\omega_n) e^{-i\omega_n t} \tag{2.23}$$

where again the summation is performed over both positive and negative frequencies.

In linear regime, the i^{th} component of the polarization in frequency domain will be expressed by:

$$P_i^L(\omega) = \epsilon_0 \chi_{ij}^{(1)}(\omega;\omega) E_j(\omega) \tag{2.24}$$

where $\chi_{ij}^{(1)}(\omega;\omega)$, the linear electric susceptibility, in isotropic medium is a scalar quantity which is related to the refractive index according to the relationship $n(\omega) = Re\left(\sqrt{1+\chi^{(1)}(\omega;\omega)}\right)$[6]. In nonlinear regime, assuming that the medium possesses a second order electric nonlinear susceptibility $\chi^{(2)}$, a second order nonlinear polarization has to be taken into account. The i^{th} component of this nonlinear polarization is expressed by:

$$P_i^{NL}(\omega_n + \omega_m) = \epsilon_0 \sum_{jk} \sum_{(nm)} \chi_{ijk}^{(2)}(\omega_n + \omega_m; \omega_n, \omega_m) E_j(\omega_n) E_k(\omega_m) \tag{2.25}$$

where i, j, k refer to the Cartesian components of the fields. The notation (nm) indicates that, in performing the summation over n and m, the sum $\omega_n + \omega_m$ is to be held fixed, although ω_n and ω_m are each allowed to vary. The equation (2.25) can be written as:

$$P_i^{NL}(\omega_n + \omega_m) = \epsilon_0 D \sum_{jk} \chi_{ijk}^{(2)}(\omega_n + \omega_m; \omega_n, \omega_m) E_j(\omega_n) E_k(\omega_m) \tag{2.26}$$

where D is called *degeneracy factor* and is equal to the number of distinct permutations of the applied field frequencies ω_n and ω_m.

If we now consider the equation (2.17) and calculate the curl of both the members, exploiting the equation (2.18) we obtain:

$$\boldsymbol{\nabla} \times \boldsymbol{\nabla} \times \boldsymbol{E} + \frac{1}{c^2}\frac{\partial^2 \boldsymbol{E}}{\partial t^2} = -\frac{1}{\epsilon_0 c^2}\frac{\partial^2 \boldsymbol{P}}{\partial t^2} \tag{2.27}$$

where we used the relationship $c^2 = 1/\mu_0\epsilon_0$, with c the speed of the light in free space. Applying a well known identity of the vector calculus to the electric field in the equation (2.27) and assuming that even in nonlinear optics the term $\boldsymbol{\nabla}(\boldsymbol{\nabla} \cdot \boldsymbol{E})$ is negligible for cases of interest, we obtain the following form for the nonlinear wave equation in the time domain:

$$\boldsymbol{\nabla}^2 \boldsymbol{E} - \frac{1}{c^2}\frac{\partial^2 \boldsymbol{E}}{\partial t^2} = \frac{1}{\epsilon_0 c^2}\frac{\partial^2 \boldsymbol{P}}{\partial t^2} \tag{2.28}$$

If we separate the polarization vector and the displacement field in their linear and nonlinear part, respectively as $\boldsymbol{P} = \boldsymbol{P}^{(1)} + \boldsymbol{P}^{NL}$ and $\boldsymbol{D} = \boldsymbol{D}^{(1)} + \boldsymbol{P}^{NL}$, with $\boldsymbol{D}^{(1)} = \epsilon_0 \boldsymbol{E} + \boldsymbol{P}^{(1)}$, we can write the nonlinear wave equation (2.28) in the form:

$$\boldsymbol{\nabla}^2 \boldsymbol{E} - \frac{1}{\epsilon_0 c^2}\frac{\partial^2 \boldsymbol{D}^{(1)}}{\partial t^2} = \frac{1}{\epsilon_0 c^2}\frac{\partial^2 \boldsymbol{P}^{NL}}{\partial t^2} \tag{2.29}$$

In a lossless and dispersionless medium $\boldsymbol{D}^{(1)} = \epsilon_0 \boldsymbol{\epsilon}^{(1)} \cdot \boldsymbol{E}$, where $\boldsymbol{\epsilon^{(1)}}$ is a real, frequency-independent dielectric tensor, whose elements are defined as $\epsilon_{ij}(\omega_n) = \delta_{ij} + \chi_{ij}^{(1)}(\omega_n)$, with ω_n the n^{th} frequency component of the electric field, $\chi_{ij}^{(1)}$ the components of the linear susceptibility tensor. If the medium is also isotropic, $\boldsymbol{\epsilon^{(1)}}$ is a scalar quantity $\epsilon^{(1)}$ defined as the relative permittivity of the medium. So, for the simplest case of an isotropic, lossless and dispersionless medium, the nonlinear wave equation becomes:

$$\boldsymbol{\nabla}^2 \boldsymbol{E} - \frac{n^2}{c^2}\frac{\partial^2 \boldsymbol{E}}{\partial t^2} = \frac{1}{\epsilon_0 c^2}\frac{\partial^2 \boldsymbol{P}^{NL}}{\partial t^2} \tag{2.30}$$

The equation (2.30) represents an inhomogeneous wave equation where the nonlinear term on the right-hand side is the source of an electric field $\boldsymbol{E}(t)$, while if this term is absent, the equation (2.30) admits as solutions free waves which propagate with velocity c/n, with $n^2 = \epsilon^{(1)}$.

When the medium is dispersive it is necessary to decompose each field involved in the description of the light wave propagation in nonlinear regime in its frequency components and each frequency component in its complex amplitude. Neglecting dissipation, we can write:

$$\boldsymbol{D}_n^{(1)}(\boldsymbol{r},t) = \epsilon_0 \boldsymbol{\epsilon}^{\mathbf{(1)}}(\omega_n) \cdot \boldsymbol{E_n}(\boldsymbol{r},t) \tag{2.31}$$

where $\boldsymbol{\epsilon}^{\mathbf{(1)}}$ is the real, frequency-dependent dielectric tensor. The nonlinear wave equation (2.30) becomes:

$$\boldsymbol{\nabla}^2 \boldsymbol{E}_n - \frac{\epsilon^{(1)}(\omega_n)}{c^2}\frac{\partial^2 \boldsymbol{E}_n}{\partial t^2} = \frac{1}{\epsilon_0 c^2}\frac{\partial^2 \boldsymbol{P}_n^{NL}}{\partial t^2} \tag{2.32}$$

2.2.2 Parametric interactions in $\chi^{(2)}$ media

A parametric process is characterized by the same initial and final quantum-mechanical status of the system and by the fact the population can be moved from the ground level for a brief time when it is in a virtual level. A relevant feature of a parametric process is that the energy of the photons is always conserved [9]. Because of the smallness of the nonlinear polarization term, it is preferable to solve the equation (2.30), which describes the parametric interactions in a medium characterized by a non zero value of $\chi^{(2)}$, by means of a perturbative approach [43]. For the sake of simplicity we assume that all the elements of the tensor $\chi^{(2)}_{ijk}$ are null apart from $\chi^{(2)}_{xxx} = 3\chi^{(2)}_{xyy} = 3\chi^{(2)}_{yxy} = 3\chi^{(2)}_{yyx}$ (please consider as coordinate system the one reported in Fig. 2.1), such as for poled silica glass [44] and that the interacting wave is linearly polarized along the $\hat{x}$ direction in such a way the only component of the second order nonlinear susceptibility tensor to be considered is $\chi^{(2)}_{xxx}$. If we assume that two monochromatic waves (ω_1 and ω_2) interact with the $\chi^{(2)}$ medium, we can obtain the expressions of the Fourier components of $\boldsymbol{P}^{NL}(\omega_n)$ for the different parametric processes which happen in the nonlinear medium [9]:

$$\begin{aligned}
P(2\omega_1) \propto \chi^{(2)} E_1^2 &\qquad (SHG)\\
P(2\omega_2) \propto \chi^{(2)} E_2^2 &\qquad (SHG)\\
P(\omega_1+\omega_2) \propto \chi^{(2)} E_1 E_2 &\qquad (SFG)\\
P(\omega_1-\omega_2) \propto \chi^{(2)} E_1 E_2^* &\qquad (DFG)\\
P(0) \propto \chi^{(2)} (E_1 E_1^* + E_2 E_2^*) &\qquad (OR)
\end{aligned} \tag{2.33}$$

where SHG stands for second harmonic generation, SFG for sum frequency generation, DFG for difference frequency generation, OR for nonlinear optical rectification and the quantity E^* represents the complex conjugate of the electric field amplitude. All the expressions (2.33) represent the nonlinear source terms for the electric field on the left-hand side of the equation (2.30) and can be treated separately because in any case only one of the nonlinear effects cited will be efficiently produced according to the phase-matching condition fulfilled.

If we introduce a new tensor d, whose matrix elements are defined by:

$$d_{ijk} = \frac{1}{2}\chi^{(2)}_{ijk} \tag{2.34}$$

and consider that it is symmetric in the last two indices jk if the Kleinmann symmetry condition is valid (which means that the frequencies involved in the nonlinear interaction are much smaller than the lowest resonance frequency of the material system where they interact in such a way that the nonlinear susceptibility is independent of the frequencies [9]), we can obtain the contracted notation d_{il} according the rules reported in the table 2.1 [9].

jk	11	22	33	23,32	31,13	12,21
l	1	2	3	4	5	6

TABLE 2.1: Rules for obtaining the contracted notation of the tensor d. The numbers 1, 2, 3 represent the coordinates x, y, z in any order because of the validity of the Kleinmann symmetry, which states that the indices ijk can be freely permuted.

For a fixed geometry (i.e., for fixed propagation and polarization directions) it is possible to express the nonlinear polarization giving rise to SHG by means of the scalar relationship [9]:

$$P^{NL}(2\omega) = 2\epsilon_0 d_{eff}(2\omega;\omega,\omega)E^2(\omega) \tag{2.35}$$

where $E(\omega) = |\boldsymbol{E(\omega)}|$, $P(\omega) = |\boldsymbol{P(\omega)}|$ and d_{eff} is obtained by first determining $\boldsymbol{P}$ explicitly through use of Eq. 2.26 and considering that the nonlinear medium where the interaction takes place is characterized by a particular form of the matrix corresponding to the tensor d. According to the particular type of tensor d it is possible to distinguish the nonlinear crystals in different categories, such as for example tetragonal, cubic, trigonal, etc [9].

2.2.3 Second harmonic generation (SHG)

Second harmonic generation is a nonlinear effect created in a nonlinear medium possessing a non-negligible second order susceptibility $\chi^{(2)}$ when it is illuminated by a light wave of a certain power and which can be assumed, for the sake of simplicity, monochromatic, collimated and continuous. SHG is a three waves process, described schematically in Fig. 2.9, and can be considered a special case of SFG, where two photons of frequency $\omega_1 = \omega_2 = \omega$ interact with a photon of frequency $\omega_3 = \omega_1 + \omega_2 = 2\omega$. The second order nonlinear polarization vector related to the SHG, in case of interacting electric field aligned along the $\hat{x}$ direction and considering only the component of the second order nonlinear susceptibility tensor $\chi^{(2)}_{xxx}$, can be expressed by [9]:

$$P^{NL}(\omega_3) = 2\epsilon_0 d_{33}(\omega_3;\omega,\omega)E^2(\omega) = 2\epsilon_0 d_{33}(\omega_3;\omega,\omega)A^2(\omega)e^{i2k(\omega)z} \tag{2.36}$$

where $k(\omega) = n(\omega)\omega/c$, A is the spatially slowly varying field amplitude of the electric field corresponding to the frequency ω, and d_{33} is a component of the tensor d, which in our case is expressed by:

$$d_{33}(\omega_3;\omega,\omega) = \frac{\chi_{333}(\omega_3;\omega,\omega)^{(2)}}{2} = \frac{\chi_{xxx}(\omega_3;\omega,\omega)^{(2)}}{2} \tag{2.37}$$

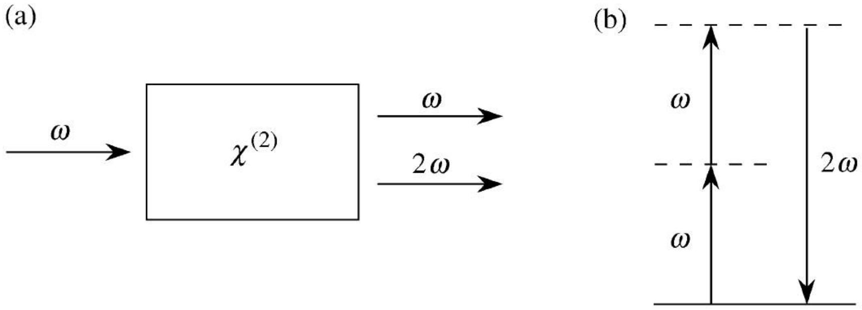

Figure 2.9: (a) Geometrical illustration of the SHG; (b) Quantum mechanical view of the SHG: two photons at frequency ω are destroyed while a photon at frequency 2ω is created [9].

The perturbative approach consists in the assumption that the solutions to the full nonlinear wave equation (2.30) are similar in their form to the solutions of the wave equation where the nonlinear source term is absent (plane waves) [43]. Furthermore, if we assume that the electric field magnitude A depends only on the spatial coordinate z and we use the equation (2.36) for $P^{NL}(\omega_3)$, we obtain the nonlinear wave equation for the second harmonic spatially slowly varying field amplitude A_3:

$$\left[\frac{\mathrm{d}^2 A_3}{\mathrm{d}z^2} + 2ik(\omega_3)\frac{\mathrm{d}A_3}{\mathrm{d}z} - k(\omega_3)^2 A_3 + \frac{\epsilon^{(1)}(\omega_3)\omega_3^2 A_3}{c^2}\right] e^{(ik(\omega_3)z-\omega_3 t)} + \; c.c.$$

$$= \frac{-2d_{33}\omega_3^2}{c^2}\left[A^2 e^{i(2k(\omega)z-\omega_3 t)} + c.c.\right] \tag{2.38}$$

where $k(\omega_3) = n(\omega_3)\omega_3/c$. The equation (2.38) can be simplified if we consider that the equality is still preserved if we drop from both the sides the exponential time dependent terms and the complex conjugate terms. Furthermore we can assume that the *slowly varying envelope approximation (SVEA)* is valid:

$$\left|\frac{\mathrm{d}^2 A_3}{\mathrm{d}z^2}\right| \ll \left|k(\omega_3)\frac{\mathrm{d}A_3}{\mathrm{d}z}\right| \tag{2.39}$$

The nonlinear wave equation for the second harmonic spatially slowly varying field amplitude A_3 becomes:

$$\frac{\mathrm{d}A_3}{\mathrm{d}z} = \frac{i\omega_3^2 d_{33}}{k(\omega_3)c^2} A^2 e^{i\Delta k\cdot z} \tag{2.40}$$

where Δk (the momentum mismatch) is expressed by the equation:

$$\Delta k = k(\omega) + k(\omega) - k(\omega_3) = 2k(\omega) - k(\omega_3) \tag{2.41}$$

For each of the two incoming photons of frequency ω the nonlinear wave equation can be written as:

$$\frac{\mathrm{d}A}{\mathrm{d}z} = \frac{2i\omega^2 d_{33}}{k(\omega)c^2} A_3 A^* e^{-i\Delta k\cdot z} \tag{2.42}$$

2.2.4 Phase-matching in SHG

The equations (2.40) and (2.42), reported in section 2.2.3, are defined coupled-amplitude equations, because they establish how the amplitude of each of the two waves ω and $\omega_3 = 2\omega$ varies in consequence of the coupling to the other one [9]. If we assume to be in a regime of undepleted pump (A is constant), we will see that when $\Delta k = 0$, the second harmonic amplitude A_3 increases linearly with $\hat{z}$ and consequently the second harmonic intensity increases quadratically with $\hat{z}$ besides increasing quadratically with the pump power (see equation (2.44)). When perfect phase-matching (PPM) condition ($\Delta k = 0$) is fulfilled, the second harmonic field can extract efficiently energy from the pump while microscopically all the induced electric dipoles oscillate in phase in such a way each field emitted by any of them adds coherently to all the other electric fields, creating a condition of interference. Indeed, the PPM condition corresponds to the situation where the phase velocity of the nonlinear polarization component related to the SH $P^{NL}(\omega_3 = 2\omega)$ ($2\omega/2k(\omega)$ $= \omega/k(\omega)$ = pump phase velocity) is equal to the phase velocity of the electromagnetic wave A_3, generated by $P^{NL}(\omega_3)$ and oscillating at $\omega_3 = 2\omega$ ($2\omega/k(2\omega)$).

If the phase-matching condition is not fulfilled, the second harmonic field A_3 can be calculated integrating the equation (2.40) along the length L of the nonlinear medium:

$$A_3(L) = \frac{id_{33}\omega_3^2}{k(\omega_3)c^2}A^2 \int_0^L e^{i\Delta k \cdot z} dz = \frac{id_{33}\omega_3^2}{k(\omega_3)c^2}A^2 \left(\frac{e^{i\Delta k \cdot L} - 1}{i\Delta k} \right) \tag{2.43}$$

The intensity of the ω_3 wave is given by the magnitude of the time-averaged Poyting vector [9]:

$$I_3 = 2n(\omega_3)\epsilon_0 c |A_3(L)|^2 = \frac{2n(\omega_3)\epsilon_0 d_{33}^2 \omega_3^4 |A|^4}{k^2(\omega_3)c^3} \left| \frac{e^{i\Delta k \cdot L} - 1}{\Delta k} \right|^2 \tag{2.44}$$

After some calculations, it is possible to obtain the expression of the intensity of the second harmonic wave generated in the nonlinear medium by means of nonlinear interaction between the two pump waves [6]:

$$I_3 = \frac{d_{33}^2 \omega_3^2 I^2}{2n^2(\omega)n(\omega_3)\epsilon_0 c^3} L^2 sinc^2 \left(\frac{\Delta k \cdot L}{2} \right) \tag{2.45}$$

where the expression of $k(\omega_3) = n(\omega_3)\omega_3/c$ and the definition of the pump intensity $I = 2\epsilon_0 n(\omega)c|A|^2$ have been used. The equation (2.45) expresses the fact that the intensity of the three-wave mixing process (in this case SHG) decreases as $|\Delta k|L$ (which represents the phase difference $\Delta\phi$ accumulated in a path of length L by $P^{NL}(\omega_3)$ and A_3) increases, with some oscillations occurring. In particular, when $L = L_c = |\pi/\Delta k|$, $\Delta\phi = \pi$, and the two waves are out of phase. L_c is called *coherence length* [6].

From the definition of Δk given by the equation (2.41) it is clear that the possibility of obtaining a perfect phase-matching condition depends on the possibility of choosing the refractive indices of the medium related to the frequency components involved in the nonlinear phenomenon in such a way the condition can be fulfilled. This means that it will be impossible to obtain the condition $\Delta k = 0$ if all the fields involved propagate along the same direction, because of the intrinsic dispersion of the medium. Nevertheless there are few techniques to circumvent this limit, such as for example the *Birefringent phase-matching (BPM)*, which exploits the dependence of the refractive index on the propagation direction to obtain a PPM condition [45]. The procedure to obtain BPM requires to polarize the radiation with the highest value of frequency (the second harmonic in our case) along the direction which gives the lowest refractive index and vice-versa. In order to carefully control the refractive indices involved into the process of SHG it is possible to use two different methods, namely the *angle tuning* and the *temperature tuning*. The description of these two methods is beyond the scope of this thesis, so it will not be discussed.

2.2.5 Quasi-phase-matching (QPM) in SHG

The PPM condition cannot be obtained in materials which lack any birefringence or are characterized by a birefringence not big enough to compensate the wavevector mismatch Δk. However in cases where normal phase-matching condition cannot be fulfilled it is possible to resort to a quasi-phase-matching (QPM) technique [28]. The working principle of this technique is based on the idea of compensating periodically the delay accumulated by the slower wave from the faster one by means of a spatial modulation of the nonlinear coefficient. This technique is perfectly suitable for materials where it would be otherwise impossible to produce phase-matching, such as for example the silica glass a poled fibre is made of. A typical medium where the QPM technique is used is defined periodically poled material, which is a structure fabricated in such a way that the orientation of one of the crystalline axes is inverted periodically as function of the position along the propagation axis. The inversion of the orientation corresponds to the inversion of the sign of nonlinear tensor element d_{33}, which can compensate the Δk simply adding (between *pump* (which possesses the same phase velocity of $P^{NL}(\omega_3)$) and *SH*) a further phase shift of π which brings back in phase $P^{NL}(\omega_3)$ and A_3. In Fig. 2.10 are reported the schematic of a periodically poled material and the visual explanation of the QPM condition.

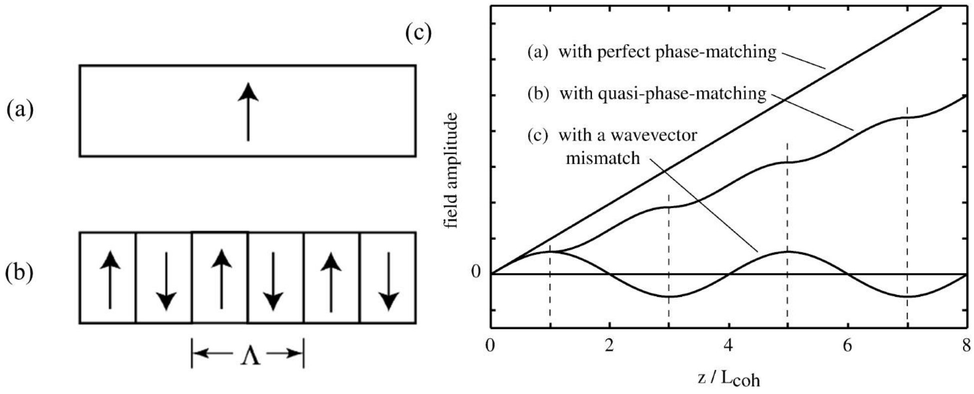

FIGURE 2.10: (a) schematic of a homogeneous single crystal; (b) schematic of a periodically poled material with crystalline axis c inverted with a period Λ; (c) comparison of the trends of the second harmonic field amplitude vs. propagation distance z/L_c, where L_c is the coherence length of the nonlinear interaction [9].

2.2.6 SHG in poled optical fibres

In this section it will be reported the model which describes the nonlinear phenomenon of SHG in a silica fibre which possesses a non-negligible $\chi^{(2)}$. This kind of fibre will be described exhaustively in chapter 3. In the meantime we assume simply that it can be considered a $\chi^{(2)}$ material, where the second order susceptibility tensor is characterized by the conditions already discussed in section 2.2.2, namely: all the elements of the tensor $\chi^{(2)}_{ijk}$ are null apart from $\chi^{(2)}_{xxx} = 3\chi^{(2)}_{xyy} = 3\chi^{(2)}_{yxy} = 3\chi^{(2)}_{yyx}$.

The model to describe nonlinear phenomena in an optical fibre is developed in the so-called *weakly guiding approximation* [46], which assumes that $\Delta n = (n_{co} - n_{cl}) \ll 1$, a condition which will be fulfilled in all our experimental conditions where step-index fibres will be involved. The base of the model, developed by Marcuse [47, 48] and Snyder and Love [49], is the assumption that the fibre modes can be approximated by the LP_{lm}(*Linearly Polarized*) modes, so the electromagnetic field E, propagating along the $\hat{z}$ direction and polarized along the $\hat{x}$ direction, is expressed by:

$$E_x(z,r,\phi,t) = \frac{1}{2}\sum_{l,m}\left[A_{lm}(z)LP_{lm}(r,\phi)e^{i(\beta_{lm}z-\omega t)} + c.c.\right] \tag{2.46}$$

where β_{lm} is the propagation constant for the mode l,m and the LP_{lm} modes are normalized in such a way $\langle LP_{lm}|LP_{jk}\rangle = \delta_{jl}\delta_{km}$. If the expression (2.46) is introduced into the nonlinear wave equation (2.30), and the SVEA approximation

(2.39) is taken into account, it is possible to obtain a coupled-amplitude equation similar to the (2.38), where the main difference consists in the fact that in the case of an optical fibre it is necessary to consider the presence of many modes in the interaction, each characterized by its particular β vector. Furthermore it is possible to assume that the optical fibre is single-mode at the pump frequency, allowing for the generation of the LP_{01} mode only.

If we want to obtain the nonlinear wave equation for the SHG in an optical fibre, we can consider the QPM condition, which can be represented by a nonlinear coefficient d periodic function in $\hat{z}$ of period Λ [28]:

$$d(r,\phi,z) = \sum_m \tilde{d}_m(r,\phi)e^{-iK_m z} \tag{2.47}$$

where:

$$K_m = \frac{2\pi m}{\Lambda} \tag{2.48}$$

and

$$\tilde{d}_m(r,\phi) = \frac{1}{\Lambda}\int_0^{\Lambda} d(r,\phi,z)e^{iK_m z}dz \tag{2.49}$$

In the particular case of a square wave modulation of the nonlinear coefficient d, where d can assume periodically only two values, namely 0 and d_{MAX} with a period of Λ, the equation (2.49) becomes:

$$\tilde{d}_m(r,\phi) = \frac{d_{33}(r,\phi)}{m\pi}e^{im\pi}\sin{(m\pi D)} \tag{2.50}$$

where d_{33} is the nonlinear tensor component defined by the equation (2.37) in the specific case of a poled fibre and D is the duty cycle, the ratio between the length of the positive portion of the modulation and the period. In case of a square wave modulation, for $m = 1$, the highest value of the nonlinear coefficient if obtained for a duty cycle of 50%. The two coupled amplitude nonlinear equations for the second harmonic and the pump fields in a SHG process in optical fibres are given by:

$$\frac{\mathrm{d}A_{2\omega}(z)}{\mathrm{d}z} = i\frac{\omega}{c(n_{2\omega}^{eff})}A_{\omega}^{2}(z)d_{eff}^{SH}I_{OVL}^{SH}\sum_{m}e^{i[\beta(2\omega)-2\beta(\omega)-K_m]z} \tag{2.51}$$

$$\frac{\mathrm{d}A_{\omega}(z)}{\mathrm{d}z} = i\frac{\omega}{c(n_{\omega}^{eff})}A_{2\omega}(z)A_{\omega}^{*}(z)d_{eff}^{SH}I_{OVL}^{SH}\sum_{m}e^{-i[\beta(2\omega)-2\beta(\omega)-K_m]z} \tag{2.52}$$

with:

$$d_{eff}^{SH} = \frac{\iint_{S_{fibre}} \tilde{d}_m(r,\phi)LP_{2\omega}(r,\phi)LP_{\omega}^{2}(r,\phi)d\sigma}{I_{OVL}^{SH}} \tag{2.53}$$

$$I_{OVL}^{SH} = \iint_{S_{fibre}} LP_{2\omega}(r,\phi)LP_{\omega}^{2}(r,\phi)d\sigma \tag{2.54}$$

where the integration is calculated over the cross-section of the fibre S_{fibre} and I_{OVL}^{SH} is the integral overlap for the SHG.

It is useful to obtain an expression for the power associated to each envelope $A(z)$. It is possible to write the average intensity as:

$$I(\boldsymbol{r}) = \frac{1}{2}\epsilon_0 cn\left|A(z)\right|^2\left|LP_{01}(r,\phi)\right|^2 \tag{2.55}$$

where LP_{01} represents the fundamental linearly polarized mode. The power associated to each envelope $A(z)$ is:

$$P(z) = \iint_{S_{fibre}} I(\boldsymbol{r})d\sigma = \frac{1}{2}\epsilon_0 cn\left|A(z)\right|^2 \tag{2.56}$$

The second harmonic power P_{SH} and the second harmonic efficiency η_{SH} can be easily expressed as functions of the pump power P_{ω}, the interaction length L and the *area overlap* $A_{OVL} = |1/I_{OVL}|^2$:

$$P_{SH} = \frac{2\omega^2\left|d_{eff}^{SH}\right|^2 L^2 P_{\omega}^2}{\epsilon_0 c^3 (n_{\omega}^{eff})^2 (n_{2\omega}^{eff}) A_{OVL}} sinc^2\left(\frac{\Delta K\cdot L}{2}\right) \tag{2.57}$$

$$\eta_{SH} = \frac{2\omega^2\left|d_{eff}^{SH}\right|^2 L^2 P_{\omega}}{\epsilon_0 c^3 (n_{\omega}^{eff})^2 (n_{2\omega}^{eff}) A_{OVL}} sinc^2\left(\frac{\Delta K\cdot L}{2}\right) \tag{2.58}$$

where at the first order of approximation:

$$\Delta K = \beta(2\omega) - 2\beta(\omega) - K_{m=1} = \beta(2\omega) - 2\beta(\omega) - 2\pi/\Lambda \tag{2.59}$$

If the QPM condition is fulfilled ($\Delta K = 0$), the SH efficiency is given by:

$$\eta_{SH} = \frac{2\omega^2 \left| d_{eff}^{SH} \right|^2 L^2 P_\omega}{\epsilon_0 c^3 (n_\omega^{eff})^2 (n_{2\omega}^{eff}) A_{OVL}} \tag{2.60}$$

It is worth highlighting that the expression (2.60) is valid strictly only when the SHG process involves a single frequency and a CW pump. If the light wave which interacts with the nonlinear medium contains a large spectrum of wavelengths and consists of an intense pulses train, the SHG process becomes more complex, mixing processes among the various wavelengths involved cannot be anymore neglected and furthermore the approximation of undepleted pump is not anymore valid (A_ω cannot be considered anymore a constant during the nonlinear interaction).

It is interesting to consider that while in the case of a periodically poled material as the one reported in Fig. 2.10 (b) the QPM consists in bringing back in phase $P^{NL}(\omega_3)$ and A_3 adding a futher π phase shift every L_c, in the periodically poled fibres the mechanism to bring back in phase $P^{NL}(\omega_3)$ and A_3 is different. After an interaction length (between *pump* and *SH*) of L_c, where $d_{33} \neq 0$, $P^{NL}(\omega_3)$ and A_3 accumulate a phase difference of π. At this point the region of the fibre with $d_{33} = 0$ begins, and so $P^{NL}(\omega_3) = 0$ and A_3 is not generated anymore and only the *pump* and the *SH* generated in the previous nonlinear region of the fibre travel. After a further length of L_c, *pump* and A_3 previously generated are back in phase and so A_3 can be generated again and added coherently to the previous one. This procedure, repeated periodically along a certain length L, gives rise to a QPM SHG, whose efficiency is smaller than a periodically poled material based on the inversion of d. In Fig. 2.11 the SH intensity is plotted vs. length of propagation in a periodically poled silica fibre (PPSF).

Another important consideration is that the efficiency of SHG in QPM condition (even in the case of a periodically poled material based on the inversion of nonlinear coefficient d) is smaller than the corresponding value which could be ideally

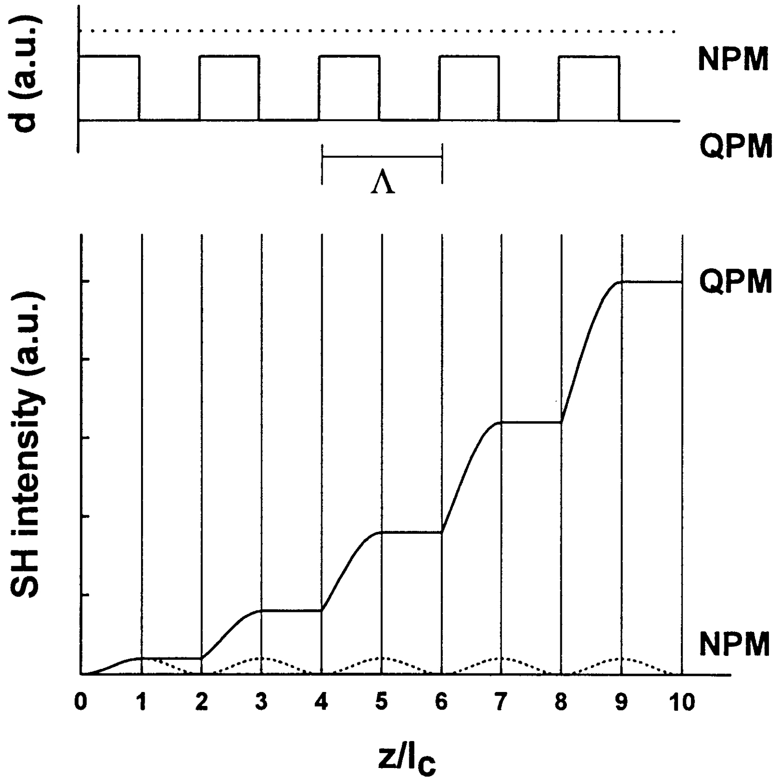

Figure 2.11: First-order quasi-phase matching in a periodically poled optical fibre. The nonlinear coefficient d is modulated over a period equal to twice the coherence length by periodic alternation of poled and unpoled sections. The step growth for the SH intensity is quasi-quadratic (solid curve). The non phase-matched (NPM) case is also shown [50].

obtained in PPM condition. This becomes straightforward if we consider the definition of d_{eff}^{SH} expressed by the Eq. 2.53, whose value depends on the value of $\tilde{d}_m(r,\phi)$, which, even at the first order of phase matching, is smaller than d_{33}.

Speaking about pulsed pump radiation, it is relevant the definition of the *bandwidth* of the SHG process, that is the range of wavelengths where the frequency conversion is efficient, which, in first approximation, is given by [51]:

$$\Delta\lambda \simeq \frac{0.44\lambda_F^2}{cL \cdot GVM} \tag{2.61}$$

where λ_F is the wavelength of the pump, GVM is the group velocity mismatch, defined as [52]:

$$GVM = \left|v_g^{-1}(2\omega) - v_g^{-1}(\omega)\right| \tag{2.62}$$

with v_g the group velocity, defined as:

$$v_g = \left.\frac{\partial \omega}{\partial \beta}\right|_{\omega} \tag{2.63}$$

The role of GVM can be expressed by the fact that in order to have an efficient nonlinear interaction, the two interacting fields must overlap in space. If the GVM is a relevant quantity, after a certain interaction length $L_{GVM} = \tau/GVM$, with τ the pulse duration, the two fields will have walked off, reducing the SH efficiency [53]. Another spurious effect which could reduce the SH efficiency happens whenever the pulse duration of the pump radiation is so small (its optical spectrum is so wide) that the bandwidth could be not large enough to allow phase-matching for all the wavelengths involved, filtering some of them [54].

2.2.7 Other second order nonlinear effects in poled silica fibres

The SHG produced in a periodically poled silica fibre (PPSF) can allow for the implementation not only of basic frequency doublers, but also of some more complex all-fibre nonlinear photonic devices such as for example sources of higher-order harmonics (in particular in the UV region of the light spectrum) where the periodically poled fibre can be used as source of the second harmonic which mixes with the pump in microfibres via a four-wave mixing process [55]. See sections 5.3.1 and 5.3.2 for details and references about this type of application.

Another kind of device which could be realized by using PPSFs is represented by light sources whose spectrum is composed of a sequence of equally spaced frequency components (*Purely Quadratic Frequency Combs*), based on the resonance between the pump and the second harmonic generated into the periodically poled fibre, which is used as resonator in this case [26]. See section 7.2.4.1 for a more exaustive explanation of this application.

Apart from harmonic generation, the effective second order susceptibility $\chi^{(2)}_{eff}$, induced in an optical fibre via thermal poling, could be even exploited to produce some other nonlinear effects with the aim of creating sources of polarization-entangled photon pairs (based on the *Spontaneous parametric down conversion*

(SPDC)) and all-fibre beam modulators or switches (based on the *Linear electro-optic (Pockels) effect*). In the next two sections a brief reminder about these different second order nonlinear phenomena is reported.

2.2.7.1 Spontaneous parametric down conversion (SPDC)

In the section 2.2.2, among the possible nonlinear effects associated with a non-zero second order susceptibility $\chi^{(2)}$, we included DFG, whose Fourier component is given by the fourth one of the equations (2.33). This effect occurs when a photon of frequency ω_3 equal to the difference between the frequency ω_1 and the frequency ω_2 is generated. In terms of the energy diagram (see Fig. 2.12), for every photon that is created at the difference frequency $\omega_3 = \omega_1 - \omega_2$, a photon at the higher input frequency ω_1 must be destroyed and a photon at a lower input frequency ω_2 must be created. Thus, the lower frequency input field is amplified by the process of DFG. For this reason, the DFG process is also known as "optical parametric amplification" (OPA). According to the photon energy level description, the atom firstly absorbs a photon of frequency ω_1 and jumps to the highest virtual level. This level decays by a two-photon emission process that is stimulated by the presence of the ω_2 field, which is already present. The two-photon emission process can occur even if the field ω_2 is not applied. The generated fields in such a case are very much weaker, since they are created by spontaneous two-photon emission from a virtual level. This process is known as "parametric fluorescence" or "spontaneous parametric down conversion" (SPDC) [9].

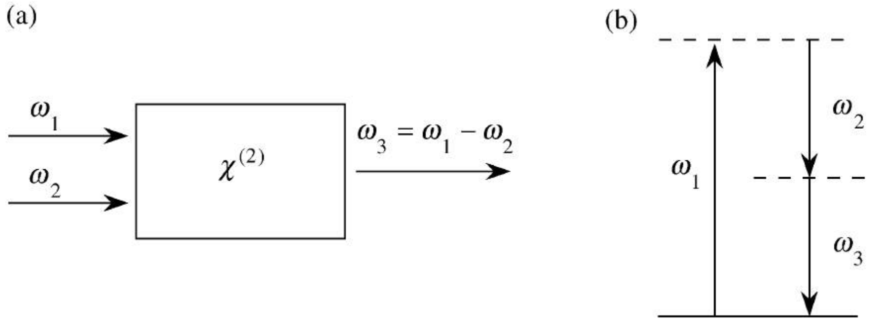

FIGURE 2.12: (a) Geometrical illustration of DFG; (b) energy diagram of the DFG: a photon at frequency ω_1 is destroyed and two photons respectively at frequencies ω_2 and ω_3 are created [9].

If the nonlinear medium where the DFG is produced is placed into an optical resonator (see Fig. 2.13), the frequency ω_2 can be amplified. A device like this one is called "optical parametric oscillator" (OPO), which is a tunable device because, for a given frequency ω_3 any frequency $\omega_2 < \omega_1$ can fulfil the condition $\omega_2 + \omega_3 = \omega_1$. Practically it is possible to control the output frequency of an optical parametric oscillator by adjusting the phase-matching condition. The applied field frequency ω_1 is called *pump*, the desired output frequency ω_2 is called *signal* and the other output frequency ω_3 is called *idler*.

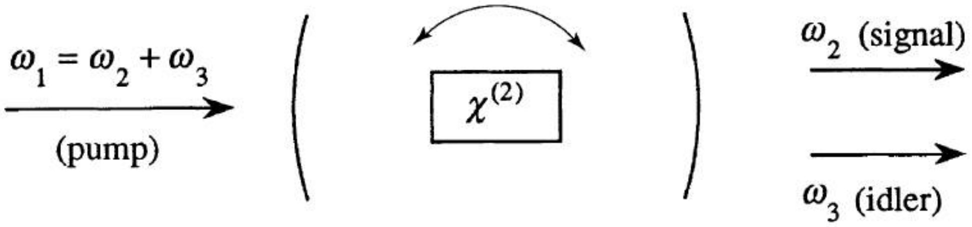

FIGURE 2.13: The optical parametric oscillator. The cavity end mirrors have high reflectivities at frequencies ω_2 and/or ω_3. The output frequencies can be tuned by means of the orientation of the crystal [9].

In section 7.2.4.2 it will be explained better how the SPDC can be exploited in a PPSF to generate polarization-entangled photon pairs.

2.2.7.2 Linear electro-optic (Pockels) effect

The linear electro-optic effect is a second order effect which can be observed when two optical fields (one oscillating at frequency ω and the other one static) interact inside a nonlinear medium. This effect can be described in terms of nonlinear polarization adapting the equation (2.25) to the described situation [6]:

$$P_i^{NL}(\omega) = 2\epsilon_0 \chi_{ijk}^{(2)}(\omega; \omega, 0) E_j(\omega) E_k(0) \tag{2.64}$$

where $E_j(\omega)$ is the applied optical field and $E_k(0)$ is the static electric field and the degeneracy factor $g_{\alpha\beta}$ is 2 in this case. If we consider the global expression of the polarization, we note that there is an extra term which is linear in the optical field and whose magnitude is proportional to the static electric field. In terms of the effect on the optical wave of frequency ω, the presence of the extra term given by the equation (2.64) is equivalent to a change in the linear susceptibility of the material $\chi^{(1)}$ of an amount proportional to the static electric field. In other words the refractive index of the material at the optical frequency ω depends on the static electric field. This dependence allows to use this effect in beam modulators or switches.

2.3 Thermal poling

2.3.1 Structure of silicate glasses

A glass is defined by the *American Society for Testing Materials* (*ASTM*) [56] as an "inorganic product of fusion which has been cooled to a rigid condition without crystallization", so it is considered a branch of the group of amorphous solids whose atomic structure lacks the so-called "long range regularity", typical of a crystalline material, as shown in Fig. 2.14. If we consider the most common kind of glass, called vitreous silica (or fused quartz), we see that the basic molecule which defines its composition is SiO_2 (silicon dioxide). In this type of glass each silicon is bonded tetrahedrally to four oxygen at a distance of $Si - O = 0.162\ nm$ while each oxygen is bonded to two silicons [58]. Different varieties of silica glass can be obtained by melting SiO_2 with other raw materials. If for example some Na_2CO_3 (soda, or sodium carbonate) is added to the initial molten mixture, it is

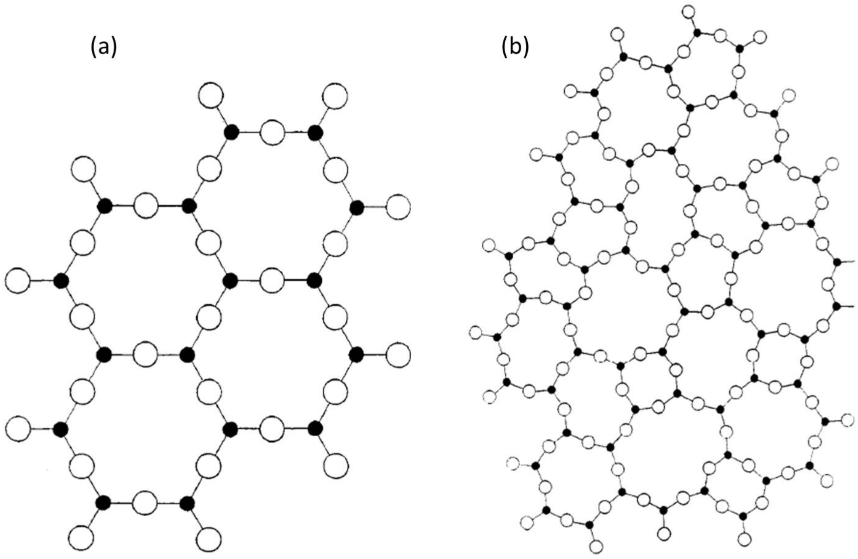

FIGURE 2.14: Schematic of the arrangement in two dimensions of (a) a crystal of composition A_2O_3 and (b) the glass network of the same compound. The letter "A" stands for a whatever atom of a silicate group bound to the three oxygen atoms in the 2D crystal [57].

possible to create the so-called soda-silica glass. In this case, because of the oxygen introduced by the soda, each silicon is still bonded to four oxygens, while each oxygen cannot be bonded anymore to two silicon atoms, in such a way that there are two types of oxygen bonds, those with two silicon atoms and those with just one silicon, also defined as non-bridging oxygen (NBO^-) centres [59]. In other words there are holes in the silicon-oxygen network, and it is in these holes that the sodium ions Na^+ are situated randomly, being surrounded by approximately six oxygens as immediate neighbours [60]. In Fig. 2.15 the two dimensional schematic diagram of the soda-silica glass is shown. Any phenomenon of electrolytic conductivity produced in glasses like soda-silica can be seen as the stepwise series of displacements of the Na^+ ions between each of the holes in the $Si - O$ network. A glass can be made of many of these inclusions, such as for example, $Ca^{+2}, K^+, Pb^{+2}, Li^+$, etc [57]. The fused silica Germania doped step-index fibres used in this thesis work are made with the inclusion of some of those impurities which represent, as it will be clear in the next few sections, the main characters of the thermal poling process.

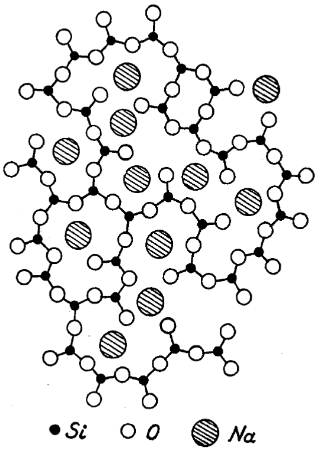

FIGURE 2.15: Two dimensional schematic diagram of the soda-silica glass structure. It can be seen that there are some oxygen atoms bonded to two silicons whereas some others to just one silicon [60]. The sodium ions are located into the holes of the $Si-O$ network, and represent impurities into the glass structure.

2.3.2 Evidence of second order nonlinearities in silica fibres

An amorphous dielectric medium can be considered macroscopically isotropic and centrosymmetric and then invariant by parity inversion, the operation which transforms a vector in another one characterized by the same spatial coordinates in absolute value but with the sign inverted [61]. In centrosymmetric materials the relationship between the polarization and the electric field of the light wave interacting with the medium (see equations (2.14) and (2.25)) possesses an odd symmetry, which means that the polarization vector lacks any term of even power of the electric field [7]. Therefore a glass, which is an amorphous medium, should lack the second order nonlinear susceptibility $\chi^{(2)}$, because of the parity invariance [6]. So, in silica fibres $\chi^{(2)}$ is nominally zero and nonlinear effects linked to the second order susceptibility are negligible.

Nevertheless, in the 1980's there were experimental evidences of some nonlinear effects observed in optical fibres. In particular in the period 1980-1982 the early observations of phase-matched SFG by using waveguide modes of optical fibres were reported. A Q-switched and mode-locked Nd:YAG laser at 1.064 μm was used as pump and the sum-frequency light was generated from the pump and the Stokes lines due to inelastic (Raman) scattering in optical fibres [62–64]. It is due to the work of Gabriagues *et al.* the first ever reported observation of SHG in optical fibres [65] while few years later Osterberg *et al.* realized the first detailed study related to the SHG in a silica fibre pumped with 100-130-psec-long pulses and peak powers of 70 kW produced by a cw mode-locked and Q-switched Nd:YAG laser. After a period of steady illumination, weak second-harmonic radiation was observed at the output end of the fibre and, after a certain time of "preparation", the intensity of the green light increased [66, 67]. Later on it was observed that the "preparation" time could be reduced (from hours to minutes) if, together with the pump pulses, the fibre was also illuminated by light pulses with the same wavelength as the second harmonic wavelength [68]. Two models were proposed to explain this SHG in optical fibres. According to Farries *et al.* a weak non-phase-matched SHG occurs at high pump intensities due to a nonlinear electric quadrupole susceptibility [69] and initiates the self-writing of an axially periodic pattern of colour centres (created at spatial locations where the green light intensity is highest, i.e. where the pump and second-harmonic signal are in phase) which would lead to the growth of a $\chi^{(2)}$ grating [70]. The second model was proposed by Stolen *et al.*, who assume a photoinduced effect which forms the dipole-allowed second order susceptibility. Basically the pump and the external (or even the internal) seeding light (of frequency corresponding to the second harmonic of the pump) mix by means of a third order nonlinear optical rectification process to create a DC polarization at the phase-matching periodicity which orients the defects. The oriented defects can produce a direct dipole-allowed nonlinear susceptibility $\chi^{(2)}$, which has the proper periodicity for phase-matched SHG [68]. Therefore the fibre organizes itself for phase-matching and the permanently written periodic nonlinearity created into the fibre produces an efficient SHG in the fibre.

Despite some evident limits of the photoinduced second order nonlinear effects generated in optical fibres, such as for example the length of the self-written phase-matched gratings, which is limited by the chromatic dispersion of the medium and the phase modulation [68], the relatively low SH efficiency estimated [71] and the dependence of the SH efficiency by the dopants/defects in the glass [72], which made them not very attractive, a big effort was produced to explore the chance of making these nonlinear phenomena generated in optical fibres more efficient, and the dream of replacing expensive nonlinear crystals with cheap all-fibre nonlinear devices was not completely abandoned.

Given that it was supposed that the origin of the creation of the self-written grating was the DC polarization generated by a third order nonlinear optical rectification process, the idea of exploiting DC electric fields applied externally to the fibre started to circulate among the researchers. Finally Kashyap demonstrated the possibility to generate a phase-matched electric-field-induced second harmonic (EFISH) in single-mode Germania-doped silica fibres [73]. By using a rotatable interdigitated electrode structure it is possible to apply a spatial electric field across the core, which is periodic along the propagation direction of the fibre. As a result, the spatial static field induces a periodic effective second order nonlinearity $\chi^{(2)} \propto \chi^{(3)}\boldsymbol{E}$, where $\boldsymbol{E}$ is the electric field applied across the core and $\chi^{(3)}$ is the third order nonlinear susceptibility of the silica glass which the optical fibre is made of. The rotation of the electrode allows for the control over the periodicity of the applied electric field which compensates the wavevector mismatch between the pump and the second harmonic propagating along the fibre (see section 2.2.5).

2.3.3 Permanent induction of effective $\chi^{(2)}$ in glasses

Although the work of Kashyap [73] demonstrated the possibility of producing efficient SHG in optical fibres by means of the application of an external periodic electric field via a mechanism of third order nonlinear optical rectification, the SHG was still a temporary effect, in the sense that if the externally applied electric field was removed, the second harmonic generation process would stop.

Finally in 1991 Myers *et al.* demonstrated the possibility of inducing a large effective second order nonlinear susceptibility ($\chi^{(2)} \sim 1\ pm/V$) in centrosymmetric materials such as silica glass (bulk) in a permanent way [10]. The method is called *thermal poling* and consists in the application of a high difference of potential ($3 - 5\ kV$) through a bulk piece (thickness of 1.6 mm) of fused silica heated up at a temperature in the range $250 - 325$ °C for a time between 15 and 120 minutes. The heating process is followed by a cooling process during which the difference of potential is still maintained across the sample. It was demonstrated that the nonlinearity is induced permanently only in the first few microns of the sample near the surface where the anodic potential is applied. The SH signal was measured by illuminating the bulk sample with 10 ns and 10 MW/cm^2 pulses generated by a Q-switched Nd:YAG laser with a repetition rate of 10 Hz and collecting the SHG signals by means of a photomultiplier tube (signal to noise ratio of 500:1). The value of $\chi^{(2)}$ induced was evaluated by comparison of the SHG signals with those generated by two reference samples, that are a crystal quartz (the crystalline form of SiO_2) and a crystal of $LiNbO_3$ (*Lithium niobate*), whose values of $\chi^{(2)}$ are well known. They found that the $\chi^{(2)}_{33}$ value for fused silica is the 20 % of the typical value of the $\chi^{(2)}_{22}$ measured for $LiNbO_3$ [10].

An important experimental observation realized in this first poling attempt comes from the comparison of the different values of second order nonlinearities measured for different types of silica glasses tested ($Optosil^{TM}$, $Homosil^{TM}$, $Infrasil^{TM}$ and $Suprasil^{TM}$ [74]), in particular the fact that the values were all similar apart from the one induced in $Suprasil^{TM}$ (characterized by a concentration of “impurities” much smaller than the others), which is one order of magnitude smaller. The fact that the induced effective $\chi^{(2)}$ is smaller in a glass with a smaller concentration of impurities already suggests that an important role in the thermal poling process is due to the impurities concentration of the glass.

After the work of Myers *et al.* many other researchers started to study the thermal poling process with the aim of gaining a deeper understanding of the chemical and physical mechanisms behind the creation of an effective $\chi^{(2)}$ in silica glass and also improving the magnitude of the nonlinearity modifying the relevant parameters involved in the process, such as for example the temperature of the sample, the duration of the process, the magnitude of the voltage applied, the kind of glass used and the respective value of $\chi^{(3)}$, etc.

In 1994 a first attempt of explaining theoretically the dynamics of the thermal poling process was realized by Mukherjee *et al.*, who proposed a model based on simple ionic charge transport together with bonds re-orientation [75]. It assumes that, because of the application of the external electric field, the impurity charges present into the glass sample re-organize themselves in order to generate locally static electric fields which in turn orient the bonds (related to impurities or $Si-O$ bonds. The induced $\chi^{(2)}$ is expressed by [75]:

$$\chi^{(2)} \approx \chi^{(3)} E_{dc} + \frac{Np\beta}{5k_B T} E_{dc} \tag{2.65}$$

where the first term of the right-hand side represents a third order nonlinear optical rectification process with $\chi^{(3)}$ third order nonlinear susceptibility of the material the fibre is made of and E_{dc} static electric field created into the poled sample by means of a charge transport process. The second term of the right-hand side describes the electric-field-induced orientation of the molecular second order hyperpolarizability β, with k_B the Boltzmann constant, T the absolute temperature of the sample, p the permanent dipole moment associated with the bond, N the number of dipoles involved in the process and a uniaxial molecular system assumed for the sake of simplicity.

The work of Mukherjee *et al.* introduced for the first time the concept of *depletion region* formation, that is the creation of a space-charge region, located near the anodic electrode, which is depleted of ionic charge impurities. This region consists of the NBO^- centres, already introduced in the section 2.3.1, which have lost the ionic charges initially electrostatically bonded to them, because of the application of the external electric field at high temperature (high mobility of the ions) [75].

The model for the space charge region formation was borrowed from the work of Von Hippel *et al.*, published in 1953 [76], which was focused on the study of the formation of space charges in dielectric media, in particular colored alkali halide crystals. In this case the mobile charges are electrons, which are initially

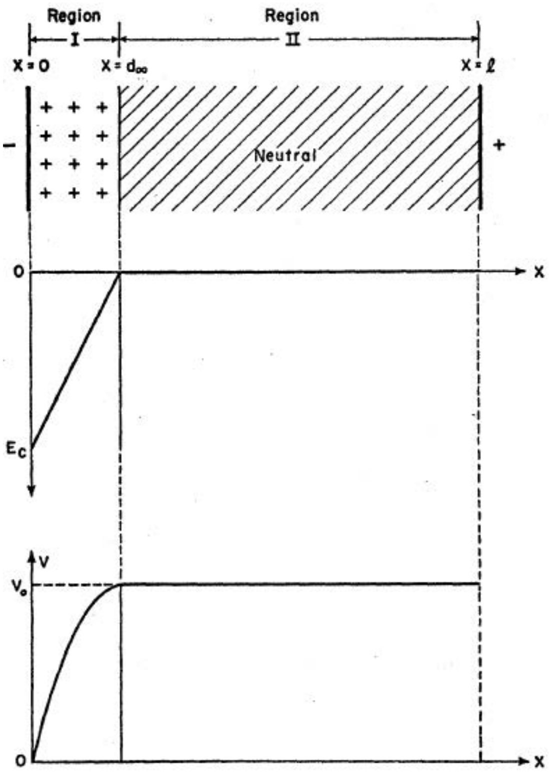

FIGURE 2.16: Theoretical model of the space charge, field strength and voltage distribution of a colored alkali halide crystal after charging. The formation of two regions, one bleached (I) and the other one unbleached (II) is reported as main result of the charging process [76].

uniformly distributed into the medium and are mobilized by the absorption of light and moved by applying a difference of potential through the medium. In their motion towards the anode the electrons leave behind halogen defects as positive countercharges. For a particular value of the difference of electric potential applied, and ignoring any diffusion phenomenon, it is possible to obtain a final state of the dielectric medium represented in Fig. 2.16.

2.3.3.1 Single-carrier model for space-charge region formation

The early model for the space-charge region formation, inspired to the work of Von Hippel *et al.* [76], included only a single kind of charges, namely the impurities present in the fused silica matrix, such as for example Na^+. Assuming the initial concentration of the impurity charges spatially uniform inside the medium and considering these charges free at high temperature ($\approx$ 300 °C) and the NBO^- centres motionless, if we apply a difference of potential (voltage) V between the two electrodes contacted with the two opposite facets of the bulk piece of silica, the charges migrate from the anode towards the cathode, leaving behind a space-charge region negatively charged, located near the anodic surface and characterized by a width [77]:

$$w_0 = \sqrt{\frac{2\epsilon V}{eN}} \tag{2.66}$$

where ϵ is the dielectric constant of the medium, V the voltage applied through the sample, e the electronic charge and N the initial density of impurity charges. From the Poisson's equation we can argue that a static electric field E_{dc} is established between the anode and the negatively charged region whose magnitude is given by [77]:

$$E_{dc} = \begin{cases} \frac{eN}{\epsilon}(w_0 - x) & 0 < x < w_0 \\ 0 & x > w_0 \end{cases} \tag{2.67}$$

where we have assumed that the external electric field is aligned along the x axis in such a way the system can be considered unidimensional and that, because of the creation of the depleted region, the voltage initially applied through the whole sample is actually contracted just to the depletion region. It is worth noting that the charge density N, associated with immobile non-bridging oxygen hole centres (NBO^-), is equal to the mobile Na^+ density of $\approx 2 \times 10^{16}\ cm^{-3}$ for type II silica [74]. This gives $w_0 \approx 10\ \mu m$ and a maximum electric field $E_{dc} \approx 1 \times 10^7\ V/cm$ at the surface for $\epsilon = 3.8\ \epsilon_0$, which approaches the nominal fused silica breakdown field strength (which is the maximum value of the electric field strength which can be applied through a dielectric before it starts to conduct, causing the break of the medium due to the electrical discharge that crosses it [78]) [74]. The time evolution of the depletion region width $w(t)$ is described by [77]:

$$w(t) = w_0 \tanh\left(\frac{t}{2\tau}\right) \tag{2.68}$$

where $\tau = w_0 L/2\mu V$, with L the total width of the sample along the x axis and μ the mobility of the impurity charges at the temperature of the poling experiment. If the temperature of the sample poled for a certain time is quickly reduced from $250 - 325$ °C to room temperature with the voltage still applied through the sample, the mobility of the charges will drop quickly and the electric field E_{dc} can be frozen into the glass, resulting in a second order nonlinearity $\chi^{(2)}$ given by the formula (2.65).

2.3.3.2 Multiple-carrier model for space-charge region formation

Although the early experimental results seemed to confirm the formation of a negatively charged region underneath the anodic surface of the bulk silica sample [79–81], as predicted by the single carrier model described in the section 2.3.3.1, other observations indicated that in a thermal poling process of silica there is something more complex than a simple uniformly negatively charged region. In particular Kazansky *et al.* found regions of alternating charge below the anode [82] while Myers *et al.* found that the depth of the nonlinearity generated in poled bulk samples was greater for samples poled for 2 hours than for 15 minutes [10]. If the depletion region was a uniformly negatively charged region and the electric field frozen into the glass was expressed by the equation (2.67), according to the equation (2.65), the $\chi^{(2)}$ induced would be peaked in the region closest to the anode and not at a certain distance as commonly observed in the early poling experiments [83].

In 1998 Alley *et al.* studied in a deeper way the dynamics of space charge in thermally poled fused bulk silica and observed some experimental facts that could not be explained by means of a simple single carrier model. A bulk piece of fused silica was sandwiched between two electrodes through which it could be applied a voltage of $\pm\ 5\ kV$ and located in a chamber equipped with a heater. A CW mode-locked Nd:YAG laser beam delivered an average power density of $\approx\ 10\ kW/cm^2$ on the surface of the sample while the SH light was collected in reflection at a certain angle by a photomultiplier and the current flowing through the sample was monitored by means of an electrometer connected between one of the electrodes and the ground [77]. The most relevant experimental observations were a transient SH signal revealed under the new cathode after the electric field reversal, which is evidence of a significant voltage drop occurring under the new cathode, inconsistent with the single carrier model, and multiple time scales for signal formation, which require the presence of carriers characterized by different mobilities. Alley *et al.* postulate that the space-charge region formation is heavily affected by the injection of a second ionic species, which is associated to hydrogenated species (such as H^+ or H_3O^+). If these hydrogenated species, characterized by a much smaller mobility than the impurity charges ($\mu_{H^+} \approx 10^{-4}\mu_{Na^+}$) are present at the fused silica surface, produced by high field ionization or from field-assisted evolution of OH bonds into H_3O^+ [84, 85], they can be injected into the glass matrix and contribute to the space charge formation via a $field\ assisted\ ion-exchange\ process$, which consists of a slow replacement of the impurity charges removed from the NBO^- centres with the hydrogenated ions injected. An important observation by Yamamoto *et al.* is that glass surfaces are much more hydrated than the bulk, confirming in this way the possibility of an enormous reservoir of hydrogenated species ready to be injected into the glass matrix at high temperature.

Besides the work of Alley *et al.*, increasing attention was dedicated in the same period (late 1990's) by many researchers towards the improvement of the understanding of the space-charge region formation and its relationship with the second order nonlinearity induced and to look for the experimental confirmations to the validity of the multiple carrier model. Various experimental methods were developed with the aim, for example, of studying the composition of the space-charge region by means of secondary ion mass spectroscopy [86], visualizing the space-charge region via a decorative etching in HF (Hydrogen Fluoride) [87] and studying its dynamics by means of interferometric techniques [88–91], measuring the second order nonlinearity via SH microscopy [92] and studying the temporal evolution of the second order nonlinear coefficient and of the nonlinear thickness by using the high-resolution all-optical Maker's fringes technique [93–95].

In 2005 Kudlinski *et al.* published a more complete multiple carrier theoretical model for space-charge region formation and induced second order nonlinearity in bulk silica glasses [96]. This work is based not only on most of the experimental observations reported so far since the first idea of multiple carrier model elaborated by Alley *et al.* [77], but also on some previous attempts of theoretically modeling the thermal poling process. The samples used in this work are two bulk pieces (of different thickness) of fused silica glass ($Infrasil^{TM}$), characterized by the presence of some types of impurity carriers (typically Na^+, Li^+, K^+, ...) located in the glass matrix with a concentration value of 1 ppm. When these ions are thermally activated, the application of an external electric field causes their electromigration toward the cathode of the system. As a consequence, a negative space charge is created under the anodic surface, due to the fact that negative charges are motionless in the glass matrix (NBO^- centres). A high electric field E_{dc} close to the dielectric breakdown field is then induced within the depletion region and a second order nonlinearity is then created:

$$\chi^{(2)} = 3\chi^{(3)}E_{dc} \tag{2.69}$$

where we are assuming a system unidimensional with the electric fields involved all linearly polarized along the same direction for the sake of simplicity. For the first seconds of the electromigration process the single-carrier model can be still used to describe the time evolution of the depletion region formation [97], allowing for a description which is the one inspired by Von Hippel *et al.* [76], while after a certain time, defined *optimum time (t_{opt})* [94], it is necessary to use a multiple carrier model to describe the temporal evolution of the poling process [77, 98, 99]. If we consider the fast carriers (impurity charges) and the slow carriers (hydrogenated species) and both the migration and the diffusion phenomena, the equation of continuity and the Poisson's equation can be written [96]:

$$\frac{\partial p_i}{\partial t} = -\mu_i \frac{\partial (p_i E)}{\partial x} + D_i \frac{\partial^2 p_i}{\partial x^2} \tag{2.70}$$

$$\frac{\partial E}{\partial x} = \frac{e}{\epsilon}\left[\sum_i (p_i - p_{0,i})\right] \tag{2.71}$$

where p_i, $p_{0,i}$ and μ_i are respectively the instantaneous concentration ($ions/m^3$), the initial (at $t = 0$) concentration and the mobility (at the temperature where the poling experiment is realized) of the i^{th} species, e is the electron charge, $\epsilon = 3.8\epsilon_0$ is the permittivity of the medium and $D_i = k_B T \mu_i / e$ is the diffusion constant of the i^{th} species, with k_B the Boltzmann constant and T the temperature of the medium. The system of equations (2.70) and (2.71) gives the spatial distribution of the electric field in the sample as function of the poling duration.

The assumptions related to the voltage applied are that the potential at the anodic surface ($x = 0$) is V_{app}, while the potential at the cathodic surface ($x = l$) is zero. So, the first boundary condition is:

$$\int_0^l E dx = V_{app} \tag{2.72}$$

While the impurity charges (such as Na^+) are already present into the sample with the initial uniform concentration $p_{0,Na}$, the hydrogenated species possess an initial density $p_{0,H} = 0$ and are injected into the glass with an injection rate which depends on the electric field strength at the anodic surface. Therefore the second boundary condition can be written as:

$$\left(\frac{\partial p_H}{\partial t}\right)\bigg|_{x=0} = \sigma_H E(x=0) \tag{2.73}$$

where σ_H is an adjustable parameter used to describe the charge injection into the glass of the hydrogenated species.

The samples used in this work were disks of fused silica ($Infrasil^{TM}$) of different thickness, sandwiched between two Si electrodes, heated at 250 °C, and poled at 4 kV for different temporal durations. The value of $\chi^{(2)}$ induced in the poled samples was estimated by means of the "layer peeling" method developed in a previous work of Kudlinski *et al.* [100]. This method allows for measuring the $\chi^{(2)}$ at different depths inside the glass sample under investigation. A comparison between the values of $\chi^{(2)}$ measured with the "layer peeling" method and the ones theoretically obtained by means of the two-charge carriers model is reported in Fig. 2.17 for the two samples of respectively 200 μm and 500 μm thickness. Apart from the good agreement between the $\chi^{(2)}$ values experimentally measured and theoretically obtained by means of the two-charge carriers model, it is worth noting that the peak of the $\chi^{(2)}$ reaches a maximum value in correspondence of a certain time of poling (namely 5 mins for the sample 200 μm thick and 10 mins for the one 500 μm thick), which can be considered as the t_{opt} discussed previously and that the depth under the anodic surface where the $\chi^{(2)}$ has a non-zero value increases with poling time. It is important also to highlight that the shape of the $\chi^{(2)}$ profile is triangular for poling durations shorter than the t_{opt}, while it tends to flatten for longer poling times. Another relevant clarification about the theoretical simulations reported in Fig. 2.17 is that while the values of $p_{0,Na}$ and μ_{Na} used in the model are the ones experimentally obtained ($p_{0,Na} = 9.5 \times 10^{22}\ m^{-3}$ and $\mu_{Na} = 1.5 \times 10^{-15}\ m^2V^{-1}s^{-1}$), the values of μ_H and σ_H have been adjusted to best fit the experimental data.

The description of the dynamics of the space-charge region formation has been theoretically realized and assumes that, because of the application of the voltage through the whole sample, an electric field is established equal to V_{app}/l and, because $\mu_{Na} \gg \mu_H$, initially a depletion layer beneath the anodic surface of the glass is created due to the sodium ions migration toward the cathode. The induced electric field at the surface increases and screens the applied electric field in the

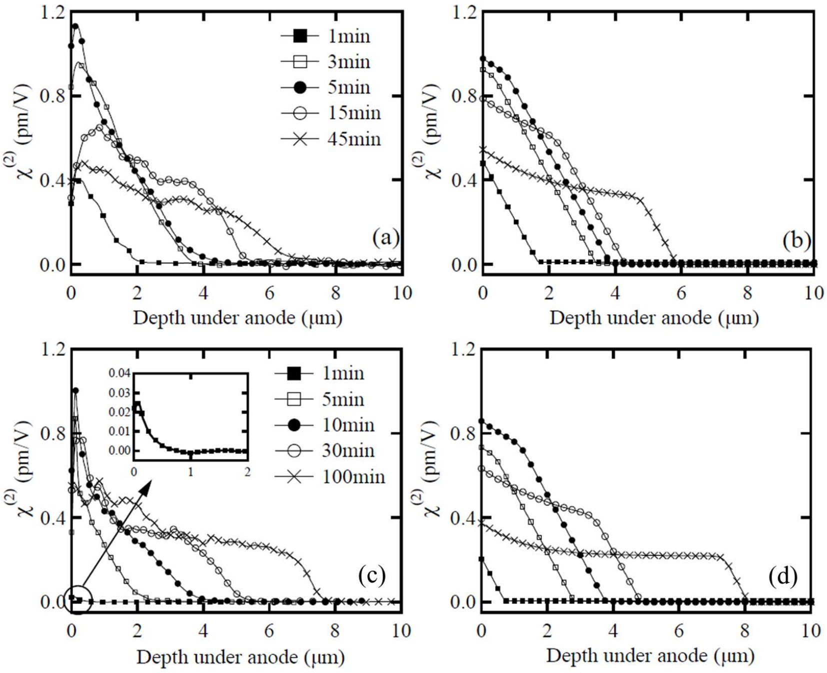

FIGURE 2.17: (a) Experimental values of the $\chi^{(2)}$ obtained by means of the "layer peeling" method for a fused silica sample ($Infrasil^{TM}$) 200 μm thickness; (b) theoretical values of the $\chi^{(2)}$ obtained by means of the two-charge carrier model for the same sample reported in (a); (c) experimental values of the $\chi^{(2)}$ obtained by means of the "layer peeling" method for a fused silica sample ($Infrasil^{TM}$) 500 μm thickness; (d) theoretical values of the $\chi^{(2)}$ obtained by means of the two-charge carrier model for the same sample reported in (c) [96].

region of the sample located outside the depletion region. The maximum value of E_{dc} ($\approx 10^9$ V/m) is reached when the space-charge region is fully established. At this time the concentration of the injected carriers per second increases quickly reaching a value of 7.5×10^{22} $m^{-3}s^{-1}$ (according to the equation (2.73)). At the same time, the drift velocity of these injected hydrogenated species $v_H = \mu_H E_{dc}$ becomes comparable to the velocity of the sodium ions, which are located outside the depletion region, where the applied electric field is actually reduced because screened by the presence of the space charge. For poling times longer than few minutes, these injected ions move deeper and deeper into the glass replacing little by little the previously removed sodium ions, neutralizing in this way the NBO^- centres. In Fig. 2.18 the results of the simulations are reported for a poling time of 100 minutes.

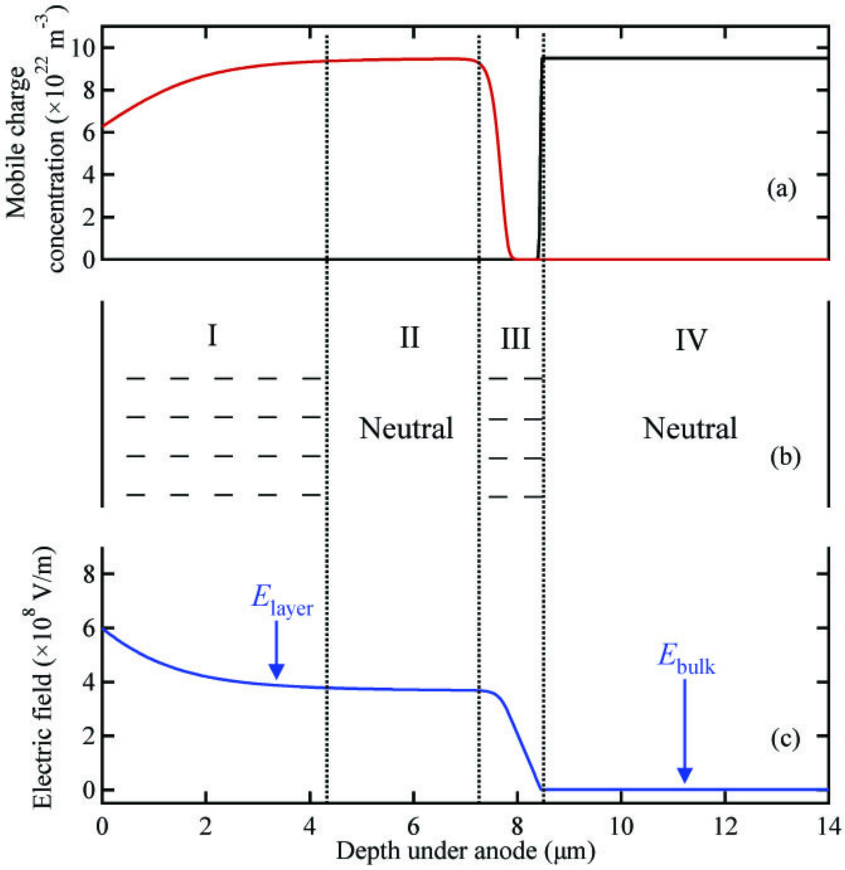

FIGURE 2.18: Theoretical results related to a 200 μm-thick sample of fused silica ($Infrasil^{TM}$) poled for 100 minutes. (a) Representation of the mobile charge concentration (the black line represents the sodium density while the red one the injected carrier density); (b) schematic of the charge distribution; (c) electric field distribution [96].

2.3.4 Thermal poling of silica fibres

The first attempt of poling a silica fibre was realized by Kazansky *et al.* in 1994 [101], when a D-shaped fused silica Germania-doped step-index fibre was poled using the setup reported in Fig. 2.19. After some works where the same poling configuration was used [101–103], in 1995 a twin-hole step-index silica fibre was poled for the first time by applying the voltage to two electrodes inserted into two holes running along the fibre [104]. Fig. 2.20 reports a cross-section of this kind of fibre, which became the new standard geometry for thermal poling of optical fibres [50, 105–108].

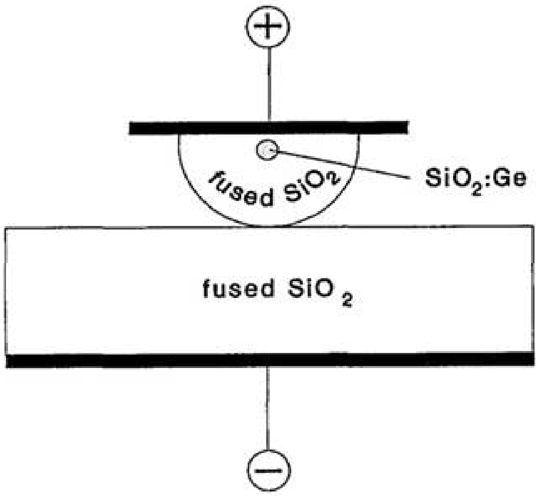

FIGURE 2.19: Schematic of a D-shaped optical fibre arranged for thermal poling. The side-polished fibre is placed on top of a silica substrate and the whole setup is sandwiched between two electrodes through which the voltage is applied. The setup is placed inside an oven [101].

2.3.4.1 Cathode-less poling configuration

The conventional anode-cathode configuration for thermal poling of silica fibres, represented in Fig. 2.20 (b), produces a space-charge region which develops only around the hole where the anodic electrode is inserted. The space-charge region can be visualized by means of a decorative etching process of the cleaved facet of the poled fibre in HF (diluted at ≈ 50 % in DI water) for ≈ 1 *minute* and is represented in Fig. 2.21. The anode-cathode configuration is however affected heavily by the limit of the small distance ($\approx 10-20\ \mu m$) between the two holes where the electrodes are inserted, which increases significantly the risk of breakdown through the silica due to the application of high voltages.

In 2009 Margulis *et al.* demonstrated that it is possible to create a depletion region around both the electrodes inserted in the cladding holes of a twin-hole silica fibre by connecting them to the same anodic potential, without any cathode. Fig. 2.22 shows the cross-sections of two twin-hole silica fibres poled respectively by means of single and double-anode configuration. They observed also that the effective second order nonlinearity created by means of this cathode-less method of poling is larger than the one created by means of conventional anode-cathode configuration and demonstrated that the new method of poling (or “charging”, according to their definition) is more stable than the conventional one in terms of annealing time of the $\chi^{(2)}$ measured at the temperature of 250 °C [13].

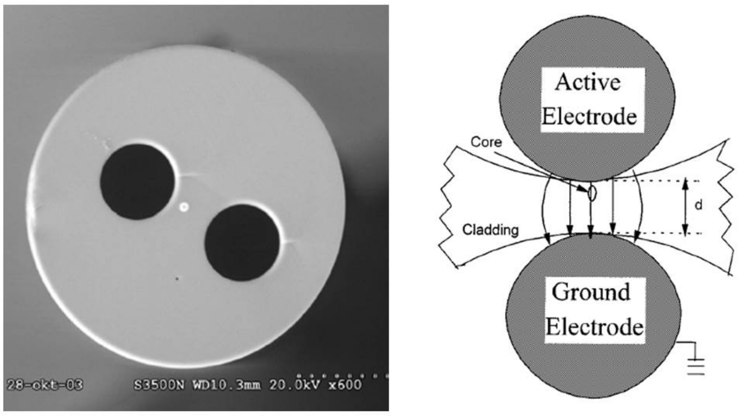

(a) (b)

FIGURE 2.20: (a) SEM image of a twin-hole silica fibre for thermal poling via internal electrodes [108]; (b) Schematic of the electrical configuration anode-cathode for thermal poling [105].

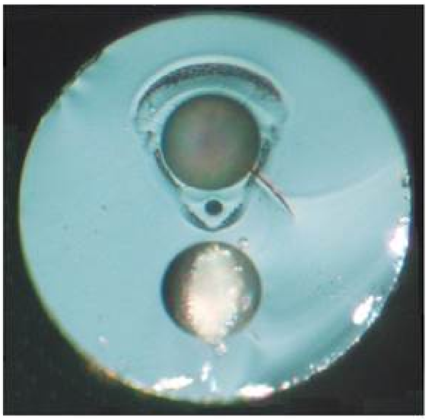

FIGURE 2.21: Cross-section of a twin-hole silica fibre poled via the anode-cathode configuration and etched in HF for 1 min. The ring visible around the hole where the anode is located represents the space-charge region whose mechanism of formation has been described in the section 2.3.3.2 [108]. As expected, according to the electromigration mechanism of the impurity charges, the space-charge region develops only around the anodic surface.

The theoretical explanation of the depletion region formation in the "cathode-less"configuration requires the introduction of a mechanism called "avalanche-like positive feedback". Considering the two-dimensional plot of the equipotential surfaces in a fibre before any charge transport starts (see Fig. 2.23), and assuming that both the electrodes are at the same positive potential (+ 5 kV) and the external surface of the fibre is grounded by means of the negative charge supplied by the air, Margulis *et al.* highlight that the potential at the fibre core is approximately 500 V lower than the potential at the electrodes. So the ionic charge

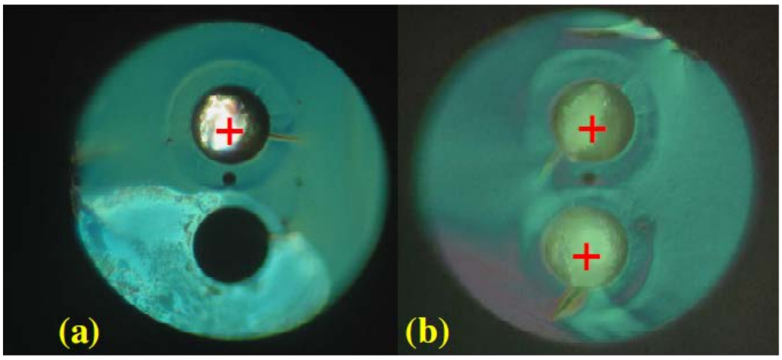

FIGURE 2.22: (a) Cross-section of a twin-hole silica fibre poled via single-anode configuration and etched in HF for 1 min; (b) Cross-section of a twin-hole silica fibre poled via double-anode configuration and etched in HF for 1 min [13].

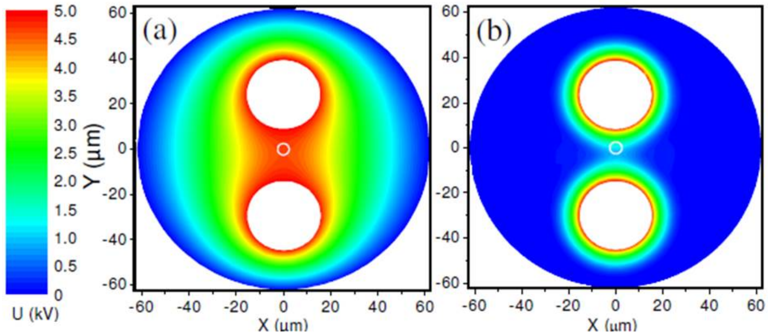

FIGURE 2.23: Equipotential maps of a fibre subjected to an electrical potential of 5 kV applied to both the internal electrodes, assuming electrically grounded the outer surface of the fibre. (a) represents the initial situation, where there is a small drop of potential between each electrode's surface and the fibre's core, due to the non-zero resistivity of the glass. (b) shows the situation after a certain time, when a depletion region has been already created and the drop of potential through the core has grown because of the increase of the resistivity of the core region, due to its depletion from impurity charges [13].

transport starts (at high temperature) because of this small potential difference. Therefore a depletion region begins to be created around both the anodes, even if it is not circular at the beginning. This non circularity of the depletion region modifies the uniform distribution of ions at the beginning of the process. Because of the positive charge migration from the electrodes, there is an increase of the resistivity of the glass, which produces a drop of the potential at the core of the fibre. This situation creates even more charge displacement and increases the potential difference between the electrodes and the centre of the fibre. This process of "avalanche-like positive feedback"finally results in a complete depletion, such as in conventional poling processes.

After the work of Margulis *et al.*, An *et al.* tested and compared different electrodes configurations for thermal poling of twin-hole silica fibres, namely anode-cathode, single-anode, double-anode, single-cathode and double-cathode. Their study demonstrated that the best configuration in terms of induced effective $\chi^{(2)}$ is the double-anode one [109].

2.3.5 Chemistry of silica etching processes

Etching a solid (both vitreous or crystalline) material means literally removing part of it by breaking the molecules constituing its solid matrix. The process is based on the exploitation of some chemical reactions between the "reactants" and the surface of the solid to be etched. There are dry etch processes, which use gas phase etchants in plasma, both chemical and physical (sputtering process) and wet etch processes, where the reactants are liquids [110]. As will be clearer in chapter 3, the so-called *wet decorative etching* (mostly realized by means of HF based solutions) was exploited during my research path to identify the nonlinear region (space-charge region) created by thermal poling in silica fibres [87]. Because of the isotropy of the silica basic structure, also the wet etching process in HF can be considered an isotropic process, which could allow for an homogeneous reduction of the roughness of a glass surface. What defines the etch rate of a particular material, apart from the chemical composition of its solid matrix and the concentration of the etchant solution, is the charge status of the material to be etched.

The work of Alley *et al.* reports that the etch rate of a thermally poled bulk piece of fused silica in a HF based solution depends on if it is electrically neutral or negatively charged. In particular it seems that the etch rate of the neutral part of the sample to be etched is faster than the etch rate of the negative part. This difference allows for visually distinguishing (by means of an atomic force microscope (AFM) or even a simple optical microscope) the two regions of the poled glass respectively neutral and negative, that is the space-charge region. In Fig. 2.24 the AFM image of a poled bulk fused silica sample, etched in a HF based solution (49 % of dilution in DI water), is reported [87].

In order to understand how the different charge status could affect the etch rate of silica, it is worth reporting the wet etch process of silicon dioxide (SiO_2) in a

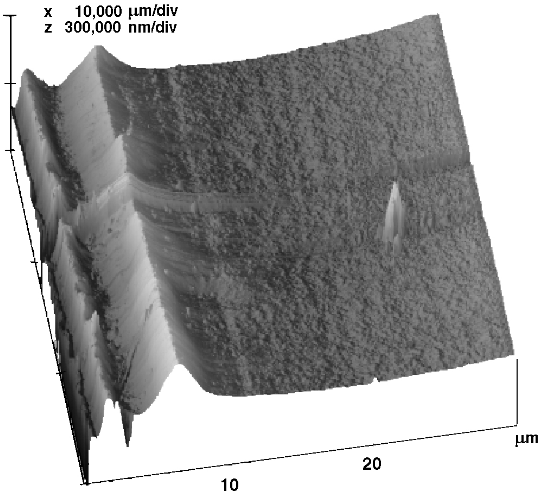

FIGURE 2.24: AFM image of a poled fused-silica coverslip etched in HF solution transversely to the poling direction. The anode was located on the left edge of the shown sample. Two ridges (corresponding to regions of the sample etched at a slower etch rate) are evident. [87].

HF based solution [111]:

$$SiO_2 + 6HF \rightarrow H_2SiF_6 + 2H_2O \tag{2.74}$$

The equation (2.74) is a simplification of the reactions occurring during the heterogeneous SiO_2 dissolution process. As already reported in the section 2.3.1, vitreous (as well as crystalline) SiO_2 consists of tetragonal SiO_4 units connected at all four corners with four other SiO_4 units by covalent $\equiv Si - O - Si \equiv$ (siloxane) bonds. In this way a covalently interconnected three-dimensional silicate network structure is formed. It is necessary to break all four siloxane bonds in order to break down the network and release a silicon from the glass, in other words to etch the glass. HF, dissolved in water, is a weak acid and its solutions contain H^+, F^- and HF_2^- ions and undissociated HF molecules. The property of HF based solutions to attack the glass is related to the presence in solution of the fluorine-containing species, and the most complete model of the chemical dissolution mechanism of SiO_2 in HF based solutions has been presented by Prokopowicz-Prigogine in 1989 [112]. According to this model the reaction rate of the dissolution process is dominated by the adsorption (that is the adhesion of the ions to the glass surface) of the HF molecules and of the HF_2^- and H^+ ions, while the reactivity of F^- is negligible. The HF_2^- ions are adsorbed on surface silanol groups, the HF molecules on vicinal silanol groups and the H^+ ions on surface bridging oxygens in siloxane units. The adsorption of HF and HF_2^- increases the electronic density on the bridging oxygen in the siloxane unit. This in turn makes these oxygens more basic (in the sense of Bronsted-Lowry of a proton (hydrogen ion) acceptor), so more H^+ ions are adsorbed, which leads to more siloxane bonds being broken per time unit, i.e. a sort of catalytic effect.

It is important understanding what happens when network modifiers such as for example Na_2O, are introduced into the vitreous matrix of the SiO_2, which is actually what happens in fused silica, the kind of silica the optical fibres we used in our thermal poling experiments are made of. It is possible to assume that each modifier is incorporated by breaking a siloxane bond, forming non-bridging oxygens by means of the reaction [111]:

$$Na_2O + \equiv Si - O - Si \equiv \rightarrow 2 \equiv SiO^- Na^+ \tag{2.75}$$

The presence of already broken siloxane bonds strongly increases the etch rate of the glass in HF based solutions. If the Na^+ ions are removed from their position, because of the application of an electric field (such as in thermal poling experiments), the non-bridging oxygens become negatively charged in such a way they attract less the fluorine-containing species, reducing the overall etch rate of the glass. According to this explanation, the etch rate of the negatively charged region of a glass should be smaller than the correspondent neutral part, as often confirmed experimentally [87, 88, 113]. This is the mechanism which allows to create a differential etching process of poled fibres, highlighting visually the space-charge region.

2.3.6 Alternative methods for permanent creation of $\chi^{(2)}_{eff}$ in silica samples

Besides the thermal poling method, which is the one I have been exploring during my PhD research project, there are alternative methods for creating permanently a second order nonlinearity in bulk glasses and silica optical fibres. The "UV-excited poling", for example, consists in the UV irradiation of a Germania-doped silica sample while a high dc electric field is applied through it. The mechanism behind the creation of the permanent nonlinearity seems to be due to the combined effect of an internal space charge field formation (due to some charges produced during the formation of GeE' centres, which are color centres consisting of a Ge atom surrounded by three oxygen atoms and a singly occupied dangling bond) and an increase of the third order nonlinear susceptibility $\chi^{(3)}$ of the glass (due to the formation of crystallites), both effects produced during the UV exposure of the sample [114]. Values of $\chi^{(2)}_{eff}$ up to $\approx$ 6 pm/V have been measured for bulk samples UV-poled while an electro-optic modulator in germanosilicate fibre UV-poled was realized for the first time by Fujiwara *et al.* in 1995 [115]. The quite fast decay of the induced nonlinearity represents one of the main drawbacks of this technique.

Another technique for inducing permanently a $\chi^{(2)}_{eff}$ is the "electron implantation", which was used for the first time in glass samples by Kazansky *et al.* in 1993 [116]. A scanning electron microscope is used for electron-beam irradiation of the sample. The injection of electrons inside the glass produces a space charge electrostatic field perpendicularly to the surface of the sample. This field, exactly like in the mechanism of space-charge region formation in thermal poling experiments, generate a permanent $\chi^{(2)}_{eff}$ via a third order nonlinear optical rectification process. The main results are the SH efficiency increasing with the electron energy up to 40 keV and the fact that the irradiation time seems not to affect at all the SH efficiency after 1 minute of exposure. The main deficiency of the technique is the presence of strong inhomogeneities in the SH signal obtained from different irradiated regions of the glass, probably due to inhomogeneous distributions of charge near the surface caused by electrical breakdown of the glass at high electron currents.

Further possibilities to generate permanent second order nonlinear susceptibility in silica are the "proton implantation" [117] and the "corona discharge-assisted poling"[118, 119]. It is worth highlighting that, among the methods cited, thermal poling has been used extensively during the past years, due to its ability to provide robust and reproducible results with efficient nonlinear sample characteristics and its simplicity of implementation if compared to the other ones [120].

Chapter 3

Induction poling technique

3.1 State of art of thermal poling

As already discussed in section 2.3.1, the most recent advances in the thermal poling technique applied to optical fibres are represented by the works of Margulis *et al.* [13] and An *et al.* [109], in 2009 and 2012. The main result is the observation that it is possible to create a space-charge region without using the conventional configuration with the anode and cathode inserted in each hole of a twin-hole step index fibre (see Fig. 2.21), but by simply contacting the electrodes to the same anodic potential and assuming that the external surface of the silica fibre is grounded via the free charges present in the atmosphere which surrounds the poling setup. As can be easily seen from the cross-sections of a fibre poled by means of this "cathodeless" configuration, reported in Fig. 2.22, a space-charge region is created around each of the two holes of the fibre, which doubles the value of the induced $\chi^{(2)}_{eff}$ with respect to the value obtained with a conventional poling configuration [13]. The main advantage of this "cathodeless" setup is the possibility of reducing the risk of electrical breakdown which is likely to be produced through the glass when a high voltage is applied between two electrodes separated by a tiny distance ($\approx 20 - 30\ \mu m$).

Nevertheless there are many issues which the two cited works [13, 109] do not address at all, such as for example the length of the fibre poled, which is limited by the manual insertion of very small diameter ($\Phi\ \approx 10 - 25\ \mu m$) metallic wires to be used as electrodes embedded in the holes of the fibre (the reason behind the need of increasing the length of the poled fibres comes from the definition of the efficiency of SHG, which scales quadratically with the interaction length L between the pump and the second harmonic radiation (see equation (2.60))). The manual insertion, apart from being limited by human capability to few centimetres of length and being a very time consuming process which often needs to be repeated many times before being successful, is also characterized by the inhomogeneity of the space-charge region depth along the fibre length, due to the fact that the wire inserted does not fill completely the empty space of the hole and the distance between the wire surface and the edge of the hole can differ along the length of the fibre, producing a space-charge region whose depth can change considerably (even tens of percent) along the fibre.

An alternative approach to the issues presented by the manual insertion of the electrodes was proposed by Knape *et al.* in 2007. The electrodes were embedded by pumping into the two cladding holes eutectic alloys such as BiSn (melting temperature of 138 °C) or AuSn (melting temperature of 280 °C) in their molten state. The electrical connection to both the embedded electrodes was realized by side polishing the fibre in correspondence of two points of the two channels and inserting the wire into each hole while the alloy (re-solidified at room temperature) was locally re-melted to ensure a robustly bonded electrical connection (see Fig. 3.1). Although this approach allows to increase the length of the poled fibre to reach potentially a number of metres, it presents some issues. One of the main practical issues presented by the approach of Knape *et al.* is the need of side polishing of the fibre to reach the embedded electrodes. This requirement for side polishing results in a low device yield because the probability of breaking fibres

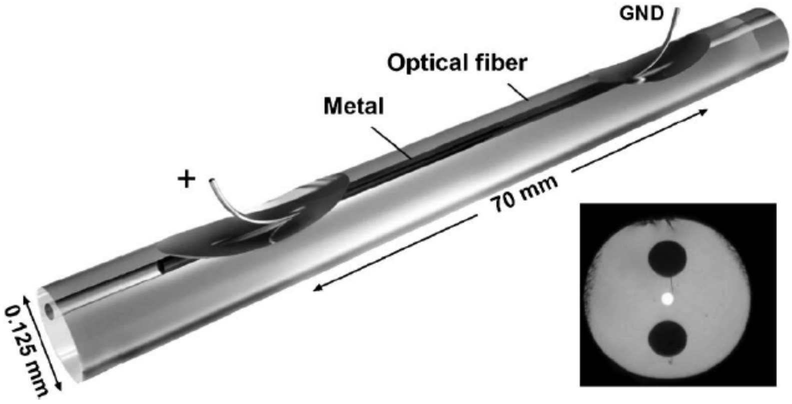

FIGURE 3.1: Schematic picture showing a twin-hole fibre equipped with two molten metal electrodes. The two channels are side polished to allow to access the electrodes with the wire used for the connection to the anodic and ground potential respectively. [12].

during the various phases of the poling process is very high. The other relevant issue is the need of removing the eutectic alloy from the two cladding holes of the fibre. The presence of the metal increases the absorption losses of the light traveling through the fibre so it could be necessary to remove the electrodes in the applications where the reduction of the losses is a relevant target, such as for example in frequency doublers. The difficulty of removing the electrodes is due to the fact that they need to be heated up to a temperature possibly higher than their melting temperature and then pressurized. In chapter 4 the issue of the removal of metallic electrodes will be discussed in detail.

From the arguments already discussed so far, it is quite clear that, apart from the limitations in length of the nonlinear devices which could be realized by thermal poling, another issue not yet addressed is represented by the need of a physical contact between the electrodes embedded into the waveguide and the high voltage power supply, as was already discussed earlier, by using metallic wires to be inserted into the cladding holes of the twin-hole step index fibre, or by side polishing the fibre to access the molten metal electrodes. In both cases, the problem of the physical contact can be considered a challenge.

Furthermore both the issues (length of the poled fibre and necessity of direct contact between the power supply and the embedded electrodes) appear even more intractable for poling solid core PCFs (see Fig. 2.4 (a)). The small size of the holes which the microstructure is made of (typically of few μm), for example, would not allow for a facile insertion of any kind of metallic electrode for thermal poling experiments. And if somehow it was possible to embed a molten metal electrode into the holes of the microstructure, directly accessing the electrodes created in this kind of structured fibre would be very difficult, even by means of side polishing of the fibre's cladding.

It is worth, at this point of the thesis, highlighting that conventional structures, such as step-index fibres, are necessarily limited in the maximum value of the induced $\chi^{(2)}_{eff}$ (see equation (2.69)) by the intrinsic value of $\chi^{(3)}$, which, for example for silica is $\approx\ 10^{-22}\ m^2/V^2$ [121–124] and by the dielectric strength of silica which limits the maximum electric field E_{dc} which can be frozen into the glass before it breaks. At a poling temperature of 280 °C the *breakdown field* is reported to be of $\approx 5 \times 10^8\ V/m$ [90, 113]. In order to move beyond these limitations, it could be necessary to explore, for example, photonic crystal fibre poling to allow for exquisite control over optical mode confinement, effective group index, dispersion, etc., thus potentially increasing the efficiency of second order nonlinear processes. A promising starting point is represented by the theoretical work published by Monro *et al.* in 2001, where it was demonstrated that, by appropriate choice of holey fibre geometry, thermally poled solid-core PCFs could be up to four order of magnitude more efficient than conventional poled fibres [125]. This higher efficiency is actually obtained by reducing the area overlap (see equation (2.60)). Two examples of the geometry of the microstructure of a solid-core PCF are reported in Fig. 3.2.

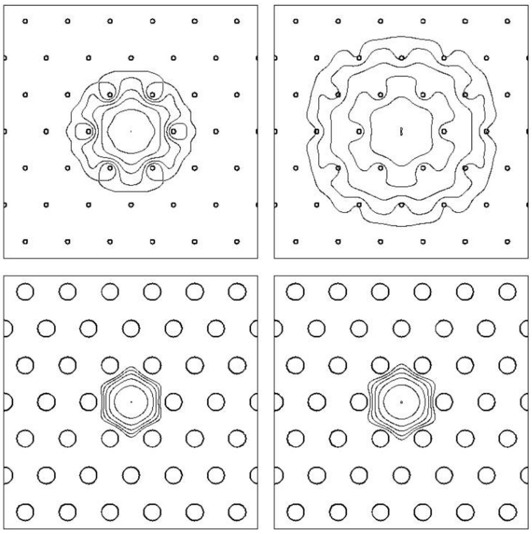

FIGURE 3.2: Propagation modes at 0.775 μm (left side) and at 1.55 μm (right side) for two types (top and bottom one) of PCF geometry [125].

Although already in 2001 Faccio *et al.* demonstrated the thermal poling of a holey fibre, the value of SH efficiency obtained was comparable to many standard poled germano-silicate fibres [126]. The reason of this relatively small value, compared to the expected one, depends, according to the authors, on the fact that the thermal poling conditions and the holey fibre geometry were not optimized. Furthermore it is necessary to consider even the issue of the phase mismatch between pump and SH which needs to be solved via QPM. Indeed, even if it is possible to tailor the geometry of these microstructured fibres in order to obtain a zero GVM over a quite long range of wavelegths, it is instead impossible to obtain a zero index mismatch and consequently a zero phase velocity mismatch at the pump and SH wavelengths [127].

Another way forward, to overcome the limitations of the step-index fibres, is the idea of functionalising PCFs via the deposition of materials intrinsically nonlinear (such as for example semiconductors or 2D-materials), in order to exploit at the same time the guidance properties of the microstructured fibres together with the nonlinear properties of the deposited materials. This topic will be discussed more exhaustively in chapter 6.

After this foreword, it can be assumed that the principal motivation behind my research activity is overcoming the issues just cited, which prevented from realizing long, low-losses and efficient all-fibre nonlinear devices so far. My ideal aim would be the implementation of an integrated technological platform which could allow for facile poling of long fibres characterized by any kind of geometry, such as the solid-core and hollow-core PCFs.

3.2 Initial thermal poling configurations

3.2.1 Early experimental observations

The first experiment realized is the replica of one of the experiments reported in the work of Margulis *et al.* [13], namely the thermal poling of a fused silica fibre in single-anode configuration. The main target of this first experiment is to familiarize with thermal poling experiments and so the mere observation of a space-charge region in a thermally poled silica fibre is considered already a first optimal objective. A fused silica three-hole fibre (THF), manufactured in Optoelectronics Research Centre, (outer diameter (OD) = 250 μm, empty central hole of ≈ 9 μm and two side holes running along the length of the fibre of respectively ≈ 30 μm and 50 μm of OD (see Fig. 3.3)) was used as sample to be poled. The fibre is made of a kind of glass ($Infrasil^{TM}$) characterized by an initial homogeneous concentration of impurity charges, which should allow for the electromigration process which creates the induced $\chi^{(2)}_{eff}$ (as explained in section 2.3.3).

The setup to realize this first thermal poling experiment in cathodeless configuration is reported in Fig. 3.4. The fibre to be poled (length of ≈ 6 cm), equipped with a looped tungsten wire as electrode, is placed on top of a microscope slide in a Petri dish. The whole setup is then placed on top of the ceramic surface of a hotplate. After reaching the temperature of ≈ 300 °C, the voltage of 4.3 kV is applied to the wire for a total time of 2 hours, then the hotplate is switched off while the voltage is still provided to the electrodes until the sample cools down

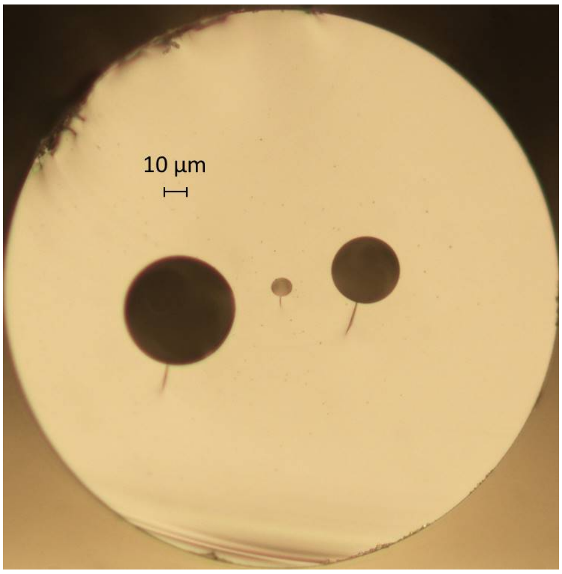

FIGURE 3.3: Cross-section of the fused silica three-hole fibre (THF) used as test sample for the early experiments about induction poling.

to room temperature. The anodic electrode is a solid tungsten wire (thickness of $\approx 25\ \mu m$), manually inserted inside one of the two holes of the fibre.

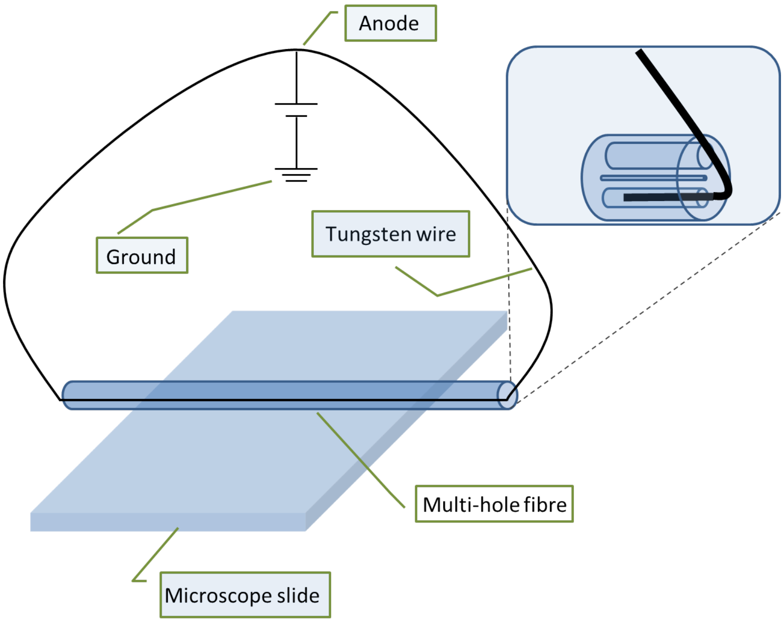

FIGURE 3.4: Schematic of the setup for cathode-less poling of silica optical fibre in single-anode configuration. The fibre to be poled is the same shown in Fig. 3.3 and equipped with a tungsten wire connected to the electric potential of 4.3 kV. The fibre is heated up at ≈ 300 °C and the duration of the poling experiment is 120 minutes. It is worth noting that the tungsten wire used as electrode is looped before being connected to the anode.

As reported in section 2.3.3.2, the easiest way to indicate if a second order nonlinearity is potentially created in a glass thermally poled is a process of wet decorative etching transverse to the poling direction to reveal a cross-section of the nonlinear region [87]. The working principle of this technique is based on the difference in the etching rate between the neutral (faster) and the negatively charged (slower) regions of the poled glass. A more detailed description of the chemistry of the wet etching process of glasses has been reported in the section 2.3.5. According to the results reported in Fig. 2.22, a ring should appear around the hole where the electrode connected to the anode was located during the thermal poling. It represents the negatively charged region depleted of the positive impurity ions, migrated because of the electric field applied through the fibre. That ring should correspond to a ridge similar to the ones observed by Alley *et al.* in their work [87].

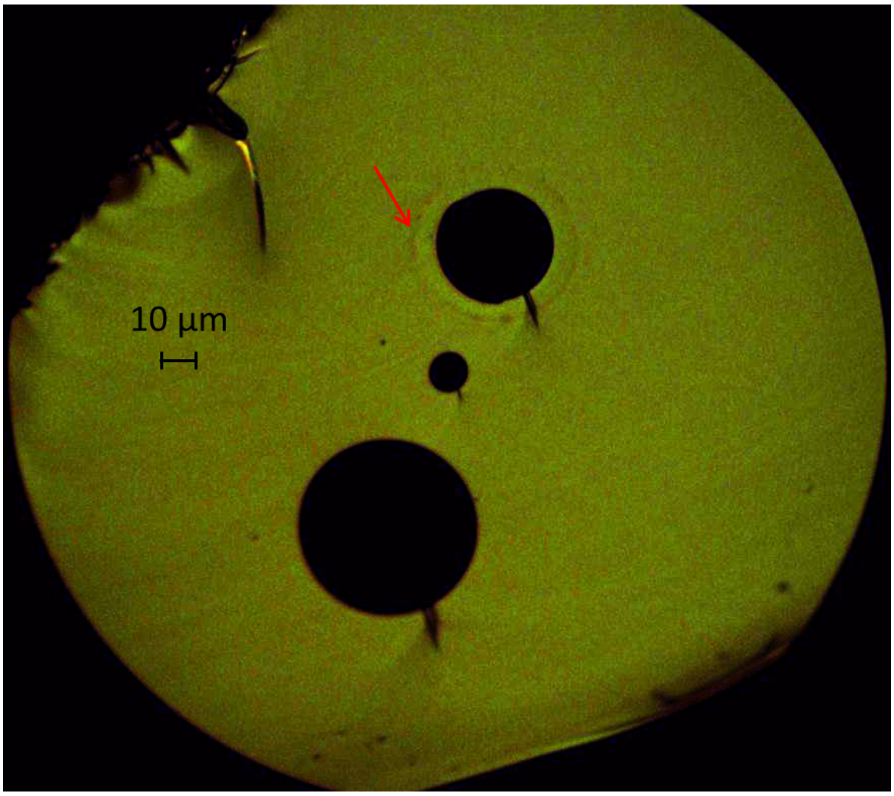

Figure 3.5: Cross-sectional micrograph of the HF etched sample (THF) poled using the setup shown in Fig. 3.4. The red arrow indicates the space-charge region highlighted by means of the differential HF decorative etch process.

The fibre, poled by means of the setup reported in Fig. 3.4, has been cleaved in different positions along its length, subsequently immersed for 60 seconds in a buffered solution of HF in DI water and then rinsed with DI water to remove the residues of acid. The cleaved and etched cross-sections of the poled sample have been observed with a microscope. A picture of the etched cross-section of the fibre

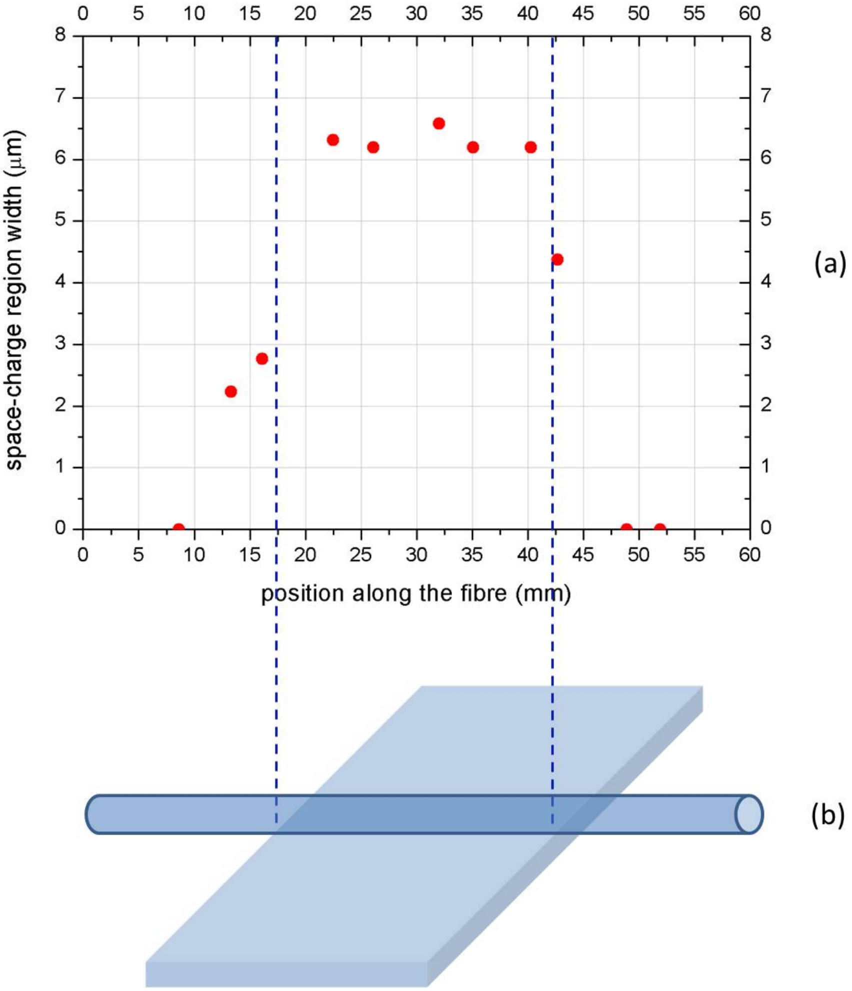

Figure 3.6: (a) Trend of the width of the space-charge region with the position along the poled sample. The zero on the X axis is referred to one end of the fibre, located outside the microscope slide, as shown in (b). The two blue dotted vertical lines identify the limits of the region of the poled fibre located on top of the microscope slide in contact with the hotplate.

is reported in Fig. 3.5 while the graph which shows the trend of the space-charge region width along the length of the fibre is reported in Fig. 3.6. The width of the space-charge region obtained by poling the THF is quite homogeneous along a length corresponding exactly to the section of the fibre lying on top of the microscope slide.

3.2.2 Physical identification of a groundplane of the thermal poling setup

A potential upgrade of the thermal poling setup reported in Fig. 3.4 could be the physical identification of a groundplane (see Fig. 3.7). It is worth recalling that in the work of Margulis *et al.* only the external surface of the fibre's cladding is assumed to be grounded through the charges present in the surrounding air.

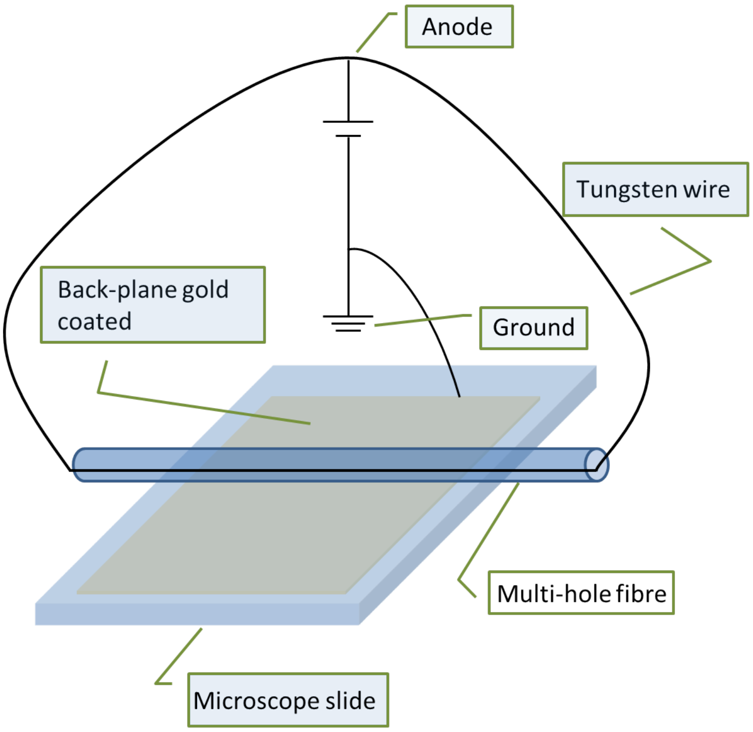

FIGURE 3.7: Schematic of the setup for cathode-less poling of silica optical fibre in single-anode configuration. The main difference with respect to the setup reported in Fig. 3.4 is that a well-defined groundplane is introduced into the setup. A metallic coating (Chromium + Gold) deposited on the back face of the microscope slide (by means of an e-beam evaporator) is grounded during the poling experiment. The experimental conditions are identical to those shown in Fig. 3.4.

The groundplane is represented by a metallic coating (Chromium + Gold) deposited on the glass by means of an e-beam evaporator. The size of this groundplane was optimized after few test experiments focused on finding the biggest surface of a groundplane which prevented the system from an electrical breakdown through the air between each end of the fibre and the groundplane. The rectangular shape of 68 $mm \times$ 19 mm of side length was found as the maximum value of area which fulfilled this requirement. The evaporated metallic layer is connected to the ground terminal provided by the high voltage power supply through a tungsten wire attached to it by means of a piece of Kapton tape. The same type of THF represented in Fig. 3.3 was poled in the same experimental conditions reported in the caption of Fig. 3.4 and the graph showing the space-charge region width along the sample poled, highlighted by HF etching (see Fig. 3.8), is reported in Fig. 3.9.

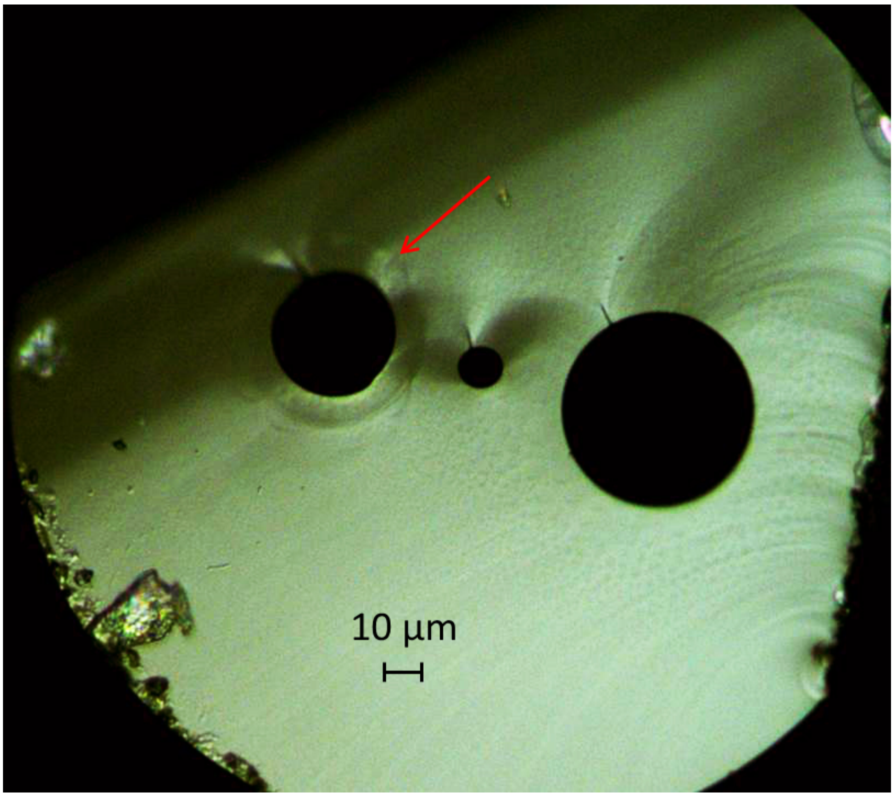

Figure 3.8: Cross-sectional micrograph of the HF etched sample (THF) poled by means of the setup shown in Fig. 3.7. The red arrow indicates the space-charge region highlighted by HF decorative etch process.

The trend of the space-charge region width along the length of the sample poled, as reported in Fig. 3.9, resembles the one obtained in Fig. 3.6. The aspect which can be highlighted is that the space-charge region width, with respect to the one obtained by means of the setup reported in Fig. 3.4, where the ground of the system was not identified precisely, shows a larger value, an experimental indication that the physical identification of a groundplane enhances the space-charge region width. Later in the thesis (see section 3.5) a numerical model related to the thermal poling in cathodeless configuration will be implemented by using the software *COMSOL*^{TM} Multiphysics, so a confirmation to this experimental observation could be found.

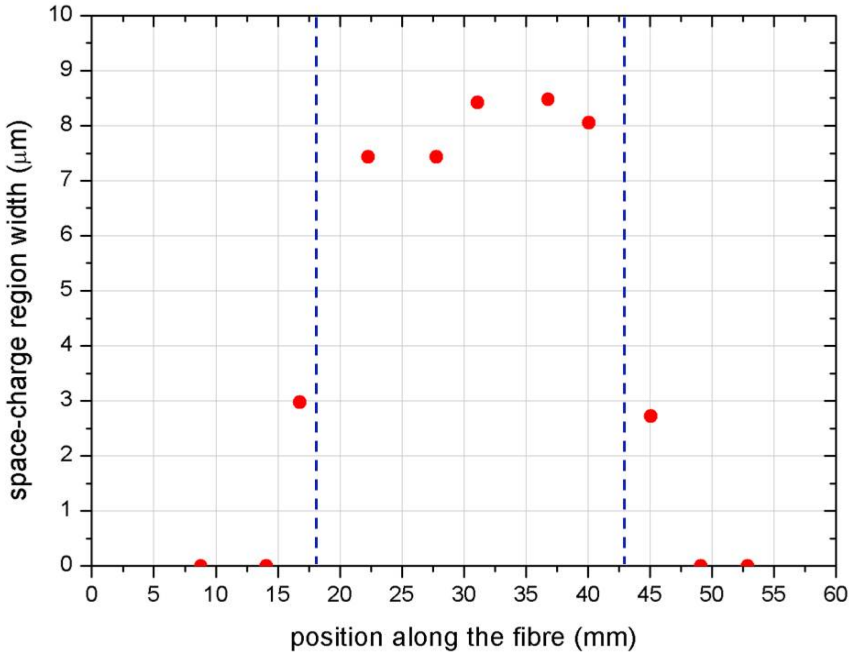

FIGURE 3.9: Trend of the width of the space-charge region with the position along the poled sample. The zero on the X axis is identical to that shown in Fig 3.6. The two blue dotted vertical lines identify the limits of the region of the poled fibre located on top of the microscope slide in contact with the hotplate.

3.3 First experiment of thermal poling by electrostatic induction

After the first explorative part of my experimental work (discussed in the section 3.2), mainly devoted to the optimization of a thermal poling setup of fused silica three-hole fibre samples by means of metallic electrodes embedded inside the holes of the fibre, with the aim of studying how some experimental conditions have affected the dynamics of the space-charge region formation (such as for example the identification of a groundplane), another avenue to explore is the idea of creating a system for generating electrostatic induction between an electrode taken at a certain potential and a floating electrode, located adjacent to the inductor. The setup implemented is shown in Fig. 3.10 and consists of two samples of THF, namely the *inductor* (≈ 6 *cm* of length) and the *sample* (≈ 3 *cm* of length). The inductor is equipped with two tungsten wires (inserted manually inside the two larger holes), while the sample is selectively filled in one of the two larger holes with a molten metal alloy (BiSn) by means of a pressurization system similar to the one reported in Fig. 3.11 [128].

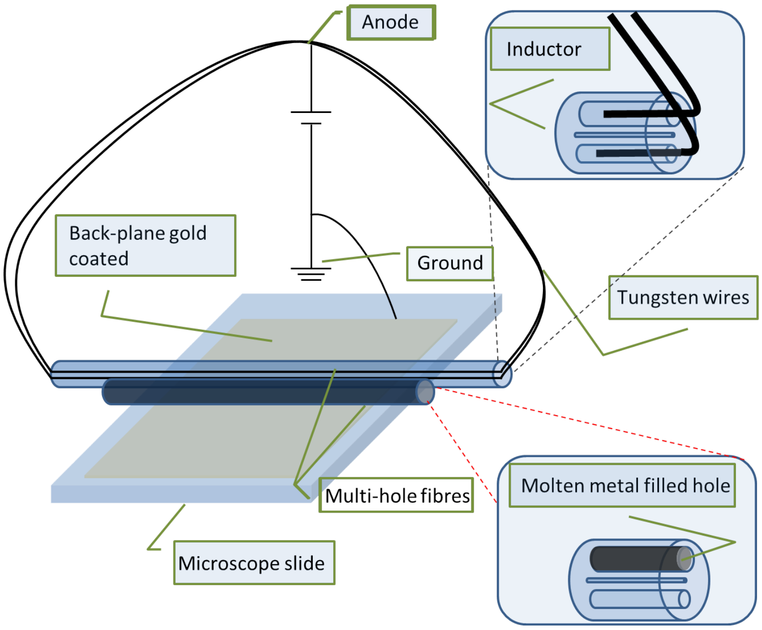

FIGURE 3.10: Schematic of the setup for the first electrostatic induction poling experiment. The inductor is a piece of fused silica THF equipped with two solid tungsten wires manually inserted in the two larger holes, while the sample is a piece of fused silica THF equipped with a single molten metal alloy (BiSn) electrode. The inductor is in double anode looped configuration while the sample is mounted immediately adjacent to the inductor, and both are adhered to the surface of a standard microscope slide that has an evaporated gold layer on the opposite face, used as the grounding backplane.

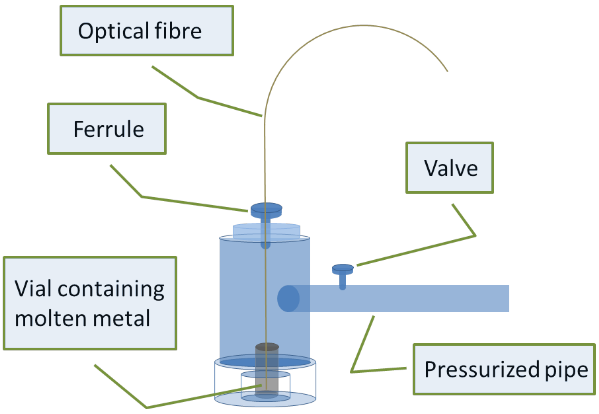

FIGURE 3.11: Schematic of the pressurization system used to fill the internal channels of a THF with molten metals. The fibre is immersed into a glass vial containing the metal and is fixed to the pipe by means of a ferrule. The pressurized arm of the pipe contains ≈ 300 *psi* of CO_2 or He. The whole system is inserted in a oven where it is heated up to 150 °C and then the valve is opened to allow the gas to push the liquid metal through the channel of the fibre previously selected by means of an epoxy resin selective sealing process.

The embedded electrode is realized by inserting the whole system, including the pipe and the fibre to be filled, in a oven and heating it up at a temperature of 150 °C, slightly higher than the melting temperature of the BiSn (138 °C). One hour later the valve of the pressurized pipe (containing some gas, such as for example CO_2 *or* He, at a pressure of $\approx$ 300 *psi*) is opened in such a way the gas pushes the molten alloy (held in a small glass vial) through the selected channel of the fibre (the selective filling is realized using an epoxy resin with a procedure similar to the one described by Sparks *et al.* in 2011 [129]). During the poling experiment the two tungsten wires (inserted into the two larger holes of the inductor) are looped and connected to the anodic potential of 4.3 kV supplied by an high voltage power supply, while the sample is mounted immediately adjacent to the inductor, and both are adhered to the surface of a standard microscope slide that has an evaporated gold layer on the opposite face, used as the grounding backplane. The duration of the poling is of 2 hours and the temperature of the sample is $\approx$ 300 °C. After this time the system is cooled down by switching off the hotplate and leaving on the voltage applied to the two anodic electrodes until the system reaches the room temperature.

After the poling experiment the two fibres have been cleaved along their whole length and etched in a HF solution with the aim of looking for some sign of induced nonlinearity on top of their cross-sections. Surprisingly, besides the expected two space-charge regions visible around the two large holes of the inductor, even around the hole of the sample initially equipped with the floating electrode a ring appeared after the etch. This ring was visible approximately along the same length of the inductor, that is in the region of the fibre placed on top of the microscope slide. In Fig. 3.12 an example of the cross-section of the sample poled by induction, cleaved and etched in HF solution for 1 minute is reported, together with the graph which shows the induced space-charge region width along the sample.

The relevance of this experimental result lies in the fact that for the first time it has been demonstrated that it is possible to thermally pole (and consequently induce a second order nonlinearity) a fused silica fibre simply embedding in it an electrode which does not need to be physically contacted. The only requirement to make the induction poling experiment successful seems to be the position of the sample (with respect to the inductor), which needs to be placed as close as possible to the inductor and the fact that the sample needs to be taken at a value of temperature high enough to guarantee the high mobility of the impurity charges which give rise to the glass poling.

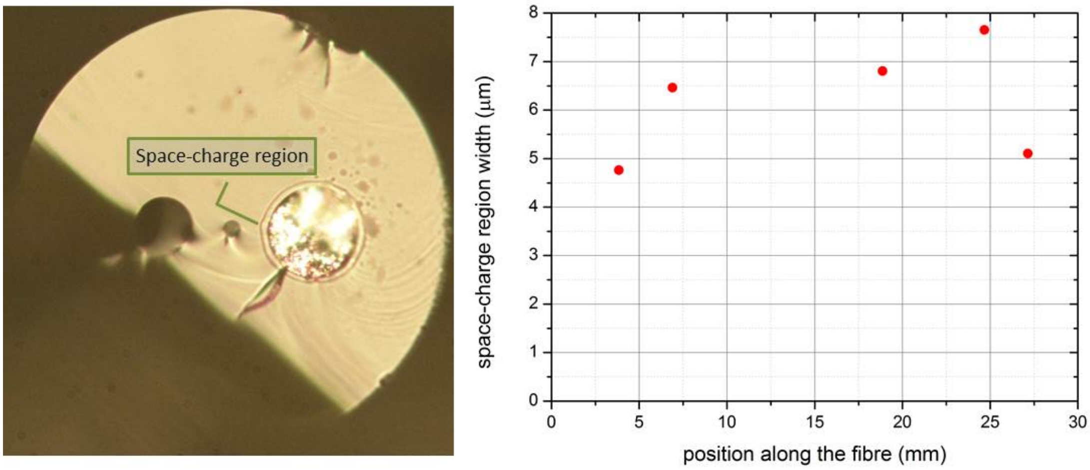

Figure 3.12: Left side: cross-sectional micrograph of the HF etched sample (THF) poled by electrostatic induction using the setup shown in Fig. 3.10. Right side: trend of the width of the space-charge region with the position along the sample. The whole length of the sample is of order $\approx$ 31 mm.

3.4 Implementation of a setup for induction poling of long samples

After the experimental results obtained and discussed in section 3.3, the next target becomes the exploration of the possibility of thermally poling a proper waveguide (such as for example a step-index optical fibre) by electrostatic induction, and possibly of doing that in such a way to pole a sample longer than the inductor. The fibre to be poled is a twin-hole pure silica fibre manufactured by Fibrecore Ltd., Southampton UK (OD of 125 μm (not including polymer coating), 4.3 μm diameter, 0.17 NA Germania-doped glass core).

The use of commercial fibres was motivated purely by their availability and simplicity, i.e., a convenient test bed to verify our understanding of the physical processes involved in induction poling and to optimize the induction poling technique. It is worth highlighting that the purity of the glass the fibre is made of does not allow a high value of $\chi^{(2)}_{eff}$ to be induced in the poled sample. Before the induction poling experiments, the cladding holes of the sample are filled with a BiSn alloy by means

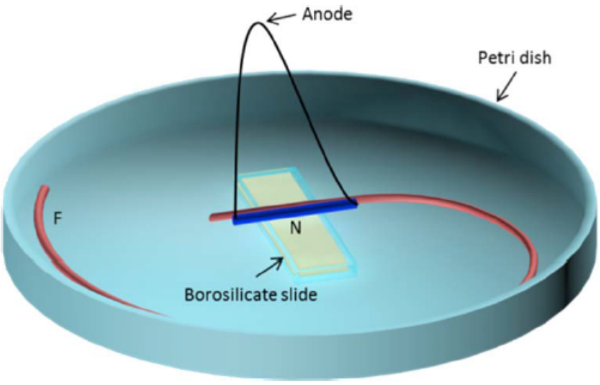

FIGURE 3.13: Schematic of the experimental setup for induction poling of optical fibres. The inductor is colored blue and equipped with two electrodes (tungsten wires) connected to the same anodic potential. This fibre serves as a dielectric barrier to prevent unwanted electrical breakdown in air. The red fibre (equipped with two embedded floating electrodes) is the sample to be poled. Both inductor and sample are adhered to a borosilicate slide and held in close proximity. The slide has a thin metallic layer evaporated onto its rear surface held at ground potential. N identifies a region of the sample near the inductor, F a section of the same sample located far away from the inductor. The entire Petri dish is heated with a (electrically earthed) hotplate at 300 °C [130].

of the technique described in Fig. 3.11. The starting point of this explorative stage of the experimental work is the setup shown in Fig. 3.10, where the two elements relevant for the success of the induction poling are the proximity of inductor and sample, and the thermal contact between the sample to be poled and the hotplate surface on top of which the Petri dish containing the setup is placed.

After few attempts focused on the improvement of both the aspects (increasing the contact surface between the two fibres and guaranteeing approximately the same temperature all along the sample to be poled), it was chosen to fix the length of the inductor (and consequently the contact surface between inductor and sample) and increase only the length of the sample, trying at the same time to guarantee a good thermal contact between sample and hotplate surface (all along the sample's length). The most successful solution found is reported in Fig. 3.13, where the inductor and the sample are adhered (immediately adjacent) to the surface of a standard microscope slide only for the length of the short side of the microscope slide ($\approx 25\ mm$), which, exactly as in the setup of Fig. 3.10, is equipped with an evaporated gold layer on the opposite face, used as the grounding backplane. The sample, whose whole length is of $\approx 20\ cm$, is wrapped around the Petri dish drawing a circular shape (see Fig. 3.13). The inductor, sample, and slide are placed in good thermal contact into a glass Petri dish placed on the surface of a hotplate.

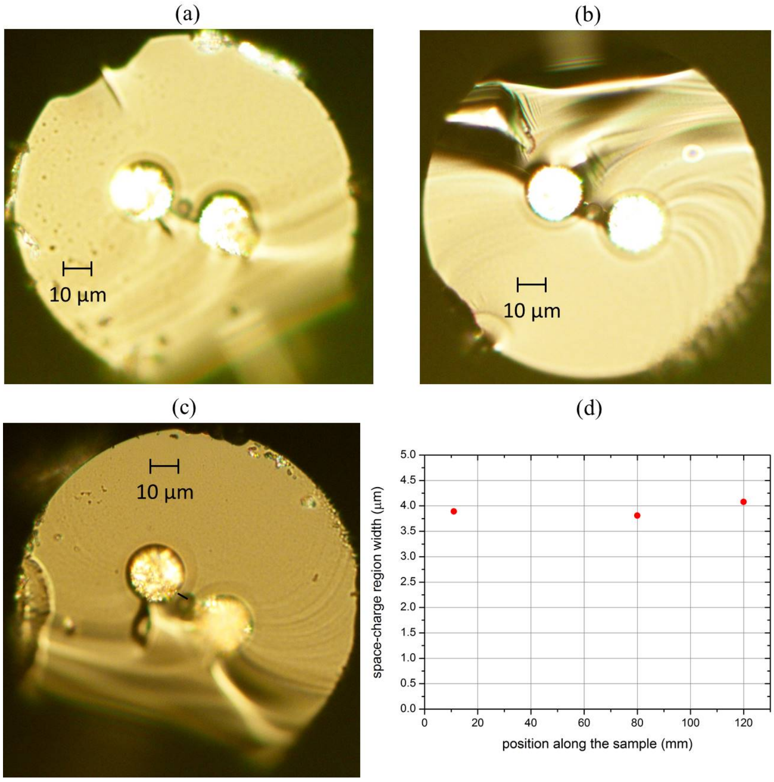

FIGURE 3.14: (a), (b), (c): three cross-sectional micrographs of the HF etched sample (twin-hole fibre) poled by electrostatic induction by means of the setup shown in Fig. 3.13. The experimental conditions of the poling experiments are $T \approx 300$ °C, $V_{app} = 4.3$ kV, time of poling = 2 hrs, cooling time = 1 hr. The cross-sections were collected in three different positions along the sample (the zero reference point is the beginning of the uncoated part of the fibre, located on the right edge of the microscope slide shown in Fig. 3.13. (d): trend of the width of the space-charge region with the position along the sample [131].

The advantage of using the circular setup just described consists in the fact that there is ideally no limit to the length of the sample to be poled by induction, provided that the fibre could be held inside the Petri dish. The experimental conditions of the first test of induction poling are the same presented in section 3.3 ($T \approx 300$ °C, $V_{app} = 4.3$ kV, time of poling = 2 hrs, cooling time = 1 hr).

The results of this thermal poling experiment are shown in Fig. 3.14, where three cross-sections of the sample poled etched in HF solution are reported, together with the graph showing the space-charge region width evolution along the length of the sample. It is quite clear that a space-charge region was induced by induction poling along a length of the sample of at least 120 mm. This result represents the first absolute experiment of thermal poling of an optical fibre by means of a no-contact technique (electrostatic induction), which potentially could allow for poling samples of metres of length.

3.5 Numerical 2D-model of induction poling

After the experimental observation (via decorative etching of the poled fibre in a HF aqueous solution) of a space-charge region created by means of an electrostatic induction mechanism, the next target of my research activity is the implementation of a numerical model which could confirm the reliability of the observed phenomenon and improve the understanding of the dynamics of the electromigration process. The numerical models presented in sections 3.5.1, 3.5.2 and 3.5.3 are implemented by using $COMSOL^{TM}$ Multiphysics, a cross-platform finite element analysis (FEA), solver and multiphysics simulation software. The finite element method is a numerical method for solving problems of engineering and mathematical physics. While the analytical solution of these problems generally require the solution to boundary value problems for partial differential equations, the finite element method formulation of the problem results in a system of algebraic equations. The method yields approximate values of the unknowns at discrete number of points over the domain [132]. To solve the problem, it subdivides a large problem into smaller, simpler parts that are called finite elements. The simple equations that model these finite elements are then assembled into a larger system of equations that models the entire problem.

3.5.1 Numerical 2D-model of cathodeless poling of silica fibres

The starting point of the process of implementation of a numerical model is the description of conventional thermal poling of optical fibres in cathodeless configuration, developed by Camara *et al.* [133] in 2014. While most of the models developed before this work were related to bulk glasses and for this reason were unidimensional [77, 96, 134–136], the model implemented by Camara *et al.* addresses for the first time the specific and complex geometry of poled fibres with internal electrodes, and so it is a two-dimensional (2D) model. The numerical simulations which constitute the model of Camara are based on a 2D implementation of an ion-exchange model (basically the one developed by Kudlinski *et al.* [96]), applied to poled fibres by using a $COMSOL^{TM}$ Multiphysics platform, and take into account the presence of a faster cation (Na^+) and a slower cation (Li^+) that are initially uniformly distributed in the glass matrix, and the injection of a hydrogen-related species (H_3O^+) from the surfaces in contact with the anodic electrodes. The physics of the numerical model is based on the transport of diluted species problem, assuming that low concentration ions ($\approx 1\ ppm$) move in the presence of diffusion and drift due to an electric field [77, 96]. The cladding holes of the twin-hole fibre are assumed to be entirely filled by metal [108], and provide a perfect equipotential. A quite dense two-dimensional mesh is chosen over the cross-section of the fibre studied, defined with the help of a scanning electron microscopy (SEM) picture of the fibre. The problem solved in x, y and t for the concentration of the i-th ion (Na^+, Li^+ and the hydrogen species, such as H_3O^+) is [133]:

$$\frac{\partial c_i}{\partial t} + \boldsymbol{\nabla} \cdot (-D_i \boldsymbol{\nabla} c_i - z_i \mu_i F c_i \boldsymbol{\nabla} V) = R_i \tag{3.1}$$

where the first term in brackets accounts for diffusion while the second one for drift in the electric field E, c is the concentration, D is the diffusivity, z is the charge, μ is the ionic mobility, F is Faraday constant, V the electric potential and R the consumption or production rate. The electric field and electric potential distribution are obtained from the Maxwell's equations in the electrostatics regime (magnetic fields are neglected).

The boundary conditions assumed in the model of Camara *et al.* are the initial electrical neutrality of the fibre (the mobile ions and the motionless NBO^- centres are characterized by the same concentration inside the fibre), the potential at the surfaces of the holes is the applied voltage during the poling process and zero when the voltage is switched off, the fact that the outer surface of the fibre is at zero volts and that the cations exit the outer surface and do not come back. The hydrogenated species is assumed to be injected from the surface of the holes and move driven by the applied electric field. Two possible situations are investigated, respectively the one of the injection rate of H_3O^+ constant, which assumes the existence of ions already at the surface of the hole (in the glass) [77], and the one of an injection proportional to the electric field on the surface of the hole, as implemented in [96].

The initial carrier concentrations assumed by Camara *et al.* in their simulations are: c(Na^+) = 1 ppm uniformly distributed in the glass at t = 0 sec; c(Li^+) = 1 ppm uniformly distributed in the glass at t = 0 sec; c(H_3O^+) = up to 2 ppm injectable from the holes, initially zero in the entire fibre, supplied at a rate that is either constant, linearly dependent on the field at the electrode edge, or decaying exponentially as the ion supply is exhausted; c(NBO^-) = 2 ppm uniformly distributed in the glass at t = 0 sec for guaranteeing the initial charge neutrality. Their values have been chosen consistently with the nominal value of the contamination level of the ILMASIL PN fused quartz used as inner cladding in preform fabrication. Nevertheless the value of cation concentration used in the model affects the maximum $\chi^{(2)}_{eff}$ recorded, and could be considered a source of errors for the model.

Another source of error in the numerical calculation is the value used for the mobility of the impurity charges. The mobility of Na^+, for example, at a given temperature, depends on the type of silica glass sample and its OH and cation content, leading to a large range of mobility values in the literature. The mobility of the cations, expressed in $m^2/V \cdot s$, is derived from the diffusivity using the steady-state condition when the current is zero and the drift of carriers cancels diffusion, in which case $\mu_{ion} = zFD_{ion}/RT$, where $z = 1$, $F = 9.65 \times 10^4\ C/mol$ and $R = 8.31\ Jmol^{-1}K^{-1}$. The diffusion coefficients are calculated from the value for sodium $D_{Na} = D_0(Na^+)e^{(-H/k_BT)}$, where the activation energy for sodium ions is assumed to be $H = 1.237\ eV$. Unless it is specified otherwise, the mobility values in the simulations at 265 °C are $2 \times 10^{-15}\ m^2/Vs$ for sodium, $0.15 \times \mu(Na)$ for Li^+ and $\mu(Na)/1000$ for H_3O^+. These values differ relatively little from those reported in literature [77, 96, 137–139], correcting for the temperature. The recorded electric field experienced by the light which propagates in the core is determined from the weighted average of the field value at five points across the core (i.e., a discrete overlap integral). The second order nonlinearity value is obtained from the expression $\chi^{(2)}_{eff} = 3\chi^{(3)}E_{dc}$ (equation (2.69)) where the chosen value of $\chi^{(3)}$ is $2 \times 10^{-22}\ m^2/V^2$ and is assumed to be invariant during the poling process [140].

In Fig. 3.15 it is possible to have an idea of the temporal evolution of the concentrations of the two impurity species already present into the glass matrix (Na^+ and Li^+) and of the hydrogenated species injected after the application of the external electric field (H_3O^+).

Apart from the dynamics of the space-charge region, Camara *et al.* studied, by means of the numerical model elaborated, the effect of changing some experimental parameters, such as for example the voltage applied, the concentration of impurities and the temperature, on the final value of the $\chi^{(2)}_{eff}$ obtained. They found that

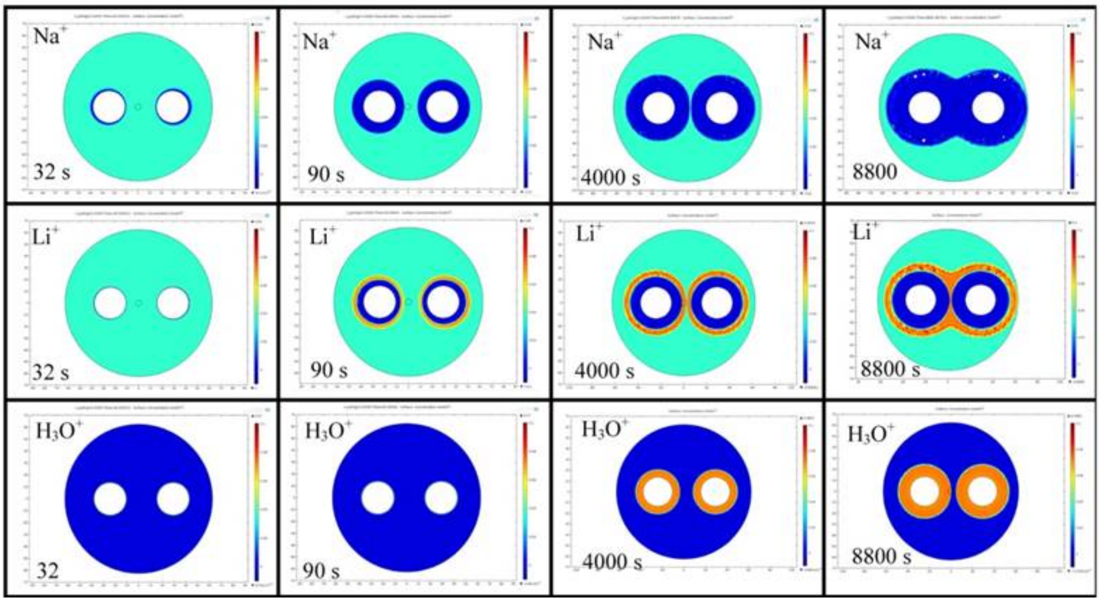

FIGURE 3.15: Temporal evolution of the mobile cations for a Germania doped twin-hole fused silica fibre poled in a cathodeless configuration (the two electrodes embedded in the two holes are both connected to the same potential of 5 kV). The injection of the hydrogenated species H_3O^+ is assumed to be inexhaustible and capable to neutralize the NBO^- centres depleted of the impurity positive ions moved because of the application of the external electric field [133].

not only the value of the second order nonlinearity induced by cathodeless poling increases with the value of the voltage applied, but also that the time after which this maximum value is obtained scales approximately following a dependence of type $1/V_{app}$. They discovered also that the initial impurity concentration, for values bigger than 1 ppm, does not affect significantly the final value of $\chi^{(2)}_{eff}$, whereas it has a stronger effect for values of concentration below 0.2 ppm.

The effect of the poling temperature on the final value of $\chi^{(2)}_{eff}$, instead, is more complex to explain. In general, increasing the temperature of the sample to be poled increases the mobility of the ionic species involved in the thermal poling experiment, which should make the dynamics of the process simply faster. This does not mean that for higher temperatures the $\chi^{(2)}_{eff}$ value in a defined point of the fibre is bigger. Indeed the ideal temperature of poling (the one which produces the highest possible value of $\chi^{(2)}_{eff}$) is strictly related to the duration of poling, which can be considered another relevant parameter to optimize when a thermal poling process is realized. If the temperature is higher, and consequently the mobile charges are faster, it could be likely that the hydrogenated species will be able to neutralize an higher number of NBO^- centres, reducing the number of negative charges in the space-charge region and in such a way reducing the frozen-in electric field which determines in the end the value of the $\chi^{(2)}_{eff}$.

A very important parameter which affects the value of $\chi^{(2)}_{eff}$ is the actual position of the fibre's core with respect to the two cladding holes, because the value of the frozen-in electric field could slightly change along the space-charge region radius. It is worth highlighting that in case of optimization of the process of fabrication of a nonlinear all-fibre device, which is one of the targets of my thesis work, it is relevant to take into account this aspect.

3.5.2 Upgrade of the numerical 2D-model for cathodeless poling of silica fibres

Before elaborating the numerical 2D-model for the induction poling of long silica fibres (see Fig. 3.13), in first instance the model created by Camara *et al.* has been slightly modified in order to adapt it as much as possible to the actual arrangement of our experimental setup for the preliminary experiment of cathodeless poling of silica samples, described in section 3.2 and reported in Fig. 3.7.

The first relevant change produced to the Camara's model is the definition of the ground of the system. In the model of Camara the external surface of the fibre is assumed physically contacted to the ground of the high voltage power supply which supplies the electric potential to the electrodes embedded into the cladding holes of the twin-hole fibre. We, instead, assume that the external surface of the fibre is not grounded. This choice is due to the fact that in the induction poling experiment (which is the experiment we really want to model), if the surface of the *inductor* was assumed grounded, it would screen the electric field lines, not allowing them anymore to penetrate even the *sample* to be poled by induction (see Fig. 3.10). In other words the sample would not see the electric potential applied to the electrodes embedded into the inductor and so it would not be poled at all. In order to guarantee the consistency of the electrostatic module of the numerical model, it is in any case necessary to identify the ground of the system somewhere else. For this reason the sample to be poled in cathodeless configuration (in the numerical model) has been inserted in the centre of a virtual metallic box (containing air) whose walls are all contacted to the electrical ground of the power supply. This choice allows to simulate the fact that the ground of the system in the actual experiment is in any case located somewhere around the sample, for example the hotplate coil. For the sake of reliability of the model, the fibre, in the modified model, is assumed to be placed on top of a borosilicate slide, which has a defined backplane in such a way it can be possible to choose to identify the ground also in correspondence of the backplane of the microscope slide, as reported in Fig. 3.7. In this way the effect of distance (on the dynamics of the electromigration process of the impurity charges) between groundplane and sample to be poled can be studied.

The model has been simplified limiting the study to a single "fast" carrier (Na^+) besides the hydrogenated species (H_3O^+). The initial concentration of the Na^+ is assumed to be the same of the Camara's model (1 ppm) (even if the actual fibre used for the early experiments of induction poling is the pure silica Fibercore sample described in section 3.4), while the geometry of the fibre is different from the one chosen by Camara *et al.* in their simulations. The fibre used in our experiments has indeed the two holes (of $\approx$ 19 μm of diameter) located in a symmetric position with respect to the centre of the fibre (the edge of each hole is at a distance of $\approx$ 6 μm from the fibre's core).

Fig. 3.16 and 3.17 show the temporal evolution of the impurity charges concentration realized in cathodeless configuration and obtained by means of the modified Camara model (MCM) implemented for a thermal poling process of 120 mins. The impurities mobility and diffusion coefficients have been calculated for a temperature of the sample of 300 °C, while a positive potential of 4.3 kV is applied to both the electrodes embedded into the twin-hole silica fibre. The groundplane is located at a distance of 1 mm from the fibre in the first simulation and is "absent" in the second one (in the sense that only the box's walls are grounded). The main aim of these simulations is how the presence of a groundplane, located at a certain distance from the sample to be poled, affects the dynamics of the space-charge region formation.

The simple qualitative comparison between the temporal evolutions of the two concentrations of the impurity charges involved in the electromigration process (shown in Fig. 3.16 and in Fig. 3.17), calculated respectively by means of the model with the microscope slide of 1 mm thickness grounded and one with the microscope slide not grounded (the physical ground of the system is located at the walls of the box (a square of 10 cm of side) where the whole system is inserted), demonstrates that even if there is a slight difference between the two cases, it

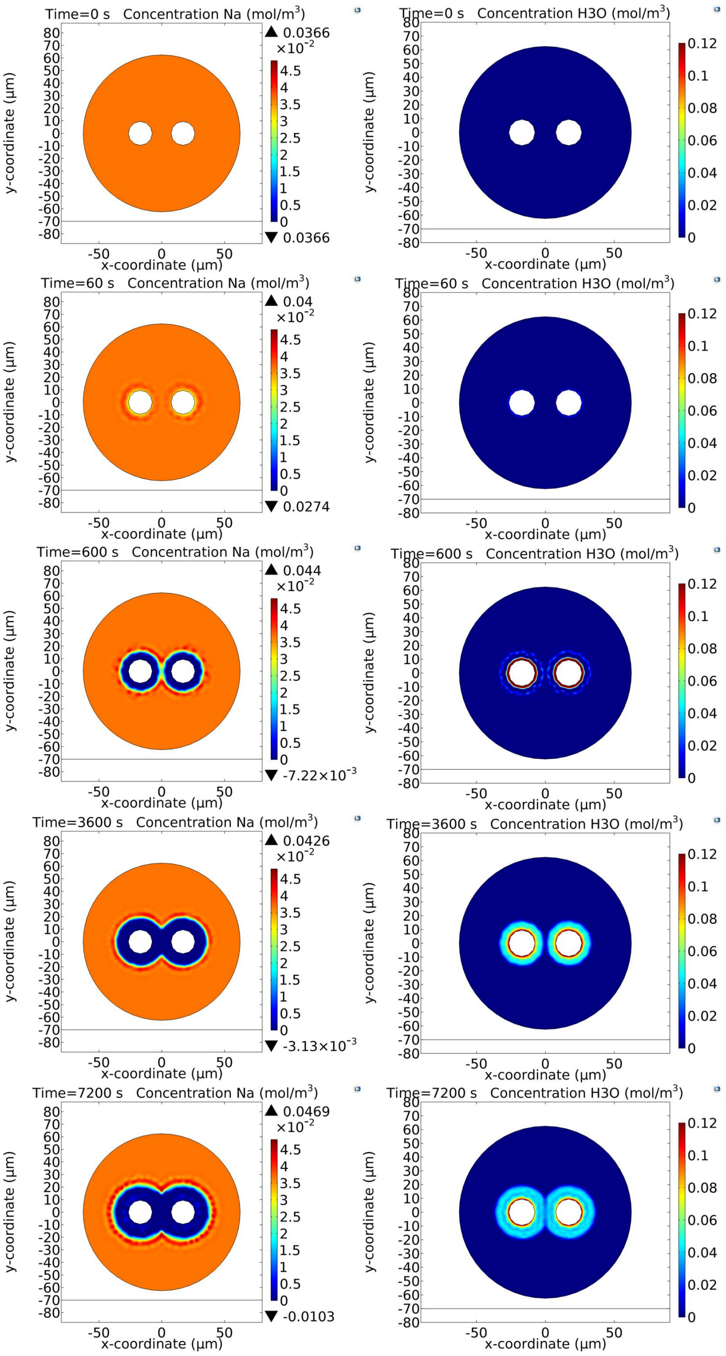

FIGURE 3.16: Temporal evolution of the two types of mobile positive ions (Na^+ in the left column and H_3O^+ in the right one) obtained via the modified Camara model (MCM). The most relevant variation to the original model is represented by the external surface of the fibre, which is not grounded, while the back plane of the microscope slide (1 mm thick) is grounded. The fibre's geometry is that of the Fibercore sample described in section 3.4. For the sake of simplicity the initial concentration of the impurity charges is arbitrarily assumed equal to 1 ppm, the same value of the fused silica fibre simulated by Camara. The temperature of the experiment is assumed 300 °C while the injection of the hydrogenated species H_3O^+ is assumed to be inexhaustible and capable to neutralize the NBO^- centres depleted of the impurity positive ions moved because of the application of the external electric field. The voltage applied to both the electrodes embedded into the sample corresponds to 4.3 kV.

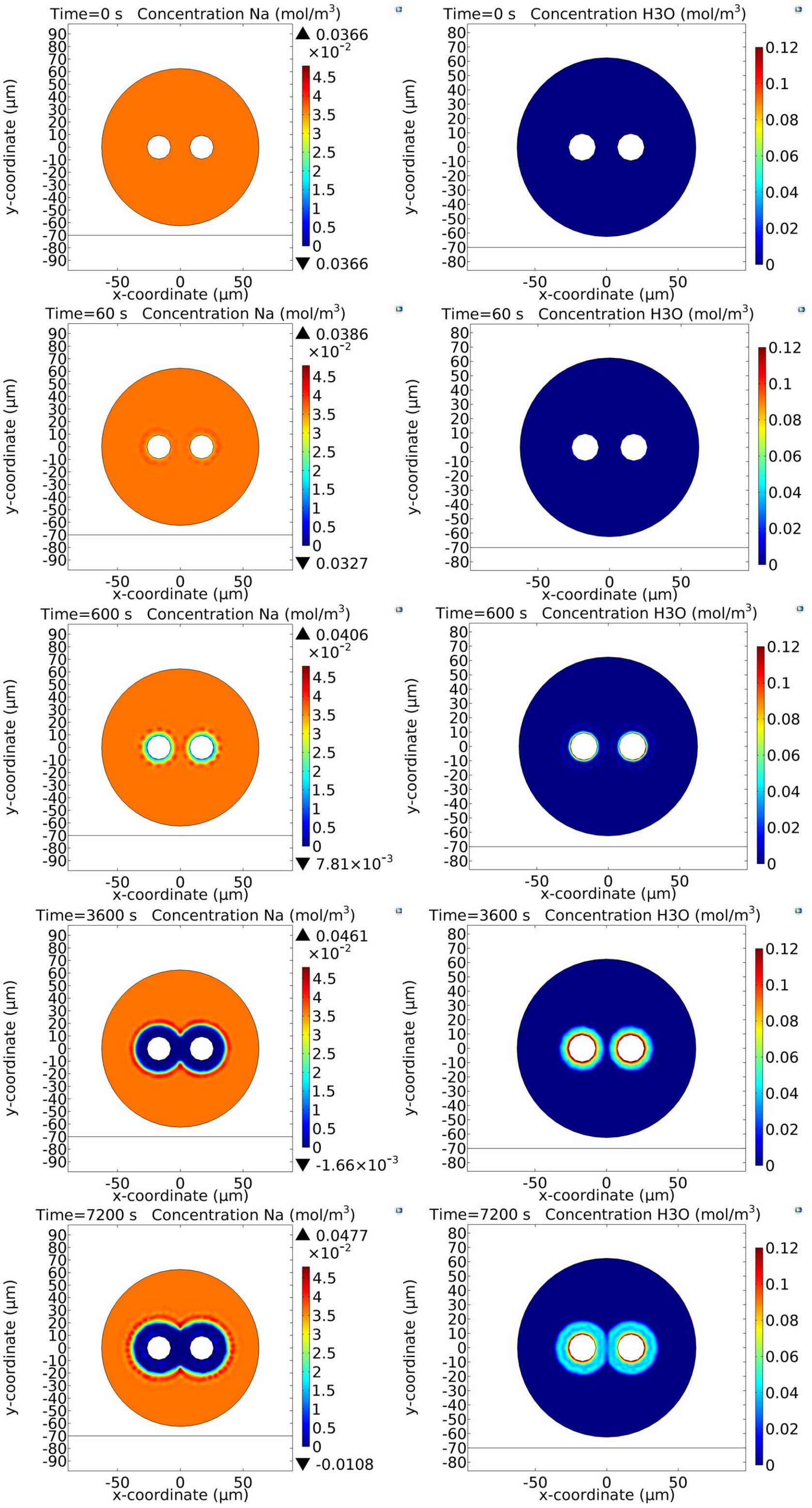

FIGURE 3.17: Temporal evolution of the mobile positive ions obtained via the MCM. The external surface of the fibre is not grounded, like the backplane of the microscope slide where the sample to be poled lies. The ground of the setup is located at the walls of the box (10 cm of side length) where the setup is located. The fibre's geometry, the initial concentration of the impurity charges, the temperature and the voltage applied are the same reported in Fig. 3.16.

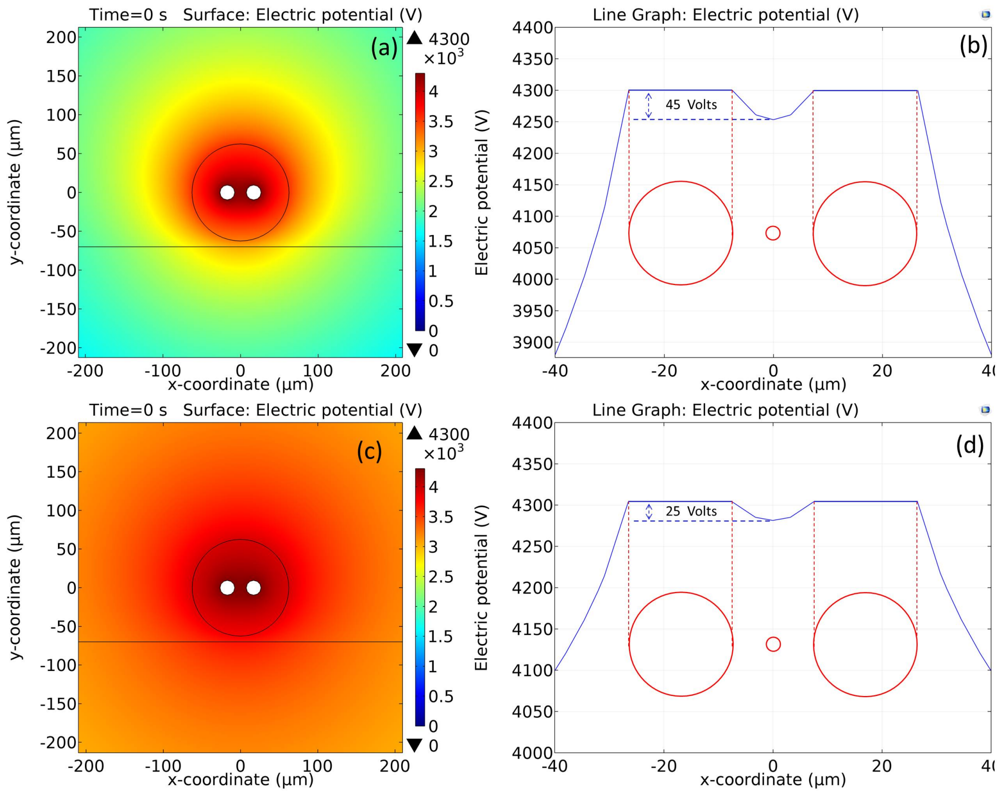

FIGURE 3.18: (a) Simulated initial 2D electrostatic potential distribution before charged ion migration begins to generate the space-charge region (the black line under the sample corresponds to the top surface (located at a distance of few microns from the external surface of the fibre for reasons related to the choice of the numerical simulation meshes) of a microscope slide whose back side (not visible in the figure) is grounded); (b) electrostatic potential values recorded along a line scan through the geometric centres of the sample obtained using the MCM reported in Fig. 3.16 (groundplane at 1 mm of distance); (c) simulated initial 2D electrostatic potential distribution before charged ion migration begins to generate the space-charge region (the black line under the sample corresponds to the top surface of a microscope slide whose back side (not visible in the figure) is not grounded); (d) electrostatic potential values recorded along a line scan through the geometric centres of a sample obtained using the MCM reported in Fig. 3.17 (groundplane "absent").

does not give us any interesting information. A more quantitative knowledge about the effects of the presence and distance of a groundplane of the fibre to be poled can be obtained by calculating the value of the $\chi^{(2)}_{eff}$ in the fibre's core by means of the equation (2.69), where the value of the electric field after the poling process is calculated by $COMSOL^{TM}$ Multyphysics. Fig. 3.18 shows the initial 2D electric potential distribution and electric potential values recorded along a line scan through the geometric centres of the sample in both the situations where the back plane of the microscope slide (1 mm thick) is grounded and where the ground of the setup is located at the walls of the box (10 cm of side length) where the setup is located. The presence of a well-defined groundplane affects the initial drop of potential between each electrode and the centre of the fibre.

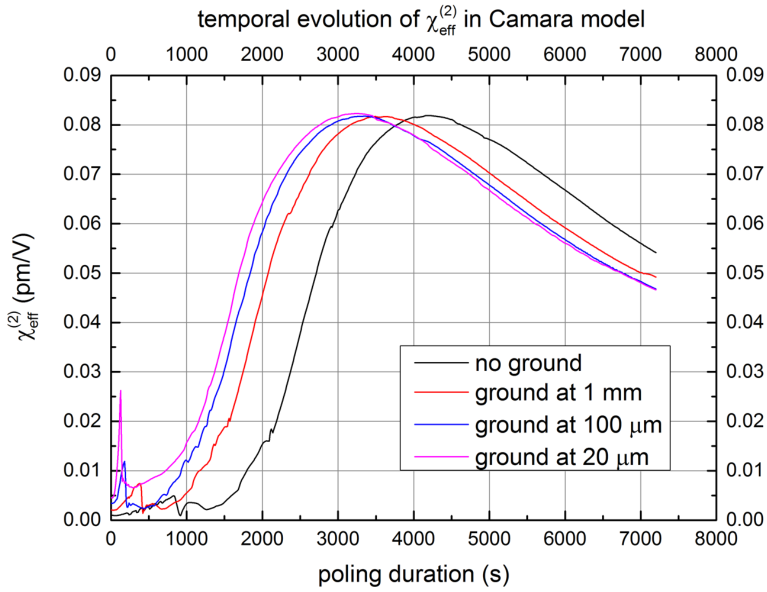

FIGURE 3.19: Temporal evolution of the value of $\chi^{(2)}_{eff}$ calculated in the centre of the fibre (core) via the MCM, for different positions of the groundplane with respect to the fibre to be poled, that are ≈ infinite (groundplane "absent"), 1 mm, 100 μm and 20 μm.

In Fig. 3.19 the graphs of the $\chi^{(2)}_{eff}$, calculated in the fibre's core by means of numerical simulations over two hours of poling are reported in different configurations of the system's groundplane, namely "absent", 1 mm, 100 μm and 20 μm.

The comparison among the different configurations indicates that the presence of the groundplane affects the temporal evolution of the $\chi^{(2)}_{eff}$ value, while it does not affect almost at all the maximum value of the $\chi^{(2)}_{eff}$ that can be obtained. So, depending on the duration of the thermal poling process, it is possible to see that, for example, the presence of the groundplane near the fibre allows to increase the $\chi^{(2)}_{eff}$ value in the fibre's core with respect to the situation where the ground is far (tens of cm) for a poling duration of less than ≈ 3000 s, while for more than ≈ 4000 s the presence of the groundplane reduces the $\chi^{(2)}_{eff}$ value which can be obtained. In other words it would be possible to optimize the poling duration according to the position of the groundplane, while it seems that, at least according to the numerical model, the presence of the groundplane should not significantly affect the maximum value of $\chi^{(2)}_{eff}$ that can be anyway obtained. It is worth highlighting that in our experiments of thermal poling the effect of the distance of the groundplane was not studied in details, because, as it will be clearer in chapter 4, the choice of the groundplane configuration was always inspired by the practical issues of the experiment to be realized each time. Furthermore even the effect of the duration of the poling on the value of $\chi^{(2)}_{eff}$ was not experimentally evaluated because of the lack of sufficient sample of fibre to be poled and eventually tested.

Another interesting consideration is that, by means of the model developed, it could be possible to study the effect on the value of $\chi^{(2)}_{eff}$ generated into the core of the fibre of other parameters, such as for example the voltage applied to the two embedded electrodes or the position of the two electrodes with respect to the core.

3.5.3 Numerical 2D-model for electrostatic induction poling of long silica samples

After testing the reliability of the 2D MCM, a model for induction poling of long samples can be implemented simply dividing the model in two submodels, one conceived to describe the dynamics of the electromigration process in the part of the setup where the two fibres (*inductor* and *sample*) are close each other (called "near model"), and one for the part of the setup where the sample is far from the inductor (called "far model"). Fig. 3.13 allows to distinguish clearly the two sections of the setup described by the two different submodels. The main difference between these consists in the fact that in the first case the sample is immersed in the electric field lines generated by the externally applied electric field while in the second case it is not. The reliability of this "double" model is based on the assumption of electrical continuity of the electrodes embedded into the sample to be poled. The working principle of the electrostatic induction poling of long samples is based on the idea that, when the two floating electrodes, embedded into the sample, are immersed in the external electric field (supplied by the inductor in the region where the two fibres are in proximity), they pick up the electric field, become electrically charged because of an electrostatic induction process and so reach a certain electric potential [141]. Furthermore, due to the fact that during induction poling, there is very little, if any, current flow through the fibre; therefore, virtually no voltage drop due to metallic series resistance, the internal floating electrodes will present a well-characterized equipotential surface throughout the entire sample. This means that any electric potential picked up by

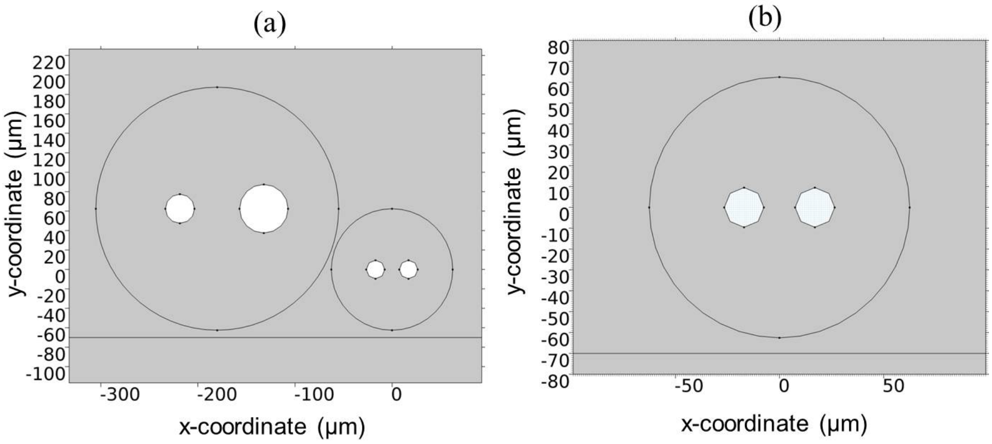

FIGURE 3.20: a) Schematic of the geometry of the two fibres used in the 2D numerical model for simulating an electrostatic induction thermal poling process. The schematic corresponds to the part of the setup where the two fibres (inductor on the left and sample on the right) are close each other. The flat surface below the two fibres is the upper part of the microscope slide where the two fibres lie. b) Schematic of the geometry of the setup for induction poling implemented in the 2D numerical model, corresponding to the part of the setup where the sample is far from the inductor.

the floating electrodes close to the inductor will be effectively transferred to any remote location throughout the fibre [130].

In Fig. 3.20 the geometry of the setup for induction poling is reported in both the positions, namely near and far from the inductor. The duration of the numerically simulated process is chosen being 120 mins.

3.5.3.1 “Near” 2D-model

The numerical model assumes that the inductor is made of a glass totally lacking any impurity charge inside, while the sample is assumed to be a fused silica twin-hole fibre with an initial concentration of 1 ppm of Na^+. It is also assumed that in the sample there is up to 1 ppm of H_3O^+ ions injectable at the cladding holes, with none present within the fibre at t = 0 s. To achieve initial charge neutrality, negatively charged, nonbridging oxygen sites with extremely low mobility are uniformly distributed inside the sample with a concentration of 1 ppm at t = 0 s. The cladding holes are also assumed to be entirely filled with metal electrodes and present an equipotential.

Furthermore, H_3O^+ ions can be injected through the electrode-cladding surface when located at electric potentials higher than the surrounding cladding. An adjustable parameter σ_2 (whose value is chosen to be the same as the well established thermal poling model reported in [96]) is used to describe the charge injection into the sample. We also need to consider the special case where the electric field is less than zero. In this case, H_3O^+ ions in the nearby cladding (either previously injected or diffused from other parts of the fibre) will have a negative injection rate, thus implying an outflow of H_3O^+ ions. However, if there are not any H_3O^+ ions (i.e., $c(H_3O^+) = 0$) at the electrode-cladding boundary, the injection rate will be zero, even with an electric field less than zero. Therefore, the variation of the injected H_3O^+ density per unit of time at the electrode-cladding surface can be written as [96]:

$$\left.\frac{\partial c_2}{\partial t}\right|_{surface} = \sigma_2 E, \qquad E \geq 0 \quad or \quad E < 0 \quad and \quad c_2 > 0 \tag{3.2}$$

$$\left.\frac{\partial c_2}{\partial t}\right|_{surface} = 0, \qquad otherwise \tag{3.3}$$

where c_2 indicates the concentration of the H_3O^+ species and σ_2 the constant chosen. In the "near model" the two fibres are located, immediately adjacent each other, on top of a borosilicate microscope slide of 1 mm of thickness, which can be equipped on its back face with a metallic coating which can be grounded. Again the four different situations have been simulated where the groundplane is respectively "absent" (and only the walls of the box of 10 cm of side length, inside which the whole setup is located, are grounded) or present and distant 1 mm, 100 μm and 20 μm from the two fibres. Fig. 3.21 reports five different pictures showing the temporal evolution, inside the sample, of the concentrations of both the Na^+ and H_3O^+ ions, calculated numerically in the part of the setup where the two fibres are in proximity and with a groundplane located at a distance of 1 mm from the two fibres (physically represented by the backface of the microscope slide where the two fibres lie). The model for the induction poling developed in $COMSOL^{TM}$ Multiphysics assumes that the voltage applied to both the electrodes embedded into the inductor corresponds to 5 kV while the electrodes embedded into the sample are floating at initially at zero potential. Fig. 3.22 reports the temporal evolution of the two concentrations when the groundplane is absent and only the walls of the box containing the whole setup are grounded. Fig. 3.23 shows the electric potential values recorded (at the instant the voltage of 5 kV is applied to the electrodes embedded in the inductor) along a line scan through the geometric centres of the sample in both the situations where the back plane of the microscope slide (1 mm thick) is grounded and where the ground of the setup is located at the walls of the box (10 cm of side length) where the setup is located. As for conventional poling (see Fig. 3.18), the presence of a well-defined groundplane in the region where sample and inductor are adjacent, affects the drop of potential between the two floating electrodes embedded in the sample and so the dynamics of the space-charge region formation.

The asymmetric evolution of the space-charge region (for example the one generated by the electromigration process of the Na^+ charges) can be compared to the one obtained in the cathodeless poling experiment (see Fig. 3.16). This asymmetric evolution is due to the presence on the sample's left side of the inductor with the electrostatic potential applied, but also to the way the process of electrostatic induction works.

Fig. 3.24 reports at the same time the equipotential lines and the arrows representing the electric field orientation at the istant when the external electric potential is applied to the inductor (simulated considering the groundplane at 1 mm from the fibres). The presence of the positively charged electrodes embedded inside the inductor (inductor-electrodes) attracts the electrons present on the surface of each floating electrode embedded in the cladding holes of the sample towards the inductor. Consequently the right half of each floating electrode embedded in the sample becomes positively charged. In other words some of the electric field lines originating from the surface of the inductor-electrodes end on the left side of the surface of each floating electrode, while other electric field lines originate from the right side of each floating electrode. This "distorted" electric field distribution starts inside the sample a process of electromigration of the positive impurity ions located near the right side of each floating electrode and initially the space-charge region evolves only towards the right direction. But there are some positive impurity charges (located near the surface which separates the left and right side of the floating electrode) which experience an electric field much weaker than the one experienced by the charges located near the electrode's part farthest from its centre. For these charges the contribution of the diffusion is higher than the one of the electromigration, so they start to migrate from the right side of the sample towards the left. This process produces the evolution of the depletion region even towards the left side of each floating electrode. This different dynamics on the two

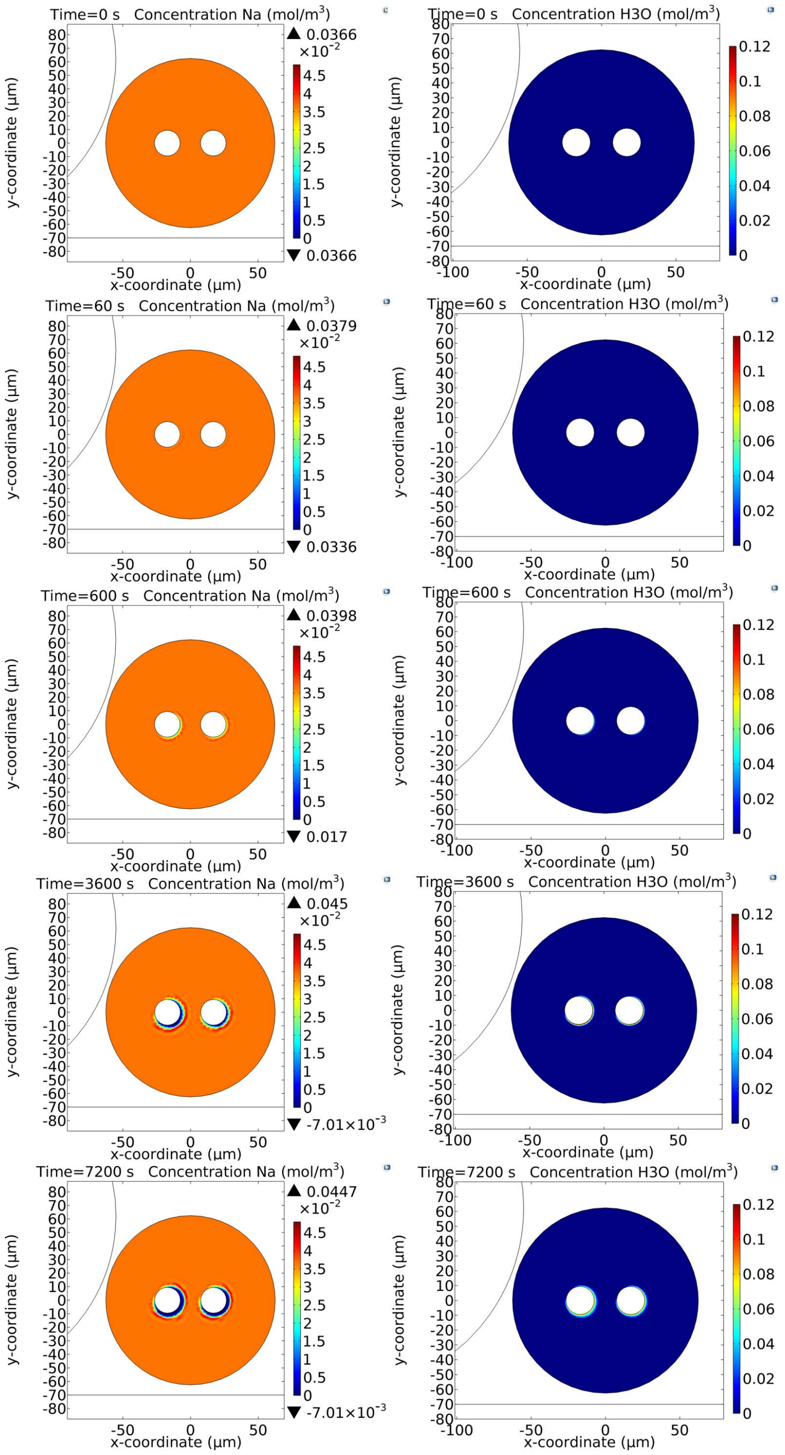

FIGURE 3.21: Temporal evolution of the mobile positive ions obtained via the “near model” for induction poling. Only the electromigration inside the sample to be poled is considered, while the mobile ions of the inductor are assumed absent. The external surface of both the fibres is not grounded while the groundplane is located at 1 mm of distance from the two fibres. The initial concentration of the impurity charges (Na^+) is arbitrarily assumed of 1 ppm. The temperature of the sample in the simulation is assumed to be 300 °C while the injection of the hydrogenated species H_3O^+ is assumed to be inexhaustible and capable to neutralize the NBO^- centres depleted of the impurity positive ions moved because of the application of the external electric field. The voltage applied to both the electrodes embedded into the inductor corresponds to 5 kV.

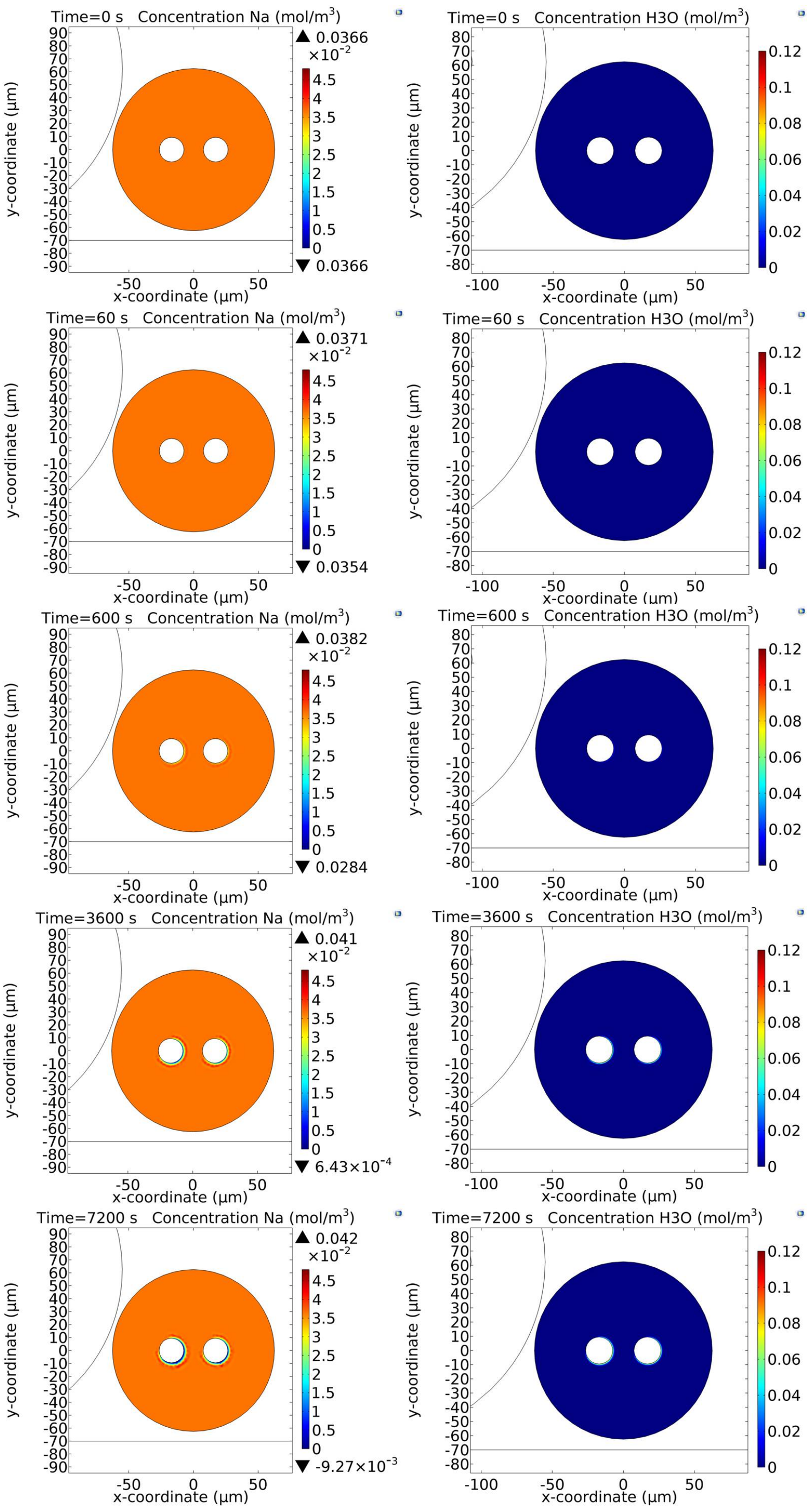

FIGURE 3.22: Temporal evolution of the mobile positive ions obtained via the "near model" for induction poling. Only the electromigration inside the sample to be poled is considered, while the mobile ions of the inductor are assumed absent. The external surface of both the fibres is not grounded while the groundplane is absent and only the walls of the box (10 cm of side) containing the whole setup are grounded. The conditions of the simulation are the same as reported in Fig. 3.21.

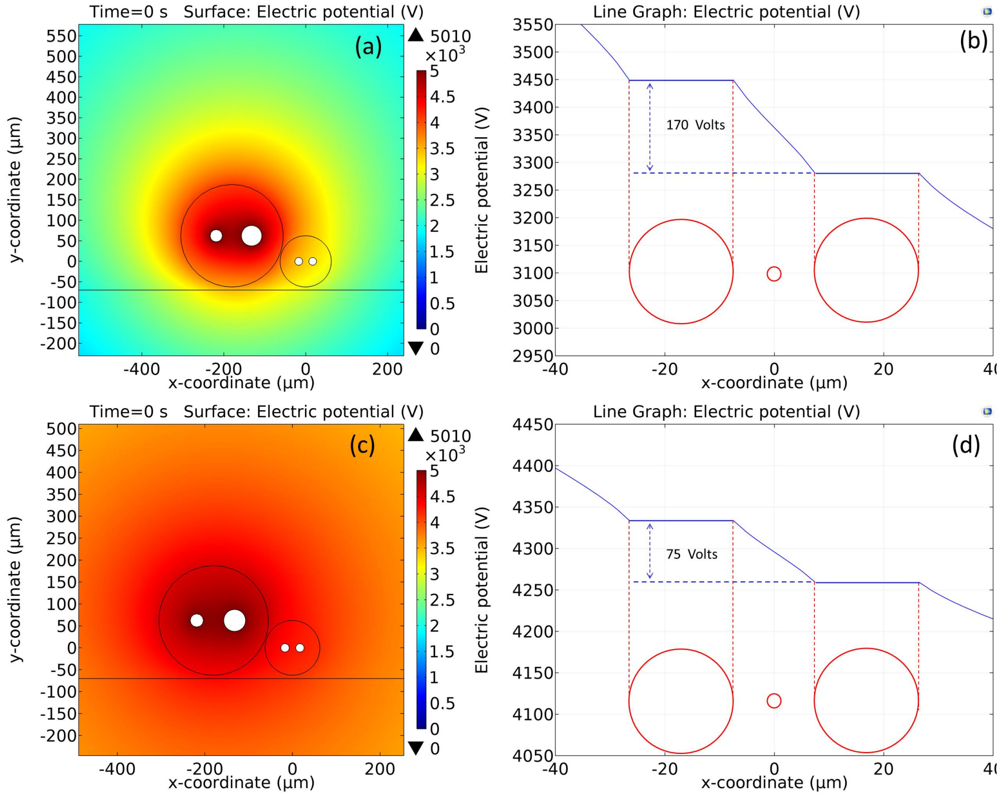

FIGURE 3.23: (a) Simulated initial 2D electrostatic potential distribution before charged ion migration begins to generate the space-charge region (the black line under inductor and sample corresponds to the top surface of a microscope slide whose back side (not visible in the figure) is grounded); (b) electrostatic potential values recorded along a line scan through the geometric centres of the sample obtained using the "Near" 2D-model reported in Fig. 3.21 (groundplane at 1 mm of distance); (c) simulated initial 2D electrostatic potential distribution before charged ion migration begins to generate the space-charge region (the black line under inductor and sample corresponds to the top surface of a microscope slide whose back side (not visible in the figure) is not grounded); (d) electrostatic potential values recorded along a line scan through the geometric centres of the sample obtained using the "Near" 2D-model reported in Fig. 3.22 (groundplane "absent").

sides of the floating electrodes produces the asymmetric shape of the space-charge regions in an induction poling experiment.

As already discussed in section 3.5.2, the images of the concentrations of the two types of impurity charges give only an idea about the space-charge regions dynamics in the two situations of "absence" and presence of a groundplane in an induction poling experiment and it is quite clear that there is a certain difference between the two situations. In order to better understand what different dynamics of the space-charge region formation means in terms of nonlinear behaviour of the poled fibre, it is necessary to calculate the value of the $\chi^{(2)}_{eff}$ in the two

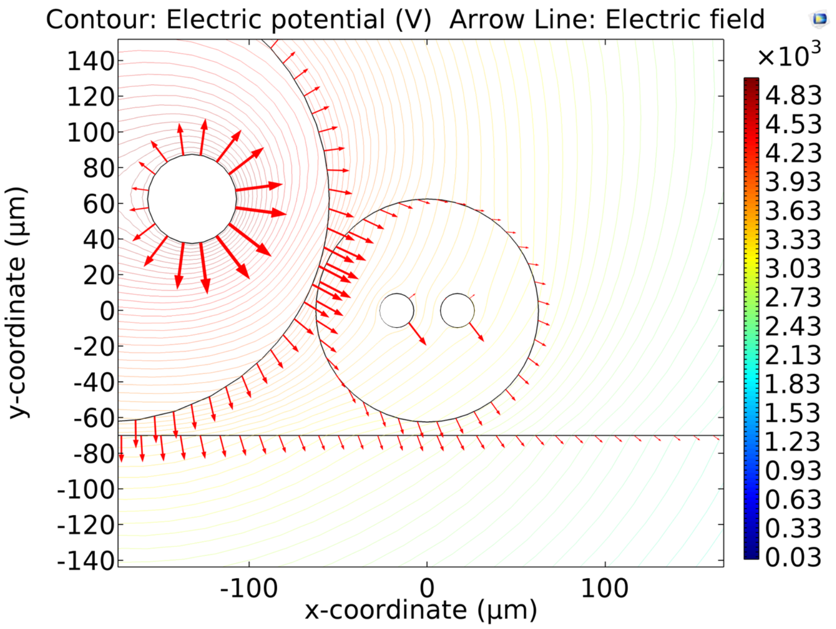

FIGURE 3.24: Simulated initial equipotential contours and electric field arrows distribution before charged ion migration begins to generate the space-charge region, obtained using the "Near" 2D-model reported in Fig. 3.21 (groundplane at 1 mm of distance).

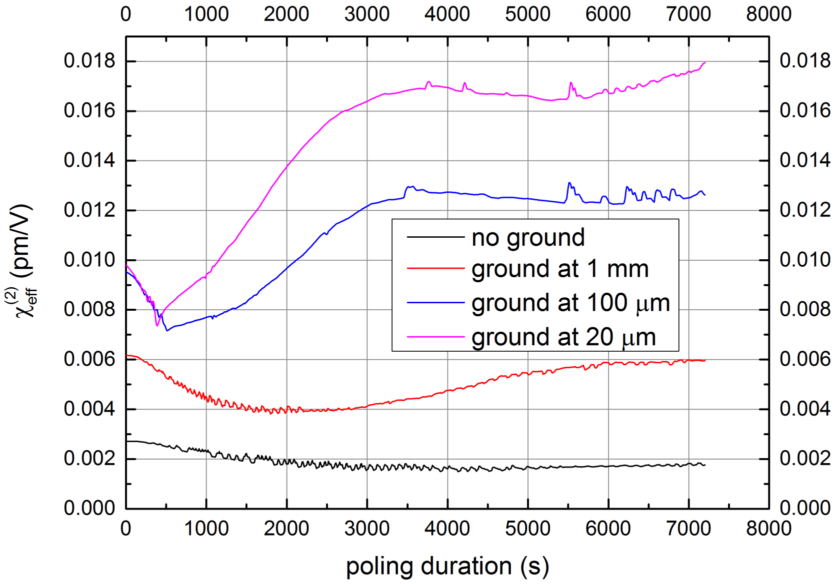

FIGURE 3.25: Temporal evolution of the value of $\chi^{(2)}_{eff}$ calculated in the centre of the fibre (core) via the MCM, for different positions of the groundplane with respect to the fibre to be poled, that are ≈ infinite (groundplane "absent"), 1 mm, 100 μm and 20 μm.

different situations. In Fig. 3.25 four plots representing the temporal variations of the value of $\chi^{(2)}_{eff}$ calculated in the fibre's core in the same configurations of the system's ground introduced in the previous section, namely groundplane located at $\approx$ infinite (groundplane "absent"), 1 mm, 100 μm and 20 μm of distance from the two fibres.

The trends shown in Fig. 3.25 demonstrate that, in contrast to what was obtained in the MCM for conventional thermal poling, in the induction poling experiments the presence of a groundplane near the two fibres gives rise to considerably different values of $\chi^{(2)}_{eff}$. In particular it is possible to affirm that closer the groundplane higher is the value of $\chi^{(2)}_{eff}$ in the sample's core. Another interesting note, comparing the results of the simulations for induction poling and cathodeless poling, is that in the induction poling configuration the value of $\chi^{(2)}_{eff}$ seems to be almost constant over a wide temporal range.

3.5.3.2 "Far" 2D-model

The numerical simulations described in section 3.5.3.1 allow us to obtain the distribution of the mobile ions over the temporal duration of the poling process and even the spatial distribution of the electric potential of the two floating electrodes embedded into the sample in the area where sample and inductor are immediately adjacent. In order to implement the numerical simulations to describe the electromigration process far from the inductor, we need to implement the MCM, described in section 3.5.2, where the values of the electric potential applied to the two embedded floating electrodes are not anymore considered constant, but are exactly the variable (in time) values of electrostatic potential calculated by means of the submodel described in section 3.5.3.1. Furthermore it will be assumed that the sample, located on top of the microscope slide, will be always in a condition of an "absent" groundplane, because actually the only ground reference is a poly-defined groundplane, given by the heater coil, which cannot be modeled. The Fig. 3.26 shows the temporal evolution, inside the sample, of the concentrations of both the Na^{+} and H_3O^{+} ions, calculated in the part of the setup where the two fibres are far apart, assuming that in the "near" model the groundplane is located 1 mm from the two fibres. In Fig. 3.27, instead, are reported the temporal evolutions of the concentrations of two types of impurity charges in the sample far from the inductor when in the "near" model a groundplane is assumed being "absent".

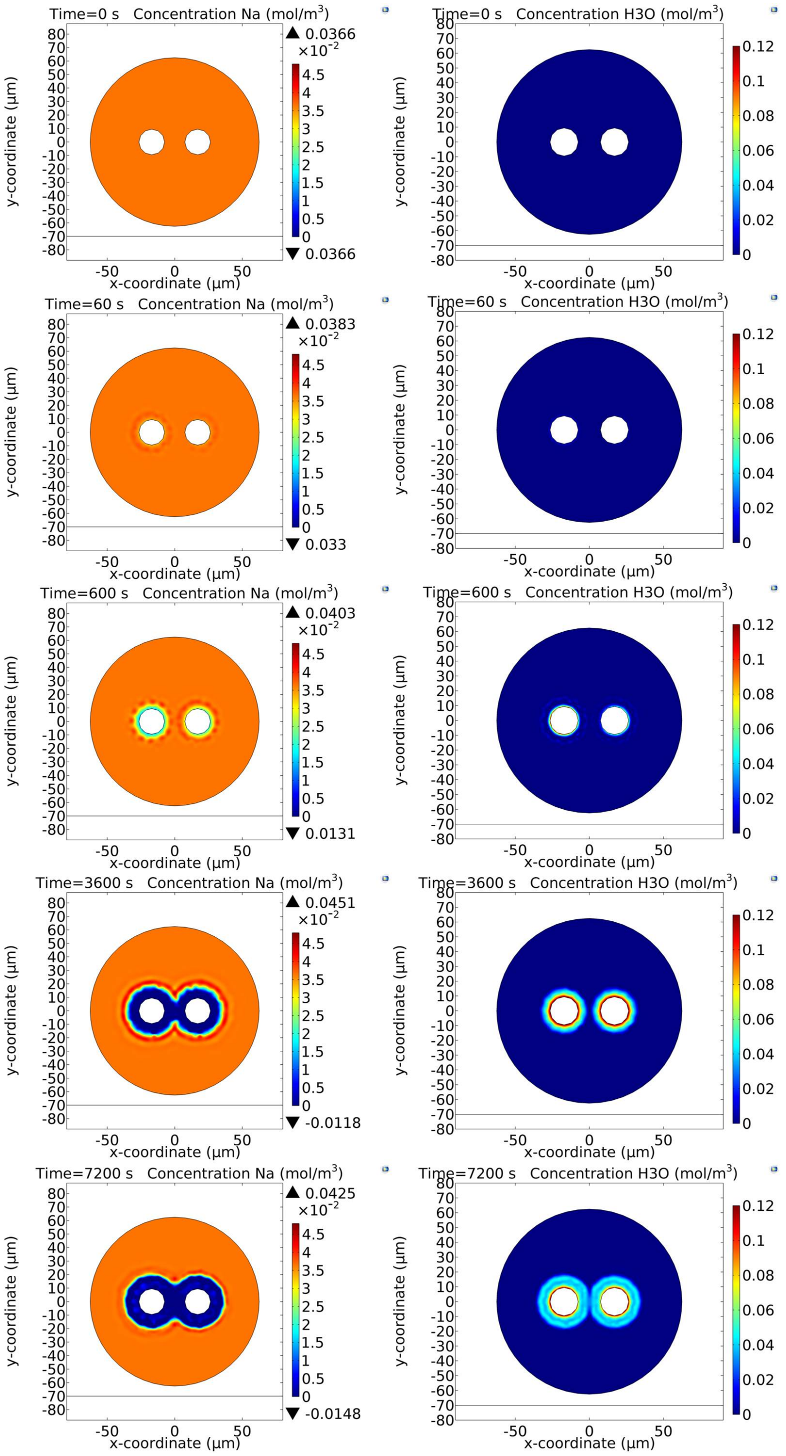

FIGURE 3.26: Temporal evolution of the mobile positive ions obtained via the "far model" for induction poling. The electric potentials applied to the two floating electrodes assume the values (variable in time) calculated by means of the "near" model reported in section 3.5.3.1 in the situation where the ground-plane is located at a distance of 1 mm from the two adjacent fibres. Apart from this ground plane only the walls of the box where the setup is placed are assumed to be grounded. The initial concentration of the impurity charges (Na^+) is assumed of 1 ppm. The temperature of the sample in the simulation is assumed to be 300 °C while the injection of the hydrogenated species H_3O^+ is assumed to be inexhaustible and capable to neutralize the NBO^- centres depleted of the impurity positive ions moved because of the application of the external electric field.

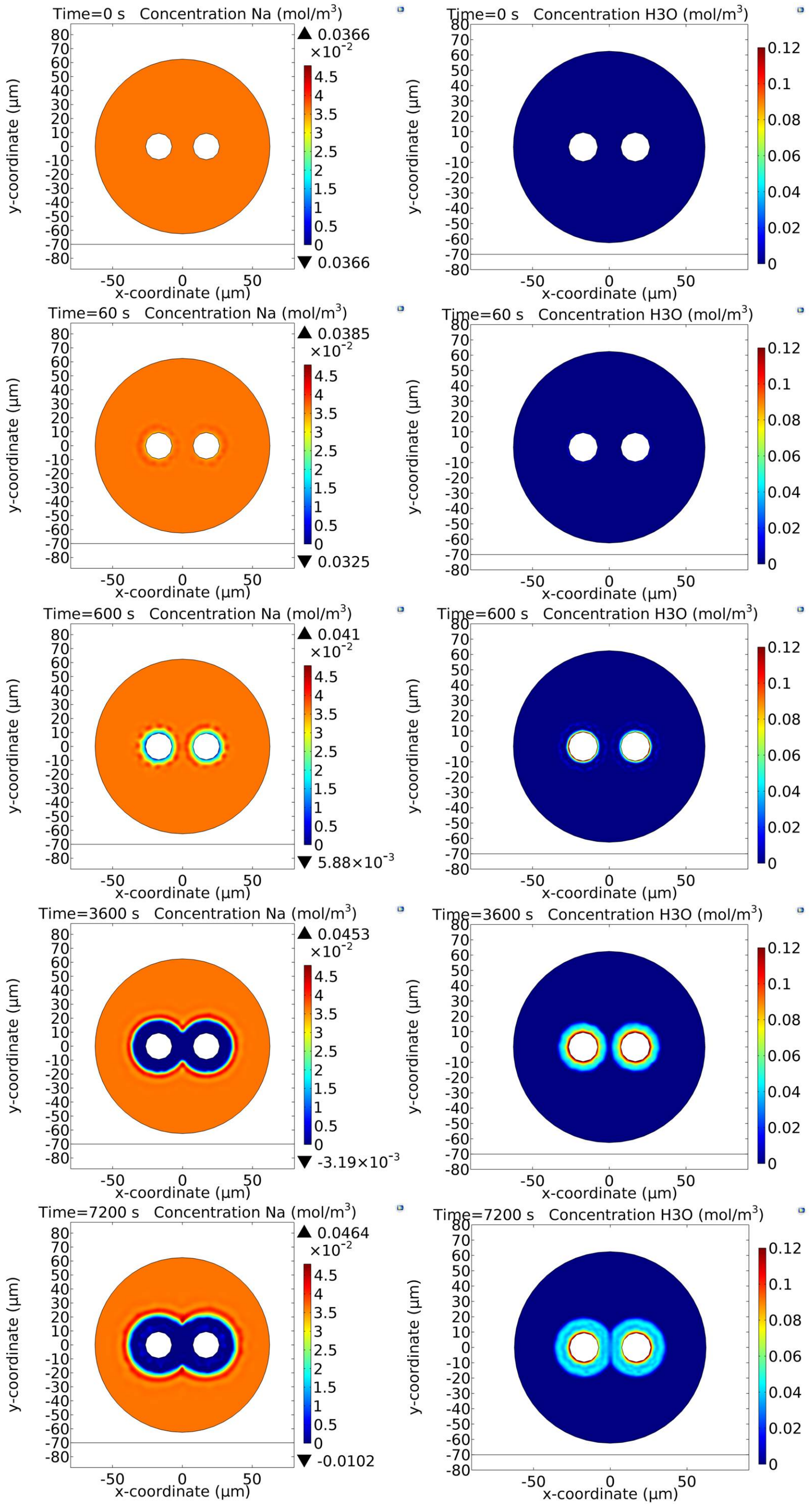

FIGURE 3.27: Temporal evolution of the mobile positive ions obtained via the "far model" for induction poling. The electric potentials applied to the two floating electrodes assume the values (variable in time) calculated by means of the "near" model reported in section 3.5.3.1 in the situation where the ground-plane is "absent". The initial concentration of the impurity charges (Na^+) is assumed of 1 ppm. The temperature of the sample in the simulation is assumed to be 300 °C while the injection of the hydrogenated species H_3O^+ is assumed to be inexhaustible and capable to neutralize the NBO^- centres depleted of the impurity positive ions moved because of the application of the external electric field.

Fig. 3.28 shows the trends of the $\chi^{(2)}_{eff}$ values calculated in the sample's core by means of the "far" model in the four different positions of the groundplane of the setup for induction poling considered in the "near" model.

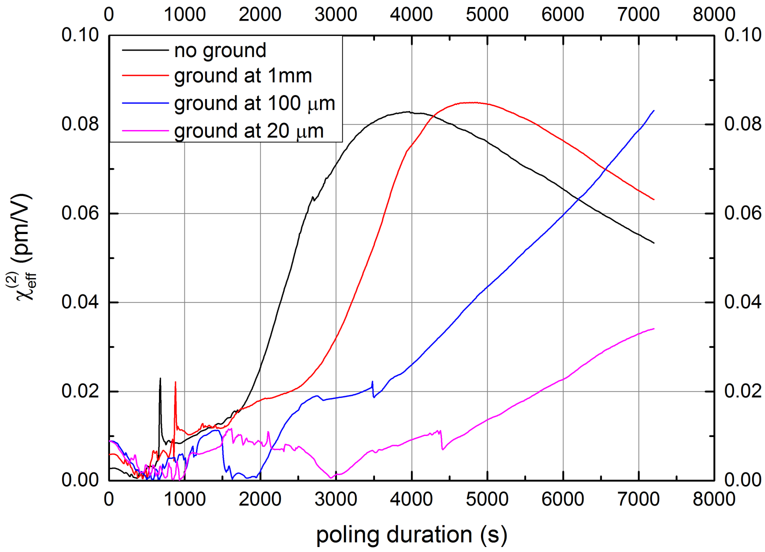

FIGURE 3.28: Temporal evolution of the value of $\chi^{(2)}_{eff}$ calculated in the sample's core via the induction poling "far" model, for different positions of the groundplane in the "near" model, that are $\approx$ *infinite* (groundplane "absent"), 1 mm, 100 μm and 10 μm.

The $\chi^{(2)}_{eff}$ values calculated in the sample's core for a fibre poled by induction for 2 hours show that the presence and the position of the groundplane in the part of the setup where the two fibres are adjacent affects not only the temporal evolution of the $\chi^{(2)}_{eff}$ in the sample's core in that position but also the evolution of the $\chi^{(2)}_{eff}$ in the sample when it is far from the inductor. It is also relevant that the presence of the inductor near the sample reduces the value of $\chi^{(2)}_{eff}$ in the region where sample and inductor are adjacent, compared to the situation where the sample is far from the inductor. Furthermore it is worth highlighting that the maximum value of $\chi^{(2)}_{eff}$ obtained in an induction poling experiment in a position in the sample far from the inductor is not very different from the one obtained in a cathodeless poling experiment, even if the absolute value of the electric potentials applied to the two electrodes embedded inside the sample is very different in the two cases.

The relevance of the theoretical model developed for the induction poling experiment in this thesis work relies in the possibility of being used to optimize the different parameters of the poling experiment (such as for example the voltage applied to the electrodes embedded in the inductor, the distance between inductor and sample, the relative orientation of the sample's cladding holes with respect to the inductor, etc.) with the final aim of increasing as much as possible the value of $\chi^{(2)}_{eff}$ obtained in the sample's core. For example, in Fig. 3.29 are reported the initial 2D electric potential distributions simulated by means of the "near" 2D-model and corresponding to two different relative azimuthal rotations of the sample with respect to the inductor (as can be seen from Fig. 3.29, azimuthal rotation can result in large variations in the electric potential initial distribution).

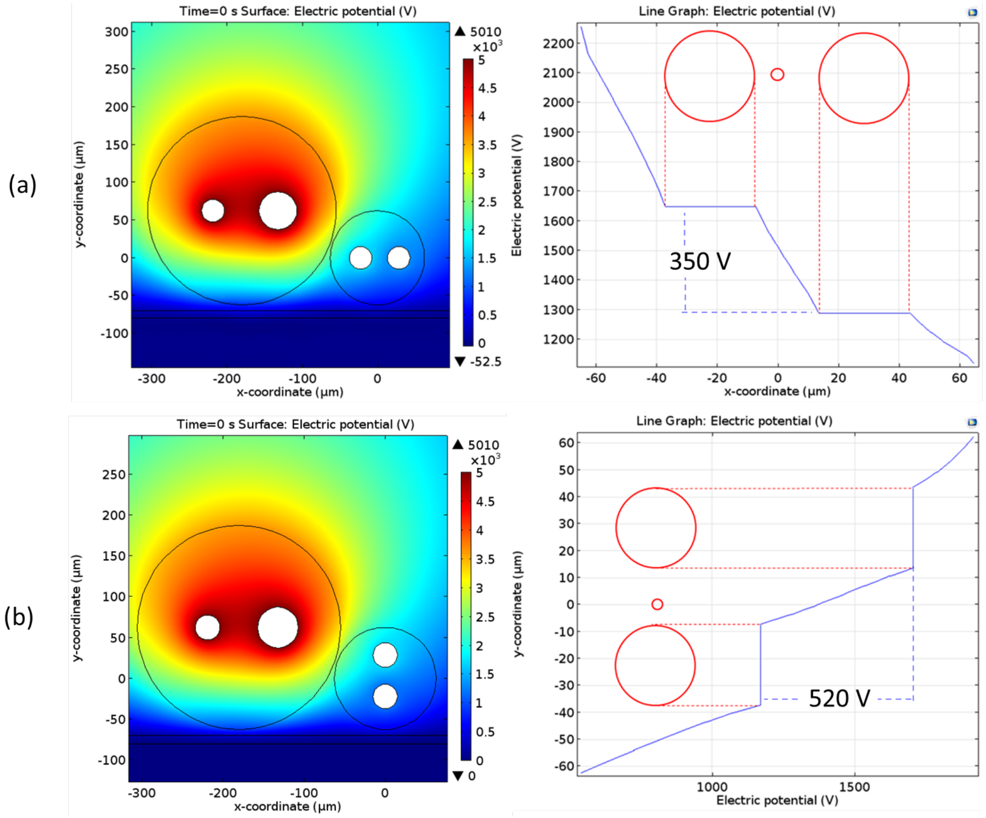

FIGURE 3.29: (a) (Left) Simulated initial 2D electrostatic potential distribution before charged ion migration begins to generate the space-charge region. The external inductor and adjacent sample fiber are shown with zero relative azimuthal rotation. (Right) A line scan through the geometric centres of the sample reveals large potential variations (350 V) that drives impurity ion migration during electrostatic induction poling. (b) (Left) 2D electrostatic potential distribution for a 90 deg relative azimuthal rotation of the sample. (Right) A line scan through the geometric centres of this sample orientation exhibits an even larger (520 V) potential difference between the internal electrodes compared with the sample in (a), resulting in faster depletion region dynamics [130].

Another interesting conclusion which can be inferred from the numerical 2D-model of the induction poling is that a well-defined groundplane can be considered as an additional electrode that distorts the electric field lines and affects the evolution of the space-charge region. In other words the groundplane can be included in the list of the parameters which can be modified to optimize the $\chi^{(2)}_{eff}$ value.

Also it is worth highlighting that bench marking numerical versus experimental results is difficult from a practical perspective as it is difficult to know exactly the physical parameters of the sample to be poled (such as for example types of impurity involved in the electromigration process, concentration of impurities, mobility of impurities, etc.). Furthermore adjusting the experimental parameters, such as for example the exact distance between the two fibres, the mutual orientation of them, etc. represents a noticeable challenge. Nevertheless the numerical simulations realized in this thesis work represent a relevant step further towards a better understanding of the induction poling process and moreover they will be useful to model thermal poling of more complex structures, such as the MOFs (see chapter 6).

3.6 Conclusions

In this chapter the concept of thermal poling by electrostatic induction has been explained together with the early attempts of experimentally realizing it. This novel technique allows for thermally poling optical fibres with embedded electrodes without the need of physically contacting them, provided that an external electrode is adjacent to the sample and that the sample is heated up at a temperature where impurities can move under the effect of the external electric field. The relevance of the physical identification of a groundplane for induction poling setups has been also studied. After reporting the implementation of a setup for induction poling of long samples, a 2D numerical model for induction poling has been presented and the temporal evolution of the space-charge region obtained in this kind of poling has been reported.

Chapter 4

Thermal poling with liquid electrodes

4.1 Issues related to usage of solid electrodes

In the section 3.4, where the method for electrostatic induction poling of long samples was described for the first time, the floating electrodes embedded in the sample ($\approx$ 20 cm long) were created by filling its cladding holes with a BiSn alloy by means of the technique described in Fig. 3.11. The reason of this choice lies on the fact that the insertion of solid tungsten wires into the cladding holes of a twin-hole optical fibre represents a big challenge, if it has to be realized for more than few centimetres. From this point of view the development of the induction poling technique represents a step forward towards the implementation of a wide-ranging technological platform capable to allow for the nonlinear functionalisation of optical fibres of any length and geometry, which represents the ideal final target of this thesis work. The possibility of poling an optical fibre without the need of a physical contact between the high voltage power supply and the electrodes embedded into the fibre could allow for poling even in experimental conditions where that physical contact represents a challenge or an intractable problem.

Nevertheless there are still some issues which the induction poling technique on its own does not solve completely. For example, the choice of filling the cladding holes with BiSn requires inserting the whole setup, including the pressurization system and the fibre to be filled, into an oven reaching the temperature where the metal alloy is liquid (138 °C). Apart from this issue, some measurements realized during a first explorative phase of our work demonstrated that the presence of metal inside the cladding holes affects heavily the transmission losses of such a device, which could reach even values of 3-5 dB/cm at a pump wavelength of 1550 nm. Self-evidently these very large losses are very detrimental, in particular with the final aim of realizing an efficient nonlinear device, such as for example a frequency doubler. The need of removing easily the electrodes after poling becomes fundamental and at this point another issue turns out, which is the removal of a solidified metal, such as the BiSn at room temperature.

4.2 Liquid electrodes

Given that even the BiSn alloy, used in the early thermal poling experiments, at the temperature of ≈ 300 °C (which is the temperature where the poling experiments are usually realized) is liquid, some new conductive materials which could be used as embedded electrodes were explored in order to make the process of their removal, immediately after the poling experiment, as simple as possible. This is the reason why it has been chosen to test some metals (including alloys) which are liquid at room temperature. In this way it would be possible to avoid the issues related to the process of removal which should be realized inside an oven, such as would be unavoidable with high melting temperature alloys (it is the case of BiSn).

It is worth, at this point, discussing the differences, in terms of electrical conduction, between a solid and a liquid conductor. If the liquid conductor is a metal, it is possible to describe the mechanism of electrical conduction in the same terms of the solid metal, that is in terms of valence electrons which are basically free to move under the effect of the application of an electric field [142].

If the liquid conductor is not metallic, but for example is an electrolytic solution (a liquid containing positive and negative mobile ions), electricity is conducted by the migration of the positive and negative ions through the liquid. So, if a channel of the twin-hole fibre was filled with an electrolytic solution and a tungsten wire was immersed into the solution in one end of the fibre and contacted to the anode of a high voltage power supply, the negative ions present in the solution would be attracted by the anode and positive ions would be repelled. The final result would be a positively charged liquid whose electric potential depends on the initial concentration of the free ions of the electrolytic solution. Indeed the electrical conductivity of a non-metallic liquid depends upon the number of ions per unit volume and upon their drift velocity. Pure solvents such as water or alcohol are relatively poor electrical conductors, with an electrical conductivity of about 10^{-4} S/m [142]. The electrical conductivity of solutions of chemical salts in water is much higher, being about 10 S/m. Such solutions are generally classed as good conductors and are called electrolytic solutions. The dissolved substance, or solute, is known as the electrolyte. While the electrical conductivity of electrolytic solutions is quite high compared to the electrical conductivity of the pure solvent, their electrical conductivity is small compared to a metallic conductor such as copper whose electrical conductivity at room temperature is about 0.6×10^8 S/m, tungsten ($\approx 1.8 \times 10^7$ S/m) or BiSn ($\approx 2.6 \times 10^6$ S/m).

In the next sections some different resolutions to the issue of the liquid electrode for thermal poling experiments will be presented, both metallic and non-metallic liquids.

4.2.1 Metallic liquids

The metallic liquids tested as electrodes for thermal poling are gallium, two gallium-based alloys (EGaIn and EGaInSn) and Mercury. Their properties, behaviour and applications are described in the following subsections. The comparison related to their exploitation in thermal poling experiments of twin-hole Ge-doped fused silica fibres for SHG will be presented instead in chapter 5.

4.2.1.1 Gallium

The first metallic liquid tested as electrode for thermal poling experiments is gallium. Gallium is a metal characterized by some peculiar properties [143–145]. Some of these features are its very long liquid range, which goes from a supercooled state at 150 K to its boiling temperature of 2510 K, its low vapour pressure even at high temperatures, and an anomalous behaviour upon its melting temperature of its density, which increases of 3.2 % while most of the metals decrease of 2-6 % [146]. The melting temperature of solid gallium is 29.76 °C. Its electrical conductivity is of $\approx 3.7 \times 10^6$ S/m, so it can be considered a good electrical conductor.

The most interesting feature of gallium is related to the structure of its liquid state. While most liquid metals can be considered as monoatomic simple liquids, this picture is not complete enough to describe the odd behaviour of gallium. One of the first intuitions on the structure of gallium is due to Ascarelli, who, in 1966, proposed a close similarity between the structure of liquid gallium and the one of the metastable $\beta - Ga$, which is the phase formed when the liquid is supercooled [147]. According to Ascarelli, $\beta - Ga$ could be considered the closest solid counterpart of liquid gallium, closer than $\alpha - Ga$, the solid gallium. A number of structural models have been proposed to explain the liquid state of gallium, and most of them agree in the assumption that in its liquid state, gallium presents two different coexisting structures, namely a layer lattice structure (which represents a reminder of the solid $\alpha - Ga$ and whose contribution is small) and a spherical close packing in the form of a straight atomic chain (typical of a simple liquid) [148]. A qualitative description of the dynamics of the melting process of gallium is provided by Park *et al.* in 1982 [146].

The anomalous behaviour of gallium appears in all its clarity when it is used as metallic electrode embedded into the cladding holes of a twin-hole silica fibre to be poled by induction. After heating a small amount of it in a glass vial on top of a hotplate at a temperature slightly higher than its melting temperature, the pressurization system already used for BiSn (see Fig. 3.11) is used to push it through the holes of the fibre. The most evident issue with the gallium usage is the reliability of the process of creation and removal of the electrodes before and after each thermal poling experiment. While most of the time it is possible to realize the two phases of the process without any big effort, sometimes the gallium solidifies after the thermal poling process, making impossible remove it from the channels at room temperature by means of the pressurization system, even using very high pressure of He (up to 1000 psi). Another possible event consists in the formation, immediately after the filling process or even during it, of some discontinuities (in form of air gaps). The Fig. 4.1 shows an example of one of these air gaps which is possible to find along the length of the fibre filled with gallium. This prevents having a continuous electrode, and so causes the failure of the thermal poling attempt.

Even in the event where everything is fine with both the processes of filling and removal of gallium, there is still an issue, related to the relatively high viscosity of liquid gallium, which leaves residues inside the channels, even after the removal

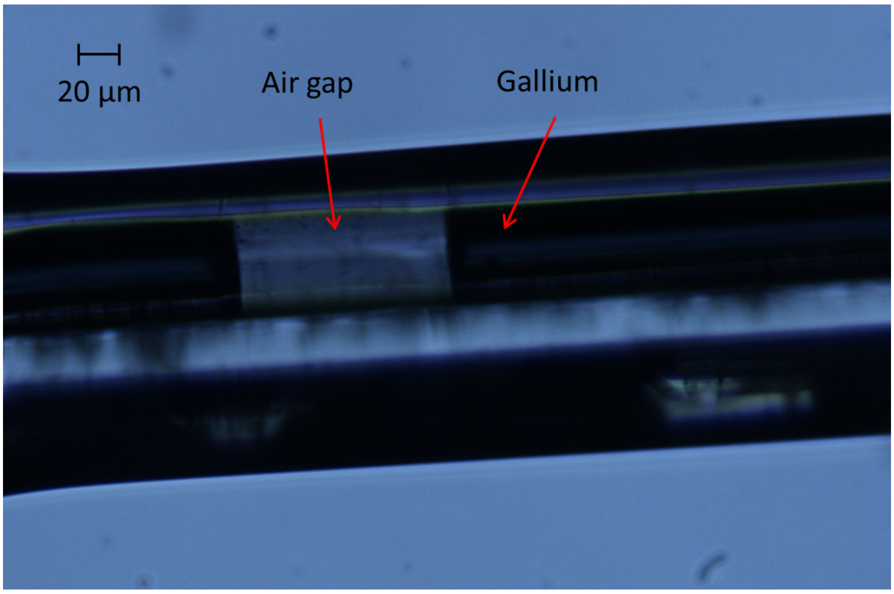

Figure 4.1: Microscope image of the lateral view of a twin-hole Ge-doped fused silica fibre (manufactured by ACREO Swedish ICT and described in detail in section 5.2.3) filled in both channels with gallium by means of the pressurization system reported in Fig. 3.11. It is possible to see clearly the air gap between two continuous filled parts of one of the two channels. The presence of these air-gaps prevents electrical continuity of the embedded electrodes.

process by means of the high pressurization system. This issue will be more evident when, in chapter 5, different nonlinear devices for SHG, realized by using different electrodes, will be compared in terms of transmission losses, clearly due to the different tendency of each substance to stick on the inner walls of the glass fibre channels.

This unpredictable behaviour of gallium motivated the search for new ways forward, even if gallium was used successfully to realize more than twenty periodically poled fibres used for SHG. Gallium was used for two different types of experiments, namely for induction poling and for cathodeless poling. In the induction poling experiments gallium replaced BiSn alloy as floating electrode embedded into the sample to be poled, while in cathodeless thermal poling experiments it replaced the tungsten wires contacted to the high voltage power supply. In this second case, after filling both the channels (or just one of the two channels via a selective filling process realized with epoxy resin) of the twin-hole silica fibre with gallium, two pieces of tungsten wire are inserted into the liquid gallium for few centimetres in one of the fibre's ends. At this point a drop of superglue is used to seal both the ends of the fibre and to fix the wires in their position during the thermal poling experiment, as shown in Fig. 4.2. Some of these fibres have been tested as sources of polarization-entangled photon pairs or as all-fibre UV sources in microfibres. These applications will be presented and discussed in detail in chapter 5.

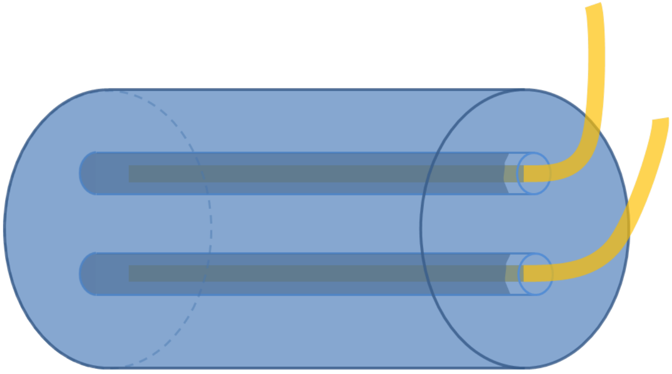

FIGURE 4.2: Schematic of one end of the twin-hole fibre filled with gallium in both the side channels. Two tungsten (gold coated) pieces of wire are inserted in both the channels and immersed into the gallium for few centimetres. A drop of superglue is later used to seal the end before the thermal poling experiment starts.

Two gallium-based alloys have been also identified as possible alternatives to pure gallium to be used as electrodes for thermal poling experiments, namely the eutectic gallium indium alloy (EGaIn) and the eutectic gallium indium tin (EGaInSn, commercially known as Galinstan). Both of them showed fewer issues than gallium in the process of filling of the fibre's channels (for example it is rare to see air gaps such as the ones reported in Fig. 4.1) but unfortunately they seem to be more problematic after the thermal poling process because they are very sticky and leaves enormous amounts of residue on the inner walls of the fibre's channels.

4.2.1.2 Mercury

Mercury is a chemical element with symbol Hg and atomic number 80. It is commonly known as *quicksilver* while its former name was *hydrargyrum* (Latin translation of its Greek name, where its symbol is originated). It is the only metallic element liquid at standard temperature and pressure (STP) conditions (since the 1982 STP is defined as a temperature of 273.15 K (0 °C) and an absolute pressure of exactly 10^5 Pa (1 bar) [149]), and so it is the only metal which is liquid at room temperature, though other three metals such as cesium, gallium, and rubidium melt just above room temperature. Its melting and boiling temperatures are of ≈ -39 °C and ≈ 357 °C respectively. It is characterized by a very high density (of $\approx 13.5 \times 10^3\ Kg/m^3$ near room temperature) and an electrical conductivity of $\approx 1.04 \times 10^6\ S/m$. This value of conductivity makes mercury a fair conductor [150] and a reasonable replacement of gallium for creating liquid electrodes embedded into the channels of an optical fibre to be thermally poled.

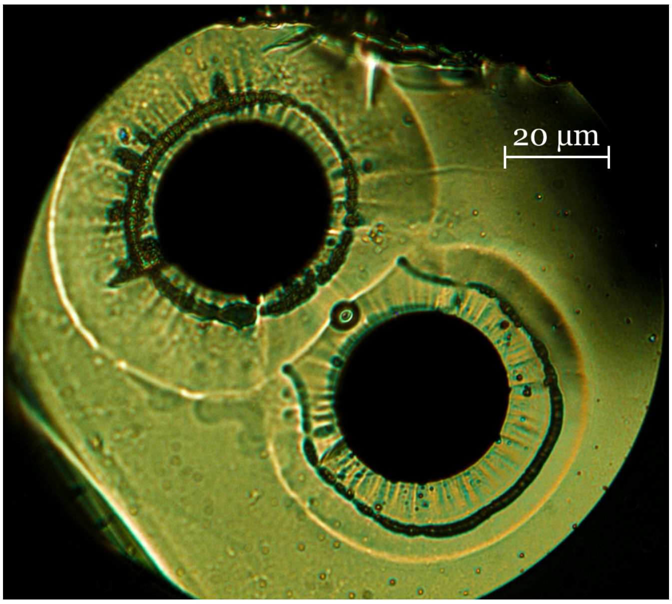

FIGURE 4.3: Cross-section of a twin-hole Ge-doped fused silica sample (manufactured by ACREO Swedish ICT and described in detail in section 5.2.3) poled in cathodeless configuration and etched for 1 minute in HF. After filling the two channels of the fibre with liquid Mercury by means of the pressurization system shown in Fig. 3.11, and inserting two short pieces of tungsten wire inside both holes (as shown in Fig. 4.2) and finally sealing both the ends of the fibre with a drop of superglue, the fibre is thermally poled applying to the electrodes a voltage of 4.3 kV at a temperature of $\approx 300\ ^{\circ}C$ for 120 minutes. The presence of few concentric rings around the two channels is due to the electromigration of impurity charges through the glass. The presence of these rings allows to assume that a second order nonlinearity has been created in the fibre, even if a more quantitative confirmation of this assumption will be reported in chapter 5 when the $\chi^{(2)}_{eff}$ for SHG will be measured for a fibre poled by means of mercury electrodes and compared to the other conductive liquids used.

The early results of the process of filling of the twin-hole fibre's channels with Mercury were very promising. It has been possible to fill 2 metre long samples creating continuous electrodes which lack any sign of air gaps. For this reason Mercury, at some point of my PhD path, replaced completely gallium as metallic electrode, in particular for poling long samples with the aim of realizing periodically poled fibres for frequency doubling, generation of polarization-entangled photon pairs or implementation of purely quadratic resonators for frequency combs. The discussion about the process of creation of these all-fibre nonlinear devices and their main applications is described in chapter 5, while in Fig. 4.3 there is an example of the cross-section (etched in HF solution) of a metre-long sample of a twin-hole

Ge-doped fused silica fibre poled in cathodeless configuration, to demonstrate the efficiency of Mercury as electrode.

4.3 Induction poling of microstructured solid core optical fibres

An interesting application of the mercury used as metallic electrode is the thermal poling of solid core PCFs, realized exploiting an electrostatic induction process analogous to the one discussed in sections 3.3 and 3.4. In section 3.1 was cited the work of Faccio *et al.* of 2001, where for the first time a solid core MOF was thermally poled. A non-phase matched second harmonic generation was observed and an electro-optic coefficient was measured of ≈ 0.02 pm/V [126]. Our first attempt of inducing a second order nonlinearity (SON) inside a solid core MOF was realized inside a silica MOF (Ya6.2-7, manufactured by A. V. Gladyshev (Moscow)).

A piece (≈ 20 cm of length) of the MOF was first filled by means of capillary action with some epoxy resin, with the aim of sealing the two cladding holes of the fibre. Then, an attempt of filling the holes of the microstructure (≈ 2 μm in diameter) with mercury was realized as usual by means of the pressurization system shown in Fig. 3.11. The pressurization arm is filled with ≈ 500 psi of He and one end of the fibre inserted into a glass vial containing Hg included inside the other arm of the system. After opening the valve, the fibre is left to be filled for 10 minutes then the valve closed and the fibre removed from the pressurization system. In Fig. 4.4 the cross-sections of the MOF are shown. Along a length of ≈ 5 cm some holes of the microstructure have been filled with mercury. After filling the small holes of the microstructure with mercury, a tungsten wire is inserted inside one of the cladding holes (the one closest to the microstructure) and the MOF is poled using a setup similar to the one shown in Fig. 3.7. The temperature of the sample is ≈ 300 $°C$ and a positive potential of 2.5 kV is applied to the embedded electrode for 120 minutes (the electric potential of 4.3 kV used so far could not be reached because of the high leakage currents developed during the experiment). After the poling process, the fibre is cleaved in the centre and the cross-section is etched for 1 minute in HF solution. The result of the decorative etching process, reported in Fig. 4.5, reveals the sign of a space-charge region edge located in the solid core of

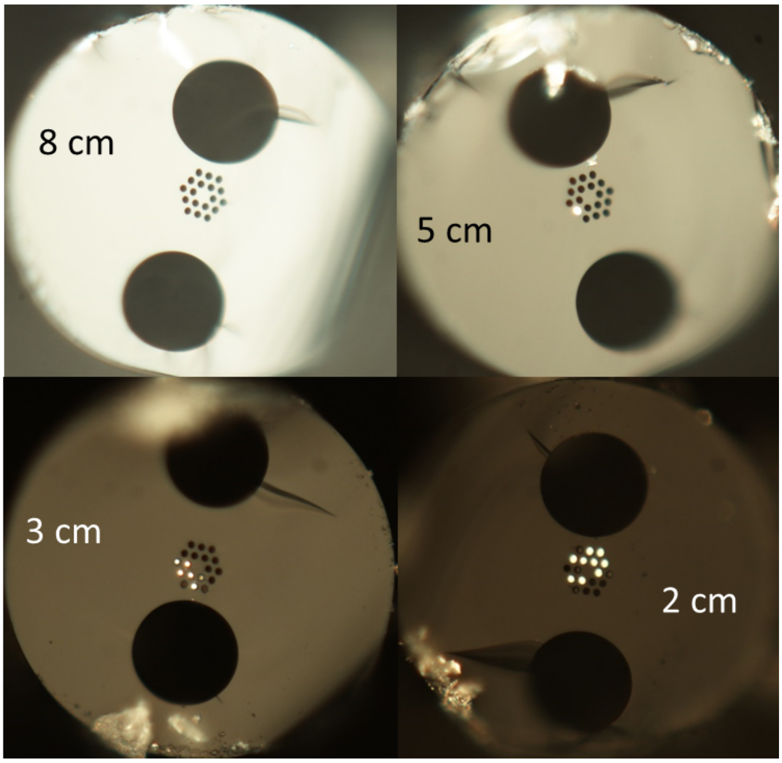

Figure 4.4: Cross-sectional micrographs of the fused silica solid core MOF filled with mercury by means of the setup shown in Fig. 3.11 after sealing the two large cladding holes with epoxy resin. The shiny spots represent the holes of the microstructure successfully filled with mercury. The distances are measured from the end of the fibre immersed inside the vial containing mercury and located inside the arm of the pressurization system.

the MOF. It is the first time that a space-charge region is highlighted in the solid core of a MOF thermally poled.

A control experiment was realized where the same type of MOF is poled in the same experimental conditions just presented but without any liquid metal inside the holes of the microstructure. As it is possible to see in Fig. 4.6, the space-charge region evolved in the whole region surrounding the cladding hole, apart from the solid core region, where there are no signs of its presence. We can therefore hypothesize that the presence of the air holes of the microstructure prevent the impurity charges from migrating into the solid core region. To confirm this hypothesis the role of the floating electrodes (created inside the microstructure of the MOF) in the evolution of the space-charge region inside the solid core region of the fibre was studied by implementing two numerical simulations (realized in $COMSOL^{TM}$ Multiphysics) related to the thermal poling of a solid core MOF similar to the one shown in Fig. 4.4 and described in the initial part of this section. Fig. 4.7 shows the space-charge region evolution after ≈ 1400 s obtained

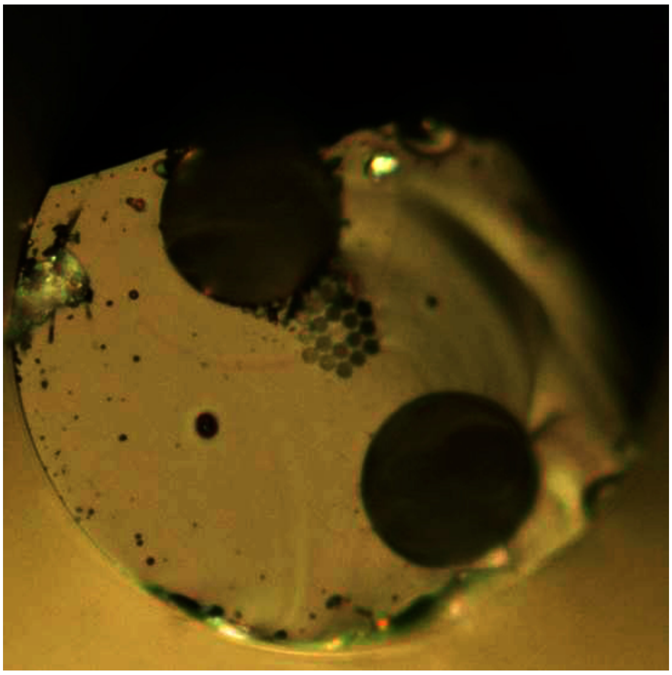

Figure 4.5: Cross-sectional micrograph of the fused silica solid core MOF poled by induction in single anode cathodeless configuration and in the experimental conditions of $T \approx 300$ °C, $V_{app} = 2.5$ kV, time of poling = 2 hrs, and etched in HF for 60 seconds. The fibre has been equipped with mercury inside the holes of the microstructure. The aim of this experiment consists in the exploitation of the conductive liquid located into the small holes as "antennas" to pick up the electric potential provided by the electrodes inserted into the cladding holes and contacted to the anodic potential of 2.5 kV. The edge of a space-charge region is visible inside the solid core of the MOF.

in two numerical simulations of poling realized in the same conditions apart from the fact that in one case two of the small holes of the microstructure were filled with a metal and in the other all the holes were empty. The presence of the metal inside the small holes allows the penetration of the space-charge region even into the solid core region, while the air-filled holes clearly prevent this event.

Although this early experiment of poling of a solid core MOF, realized exploiting the electrostatic induction between the electrode embedded into the cladding region of the MOF and the floating electrodes created inside the small holes of the microstructure by filling them with a liquid metal (such as for example Mercury) represents only a qualitative proof of the possibility of poling a MOF, it would be possible in principle to realize a UV erasure process to create a QPM condition for the SHG and measure an η_{SH} which is expected to be much higher than the one obtained in conventional step-index fibre [125]. The UV erasure process would anyway require a much more complex procedure than the one that will be

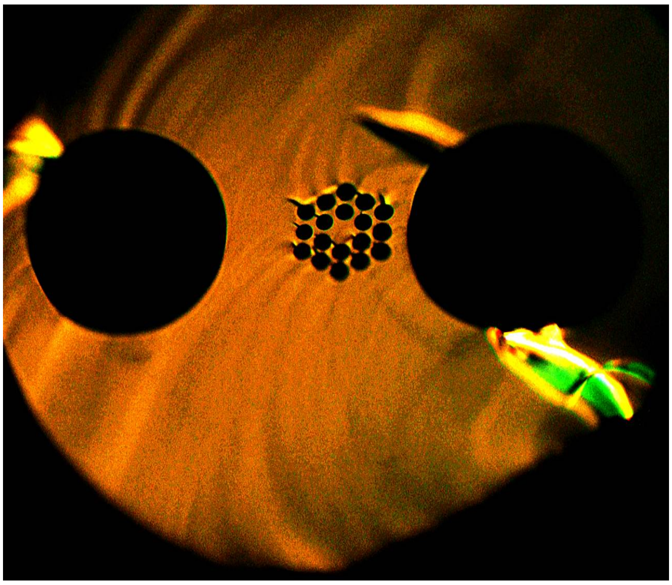

Figure 4.6: Cross-sectional micrograph of the fused silica solid core MOF poled in single anode cathodeless configuration and in the experimental conditions of $T \approx 300$ °C, $V_{app} = 2.5$ kV, time of poling = 2 hrs, and etched in HF for 60 seconds. The holes of the microstructure are empty. The edge of a space-charge region is visible in the whole region surrounding the cladding hole except from the part where the solid core is located.

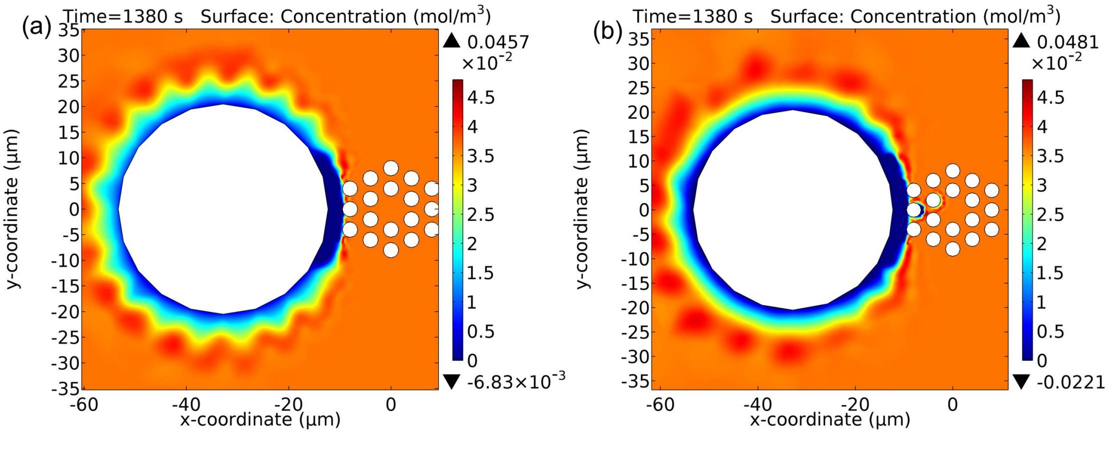

Figure 4.7: (a) Concentration of impurity charges (Na^+) after ≈ 1400 seconds calculated by means of a 2D numerical simulation in $COMSOL^{TM}$ Multiphysics (single anode configuration, $V_{app} = 2.5\ kV$, mobility and diffusion constant estimated for a temperature of the sample of 300 °C, groundplane fixed at 1 mm from the MOF) and related to the thermal poling of a solid core MOF; (b) Concentration of impurity charges (Na^+) after ≈ 1400 seconds calculated by means of a 2D numerical simulation in $COMSOL^{TM}$ Multiphysics and related to the thermal poling of the same solid core MOF where two of the holes of the microstructure are assumed to be filled with a metal.

reported in sections 5.1.1.1 and 5.1.1.2, due to the presence of the small holes of the microstructure surrounding the fibre core.

4.3.1 Electrolytic solutions

Although mercury represents a very efficient method for the creation of liquid electrodes for thermal poling of metre-long fibres because it can be easily introduced and removed afterwards from the channels of the fibre, it is undeniable that there is a relevant safety issue related to its usage. It is well known indeed that mercury is highly toxic, particularly for inhalation of its vapours [151]. Taking into account that mercury, used as electrode for thermal poling, is heated up to ≈ 300 °C, a temperature very close to its boiling temperature (≈ 357 °C), it is obvious that during thermal poling some vapours of mercury can be created. Although the thermal poling experiments are realized inside a fume hood, this circumstance still represents a hazard which should be avoided. Furthermore, even during the filling process of the channels, realized at room temperature, there is a risk of evaporation, even if the amount of mercury manipulated during these phases of the work is very tiny.

Another issue related to the use of mercury as embedded electrode is that, after its removal process, it leaves its traces on the inner surfaces of the fibre's channels. These traces are definitively less relevant than the gallium ones, but they are not negligible.

Lastly the risk of breaking fibres during the pressurization process and consequently spilling some mercury in the laboratory where the process is performed also represents a hazard.

All the considerations just reported clearly indicate that the aim of replacing mercury with something less risky is unavoidable. We therefore chose to explore some electrolytic solutions as liquid electrodes for thermal poling experiments. As already reported in the section 4.2, an electrolytic solution is a water-based solution containing a certain amount of ions (electrolytes), which could be charged up to a certain electrical potential if contacted to a voltage power supply [142].

A simple way to create an electrolytic solution is to dissolve a salt (solute) in water (solvent), producing a chemical reaction called *solvation*, which consists in a process of attraction and association of molecules of the solvent with molecules or ions of the solute. A salt is an ionic compound that results from the neutralization reaction of an acid and a base [152] and is composed of related numbers of cations (positively charged ions) and anions (negative ions) so that the product is electrically neutral (without a net charge). When they are dissolved in water, the ions they are made of separate and move independently through the solution as aqueous ions. Since ions are charged species their motion through space is equivalent to an electrical current. The property of conducting an electrical current makes the aqueous solution an electrolytic solution [142].

An important advantage of using aqueous solutions instead of metallic liquids is that it is possible to fill (either selectively or otherwise) the channels of the optical fibre to be poled without the need of any pressurization system (Fig. 3.11). The aqueous solution moves through the cylindrical channels of the fibre by capillary action.

4.3.1.1 Early experiments of thermal poling with electrolytic solutions

After discussing the practical motivations behind the idea of using electrolytic solutions to create embedded electrodes inside the fibre, it is worth describing in detail the procedure of creation of these aqueous electrodes, the types of electrolytic solutions used and the results of the early thermal poling experiments.

The first fibre used to test the possibility of using aqueous solutions as internal electrodes is the three-hole fused silica fibre represented in Fig. 3.3. It is worth highlighting that the aim of these early experiments is the observation of a space-charge region by means of a HF decorative etching. Only after getting this kind of qualitative result, it is worth transferring the same procedure to an actual waveguide structure, for example the twin-hole fused silica fibre shown in Fig. 4.3.

After filling by capillary action a sample (of the three-hole fused silica fibre) of $\approx$ 40 cm of length with a solution of hydrochloric acid diluted in DI water, two tungsten wires of $\approx$ 6 cm of length are inserted in the two holes of one end of the fibre, for a length of $\approx$ 2 cm. Then a drop of superglue is used to seal both the ends of the fibre, exactly as it is done with mercury (see section 4.2.1.2). The central part (of $\approx$ 20 cm of length) of the fibre is placed on top of a glass slide located on top of a ceramic hotplate. The temperature of 300 $^{\circ}C$ is chosen and then a voltage of 4.3 kV is applied to the tungsten wires inserted in the two channels of the fibre for 2 hours. The fibre is allowed to cool with the voltage still applied and after 1 hour the voltage is removed. After the poling experiment, the fibre is firstly observed under an optical microscope and appears completely empty. This is likely due to the the fact that, at high temperature, the aqueous solution evaporates and the liquid evacuates from the fibre channels, as they are not well sealed. The HF decorative etching of some cross-sections of the fibre located on top of the hotplate suggests that there is no space-charge region at all.

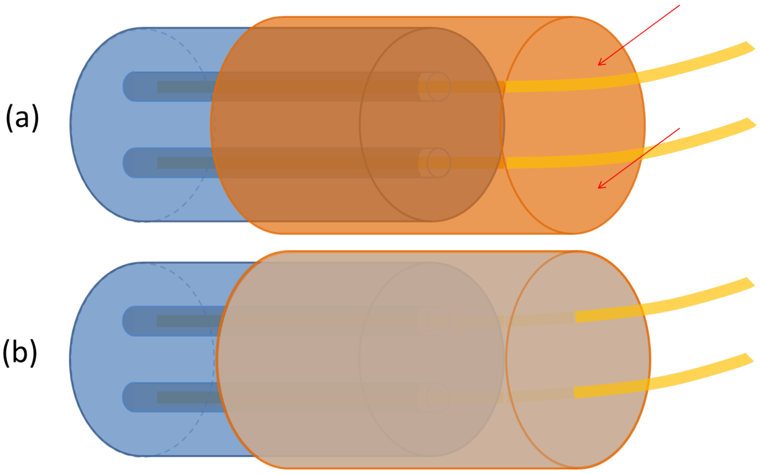

Figure 4.8: (a) Schematic representation of the procedure for creating a cap of epoxy resin in the fibre to be poled by means of aqueous solutions used as embedded electrodes. After filling the two channels of the fibre with the aqueous solution (in this case a solution of HCl diluted in DI water) by capillarity and introducing the two tungsten wires inside each channel in order to create the electrical contact between the embedded electrode and the high voltage power supply, the end of the fibre in inserted inside a capillary whose inner diameter is bigger than the outer diameter of the fibre. A drop of the epoxy resin enters the capillary from its right aperture (red arrows) until it reaches the other end of the capillary. (b) Schematic depiction of the extremity of the fibre after the epoxy resin dries for twelve hours. The grey part inside the capillary represents the solidified cap.

After this first failure, the second attempt is inspired by the aim of sealing more strongly the fibre after the filling process. In order to do that a cap is used (see Fig. 4.8). Each extremity of the fibre (previously filled with the aqueous solution) is inserted for few millimetres inside a plastic capillary of ≈ 2 cm of length and of inner diameter slightly bigger than the outer diameter of the fibre. Then a drop of an epoxy resin (EpoThin, $Buelher^{TM}$) is placed on each end of the capillary. The epoxy, by capillarity, penetrates inside the plastic capillary and surrounds the fibre for a length of ≈ 1 cm. The epoxy is left to dry overnight until it becomes solid. The sample is ready to be poled by means of the same procedure described previously.

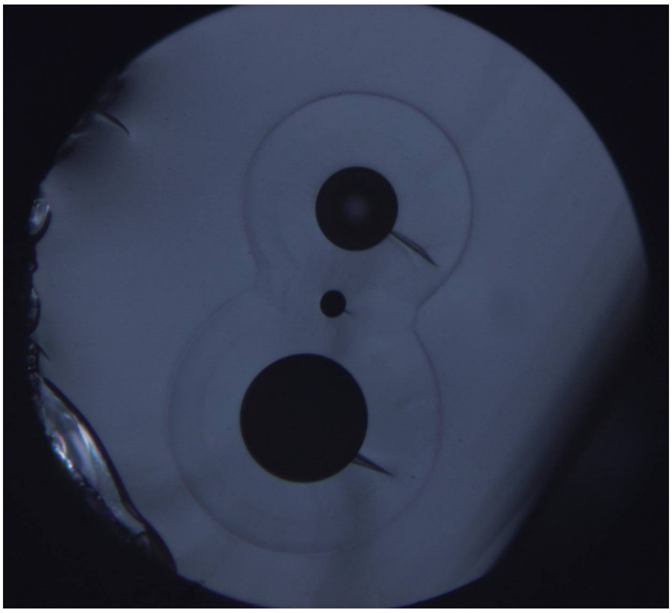

FIGURE 4.9: Cross-section of the three-hole fused silica fibre poled by exploiting an electrolytic solution containing hydrochloric acid etched in HF for 1 minute. The fibre, filled with the solution and equipped with two tungsten wires inserted in one of the two ends of the fibre, is prepared according the procedure described in Fig. 4.8 and then poled for 2 hours at a voltage of 4.3 kV and a temperature of 300 $^{\circ}C$. The section of the fibre to be etched is selected randomly in the part of the fibre located on top of the hotplate. The fibre has been sectioned and etched more than once in this region and here a representative image is shown.

The analysis by optical microscope, immediately after the poling attempt, reveals that the fibre is partially empty, in particular in the region located on top of the hotplate, while in the two extreme parts of the fibre (the ones not in contact with the hotplate and so presumably at room temperature) it is possible to see still some liquid. After pumping out the residual liquid, the fibre is cleaved in random positions along the part of it located on top of the hotplate during the poling experiment. The HF decorative etching surprisingly reveals the formation of a number of concentric rings located around each hole of the fibre (including the central small 9 μm hole, not contacted with any tungsten wire). The rings resemble the space-charge regions typical of a fibre thermally poled. In Fig. 4.9 an image of the cross-section of a THF poled using an electrolytic solution containing HCl diluted in DI water and decoratively etched in HF for 1 minute is shown.

In order to verify that the fibre has been actually poled, a second order nonlinear effect has to be observed. In chapter 5 the results of thermal poling experiments realized by means of different kinds of electrolytic solutions will be reported. Furthermore SHG produced in order to measure the value of $\chi^{(2)}_{eff}$ will be presented for the same kind of fibre poled by means of electrolytic solutions and metallic liquids.

4.4 Conclusions

After discussing the issues related to the manual insertion of solid wires inside the cladding holes of an optical fibre, the advantages of using liquid electrodes in thermal poling experiments have been explained. Different electrically conductive liquid (at room temperature) materials have been used as embedded electrodes in thermal poling experiments. An outstanding result reported is the thermal poling of fused silica step-index optical fibres realized using electrolytic solutions as embedded electrodes. A 2D numerical model has been also presented to study the role of floating electrodes embedded in the small holes ($\approx 2\ \mu m$ of diameter) of the microstructure of a solid-core PCF for a successful induction poling of this type of fibres.

Chapter 5

Periodically poled optical fibres for all-fibre nonlinear devices

5.1 SHG as test for successful thermal poling experiments

Chapters 3 and 4 report the descriptions of the two main topics developed in my PhD work, namely the technique for thermally poling optical fibres via electrostatic induction and the method for creation and removal of liquid embedded electrodes (either metallic liquids or electrolytic solutions). In order to prove the success of those two techniques in first instance a qualitative method has been used, that is the etching in HF the cross-sections of the fibre. This method allows for observing the limits of the space-charge region, which is commonly considered one of the most significant manifestations of a successful thermal poling process [87]. Nevertheless the decorative etching of the poled fibre does not allow for a quantitative estimation of the second order nonlinearity generated inside the sample, in particular in the core of the waveguide. Indeed the value of $\chi^{(2)}_{eff}$ depends on the intrinsic value of $\chi^{(3)}$ of the glass the fibre is made of and on the value of the electric field frozen into the fibre, which in turn depends on many parameters, such as for example the voltage applied to the embedded electrodes, the duration of poling, the concentration and the type of the impurities present into the glass, the exact temperature of the sample poled, etc [133]. For this reason the visualization of the space-charge region, even if represents the fact that some kind of asymmetry has been created by poling the fibre, does not give any information about the actual value of the nonlinearity created.

The observation of a nonlinear effect induced into the fibre via thermal poling would allow to estimate the $\chi^{(2)}_{eff}$ generated, permitting in this way a more quantitative comparison among the different methods of poling, the different fibres poled, the different configurations of poling and any other parameter it is desired to be tested with the aim, for example, of improving the $\chi^{(2)}_{eff}$ value as much as possible or even of understanding the effect of these parameters on the temporal evolution of the nonlinearity in each particular configuration. The second order nonlinear effect chosen to be observed is the SHG, which, if successful, could allow for the creation of all-fibre nonlinear devices such as frequency doublers. In the rest of the chapter it will be discussed how the SHG has been used to test the different thermal poling experiments but also three relevant applications will be presented, UV laser sources based on four-wave mixing in optical microfibres, sources of polarization-entangled photon pairs and purely quadratic ring resonators for frequency comb sources.

5.1.1 SHG in twin-hole fibres poled by induction

In section 3.4 the method for the implementation of a setup for thermal poling of twin-hole silica fibres (tens of centimetres long) by electrostatic induction has been described and in Fig. 3.14 cross-sectional micrographs of the HF etched sample (twin-hole fibre) poled by means of the setup shown in Fig. 3.13 are reported.

The SHG, already described in section 2.2.3 for the general case of a nonlinear medium and in section 2.2.6 for the particular case of an optical fibre poled, is a second order nonlinear effect which consists in the generation of a light wave at a frequency which is double with respect to the one of the light wave (named “pump”) interacting with the nonlinear medium, or with the nonlinear fibre. Generating the second harmonic is not enough, because, if we consider the Fig. 2.10, it is straightforward that the amplitude of the electric field generated at double frequency will oscillate, while it propagates into the nonlinear medium, around “zero” value, and so the power associated to the second harmonic generated into the nonlinear medium will be zero unless the Phase Matching condition is fulfilled (see section 2.2.4), or more in general the Quasi-Phase Matching condition is fulfilled (see section 2.2.5).

In order to create a QPM condition in a fibre poled the $\chi^{(2)}_{eff}$ generated should be periodic with a period fulfilling, at the first order, the condition [131]:

$$\Lambda_{QPM} = \frac{\lambda}{2(n^{2\omega}_{eff} - n^{\omega}_{eff})} \tag{5.1}$$

where λ is the wavelength of the *pump* and $n^{2\omega}_{eff}$ and n^{ω}_{eff} are respectively the effective refractive indices of the fibre poled in correspondence of the frequencies of the pump and of the SH, given by the expression [46]:

$$n_{eff}(\lambda) = n_{co}\left(1 - \frac{\Delta n(\lambda)}{n_{clad}(\lambda)}\left(\frac{1}{V^2}\right)\left(1 + \log(V^2)\right)\right) \tag{5.2}$$

where n_{clad} is the refractive index of the glass and is obtained from the Sellmeier equation for silica, n_{co} is calculated from the definition of numerical aperture of the fibre ($NA = \sqrt{n^2_{co} - n^2_{clad}}$), $\Delta n(\lambda) = n_{co} - n_{clad}(\lambda)$ and $V = (2\pi/\lambda)aNA$, where a and NA are respectively the core radius and the numerical aperture of the fibre.

5.1.1.1 UV erasure for QPM in poled fibres

The method identified to make the nonlinearity periodic and consequently fulfil the QPM condition, consists in a periodic erasure of the $\chi^{(2)}_{eff}$, previously created inside the fibre by thermal poling, by exposing the fibre's core to UV light. The ability of UV light to erase the nonlinearity is well known in literature. This technique has been studied in connection with photoinduced SHG in optical fibres [153, 154] and later applied to thermally poled bulk glasses [155, 156]. Bonfrate in 2000 transferred for the first time the UV erasure technique to poled optical fibres [157] and later the same method was used with different purposes, such for example SHG of light generated by high-average power lasers [158], visible light generated by SHG [159], SHG characterized by a certain broadband tunability [160], SHG bandwidth control through the realization of aperiodic gratings [161], and direct generation of polarization-entangled photon pairs [24, 162].

A generally accepted explanation of the phenomenon of UV erasure is that exposure to high energy photons leads to the release of electrons, which move through the electric field frozen into the fibre by thermal poling and annihilate it. One model to describe the dynamics of UV erasure process has been implemented by Oullette in 1988 and is based on the assumption that a poled glass can be seen as a RC circuit where the capacitance C is charged with a certain charge q [153]. On one of the two plates of the capacitance there are the electrons trapped in the NBO^- centres (representing the glass region depleted of impurity charges by the electromigration process due to the application of the external electric field) while on the other plate there are the positive charges coming from the atmosphere and attracted on the surface of the glass to satisfy the law of the charge neutrality of the glass after the poling experiment ends. If the UV photons possess enough energy to ionize the traps and free the electrons from the NBO^- centres, it will be possible to cancel the negative charge of the space-charge region and remove in this way the frozen-in electric field which causes the onset of the nonlinearity, expressed by the equation (2.69). The charges are made mobile by absorption of light, thus the light changes the effective resistance of the circuit. The current induced is then proportional to the number of ionized charges, which in turn is proportional to the number of remaining charges. But the current is also proportional to the voltage in the capacitor, which is also in turn proportional to the number of remaining charges. So it is possible to write [153]:

$$i = \frac{dq}{dt} = \frac{V}{R(q)} = -\frac{q}{R(q)C} = -\frac{q^2}{C} = -kq^2 \tag{5.3}$$

and hence, because $\chi^{(2)} \propto E_{dc} \propto q$:

$$\frac{d\chi^{(2)}}{dt} = -k(\chi^{(2)})^2 \tag{5.4}$$

which describes the decay of the SON due to the exposure to UV light. Imposing the initial condition $\chi^{(2)}(t=0) = \chi_0^{(2)}$, it is possible to find the expression:

$$\chi^{(2)}(t) = \frac{\chi_0^{(2)}}{1 + k\chi_0^{(2)} t} \tag{5.5}$$

The setup used to write the UV gratings along the poled samples is shown in Fig. 5.1 and consists in a mode-locked amplified solid state laser (Nd:YVO4, $\lambda = 1064\ nm$, pulse duration 8 ps, repetition rate 250 kHz, average power 2.5 W) equipped with a block including two nonlinear crystals, for the generation of the second harmonic (532 nm) and the third harmonic (355 nm). The poled fibre to be UV erased is clamped on two three-axis stages in turn placed on top of a linear stage (Aerotech, model ABL2000, with maximum travel length of 30 cm), while two cylindrical lenses (of focal lengths respectively of 500 and 85 mm) are used to deliver the third harmonic beam with a spot size on the fibre of 10 $\mu m \times 100$ μm.

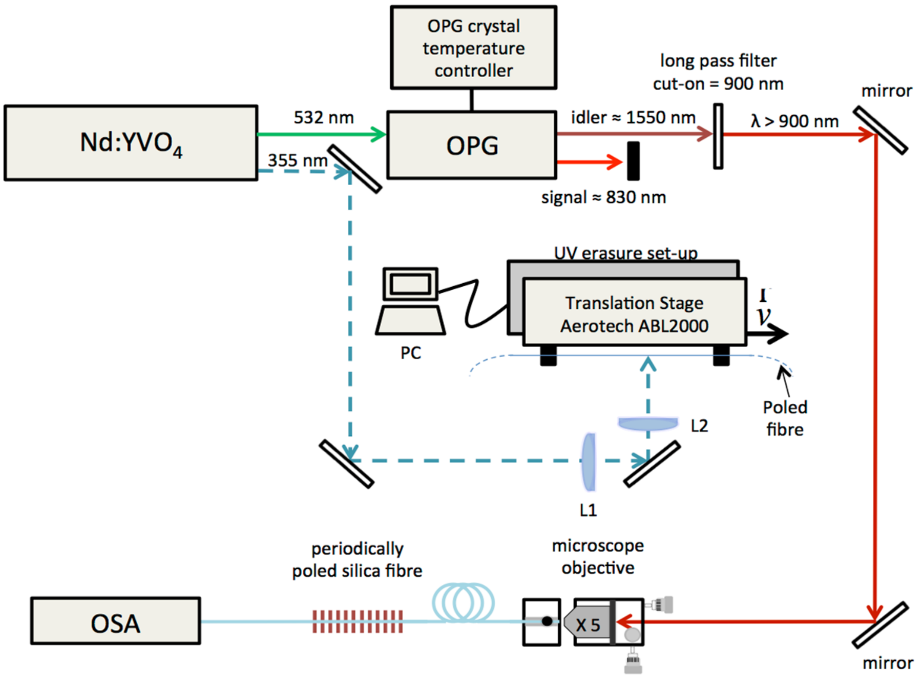

FIGURE 5.1: Experimental setup for the inscription of the QPM grating in poled fibre by 355 nm erasure. The laser beam used for the erasure process is the third harmonic of a Nd:YVO4 mode-locked pulsed laser. L1 and L2 are cylindrical lenses of focal length f = 500 and 85 mm, respectively, used to produce a spot size on the fibre of 10 $\mu m \times 100$ μm. The optical setup used for the SHG nonlinear characterization of the periodically poled fibre is also shown, consisting in the second harmonic of the Nd:YVO4 mode-locked laser, pumping an optical parametric generator (OPG), to produce a broadband infrared idler output (3 dB of bandwidth, which means ≈ 80 nm, average power of 50 mW) that is temperature tunable between 1100 and 2500 nm. The long-wave pass filter in the optical setup rejects all radiation below the cut-on wavelength (900 nm) associated with the source. This ensures that any spectra observed at wavelengths shorter than 900 nm will be due only to nonlinear processes occurring within the periodically poled fibre [131].

In Fig. 5.1 the optical setup used for the SHG nonlinear characterization is also shown, which consists in the second harmonic of the Nd:YVO4 mode-locked laser which pumps an optical parametric generator (OPG), to produce a broadband infrared idler output (3 dB of bandwidth, ≈ 80 nm, average power of 50 mW) that is temperature tunable between 1100 and 2500 nm. The long-wave pass filter in the optical setup rejects all radiation below the cut-on wavelength (900 nm) associated with the source. This ensures that any spectra observed at wavelengths shorter than 900 nm will be due only to nonlinear processes occurring within the periodically poled fibre.

After clamping the fibre on the two three-axis stages a process of alignment of the fibre with the UV beam is realized. A camera, located on top of the fibre, is used to visualize the fibre fixed to the linear stage. After checking that the cladding holes of the twin-hole fibre are aligned one on top of the other (in such a way to be aligned along a direction perfectly perpendicular to the direction of the UV beam), this condition of alignment is guaranteed all along the stage path by means of the camera. At this point the linear stage moves at constant speed while a mechanical shutter is electronically opened and closed with a frequency established by the length of the period to be written on the fibre. The duty cycle of the shutter, chosen after a process of optimization done in a preliminary process of study, is 35 %. This means that, considering a complete cycle representing a single period of the UV grating, the shutter will be open for 35 % of the time and closed for the remaining 65 % of the time. The reason behind the fact that the best choice of duty cycle does not correspond to the 50 % is the contribution of the tails of the UV beam which erases the nonlinearity as well.

5.1.1.2 Induction-poled fibres

The method for induction poling is described in section 3.4 and in Fig. 3.13 the schematic of the setup implemented for realizing the induction poling is reported. The fibre is a $\approx$ 40 cm long piece of a twin-hole pure silica fibre, manufactured by Fibercore Ltd., Southampton UK (OD of 125 μm (not including polymer coating), 4.3 μm diameter, 0.17 NA Germania-doped glass core) and already described in section 3.4. Before the poling experiment starts the *sample* is equipped with two embedded electrodes made of gallium, pumped into the two channels of the fibre via the pressurization system shown in Fig. 3.11 while the *inductor* (a 5 cm long piece of three-hole fused silica fibre (Fig. 3.2.1)) is equipped with two tungsten wires inserted in the two larger holes. The two wires are both connected to the same anodic potential of 4.3 kV for a total time of 2 hours while the whole system, placed into a Petri dish is heated up at 300 °C. The system (including *inductor* and *sample*) is later allowed to cool down (for 1 hour) to room temperature while the electric potential is still applied to the inductor.

After the experiments end, the gallium is removed from the two channels by using the same pressurization system and purged for 1 hour, in order to remove residues of metal from the inner walls of the two channels. At this point the sample (of $\approx$ 20 cm length) is spliced on each end to a $\approx$ 10 cm long piece of single mode fibre (manufactured by Thorlabs Ltd., OD 125 μm (not including polymer coating), 5.3 - 6.4 μm mode field diameter at λ = 980 nm, NA = 0.13 - 0.15 (nominal value)). These fibres have a dual role. Firstly the presence of these two fibres is useful during the process of UV erasure because it allows to clamp more efficiently the sample to be written on the stage where it is fixed, and secondly it has been observed that it helps to considerably reduce the "coupling losses" due to the splice process during the optical nonlinear characterization of the PPSF.

It is worth highlighting that in principle, if the structural properties of the fibre were exactly known, it would be possible to know exactly the period of the UV grating that would be necessary to write along the sample to obtain SHG at a desired pump wavelength. In this case the wavelength aimed to be doubled in frequency is 1550 nm, the wavelength of emission of a narrowband low power cw diode laser which would be ideal to be used as pump to generate SHG in QPM conditions without the risk of exciting higher order nonlinear processes. Because, instead, the actual physical properties (in particular the refractive index of the glass and the core's size) of the fibre poled are not precisely known (because of the tolerances on the specifications the fibres are characterized by), an empirical process of characterization of the UV erasure, which consists in writing few periods of the grating and checking the wavelengths where the second harmonic light is generated, was implemented. The experimental setup used to realize this characterization process is represented in the central part of the Fig. 5.1 and consists in a broadband infrared laser beam coupled free space into the periodically poled fibre via a microscope objective. An optical spectrum analyzer (OSA) is then used to measure the light transmitted through the sample and so to identify the eventual SH wavelength. It is very important the presence of a long-wave pass filter inserted in the optical setup before the pump is coupled into the sample, which rejects all radiation below the cut-on wavelength (900 nm) associated with the source. This ensures that any spectra observed on the OSA display at wavelengths shorter than

900 nm will be due only to nonlinear processes occurring within the periodically poled fibre.

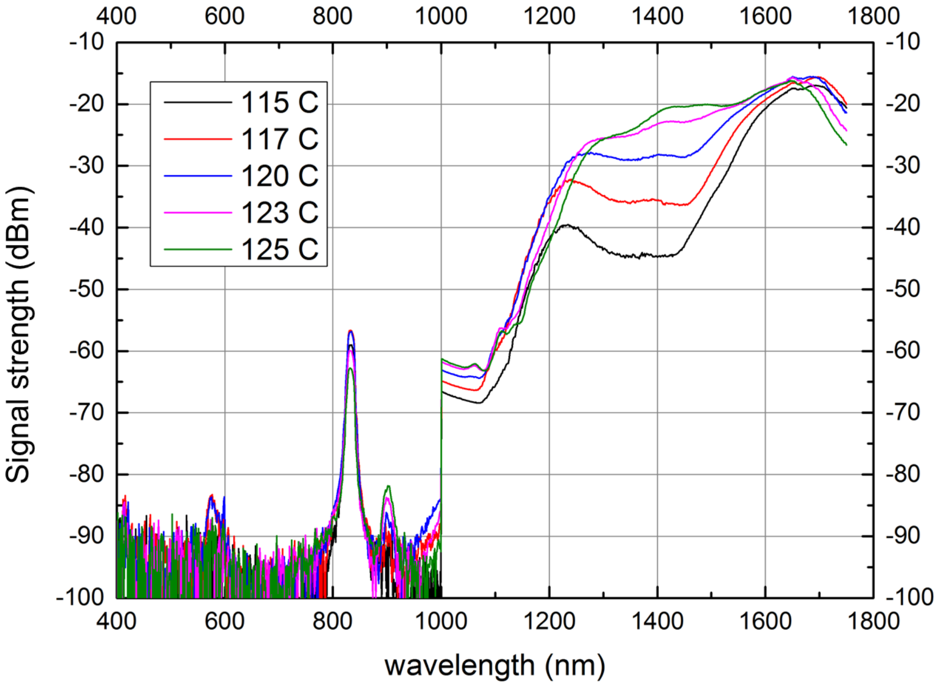

FIGURE 5.2: SHG spectra of a twin-hole pure silica sample (poled by induction by means of the setup shown in Fig. 3.13 and in the experimental conditions described previously in this section) with a QPM grating period of 57 μm written via UV erasure technique, at different temperatures of OPG nonlinear crystal.

In Fig. 5.2 the spectra, acquired (for a poled sample with a UV grating of period of 57 μm) by changing the operation temperature of the OPG nonlinear crystal, are reported. Besides the IR spectrum of the pump, which includes all the wavelengths beyond 900 nm and changes by modifying the nonlinear crystal operation temperature, it is possible to identify a peak located around 830 nm, which instead does not move from its position even changing the operation temperature of the OPG nonlinear crystal. This means that the presence of this peak is due to some nonlinear process generated inside the sample. In addition, this indicates that it is likely that its presence is due to the SH generated by a particular wavelength (linked to the grating period written inside the fibre) of the pump. The different intensity of the SH peak at the different temperatures is due to the fact that by changing the operation temperature of the OPG nonlinear crystal, the relative intensity of the component of the pump that produces SHG changes, and consequently the SH power changes.

In Fig. 5.3 the spectrum acquired for a fixed temperature of the OPG crystal by pumping a control sample which has not been poled is reported. The absence of the peak at $\approx$ 830 nm reveals the fact that its presence is definitely due to the periodical poling procedure.

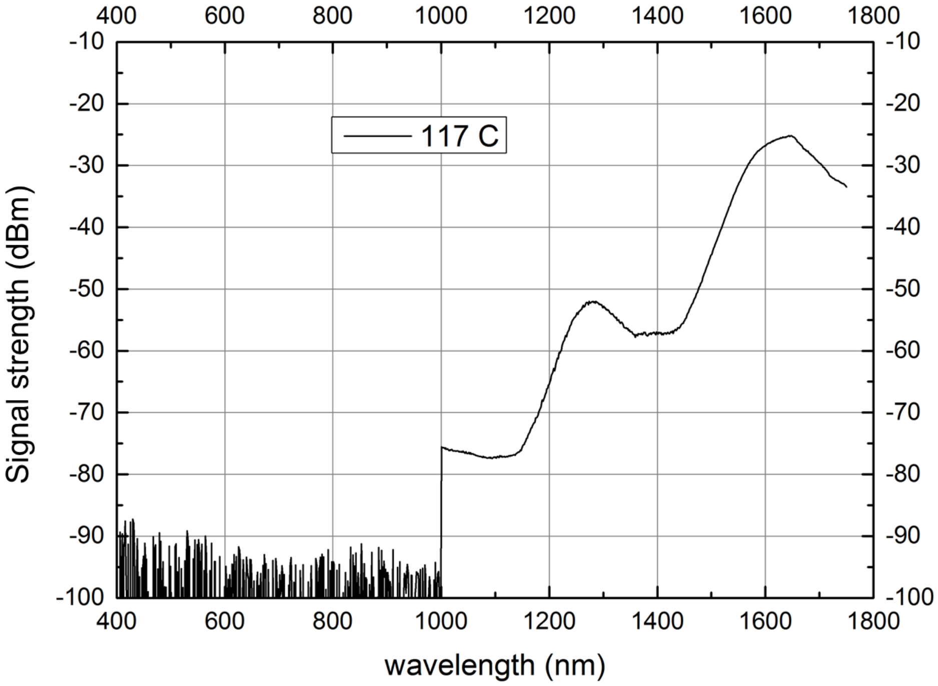

Figure 5.3: Spectrum of an unpoled twin-hole pure silica control sample at a particular operation temperature of OPG crystal.

Coming back the the fibre poled by electrostatic induction, two UV gratings of different period are written inside two samples of the same length and poled exactly in the same experimental conditions. In Fig. 5.4 the two spectra captured by the OSA and related to the two UV gratings written in the two samples are reported. From the observation of the curves, there is SHG in both the samples poled, and the SH wavelength moves according to the linear dependence from the UV grating period, exactly as expected according to the equation (5.1). Both demonstrate quite unequivocally that the induction poling is able to induce a SON inside the poled fibre.

An important consideration needs to be added at this point, related to the fact that the shape of the two tuning curves (shown in Fig. 5.4) seems to be quite different. The main reason of this difference consists in the fact that the process of UV erasure has been realized using the same setup for both the fibres poled

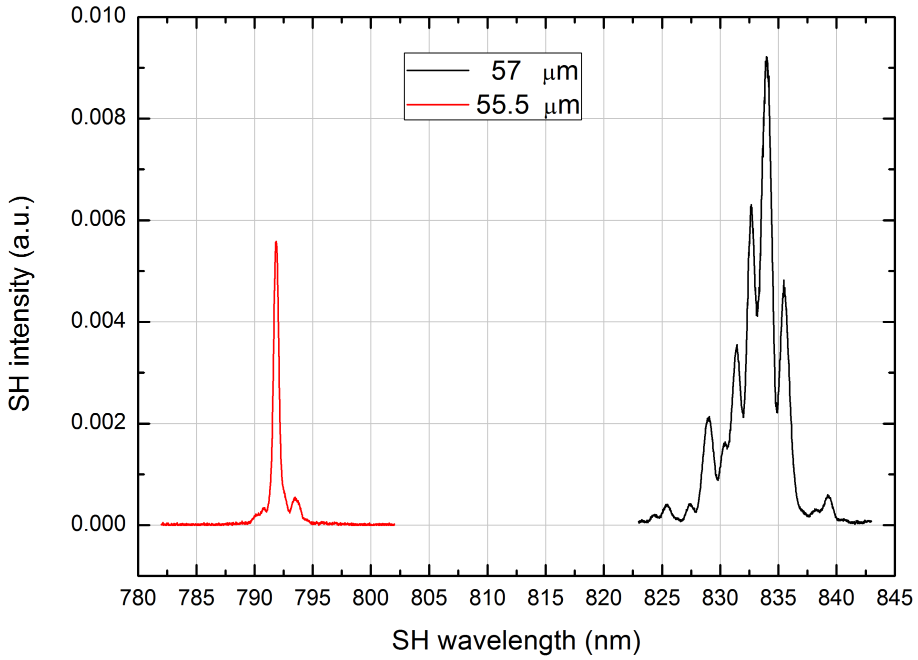

FIGURE 5.4: SHG spectra of pure silica sample poled by induction, with different QPM grating periods written via UV erasure [131].

by induction but of course in two different times and onto different fibres, even if they belong to the same fibre reel and poled in the same experimental conditions. The main issues which could compromise the repeatability of the UV erasure and consequently of the tuning curve of each PPSF are related to the process of fabrication of each device, and could include for example the process of removal of the polymer coating of the fibre (realized by means of a chemical stripping method), or the process of removal of the liquid electrodes from the two channels of the fibre. Indeed, the presence of residues of coating on the external surface of the fibre or small drops of liquid metal (gallium or something else) inside the two channels of the fibre could deflect the UV laser beam used to erase the nonlinearity compromising the periodicity of the grating written. These grating fabrication errors can cause deviations from the theoretically expected $sinc^2$ profile of the power of SH (see equation (2.57)). Other possible issues which could affect the quality of the grating are for example intrinsic defects of the fibre's cladding glass or a not enough accurate alignment of the fibre along the perpendicular direction to the UV beam during the UV erasure process.

It is worth highlighting that the process of fabrication of the UV grating needs to be realized with enough accuracy that the QPM pump wavelength (λ in formula (5.1)) is included in the bandwidth of the PPSF. From the equation (2.61) is possible to obtain the bandwidth of a periodically poled fibre of, for example, 10 cm of length, which is of $\approx$ 2 nm. If the formula (5.1) is differentiated, it is obtained the following expression [163]:

$$\frac{\delta\lambda}{\lambda} = \frac{\delta\Lambda_{QPM}}{\Lambda_{QPM}} + \frac{\delta\Delta n_{eff}}{\Delta n_{eff}} \tag{5.6}$$

where $\Delta n_{eff} = n_{eff}^{2\omega} - n_{eff}^{\omega}$ and $\delta\lambda = |\lambda_{QPM} - \lambda|$. The left hand side of the equation (5.6) represents the tolerance which can be accepted in the QPM pump wavelength, which for a wavelength of 1550 nm and a device of 10 cm of length is of $\approx$ 0.2 %. The two terms on the right hand side of the equation represent the two contributions of error in the determination of Λ_{QPM}, respectively due to errors in the period during the fabrication of the UV grating (the first term) and the determination of the period from the fibre parameters (the second term). Assuming that each of the contributions of error has the same weight (corresponding to the 0.1 %), the precision required for the fabrication of the UV grating is, for example, 25 nm for a period of 50 μm, while the error tolerated in the measurement of the n_{eff} is of $\approx 10^{-5}$ for $\Delta n = 0.01$. Because these last constraints are very restrictive and challenging, an empirical method has been chosen to find the right UV grating period corresponding to a particular wavelength of the pump (such as for example 1550 nm), which consists in writing on samples poled in the same experimental conditions UV gratings of different period and measuring the wavelengths of the SH generated by pumping the PPSF with the light produced by the broadband infrared laser and analyze the spectrum of the transmitted light with an OSA, as already explained earlier in this section. Provided that a linear dependence holds between the QPM pump wavelength (which can be defined λ_{QPM}) and the corresponding grating period Λ, it is possible to calculate the period of the grating desired $\Lambda + d\Lambda$ for realizing QPM at the wavelength $\lambda_{QPM} + d\lambda$:

$$d\Lambda = \frac{\partial\Lambda}{\partial\lambda} d\lambda \tag{5.7}$$

where $\partial\Lambda/\partial\lambda$ is the slope of the linear relationship between Λ and λ_{QPM}.

The validity of the empirical approach just described, based on the linearity of the relationship between Λ and λ_{QPM} can be compromised by an intrinsic defect which can occur in a long sample used to provide the fibres which have to be periodically poled, that is the variation of the core radius. A different core radius modifies the n_{eff} of the fibre and so shifts the QPM wavelength for the same period of grating. If the equation (5.1) is written as:

$$\Lambda = \frac{\lambda}{2\Delta n_{eff}(\lambda, a)} \tag{5.8}$$

and differentiated, it is possible to obtain:

$$d\Lambda = -\frac{\lambda}{2}\frac{1}{(\Delta n_{eff})^2}\left(\frac{\partial}{\partial a}\Delta n_{eff}\right) da \tag{5.9}$$

where $\partial\Delta n_{eff}/\partial a$ can be obtained from a linear fit between Δn_{eff} and da/a for a certain wavelength. By using the formula (5.9) it is possible to know of how much the period of the grating needs to be changed in order to compensate for a change of the fibre's core size of a certain percentage. At a wavelength of ≈ 1550 nm and for a variation of 1 % of the core size it has been estimated a variation of the period of grating of ≈ 170 nm. This value highlights once more the sensitivity of the QPM conditions to the fibre parameters. In practice, if the fibre diameter is given with a certain percentage of tolerance, it is likely that the period to be written in fibres collected from different section of the same sample will need to be different to obtain QPM at the same desired wavelength. The regularity of the fibre sizes along its length becomes, for this reason, a very critical parameter to take into account when a sample has to be used for the realization of nonlinear devices characterized by a high level of repeatability.

5.1.1.3 Experimental estimation of $\chi^{(2)}_{eff}$ in optical fibres poled by induction

The characterization of the periodically poled fibre using the broadband infrared laser source can reveal the presence of a SON, which will then allow the exact pump wavelength where the SHG is phase matched to be calculated. However, this SON does not allow us to make an accurate estimate of the value of $\chi^{(2)}_{eff}$ generated inside the fibre core due to the broad nature of the source. Indeed the bandwidth launched into the PPSF is quite broad and so could cause the generation of higher order mixing phenomena among the many wavelengths present inside the fibre. For this reason a different setup has been implemented to characterize the PPSF in such a way to generate only a SHG phenomenon and then to measure the induced $\chi^{(2)}_{eff}$.

The setup is shown in Fig. 5.5 and includes a narrow band tunable diode laser (Photonetics, model 3642 HE CL, maximum cw power = 6 mW), a in-line polarization controller (Fiberpro, model PC1100) and a Low-Power calibrated photodiode sensor (Newport, model 918D-UV-OD3). The linearly polarized pump radiation (λ = 1550 nm), sourced by the narrow band tunable diode laser is collected by means of a SMF28 fibre, which is connected to the polarization controller, which allows us to change the polarization state of light before being coupled into the sample (Fibercore sample periodically poled and spliced between two 30 cm long pigtails of SM980). The SH power is measured by means of the Low-Power calibrated photodiode sensor. It is possible to scan the SH power by changing step by step (the size of the step can be chosen) the emission wavelength of the source around the value of 1550 nm. It is necessary to consider that SH power produced in PPSF is conditioned by the coupling between the polarization state of the pump light launched into the sample and the frozen-in DC electric field created by means of thermal poling.

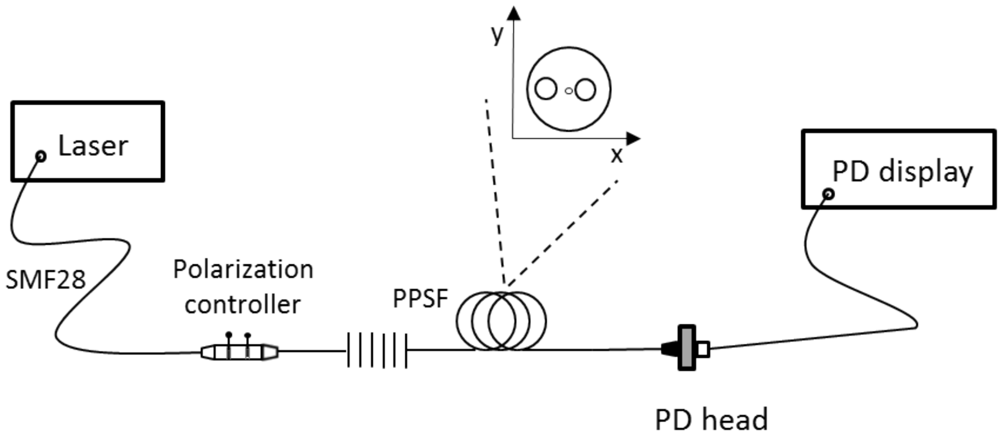

FIGURE 5.5: Setup for SHG measurements for PPSF. The source is a tunable diode laser emitting at 1550 nm (Photonetics, model 3542 HE CL, cw power = 6 mW), the polarization state of the pump radiation can be modified using the in-line polarization controller, and a Low-Power calibrated photodiode sensor (Newport, model 918D-UV-OD3) is used to measure the SH power. In the inset the cross-section of the twin-hole silica fibre periodically poled is shown. The principal polarization axes of the fibre are assumed aligned along the two orthogonal axes x and y, where x is the direction of the frozen-in electric field.

It is known that in thermally poled fibres $\chi^{(2)}$ comes from $\chi^{(3)}$ and the frozen-in DC electric field E_{dc} (see equation (2.69)). Furthermore the expression of the induced $\chi^{(2)}$ is consistent with the $\chi^{(3)}$ symmetry in silica fibres, which can be expressed by the following relations [44]:

$$\chi^{(2)}_{xxx}(2\omega;\omega,\omega) = 3\chi^{(2)}_{xyy} = 3\chi^{(2)}_{yxy} = 3\chi^{(2)}_{yyx} \tag{5.10}$$

$$\chi^{(2)}_{yyy}(2\omega;\omega,\omega) = \chi^{(2)}_{yxx} = \chi^{(2)}_{xyx} = \chi^{(2)}_{xxy} = 0 \tag{5.11}$$

where x and y are the transverse axes of the fibre and x represents the direction of E_{dc}. Because of the birefringence of the sample (due to its geometry and to the different stresses induced along the two different directions x and y during the fibre drawing process), it is possible to spectrally separate three different SH processes. If we assume that the principal polarization axes of the fibre are aligned along x and y (see Fig. 5.5), the QPM condition in the PPSF is given by:

$$\beta_i^{(2\omega_F)} = \beta_j^{(\omega_F)} + \beta_k^{(\omega_F)} + \frac{2\pi}{\Lambda} \tag{5.12}$$

where ω_F represents the frequency of the fundamental harmonic, β_s are the propagation constants, i, j, k ($= x$ or y) indicate the polarization of the waves, and Λ is the first order QPM period. We define QPM of type-I the case where $j = k$, and type-II the case where $j \neq k$. If the radiation sourced from the diode laser is launched into the device, and the wavelength is scanned in the appropriate range, it will be possible to obtain a curve which includes three different peaks, the first two related to two QPM processes of type-I ($y + y \rightarrow\ x$ and $x + x \rightarrow\ x$) and the third one related to the type-II process ($x + y \rightarrow\ y$). In Fig. 5.6 an example of the tuning curve for a random alignment of the polarization state of the light coupled into a poled fibre is reported.

After coupling 6 mW of the cw laser beam generated by the narrowband 1550 nm diode laser into the PPSF poled by induction, no SH peak has been observed. The reason for this is that the nonlinearity induced is very small, so it is visible when the power coupled into the fibre is 50 mW (beam generated by the OPG broadband infrared source) while it is not anymore distinguishable if the power is as low as the one provided by the diode laser. Somehow this result is expected because the kind of glass the Fibercore twin-hole pure silica fibre is made of is characterized by a very low content of impurity charges. Another type of fibre (fused silica, manufactured by ACREO Swedish ICT (see section 5.2.3 for further details)) and characterized by a higher concentration of impurities will be used from now on to realize our thermal poling experiments. The conclusion about the induction poling method is that it allows for the induction of a SON inside an optical fibre, even in the case of a pure silica sample. In the next sections it will be possible to see how to obtain an estimation of the $\chi^{(2)}$ starting from the tuning curves of a poled sample.

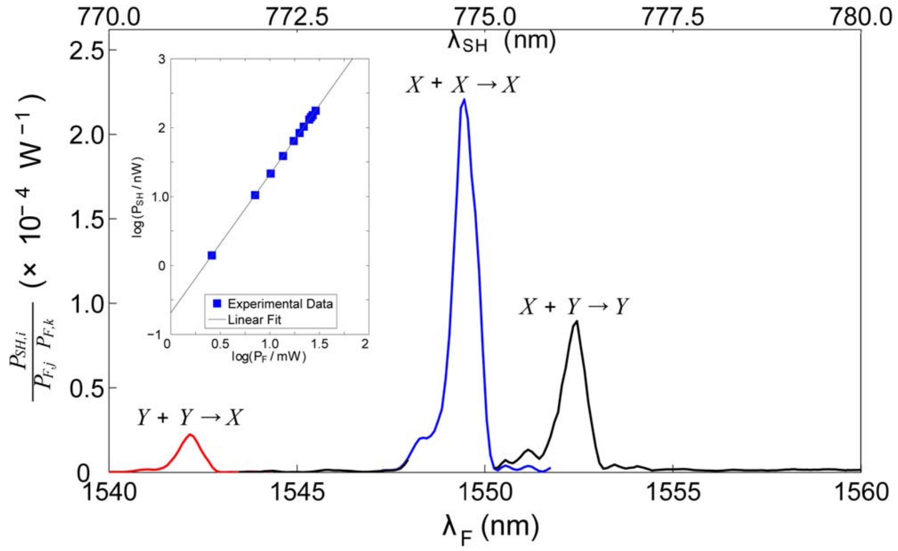

FIGURE 5.6: Measured SHG spectrum showing the nonlinear transmittance η_{SH} plotted against λ_F for each of the three observed processes. The inset shows a log-log plot of the SH power P_{SH} versus the fundamental power P_F for the $x + x \rightarrow\ x$ signal. Clearly, $P_{SH} \propto P_F^2$ [44].

5.2 Extended length cathodeless poling

In chapter 4 the method developed for equipping the twin-hole fibre's channels with metallic or electrolytic liquids to be used as embedded electrodes, is exploited with the aim of poling in cathodeless configuration samples much longer than ever been seen in literature. The first target of this part of my work is to demonstrate that by using liquid electrodes is possible to increase the length of the poled samples, removing in this way the challenging process of insertion of solid electrodes inside the channels or the one of removal of solidified metal electrodes from the channels after any thermal poling experiment. The second target of this work consists in the realization and optimization of all-fibre nonlinear photonic devices (possibly characterized by a high $\chi^{(2)}_{eff}$, long length and low transmission losses) to be used for many applications, such as for example frequency doubling in all-fibre systems for generation of high order harmonics in optical microfibres, generation of polarization-entangled photon pairs by SPDC and frequency comb in purely quadratic ring resonators.

5.2.1 Linear setup for thermal poling of long fibres

A first type of setup (see Fig. 5.7) for thermal poling of samples of 60 cm of length (equipped with liquid electrodes) was implemented, which consists of a hotplate of rectangular shape (width = 2 cm and total length of 80 cm), a borosilicate glass strip, the high voltage power supply and an insulating surround made of a special type of thermal paper (manufactured by Hodgson & Hodgson Group Ltd.).

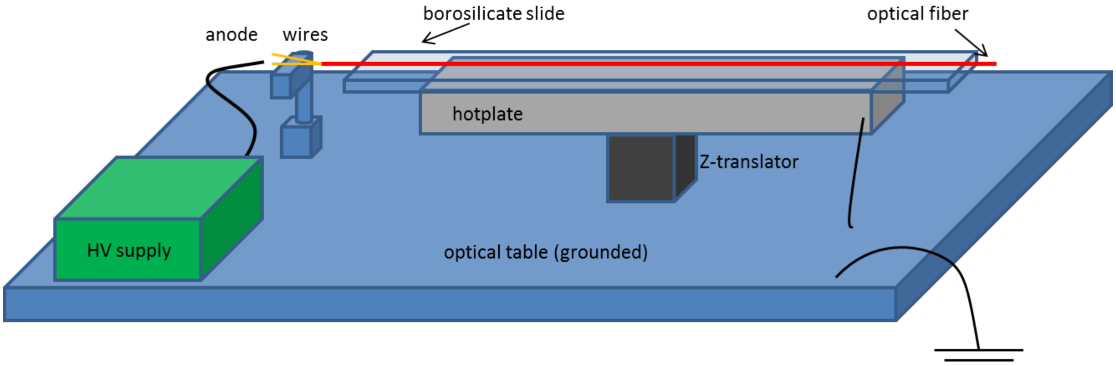

Figure 5.7: Schematic of the setup for cathodeless poling (double anode configuration) of long fibres with liquid embedded electrodes.

The hotplate consists of a metallic slab containing a resistive heating element electrically isolated from the metallic surface by means of a ceramic shell. The heating element is connected to a power supply able to provide an electrical dc current of ≈ 3 A which, for Joule heating effect, heats up the resistive element. On top of the hotplate a 10 mm thick borosilicate glass strip is adhered to the metallic slab by means of two pieces of Kapton tape in order to ensure adequate electrical insulation between the electrodes embedded into the sample and the grounded surface of the hotplate, while simultaneously maintaining a good thermal contact. The fibre to be poled is then placed on top of the glass strip and an insulating layer of thermal paper is then wrapped around the whole setup where the temperature could be maintained approximately fixed along the duration of the experiment. The voltage is then applied to the two tungsten wires inserted just inside the fibre's channels. The groundplane of this experimental setup can be considered as the resistive element included inside the hotplate or instead can be created by connecting the external surface of the hotplate to the ground of the high voltage power supply. For the sake of repeatability this second choice has been done for all the experiments of thermal poling.

5.2.2 Circular setup for thermal poling of long fibres

An alternative setup was also implemented for thermal poling of samples longer than 60 cm, which consists in a Petri dish of ≈ 15 cm of diameter. The fibre, stripped from the polymer coating for most of its length and equipped with the embedded liquid electrodes and the two tungsten wires inserted inside the two channels for few cm and the two ends sealed by means of a drop of superglue (in the case of metallic liquids) or by means of the epoxy resin cap shown in Fig. 4.8 in the case of aqueous solutions, is placed inside the Petri dish. The Petri dish is then placed on top of a ceramic hotplate and heated up at the desired temperature before any voltage is applied to the two tungsten wires. The groundplane in this type of setup is represented by the hotplate resistive element located below the ceramic plate and so it is quite far from the sample. In Fig. 5.8 a schematic representation of this setup is shown. Potentially metres long fibres can be poled by means of this type of setup. The longest fibre manufactured to date in this

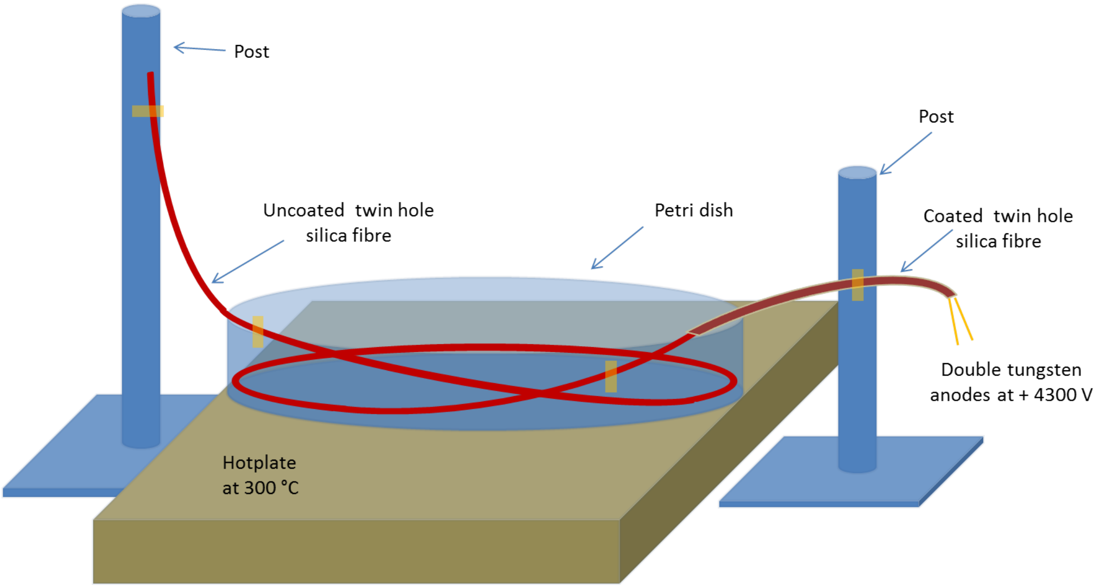

FIGURE 5.8: Schematic of the setup for cathodeless poling (double anode configuration) of a twin-hole silica fibre with embedded liquid electrodes.

thesis work is 2 m long but there are no impediments, as far as we are aware, that this length could not be increased significantly.

5.2.3 SHG in twin-hole fused silica fibres poled with liquid metallic electrodes

At this point of the work there are all the elements (induction poling technique and its numerical 2D model, method for creation and removal of liquid electrodes, two types of setup for thermal poling experiments) to create all-fibre nonlinear devices for frequency doubling and eventually even for other kinds of photonic applications. The first step towards this process of optimization and implementation is poling a fused silica sample (characterized by a relatively high concentration of ionic impurities which could allow for the activation of an electromigration process inside the glass) by means of different types of liquids used as electrodes. The target is represented by the demonstration of a SON with different types of liquids and even by the comparison of the values of $\chi^{(2)}_{eff}$ which can be obtained with the different electrodes.

Different sets of fibres (all selected from the same sample, namely a twin-hole fused silica step-index Ge-doped optical fibre (manufactured by ACREO Swedish ICT, SWEDEN, OD = 125 μm, core diameter = 4 μm, NA = 0.17), are thermally poled in a cathodeless double anode configuration and in experimental conditions which will remain approximately the same (in particular the temperature and the duration of the poling process). The principal target is the comparison between the different types of liquids used as electrodes, so, for the sake of reliability of the experiments, most of the experimental conditions need to be preserved. The only parameter which will be sometimes changed is the voltage applied during the poling process to the embedded electrodes.

In chapter 4 it has been already demonstrated that in all the attempts of poling by means of the different liquids (both metallic and aqueous) a space-charge region is observed, indicating that some sort of modification of the glass structure has been created because of the poling process. In this chapter instead a quantitative evaluation of the $\chi^{(2)}_{eff}$ induced will be performed and if the type of electrode used affects somehow its value. Another interesting comparison will be realized in terms of the transmission losses characterizing each type of nonlinear device poled with different electrodes. The reduction of the losses is one of the relevant targets which have to be considered when a nonlinear device is implemented.

The first batch of samples is poled by means of gallium used as metallic electrode. The setup used for all the samples is the linear one shown in Fig. 5.7, the electric configuration of poling is the cathodeless double anode, the two embedded gallium electrodes are created by pressurizing the fibre by means of the system of Fig. 3.11 where He at $\approx$ 300 psi of pressure is used. A first sample has been poled in the experimental conditions of V_{app} = 6.5 kV, T = 250 °C, duration of poling = 2 hours, with the aim of finding the exact value of the UV grating period to obtain QPM at a wavelength as close as possible to the value of 1550 nm. After removing the gallium from the two channels by means of the pressurization system (He at $\approx$ 1000 psi of pressure), five different UV gratings (length of the grating = 5 cm) of different period (56.75 μm, 57 μm, 57.25 μm, 57.5 μm and 57.75 μm) have been written on the fibre poled by using the setup shown in Fig. 5.1. By using the broadband infrared source shown in the same figure, the QPM wavelengths for each period have been identified. By assuming a linear trend between grating periods and QPM wavelengths, the period of grating to obtain QPM at 1550 nm has been estimated. The value obtained is 57.3072 μm (see Fig. 5.9).

After identifying the Λ_{QPM} to have QPM at $\lambda = 1550\ nm$, a new ACREO sample has been poled in cathodeless configuration and in the experimental conditions of V_{app} = 7.5 kV, T = 250 °C, duration of poling = 2 hours. After writing a 28.5 cm long grating of the period identified to have QPM at 1550 nm (57.3072 μm), the sample was characterized by using the setup shown in Fig. 5.5. After a first scan of the SH power by changing step by step (the size of the step can be chosen) the emission wavelength of the source around the value of 1550 nm, a tuning curve similar to the one shown in Fig. 5.6 is obtained. At this point, choosing the pump wavelength corresponding the central one of the three peaks of the tuning curve (corresponding to the $x + x \rightarrow\ x$ process), the power of SH measured by means of the Low-Power calibrated photodiode sensor is maximized tuning the in-line polarization controller. The tuning curves for both the generic polarization alignments of the incoming pump and for the optimized one are reported in Fig. 5.10.

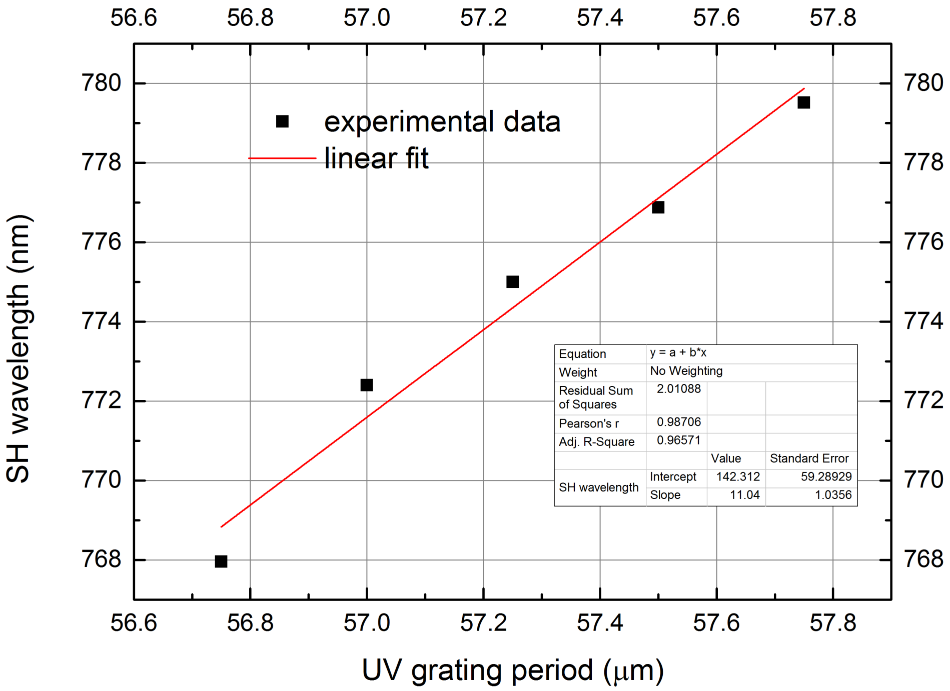

FIGURE 5.9: Graph of SH wavelengths vs. QPM periods written on the twin-hole sample poled in cathodeless configuration and with gallium electrodes. From the linear trend it is possible to obtain the value of the grating period to be written to have QPM at 1550 nm.

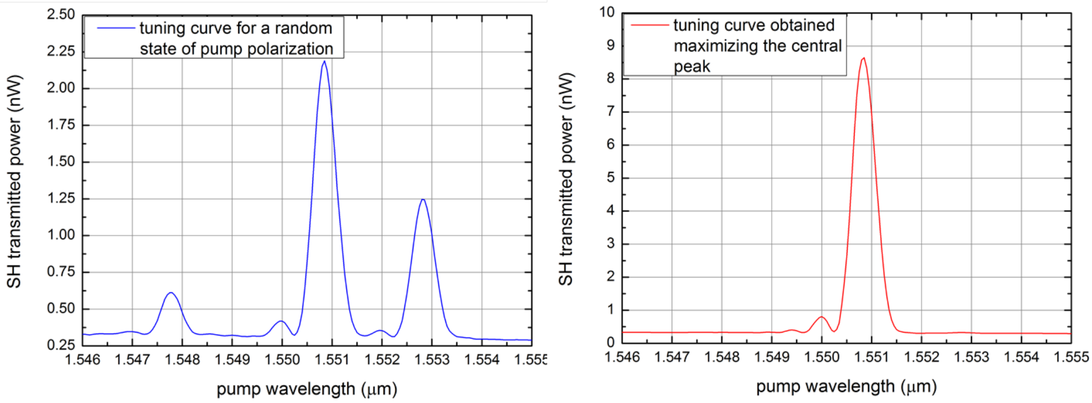

FIGURE 5.10: Tuning curves of ACREO sample periodically poled with a QPM period of 57.3072 μm, obtained by scanning (with steps of 0.1 nm) a tunable diode laser source in a small range of wavelengths around the value of 1550 nm. On the left the tuning curve obtained for a generic state of polarization of the pump beam, on the right the tuning curve obtained when the peak corresponding to the $x + x \rightarrow\ x$ process is maximized.

5.2.3.1 Estimation of $\chi^{(2)}_{eff}$ from SHG efficiency of all-fibre nonlinear devices

The method for the estimation of $\chi^{(2)}_{eff}$ is referred to the periodically poled fibre whose tuning curves are reported in Fig. 5.10, but it is of course applicable to any periodically poled sample provided that a low power narrowband cw laser is used to pump it, and so the conditions of pure SHG and undepleted pump are both valid.

Assuming that the all-fibre nonlinear device implemented for frequency doubling consists in the periodically poled fibre (ACREO) spliced in correspondence of the two ends with two pieces of SM980 fibre (single mode fibre manufactured by Thorlabs, Inc., cladding diameter = 125 μm, mode-field diameter = 5.3 - 6.4 μm at 980 nm, NA = 0.13 - 0.15), it is possible to estimate the value of $\chi^{(2)}_{eff}$ induced by thermal poling starting from the equation (2.60), which represents the expression of the SH efficiency in the case of QPM and can be written in the following way:

$$\left|d^{SH}_{eff}\right| = \sqrt{\eta_{SH}\frac{\epsilon_0 c^3 (n^{eff}_{\omega})^2 (n^{eff}_{2\omega}) A_{OVL}}{2\omega^2 L^2 P^{in}_{\omega}}} \tag{5.13}$$

All the quantities in equation (5.13) can be calculated or measured in such a way it is possible to obtain the value of $\chi^{(2)}_{eff} = 2\left|d^{SH}_{eff}\right|$. The values of $A_{OVL} = |1/I_{OVL}|^2$, n^{eff}_{ω}, $n^{eff}_{2\omega}$ have been calculated respectively by means of the equations (2.54) and (5.2) for the frequencies ω and 2ω. L is the interaction length while ϵ_0 and c are respectively the electrical permittivity of vacuum and the light speed in vacuum.

The efficiency η_{SH} which appears in equation (5.13) is the ratio between the power of the SH ($P^{out}_{2\omega}$) generated after an interaction length of L and the power of the pump entering the PPSF (P^{in}_{ω}). These last two values are not directly measurable, but they can be estimated from the insertion losses of the two different harmonics due to the two splices between the PPSF and the two buffer fibres (see Fig. 5.11). For the sake of simplicity it is assumed that the insertion losses consist only in the losses due to the splices and that there are no transmission losses (including absorption, scattering and bending losses) for both the frequencies. Furthermore it is assumed that the splice losses of the pump are equally distributed at the two splices (even if it is likely that this event is not very realistic because each splice is realized in a different time and so it is possible that the two splices contributes are actually different).

FIGURE 5.11: Schematic of the typical all-fibre nonlinear device for frequency doubling realized by splicing the PPSF with two pieces of SM980 fibre. The reason of the presence of these two "buffers" is mainly related to the fact that it was experimentally observed that splicing the PPSF with the SM980 fibre instead of with the SMF28 fibre allows for reducing the insertion losses because of a better matching of the two core's sizes spliced together. The splice losses between the SM980 and the SMF28 fibres are assumed negligible.

If the total insertion losses of the pump are defined as:

$$IL_{\omega}(dB) = -10\log\left(\frac{P'^{in}_{\omega}}{P'^{out}_{\omega}}\right) \tag{5.14}$$

and it is assumed that they are equally distributed between the two splices, it is possible to write the following expression for η_{SH}:

$$\eta_{SH} = \frac{P^{out}_{2\omega}}{P^{in}_{\omega}} = \frac{\frac{P'^{out}_{2\omega}}{SL_{2\omega}}}{P'^{in}_{\omega}\cdot SL_{\omega}} \tag{5.15}$$

where the meaning of $P'^{out}_{2\omega}$ and P'^{in}_{ω} is clarified in Fig. 5.11, $P^{out}_{\omega} = P^{in}_{\omega}$ (because the transmission losses are assumed negligible) and SL are the splice losses, which at the two frequencies are:

$$SL_{2\omega} = 10^{\frac{IL_{2\omega}}{10}} \tag{5.16}$$

$$SL_{\omega} = 10^{\frac{IL_{\omega}}{2\cdot 10}} \tag{5.17}$$

So, measuring the insertion losses for each PPSF at the pump wavelength (1550 nm in this case) and assuming, for the sake of simplicity, a value of 1 dB for the insertion losses at the SH, it is possible to obtain the value of $\chi^{(2)}_{eff}$ induced by thermal poling. In the case of the sample poled by means of gallium electrodes, whose tuning curves were reported in Fig. 5.10, the value of $\chi^{(2)}_{eff}$ is 0.056 pm/V.

It is relevant to highlight that actually the insertion losses of the whole device, besides the splice losses, include also the transmission losses due to the presence of residues of gallium (or eventually another liquid metal) after filling and emptying processes. In section 5.2.3.2 the values of the transmission losses, measured by means of cutback method, are reported and compared to the losses of a sample filled (and emptied) with mercury instead of gallium.

5.2.3.2 Transmission losses of all-fibre nonlinear devices poled with embedded liquid electrodes

In the section 5.2.3.1 it has been assumed, in the estimation of the SH efficiency of a fibre poled by means of liquid electrodes, that the insertion losses of the PPSF do not include transmission losses and consist basically only in the optical losses due to the mode-mismatch existing between the two types of fibre spliced together (splice losses). Of course this assumption is close to the truth only for a fibre not equipped at all with any liquid. Instead it is experimentally proved that the process of filling and removing any liquid (in particular gallium and mercury) leaves residues inside the channels which interact with the mode propagating through the core producing some losses. With a cutback method these transmission losses have been measured (even if over a restricted number of poled samples) in the two cases of gallium and mercury, giving as result that gallium produces higher transmission losses ($TL_{Ga}(\omega) = 0.03 - 0.07\ dB/cm$) than mercury ($TL_{Hg}(\omega) = 0.01 - 0.02\ dB/cm$). Both the transmission losses are quite high, in particular if compared with the intrinsic transmission losses of the fibre not treated ($TL_{intr.}(\omega) = 0.0012\ dB/cm$), but of course the fact that the mercury is characterized by lower losses motivated us to start working with mercury used as metallic electrode.

It is worth highlighting that the measurements of the transmission losses just reported are characterized not only by a small statistical relevance (due to the fact that they have been realized for less than 5 samples) but also by the fact that the repeatability of the process of equipment of the fibre with liquid electrodes is very low. Nevertheless its usefulness lies in the fact that the results reported correspond to the experimental observation that during the process of decorative etching residues of gallium are observed on top of the etched facet of the fibre more often than the case of fibres poled with mercury.

5.2.3.3 SHG in PPSF poled with mercury electrodes

In section 4.2.1.1 the issues related to the use of gallium as electrode for thermal poling of optical fibres have been reported, mostly related to its anomalous behaviour due to the coexistence of the two phases, namely solid and liquid, at room temperature. The random solidification of gallium, indeed, quite often does not allow for removing gallium from the fibre's channels at all, and, even when it is allowed, the removal is not very efficient. The measurements of the transmission losses reported in the previous section support this thesis and motivated the replacement of gallium with a metallic liquid whose behaviour at room temperature was more regular and less tricky. Despite its safety issues, the choice made is mercury, actually the only metal liquid at room temperature.

A first set of samples (all taken from the same reel of the twin-hole fibre manufactured by ACREO) has been thermally poled by means of the circular setup (see Fig. 5.8) in essentially the same experimental conditions of the fibres poled with gallium and reported in section 5.2.3, apart from the voltage applied, which is, as usual, the only parameter which has been slightly explored during the test experiments. After the poling experiments, all these samples have been UV erased periodically in order to produce QPM at 1550 nm and characterized by means of the narrowband low power diode laser with the method described in section 5.2.3.1. In the table 5.1 some of the nonlinear devices have been reported with their values of $\chi^{(2)}_{eff}$ estimated, their sizes and experimental condition of poling.

The value of 0.12 pm/V, obtained for the sample 2 (reported in table 5.1), represents the highest value of SON of a periodically poled silica fibre that we are aware of in the literature. Apart from this value, the interesting aspect to highlight is that by using liquid electrodes it is feasible the poling of metre-long optical fibre. The longest sample poled with mercury has been a fibre of 2 m of length. The aim of this experiment was initially to periodically erase the nonlinearity by means of the UV laser light, in order to obtain an all-fibre nonlinear device for SHG characterized by a very high efficiency. This erasure has not been yet realized so far. It represents anyway a future target, which will be presented in more details in chapter 7.

After developing the experimental method for poling optical fibres using liquid electrodes and the induction poling technique, this advantageous combination can be used to further develop fibre poling technology. The parameter space available

Samples with Hg embedded electrodes	**Sample 1** $V_{app} = 5\ kV$ $T = 250\ °C$ $L = 13.5\ cm$	**Sample 2** $V_{app} = 5\ kV$ $T = 250\ °C$ $L = 11.5\ cm$	**Sample 3** $V_{app} = 8\ kV$ $T = 250\ °C$ $L = 30\ cm$	**Sample 4** $V_{app} = 5\ kV$ $T = 250\ °C$ $L = 20\ cm$	**Sample 5** $V_{app} = 5\ kV$ $T = 250\ °C$ $L = 20\ cm$
$\chi^{(2)}_{xxx}\ (\frac{pm}{V})$	0.05	0.12	0.09	0.05	0.1

TABLE 5.1: Estimated values of $\chi^{(2)}_{xxx}$ induced by means of thermal poling in five twin-hole fused silica samples (ACREO) with embedded Hg electrodes. The experimental conditions of poling for each sample and the lengths of UV gratings are also specified. Samples 1, 2 and 3 have been erased with a period of 57.3072 μm, while sample 4 and 5 with a period of 57.1937 μm. The values of $\chi^{(2)}_{xxx}$ have been estimated for each sample maximizing the peak of the tuning curve related to the $x + x \rightarrow\ x$ process.

includes the temperature of the fibre, the duration of poling, the voltage applied to the electrodes and even the type of glass the fibre is made of (which could affect the concentration of the impurities and their mobilities but also the value of $\chi^{(3)}$ of the fibre, which affects the value of $\chi^{(2)}_{eff}$) and the geometry of the fibre (the position of the electrodes with respect to the fibre's core affects the value of the electric field frozen by means of poling), with the aim of increasing as much as possible the value of the SON created by thermal poling. From this point of view the numerical 2D-model developed and reported in chapter 3 provides some indications about the process of the optimization of the experimental conditions of the thermal poling experiments. Nevertheless, even if all these parameters can be optimized, there is always a limit in the value of $\chi^{(2)}_{eff}$ which can be finally achieved due to the intrinsic properties of the glass the fibre is made of (namely $\chi^{(3)}$ and E_{dc}). In chapter 6 this topic will be discussed in detail and a way to overcome this intrinsic limits will be presented as well.

5.2.4 SHG in twin-hole fused silica fibres poled with electrolytic solutions

Even if the results of the cathodeless poling by means of metallic liquids are very promising, as can be seen from the values of $\chi^{(2)}_{eff}$ reported in the table (5.1), which represent among the best results reported in literature so far (although these results were obtained in not optimized poling conditions), there are issues related in particular to the use of mercury to be taken into account. In the sections 4.3.1 and 4.3.1.1 some of those issues have been already highlighted, and furthermore the early experiments of poling of silica fibres with electrolytic solutions have been discussed. In Fig. 4.9, in particular, the first space-charge region ever seen by thermally poling a fused silica THF by means of a solution of HCl in DI water is reported.

The apparently successful attempt of inducing a space-charge region motivated me to transfer the same technique to a proper waveguide, in particular to the twin-hole fused silica Ge-doped step-index fibre manufactured by ACREO Swedish ICT (introduced in section 5.2.3) and later to another identical fibre manufactured by the group of Prof. Jayanta Sahu (manufactured in the O.R.C.) as well. Two samples of the ACREO fibre are equipped with two different electrolytic solutions (namely HCl and tap water) by means of the method described in section 4.3.1.1 and poled by means of the setup described in section 5.2.1. The two samples are poled in the experimental conditions of T $\approx$ 300 °C, $V_{app} = 5\ kV$ and duration of poling = 2 hrs. In Fig. 5.12 the pictures of the HF-etched cross-sections of two sample poled with electrolytic solutions and two sample poled respectively with gallium and mercury in the same experimental conditions are reported. Remarkably, given these extreme conditions, the embedded aqueous electrodes also yielded well-defined depletion regions (shown in Fig. 5.12) throughout the entire 60 cm length of the test devices; to the best of our knowledge, this is the first time that optical fibres have been thermally poled using electrolytic solutions as electrodes. This highly counterintuitive result is currently under further investigation, as it is not yet fully understood how electrical continuity is maintained during poling, while the fibre is held well above the boiling points of these aqueous solutions for extended periods. Depletion region formation throughout the entire sample is unequivocal evidence that electrical continuity was not compromised during the experiment.

Some insight can be gained into this unusual phenomenon by observing the fibre using a stereomicroscope during the heating phase of the poling, but before the application of the high voltage. The fibre was monitored both in the centre and on each of the end caps created to seal the fibre. Once it had reached $\approx$ 100 °C, some bubbles were observed in the centre of the fibre which push the aqueous solution toward the ends. At 300 °C, before applying the external voltage, the fibre sample appears to be completely empty in the 60 cm of length placed on top of the hotplate, with some liquid remaining in the parts of the fibre located close to the end caps [164]. It is possible to hypothesize that at high temperatures, the aqueous solution is close to its supercritical fluid point (which, for water, is at

374 °C and 221.1 bar). Under these conditions, it is expected that the conductance of the fluid will rapidly increase [165] and, indeed, can exhibit conductance values that are orders of magnitude higher than those of standard temperature and pressure values. This near-critical operating point, therefore, could allow the high pressure/temperature/conductance fluid created within the twin-hole fibre to act as an efficient electrode. Electrical continuity is completed via the liquid regions located at the end caps and the tungsten wires inserted inside. Further investigations to confirm this hypothesis will be addressed in future work, focusing on in-situ optical spectroscopic studies [166] for which the optical fibre platform is inherently well suited.

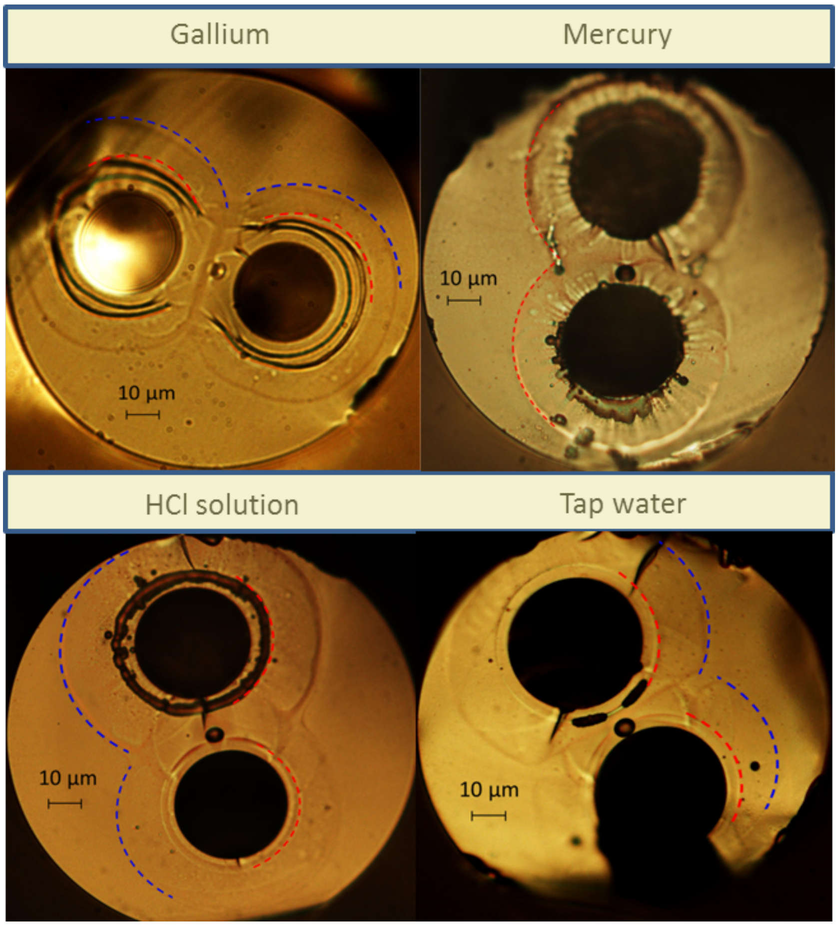

FIGURE 5.12: Cross-sectional micrographs of the HF etched samples poled using different liquid electrode types. The HF decorative etching process reveals the presence of depletion regions in all four twin-hole Ge-doped core, fused silica fibres. The observed dual concentric depletion region formation (highlighted by means of the red and blue dotted lines as a guide for the eye) is likely to be due to the Na^+ and Li^+ impurity charges involved in the electromigration process, typically characterized by differing ion mobilities in the glass [164].

The qualitative observation of the space-charge regions (reported in Fig. 5.12) induced in fibres poled with electrolytic solutions needs to be confirmed via a quantitative measurement, such as for example the SH signal generated in a PPSF. After the thermal poling process, the two fibres are UV erased according to the procedure described in section 5.1.1.1. In Fig 5.13 are reported three spectra,

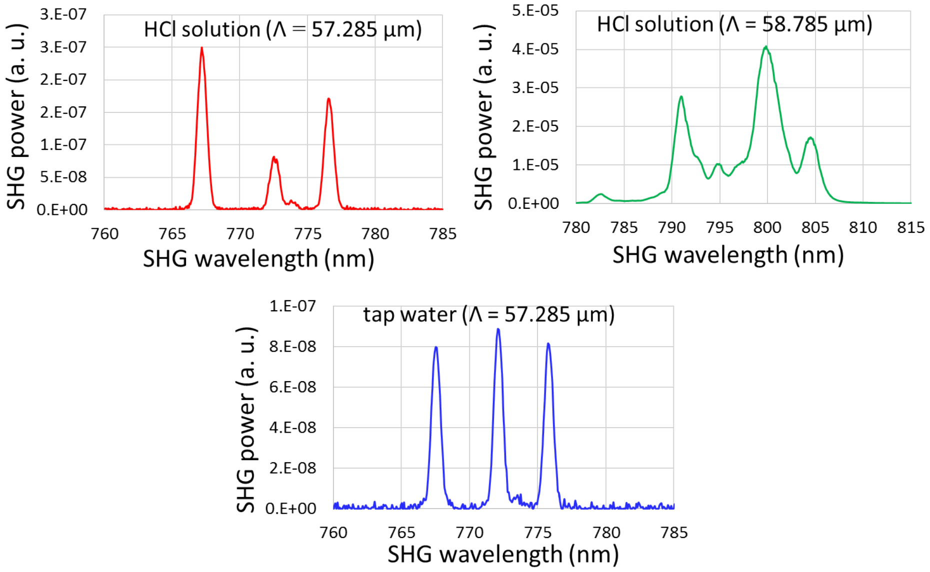

FIGURE 5.13: SHG output spectra of optical fibres poled using a HCl solution, as well as ordinary tap water, characterized using the setup shown in Fig. 5.1. Insertion loss at 1550 nm = 0.7 dB for water and 0.5 dB for HCl solution. The induced $\chi^{(2)}_{eff}$ for both aqueous solutions is estimated at $\leq$ 0.001 pm/V, assuming a fabricated device length of 20 cm and a modal overlap area of 49.43 μm^2 at 1550 nm pump wavelength. [164].

namely the two of samples poled with HCl solutions but erased with two different periods and one of the sample poled with tap water, erased with the same period of one of the two HCl samples. Each SHG spectrum consists of three peaks, corresponding to different combinations of the polarization states of the two pump photons producing the SHG. This degeneracy of the polarization is due to the birefringence of the fibre along the x and y axes, as already explained in section 5.1.1.3. The presence of the three peaks is due to the fact that the pulsed high-power pump used to characterize the samples poled using aqueous electrodes is not linearly polarized, so it always contains both components of polarization along the x and y axes. Nevertheless, the observation of distinct peaks at second-harmonic wavelengths corresponding to two different QPM grating periods that accurately follow the linear relationship expressed in Eq. (5.1) provide convincing evidence of the formation of an effective SON in these novel aqueous electrode PPSFs, which exhibit optical insertion losses (the average values of the insertion losses for HCl solution and tap water, over a number of samples (30 cm long plus the two 30 cm long SM980 fibres spliced) for each case, is respectively of 0.5 dB and 0.7 dB) lower than the metallic liquid electrode samples (the average values measured for gallium and mercury, is respectively of 1.7 dB and 1.2 dB). However, despite the potential improvement in nonlinear process efficiency conferred by this desirable characteristic, it comes at a cost, as the $\chi^{(2)}_{eff}$ values in the aqueous electrode samples is clearly inferior ($\leq\ 0.001\ pm/V$) to those with gallium and mercury (see values reported in table (5.1)). We believe this is due to higher resistivity of the electrolytic solutions compared with pure metals, thus potentially reducing the magnitude of electric field that can be frozen into the glass fibre which, in turn, leads to a decrease of the generated SON.

5.3 Applications of PPSFs poled with liquid electrodes

Some of the periodically poled samples (either the ones poled by means of gallium or mercury) have already become part of some experimental setups, with the aim of being exploited mainly as sources of SH. In the next sections the applications will be presented.

5.3.1 Phase matched parametric amplification via four-wave mixing in optical microfibres

The first application of my PPSFs, poled by means of liquid metallic electrodes, is the phase-matched parametric amplification of a certain wavelength via four-wave mixing (FWM) in an all-fibre setup including a high-power pulsed source and a PPSF producing both fundamental and second harmonic signals and an optical microfibre (OMF), where the FWM process actually happens [167].

FWM is a process in which four waves interact via the optical Kerr nonlinearity of a medium, where two photons from one or two “pump” waves (for instance at frequencies ω_1 and ω_2) are annihilated, and two new photons, called the signal (ω_3) and idler (ω_4), are created. One application of FWM is parametric amplification, where the power from one wavelength is transferred to another wavelength, which requires phase matching for efficient energy conversion in order to compensate for material and waveguide dispersion as well as nonlinear effects, often limiting the bandwidth of the process [52].

OMFs are designed from conventional fibres, mainly by heating a section of the fibre to the softening point and pulling it to reduce its diameter (flame brushing technique). By doing so, the optical core of the fibre gradually disappears, and the former cladding becomes the core, with air instead of the cladding. This allows for higher mode confinement, translating into an increased optical nonlinearity, which is a figure of merit, expressed by [168]:

$$\gamma = \frac{2\pi}{\lambda}\frac{n_2}{A_{eff}} \tag{5.18}$$

where λ is the wavelength of the pump, n_2 the material nonlinear refractive index and $A_{eff} = \pi\omega^2/4$ the beam effective area, where ω is the beam waist, which in the high confinement condition reaches its minimum value. γ can reach values of up to 100 times larger than a standard telecom SMF ($\gamma \approx\ 10^{-3}W^{-1}m^{-1}$), while, when OMFs are manufactured from highly nonlinear materials (such as lead silicate, bismuth silicate and chalcogenide glasses), γ can be up to five orders of magnitude larger than that of SMF [169]. Furthermore depending on the procedure used for tapering the fibre, it would be possible to reach relatively low losses which can be $< 1\ dB/m$ at $\lambda = 1550$ nm [168].

The phase matching and energy conservation conditions for efficient FWM, respectively, can be written as [167]:

$$\beta(\omega_4) + \beta(\omega_3) = \beta(\omega_1) + \beta(\omega_2) \tag{5.19}$$

$$\omega_1 + \omega_2 = \omega_3 + \omega_4 \tag{5.20}$$

where the subscripts 1, 2, 3, and 4 refer to the four interacting wavelengths and $\beta(\omega)$ is the propagation constant for frequency ω. It is worth highlighting that it is assumed that light at all wavelengths is propagating in the fundamental mode of the OMF as this would be the most efficient mode for FWM. In order to find the OMF diameter required to achieve phase matching condition expressed in the equation (5.19), the rigorous eigenvalue equations for a step index refractive index profile were solved for a silica OMF. The wavelengths employed are harmonics of the fundamental wavelength at 1550 nm, such that they automatically satisfy equation (5.20). Accounting for the two cases, namely the case of degenerate FWM ($\omega_1 = \omega_2$) and non-degenerate FWM ($\omega_1 \neq \omega_2$), and considering the the wavelengths of the fundamental frequency (FF), second harmonic (SH), third harmonic (TH), and fourth harmonic (FH), theoretically three different FWM schemes are considered, namely FWM between (a) FF, SH, and TH (degenerate); (b) FF, SH, TH, and FH (non-degenerate); and (c) SH, TH, and FH (degenerate).

Experimentally it was investigated only the (a) FWM scheme, with $\omega_1 = \omega_2 =$ SH, $\omega_3 =$ FF and $\omega_4 =$ TH. In Fig. 5.14 the relations between the OMF diameter and the mode propagation constants for the three different FWM schemes are reported.

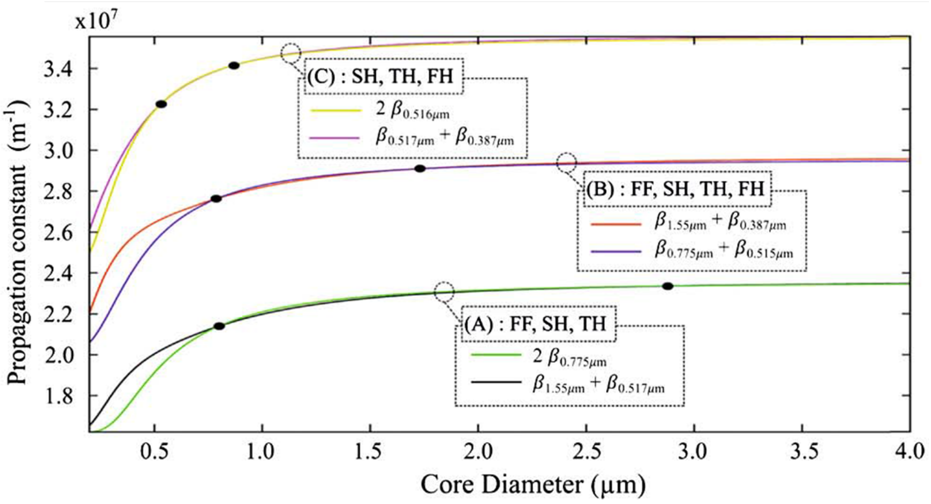

FIGURE 5.14: Relation between the OMF diameter and mode propagation constants for three different FWM schemes (simulations performed by M. I. A. Khudus); black dots represent phase matching diameters satisfying equation (5.19). FF, SH, TH and FH represent the fundamental frequency, the second harmonic (SH), the third harmonic (TH) and the fourth harmonic (FH), respectively [167].

From Fig. 5.14 it is clear that for each FWM scheme there are two phase matching diameters at which equation (5.19) is satisfied, so experimentally two different diameters at which FWM amplification is expected to occur in an OMF. These wavelengths are chosen primarily for experimental reasons, but the technique can be easily extended to any number of wavelength combinations satisfying the equation (5.20), as illustrated in Fig. 5.15 for the degenerate FWM. It can be seen that phase matching can be achieved for a wide range of pump wavelengths (λ_1) and for different values of signal wavelengths (λ_2). A plot of the dispersion of the microfibre is shown in Fig. 5.16 to indicate the change of the dispersion with OMF diameter.

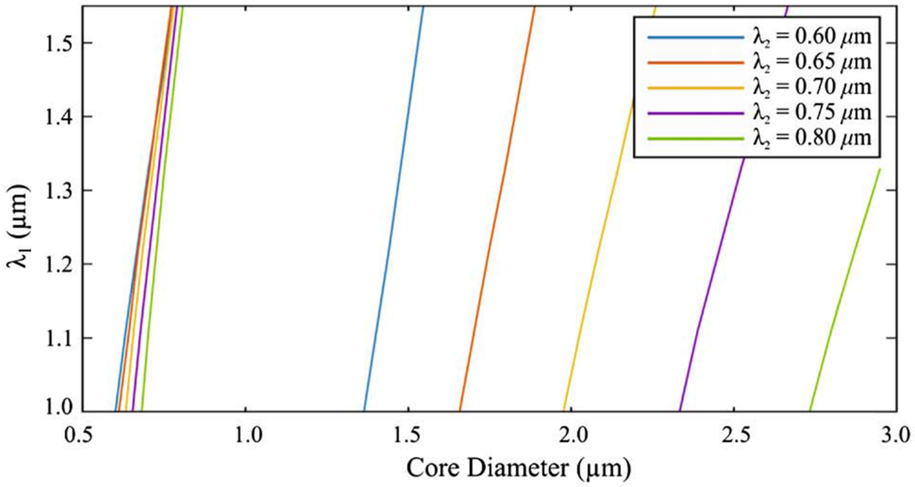

FIGURE 5.15: Degenerate FWM phase matched diameter for a set first pump wavelength, λ_1, and five different signal wavelengths, λ_2. The idler wavelength λ_3 can be calculated from $1/\lambda_3 = 1/\lambda_2 - 1/\lambda_1$. Two sets of phase matching diameters can be distinguished from the figure [167]. The simulations have been performed by M. I. A. Khudus.

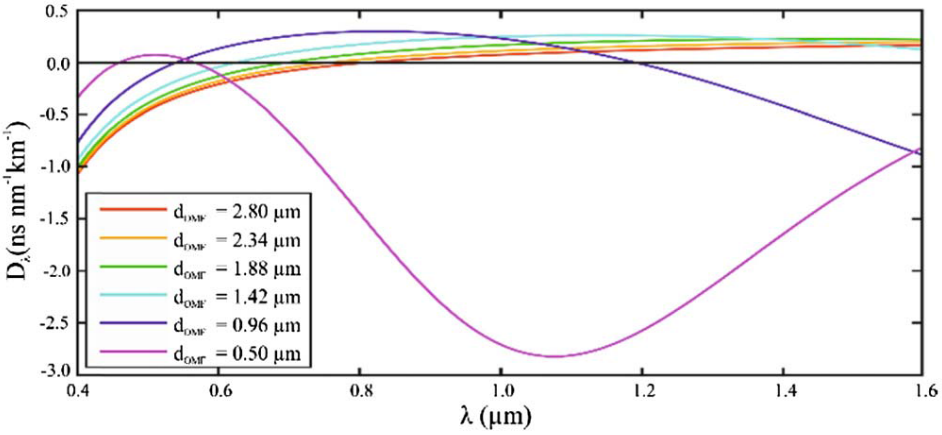

FIGURE 5.16: Variation in the dispersion of the OMF (D_λ) with wavelength λ for different OMF diameter (d_{OMF}), where it can be observed that the dispersion changes significantly for diameters $0.5\ \mu m < d_{OMF} < 1\ \mu m$ [167]. The simulations have been performed by M. I. A. Khudus.

In Fig. 5.17 the experimental setup implemented to investigate the enhancement of the idler signal in OMF is shown. The setup consists in narrowband continuous wave (CW) seed laser working in the telecom C-band wavelength region (1530 - 1565 nm), which seeds a master oscillator power amplifier (MOPA). The MOPA produces an output at a central wavelength of 1550.3 nm with a pulse width of 5 ns, repetition rate of 200 kHz, and average powers of between 300 and 800 mW, which translated into peak powers of between 300 and 800 W. The pulses are generated using an electro-optic modulator (EOM), which is then followed by an acousto-optic modulator (AOM) further along the chain to remove any inter-pulse amplified spontaneous emission (ASE) in the system to ensure that the majority of the power is contained in the pulse. Two fiberized thin film spectral filters operating in the C-band are also employed in order to improve the optical signal-to-noise ratio (OSNR) at the final output, required for an efficient SH generation. Polarization is managed by the use of two polarization controllers (PC) in the MOPA chain. The output of the MOPA was then connected to our periodically poled silica fibre (PPSF) designed to be quasi-phase matched (QPM) for efficient conversion of the FF at 1550.3 nm into the SH at 775.15 nm via SHG, which has a total insertion loss of < 0.5 dB. The PPSF is highly sensitive to polarization (as already explained in section 5.1.1.3), so the incoming polarization was controlled by two PCs before and after the fifth amplifier (Amp5 in Fig. 5.17). In order to have efficient SHG, a preliminary measurement of the QPM pump wavelength of the PPSF is realized directly connecting it to the first amplifier (Amp1) operating at a CW power of 30 mW and changing the wavelength from the tunable seed laser for maximizing the PPSF output signal of SH. Once the wavelength which produces the highest SH signal is determined, the central wavelengths of both the spectral filters are adjusted accordingly and the MOPA chain is reconnected.

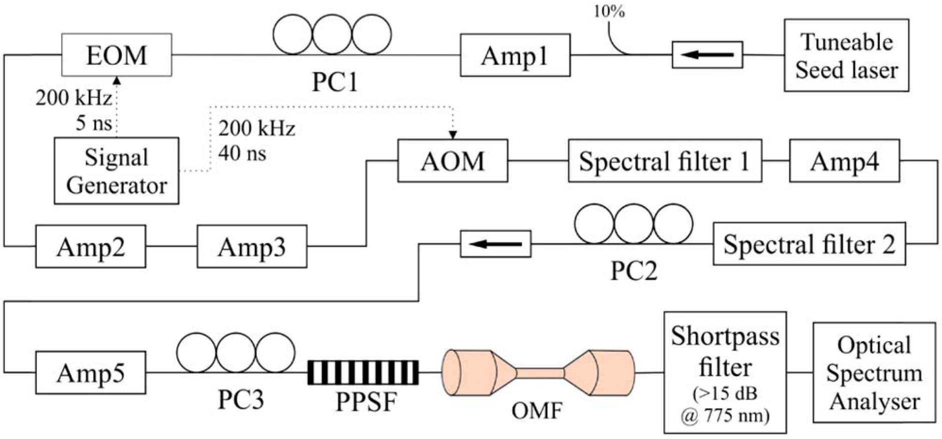

FIGURE 5.17: Schematic of the experimental setup used to investigate enhancement of the idler signal due to phase matching in the OMFs. Five amplifiers are employed in conjunction with two spectral filters in order to minimize OSNR and inter-pulse ASE. Here, PPSF is a periodically poled silica fibre; PC is a polarization controller [167].

The output power of the MOPA is then fixed at a value of 300 mW, in order to avoid pump depletion and any other undesirable nonlinear effects. At this power level, the OSNR of the MOPA output is bigger than 50 dB, suitable for a relatively efficient SHG, producing an average output power of more than 3 mW at 775 nm. This resulted in both the FF and SH wavelengths existing at the output end of the PPSF.

A byproduct of the SHG process, however, is the generation of a signal at the TH wavelength via non-phase-matched sum frequency generation (SFG), where $\omega_3 = \omega_1 + \omega_2$. The efficiency of this process is very small ($\eta \approx 10^{-9}$), because the PPSF is optimized for SHG and not for the TH wavelength, but it is big enough to provide a seed laser with which parametric amplification can occur. The simultaneous generation of the SH and TH wavelengths, in addition to the FF wavelength, allows for the frequency requirement for parametric amplification via degenerate FWM (scheme (A) in Fig. 5.14) in correspondence of two diameters of the OMF ($d_1 = 2.886\ \mu m$ and $d_2 = 0.8\ \mu m$) to be automatically satisfied. This is enhanced as the FF, SH, and TH are co-polarized and overlap spatially, both of which are a consequence of the SHG and SFG processes in the PPSF. Very long pulses were employed in order to eliminate walk-off effects (not compensated in the PPSF). The resulting output spectrum from the PPSF which has been passed through a shortpass filter before tapering is given in Fig. 5.18.

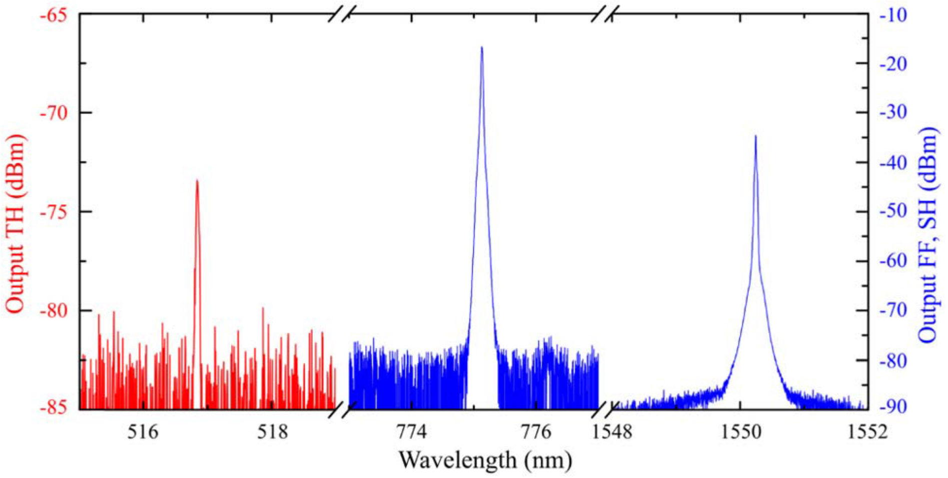

FIGURE 5.18: Initial output signal from the PPSF after a shortpass filter. The loss of the filter is wavelength dependent, with longer wavelengths registering higher losses, causing the signal at FF (1550.3 nm) to appear smaller than the SH (775.15 nm), both shown here in blue. The idler signal (516.75 nm), shown in red, is relatively small and is just above the noise level. This is the signal that will be amplified by the OMF, as shown in Fig. 5.19 [167]. The measurement has been realized in collaboration with M. I. A. Khudus.

The output from the PPSF was then spliced to a length of Z fibre (Sumitomo Electric) before being connected with a shortpass filter, designed to have a loss of more than 15 dB at 775 nm, and a broadband OSA (Yokogawa AQ6315A). The Z fibre is then tapered by using the modified flame brushing technique, which employs a microheater, with the tapering profile being carefully controlled in order to satisfy the adiabaticity criteria thereby minimizing loss [170]. A length of 6 mm of the Z fibre was tapered, from an initial diameter of 125 μm to a final diameter of 0.5 μm, in order to fully explore the entire range of the predicted phase matching diameters. At the end of the tapering process, the OMF has a full length of approximately 29 mm, with a waist length of 6 mm and a waist diameter of 0.5 μm. The 1.55 μm MOPA source, connected to the PPSF, was launched into the fibre whist being tapered. The temporal evolution of the output spectra at the peak of the idler wavelength (516.7 nm) was recorded with the OSA as shown in Fig. 5.19. A resolution of 10 nm was employed to capture all the generated signal power.

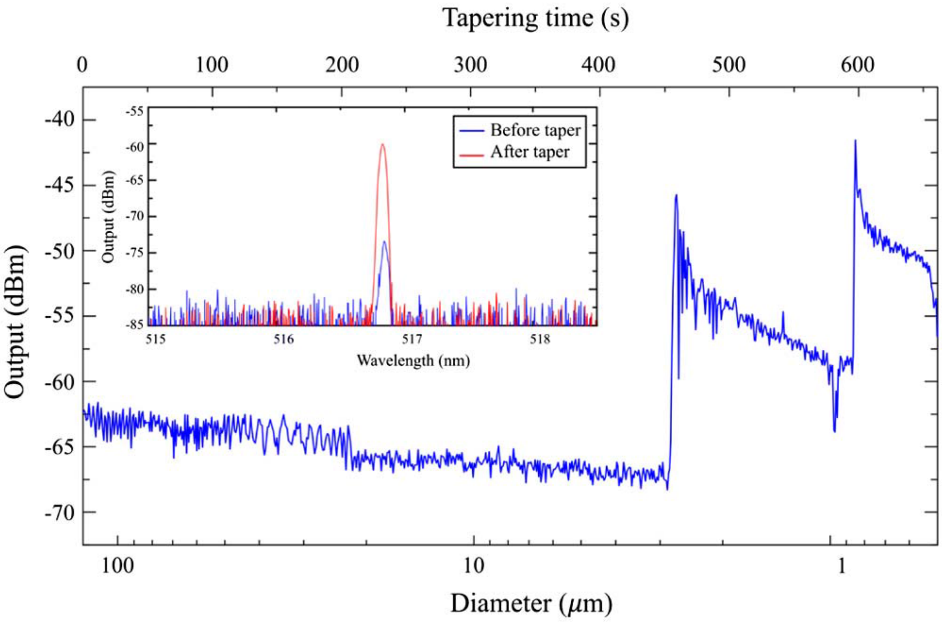

FIGURE 5.19: Evolution of the idler signal at 516.75 nm with respect to the diameter (logarithmic) and the processing time (linear) during tapering. Inset: the idler signal before and after the tapering process. The data in the inset was measured with a resolution of 0.05 nm and a higher sensitivity, as compared to 10 nm and a lower sensitivity for the main figure, resulting in the apparent discrepancy in the initial power measurement [167]. The measurement has been performed in collaboration with M. I. A. Khudus.

Initially, there is a very small signal at the idler wavelength, as explained above. This signal does not vary significantly as tapering takes place initially, with the small variation being accounted for by the tapering process itself as well as the thermal drift of the PPSF. As the OMF diameter reaches the first phase matching diameter ($d_1 \approx 2.886\ \mu m$), the output intensity increases by more than 22 dB. The signal then decreases as the fibre is tapered further, as the tapering process reduces the OMF length at which the phase matching diameter occurs, although, due to the increasing overall length of the microfibre there is a time-varying range of diameters in the OMF transition region which are phase matched and nearly phase matched, resulting in a gradual decrease in the signal. This downward trend is observed until the fibre reaches the second phase matching diameter ($d_1 \approx 0.8\ \mu m$), where the signal increases dramatically by approximately 15 dB, reaching the highest recorded output power. As the fibre is tapered even more, the signal monotonically decreases until the tapering process stops at a diameter of 0.5 μm. The slight drop in intensity observed at t = 580 s at the end of the tapering process is due to the OMF moving inside the microheater and approaching its walls. Additionally, at the end of processing, there are changes in the effective refractive index associated with temperature changes as the taper is taken out of the microheater. The inset in Fig 5.19 shows the 12 dB increase in idler output between the untapered fibre and the OMF with the 0.5 μm diameter. Fig. 5.19 indicates that if the tapering process is stopped at an OMF with a length of 6 mm and waist of approximately 800 nm, a total maximum enhancement of more than 20 dB from the original signal can be achieved, with the figure being closer to 25 dB if we use the output intensity at 5 μm as a baseline.

The final efficiency was increased from $\eta \approx 10^{-9}$ to $\eta \approx 10^{-7}$, corresponding to a parametric gain of 25 dB or 4.17 dB/mm, by using this method. This is very low compared to devices such as semiconductor optical amplifiers, where FWM efficiencies in excess of 20 dB are possible [171], but is comparable to other parametric amplifiers and is able to potentially operate across the entire optical bandwidth. The final efficiency can be improved by increasing the pump-to-signal ratio, while the overall parametric gain can be improved by the fabrication of a longer OMF and by increasing the efficiency of the SHG, which means increasing the value of $\chi^{(2)}_{eff}$ induced in the PPSF and/or increasing its length.

In conclusion the work of Khudus *et al.* of 2016, where my PPSF, optically pumped at a wavelength of ≈ 1550 nm, is used as source of second harmonic, demonstrates the possibility of using OMFs for FWM parametric amplification over a wavelength band of over 1000 nm by exploiting the tailorable dispersion characteristics of the

OMF to optimize the diameter for phase matching. The technique developed theoretically allows for the amplification and generation of an almost arbitrary set of wavelengths, as well as the possibility of building fully fiberized light sources in the ultraviolet (UV) and mid-infrared (mid-IR) wavelength ranges.

5.3.2 Sources of high order harmonics in optical microfibres

Harmonic generation involves the generation of new frequencies which are multiples of a fundamental frequency (FF) via nonlinear processes. Typically, harmonic generation is achieved by using a variety of nonlinear crystals where second/-fourth harmonic generation (SHG/FHG) is typically done by employing one/two second-harmonic-generating nonlinear crystals and third/fifth harmonic generation (THG/5HG) is obtained by sum frequency generation between the fundamental/third harmonic frequency and the second harmonic frequency [172]. These methods allow for the generation of wavelengths inaccessible by conventional laser technology, and have widespread applications such as for example fibre Bragg grating inscription and microscopy [173, 174].

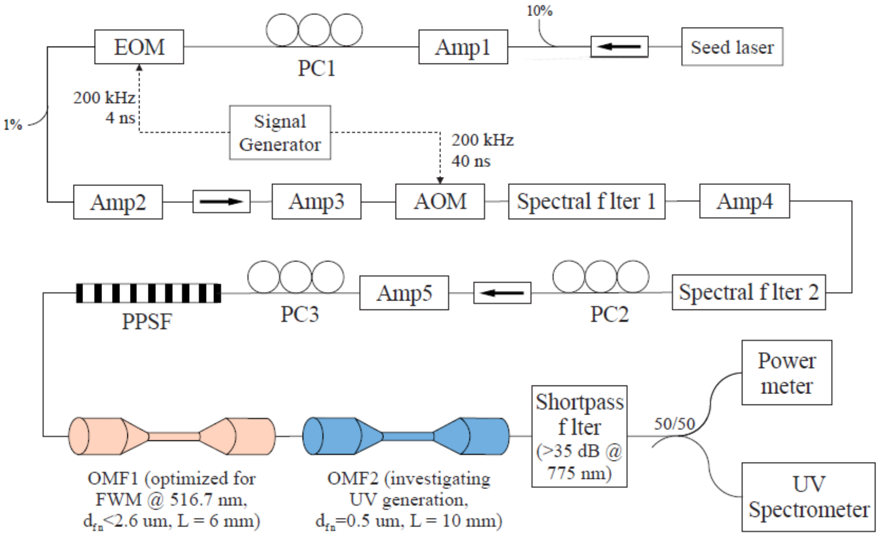

FIGURE 5.20: Experimental setup for UV generation in OMFs. Five amplifiers were employed in the MOPA chain with the pulses carved by an electro-optic modulator (EOM) and an acoustic optical modulator (AOM). Two spectral filters were employed in order to allow for an OSNR of more than 40 dB at the output. The polarization in the chain is managed by three polarization controllers (PC). PPSF designates the periodically poled silica fibre [55].

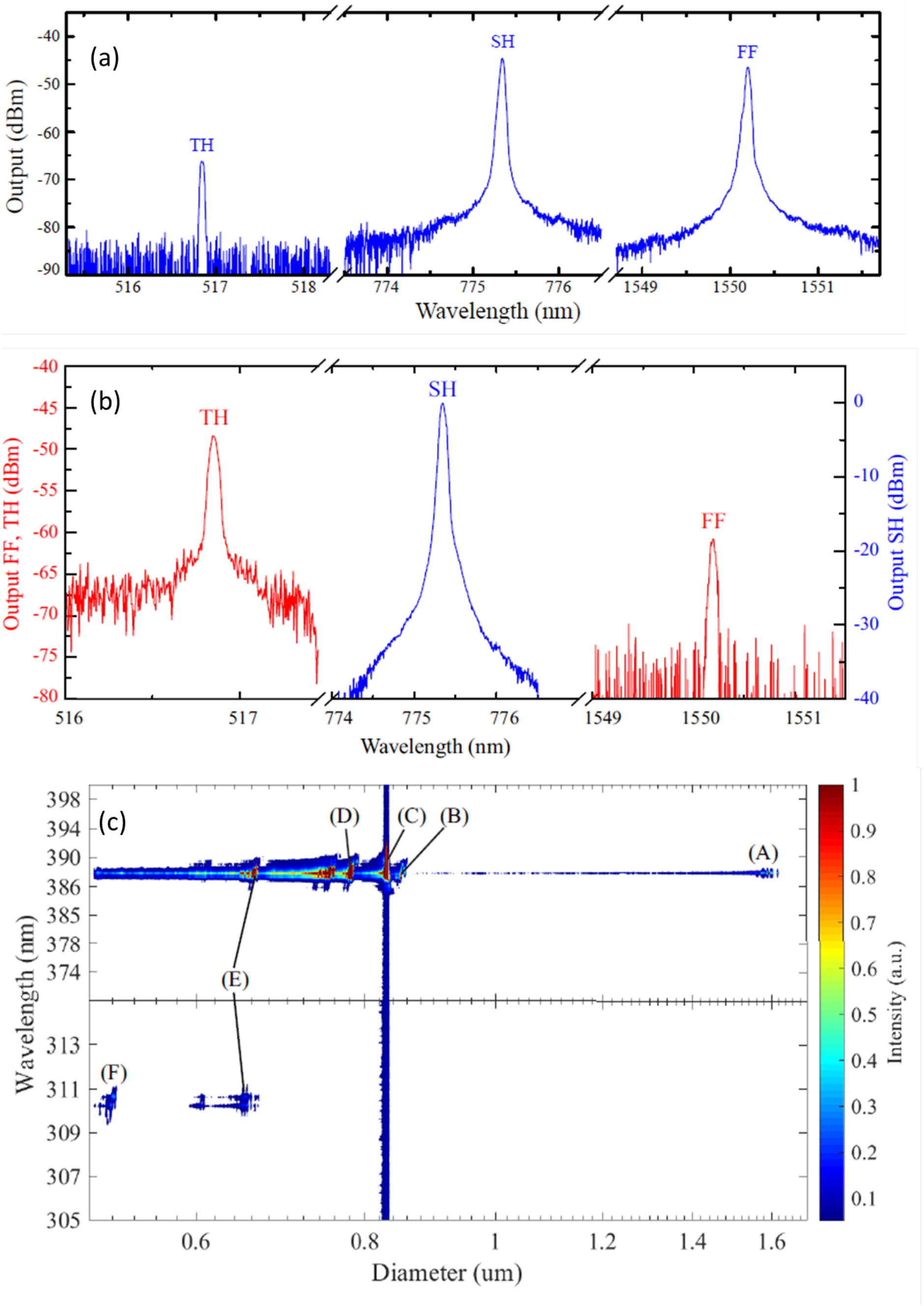

Figure 5.21: (a) Typical output spectrum after SHG from the PPSF which is spliced to a shortpass filter with losses of $> 40\ dB$ and $> 70\ dB$ at the SH and FF wavelengths, respectively; (b) Output spectrum from the OMF1 after a shortpass filter designed to remove radiation at 1.55 μm. The signal at the third harmonic wavelength (0.517 μm) has been enhanced by the parametric amplification in OMF1 to more than -50 dBm from an initial value of approximately -65 dBm; (c) Output spectrum from the OMF2 after a shortpass filter designed to attenuate the FF, SH and TH wavelengths. The detector is sensitive to visible light, which manifests as a broadband background signal which varies slightly as the OMF is tapered. Tests with higher powers at the SH and TH indicate that the signals at the SH and TH do not appear as narrowband radiation. (A)-(F) represent the FH and 5H signals [55]. The measurements have been realized by M. I. A. Khudus.

In the work of Khudus *et al.* of 2016 [55] all-fiberized FHG and 5HG from a single fiberized Erbium doped fibre source is demonstrated via a combination of QPM SHG (generated in one of our PPSF poled by means of metallic liquid electrodes) and phase-matched FWM (produced inside two OMFs). All-fiberized FHG and 5HG is achieved using cascaded nonlinear processes including SHG, THG and FWM. Firstly, a high power pulsed near-IR MOPA source is employed in conjunction with a PPSF for SHG. The TH wavelength generated as a non-phase matched byproduct of the SHG is parametrically amplified by an OMF with a specific phase matching diameter (PMD) [167]. These three wavelengths are then employed in another OMF to allow for FHG and 5HG via FWM. The theoretical approach of this experiment is exactly the same of the previous one, represented mainly by the fact that the efficient FWM requires phase matching conditions and energy conservation to be fulfilled (see equations (5.19) and (5.20)).

The experimental setup implemented to demonstrate the FHG and 5HG is shown in Fig. 5.20 and it is identical to the one implemented for the parametric amplification experiment via FWM in OMF (shown in Fig. 5.17), apart from the presence of two OMFs instead of one. The role of the OMF1 is to boost the power of the TH wavelength.

After tapering the OMF1 to a diameter which fulfilled the PM condition but also allowed the OMF1 to boost as much as possible the power of the TH wavelength without any transfer of energy to the FH, a section of the Z-fibre located between the OMF1 and the shortpass filter was tapered in order to create the second microfibre (OMF2), the one where FH and 5H are created. In Fig. 5.21 the three spectra recored after the shortpass filter spliced respectively to the PPSF, the OMF1 and the OMF2.

5.4 Conclusions

This chapter presents the experimental realization of periodically poled silica fibres via a process of UV erasure of the nonlinearity created inside the fibre by thermal poling. The experimental measurement of the SHG in optical fibres poled by the electrostatic induction technique is reported together with an estimation of the effective second order nonlinear susceptibility generated in optical fibres poled with different liquid electrodes used in cathodeless configuration. A maximum value of 0.12 pm/V has been obtained in twin-hole fused silica samples poled with mercury used as electrode. The transmission losses of fibres poled with different liquids have been also evaluated and electrolytic solutions have been identified as the best materials from the perspective of the losses reduction. Two applications have been also presented, namely the phase matched parametric amplification of light via four-wave mixing in optical microfibres and the generation of high order harmonics (namely FH and 5H).

Chapter 6

Functionalisation of microstructured optical fibres via deposition of semiconductors

6.1 Enhancement of SON in optical fibres

The use of liquid electrodes, discussed in chapters 4 and 5, allows potentially for poling optical fibres of any length (within the restrictions imposed by the periodical erasure of the induced nonlinearity by means of its exposure to UV light, such as the build-up of fabrication errors which scale with grating length), consequently increasing the efficiency of the nonlinear phenomena related to the induced SON (see, for example, the equation (2.60) for SHG). In any case the value of $\chi^{(2)}_{eff}$ created by thermal poling is defined by the intrinsic value of $\chi^{(3)}$ of the fibre's core and by the maximum value of the electric field E_{dc} which can be frozen into the fibre via thermal poling and related to the dielectric strength of the glass which the fibre is made of.

From the last considerations came two ideas to enhance the SON in optical fibres, based on the purpose of exploiting the intrinsic nonlinear properties of some materials (such as for example semiconductors or 2D-materials). The first idea consists of exploiting a step-index optical fibre whose core is made of a material characterized by a value of $\chi^{(3)}$ higher than silica, with the final aim of enhancing the effect of thermal poling (see equation (2.69)). A first chance in this sense could be represented by an optical fibre made of a type of glass possessing a value of $\chi^{(3)}$ bigger than the typical value of silica glass ($\approx 10^{-22}\ m^2/V^2$ [121–124]). It is known from literature that some glasses, belonging to the wide category defined as soft glasses (generically characterized by a softening temperature smaller than silica), show a value of $\chi^{(3)}$ bigger than silica. For example chalcogenide glasses have been found to possess a nonlinear refractive index n_2 (and consequently a third order nonlinear susceptibility $\chi^{(3)}$ (real part) [175]) $\approx$ 100 - 1000 times higher than silica [176]. Another type of soft glasses possessing a $\chi^{(3)}$ value higher ($\approx$ 10 times [177]) than silica is tellurite glass. The reason of this increased third order nonlinear susceptibility lies in their polarizability higher than silica [176]. A semiempirical relation (defined Miller's generalized rule) between $\chi^{(3)}$ and n_o (the linear refractive index of the glass) was described by Tichá *et al.* in 2002, which details the higher nonlinear susceptibility of chalcogenides glasses [178]:

$$\chi^{(3)} = \frac{A}{(4\pi)^4}(n_o^2 - 1)^4 \tag{6.1}$$

where A is a constant which is tabulated for some ionic crystals.

The early attempts of thermal poling of soft glasses have been realized by Carlson *et al.* in the 1970s and concerned alkali-containing glasses. It was demonstrated for the first time the possibility of polarizing a glass thanks to a process of dissociation of the alkali oxides contained in the glass matrix, followed by the displacement of the dissociated ions [179]. The main issue related to alkali-ion rich glasses is that the value of $\chi^{(3)}$ is comparable to the silica, if not smaller [180], which makes them uninteresting for our final purpose of increasing the induced $\chi^{(2)}_{eff}$. Furthermore it was observed a fast decay of the SHG efficiency at least in two categories of alkali-ion rich glasses, such as borosilicate and soda-lime [181].

Later some experiments of thermal poling were realized on chalcogenide bulk glasses, producing as best result an induced $\chi^{(2)}_{eff}$ of 8 pm/V [182], 8 times higher than the value obtained by Myers *et al.* in 1991 for fused silica [10]. However, it has been clearly demonstrated that even for poled chalcogenide materials the critical point concerns the stability in time of their second order optical response. It seems that this issue is related to their high photosensitivity which generates, during their illumination, a rearrangement of the glass matrix which can compete with the structural disposition created by means of thermal poling [183]. In 2007 Zeghlache *et al.*, after thermally poling a sulfide chalcogenide glass, observed, during the Maker's fringes measurements, a decay of the SH signal, implying a time-dependent second order susceptibility [184]. Besides the SH signal decay observed after few hours of exposure to the pump light of the Maker's fringes system (pulses of 10 ns of duration, 30 KW of peak power and 1.9 μm of wavelength, produced by an OPO pumped by a Nd:YAG pulsed laser operating at 532 nm and 10 Hz repetition rate), it has been observed even a progressive decay of the nonlinearity which depends on the time elapsed between the poling date and the characterization date. Because of these drawbacks related to the temporal stability of the SON induced by thermal poling, the idea of using soft glass optical fibres was not explored at all during my PhD path, in favour of the exploitation of other types of nonlinear materials. Instead, step-index optical fibres with core made of semiconductor materials characterized by an intrinsic $\chi^{(3)}$ higher than silica, always with the aim of using the equation (2.69) to enhance the SON, represent a possibility which has been explored in the thesis and will be presented later in this chapter.

The second idea to enhance the SON in optical fibres consists in the usage of step-index optical fibres with a core made of a material characterized by an intrinsic $\chi^{(2)}$ to be exploited on its own or to be added to the SON induced by thermal poling. This second idea has been initially explored during my PhD path and will be exhaustively described in the next sections.

After the presentation of the experimental and theoretical work, it will be clear that the method initially chosen to functionalise optical fibres presents too many practical and even theoretical issues to be fully pursued, and a new approach will be conceived, based on the idea of depositing thin layers of intrinsic nonlinear materials in the cladding holes of step-index twin-hole fibres (see Fig. 6.10), with the aim of observing eventual nonlinear effects on the evanescent field of the guided mode. An even more advanced approach is based on the deposition of thin layers of intrinsic nonlinear materials in Hollow-Core MOFs (see Fig. 6.15 (a)), with the aim of merging the particular guidance properties of the MOFs with two types of functions, namely a nonlinear optical function and an electronic function (linked to the deposition of semiconductors or 2D materials). The early experimental and theoretical results will be presented in this chapter as well, while in chapter 7 new future perspectives, related to this topic, will be explained in more details.

6.1.1 HPCVD for creation of semiconductor core step-index fibre

As already explained in section 6.1, the first approach chosen to functionalise optical fibres by means of the exploitation of intrinsic nonlinear materials requires the creation of a step-index fibre characterized by a core made of a material different from silica, such as for example Silicon, Germanium, or Zinc Selenide. Among these three possibilities only two (Si and ZnSe) have been studied in this thesis work. The fibre adopted for this scope is the three-hole fused silica fibre already presented in section 3.2.1 and shown in Fig. 3.3, while the technique used to create the semiconductor core is the HPCVD, invented by Sazio *et al.* in 2006 [20].

HPCVD is a hybrid technology which integrates the deposition of semiconductors and metals from chemical precursors, already developed for planar substrates (with important applications in microelectronics), and optical fibres, that are an established platform for both communications technology and fundamental research in photonics [20]. The technique was exploited initially to chemically deposit semiconductors and metals inside the pores of MOFs, such as the ones represented in Fig. 2.4, while in our case it has been used to deposit the same kind of materials inside the hollow core of the fibre shown in Fig. 3.3. It is worth highlighting that the high pressures of the gaseous precursors used ($2\ to > 100\ MPa$), well tolerated by the high tensile strength of an optical fibre ($5\ to\ 15\ GPa$) [185], allow for overcoming the experimental issues related to the mass transport of the reactants into and by-products out of such a confined space, which would be very slow using traditional techniques [20]. Each pore of a MOF can be seen as a miniature chemical reactor into which various chemical precursors can be introduced, in such a way that uniform, dense, and conformal annular deposition onto the heated pore walls over lengths of centimetres to metres becomes possible. Furthermore HPCVD allows for precisely doped, void-free wires of unary semiconductors and nearly void-free wires of compound semiconductors to be formed both in single capillaries and in patterned arrays [186]. It can also be adapted for metals, which can form coaxial heterojunctions, by the appropriate choice of precursor chemistry. It now appears that it should be possible to integrate most, if not nearly all, of the materials deposited by conventional CVD into optical fibres by means of suitable adaptation or development of the precursor chemistry that has been already demonstrated for planar substrates. Although fibre HPCVD appears to not be as scaleable to lengths as long as those that can be fabricated by drawing, semiconductor layers 10 m in length have been realized, and there are prospects for longer lengths [187]. Moreover, HPCVD is scaleable to deposition in multiple fibres from the same high-pressure precursor reservoir, potentially allowing parallel fabrication of tens to hundreds of fibre devices. In Fig. 6.1 the general schematic of the HPCVD and an image of a crystalline silicon core, deposited by HPCVD inside a silica capillary, are reported.

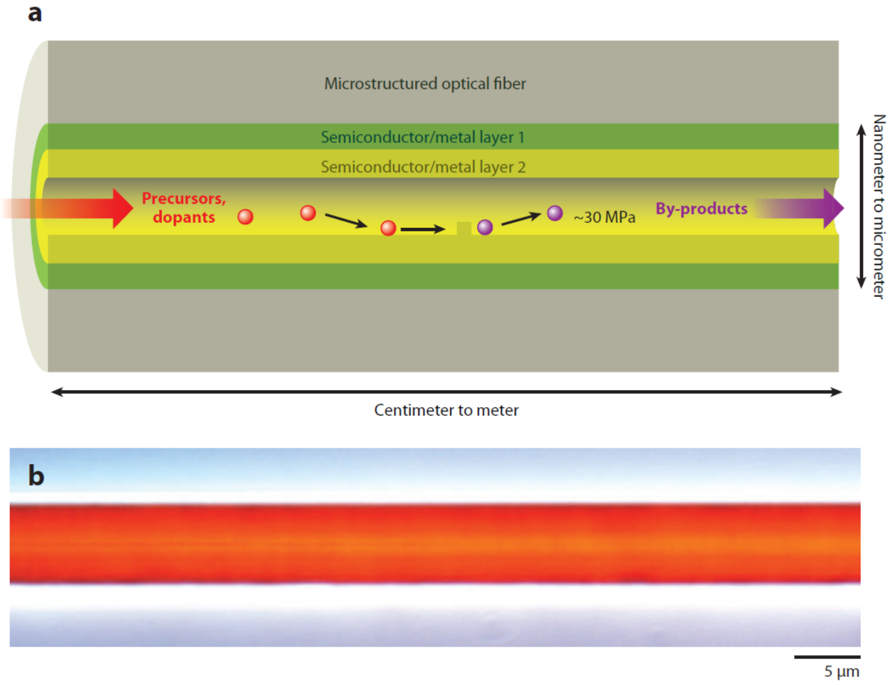

Figure 6.1: (a) Schematic of the high-pressure chemical vapour deposition (HPCVD) process; (b) diascopically illuminated optical micrograph of a 6 μm diameter crystalline silicon fibre core surrounded by silica cladding fabricated by HPCVD. Index-matching fluid removed the cylindrical lensing effect of the exterior surface of the silica cladding. The core is reddish-orange and transparent because it was crystallized by annealing [186].

To perform HPCVD in optical fibres, an appropriate chemical precursor (or precursors) has to be chosen. These precursors are introduced, often with a carrier gas such as helium, into a reservoir at high pressure. The precursors can be introduced into the reservoir either by cryogenic condensation, if their condensation temperatures are high enough, or by means of a suitable high-pressure pump. Once the precursor and carrier mixture are loaded into the reservoir, the fibre is attached to it and evacuated. Then, by opening the valve, the high-pressure precursor flows down the fibre pores (see Fig. 6.1 (a)). Upon heating the fibre with a furnace, reaction occurs to deposit layers and wires within its pores [186].

In the case of the silicon deposition (both crystalline and amorphous), the precursor is the Silane (SiH_4), which evolves to silicon through a complex series of reactions. Nevertheless, some generalizations can be made in such a way the whole process can be seen as made by a two steps reaction. The first step happens in the gas phase, and consists in the pyrolysis of Silane [188, 189]:

$$SiH_4(g) \rightarrow SiH_2(g) + H_2(g) \tag{6.2}$$

where SiH_2 is Silylene. The Silylene intermediate can react with SiH_4 and other species in a complex series of reactions that lead to solid silicon [189, 190] with hydrogen as the only byproduct. Because of the ability of hydrogen to diffuse readily through the silica, HPCVD allows for filling extreme-aspect-ratio pores to form void-free silicon and germanium optical fibre cores micrometres in diameter and centimetres long [191].

6.1.2 HPCVD semiconductor optical fibre materials

Focusing our attention only to deposition in optical fibres, HPCVD allows for creating three different types of materials, according to the choice of some experimental parameters characterizing the deposition process, which are hydrogenated amorphous silicon (a-Si:H), crystalline unary semiconductor and crystalline compound semiconductor. In the next three sections they will be briefly described in relationship to their deposition process, morphological and structural features and even nonlinear properties.

6.1.2.1 Hydrogenated amorphous silicon fibres

Pure amorphous silicon is not useful for most electronic and photonic applications because of electronic defects associated with dangling bonds [192]. Incorporation of hydrogen into amorphous silicon can passivate these defects, allowing for useful photonic and electronic properties. The acceleration of the reaction kinetics for the decomposition of pure SiH_4 in HPCVD allows for considerable reduction of the deposition temperature down to values of $\approx\ 350-400$ °C [190]. At these reduced reaction temperatures, hydrogenated amorphous silicon can be deposited as void-free, well-developed fibre cores. Hydrogenated germanium can be deposited in optical fibres as well [193]. The photonic and electronic properties of hydrogenated amorphous silicon can vary considerably, depending on the deposition conditions [192], while the quite high refractive index (of ≈ 3.5 *at* 1550 *nm*) results in very tight mode confinement such that they can be scaled to submicrometre dimensions (for example by means of a tapering process) [186].

The losses of a-Si:H core capillaries have been evaluated by Mehta *et al.* in a work of 2010, where a value of $\approx 3\ dB/cm$ was measured for a 5.6 μm silica capillary deposited by HPCVD. The deposition of the amorphous material occurred over a relatively low temperature range of 360 - 440 °C [194].

From our perspective, which is focused on the exploitation of the intrinsic nonlinearities of a semiconductor core step-index fibre, the most relevant aspect to highlight of the a-Si:H is represented by its enhanced nonlinear properties (even if compared to its crystalline form), such as for example the nonlinear coefficient (see equation (5.18)) based on the Kerr index, which was found to be at least 5 times bigger than the one measured for crystalline silicon [195]. If compared to the intrinsic third-order nonlinear susceptibility ($\chi^3(-\omega; \omega, 0, 0)$) of silica, whose value was estimated (via a measurement of the Kerr effect) to be of $\approx 2 \times 10^{-22}\ m^2/V^2$ [196], the value of $\chi^3(-\omega; \omega, 0, 0)$ measured for a-Si:H is $\approx$ 1000 times higher [197] at wavelengths near the telecom regime (1550 nm).

To date, a number of important photonic functions have been demonstrated in a-Si:H waveguides on-chip including all-optical modulation, photon pair generation, and parametric amplification. The ability to incorporate silicon materials into the optical fibre geometry not only provides a route towards integrating such devices within existing fibre networks, but also opens up the potential for the waveguiding properties of the devices to be manipulated in ways not possible on-chip [198].

6.1.2.2 Crystalline unary semiconductor fibres

In 2006 Sazio *et al.* reported for the first time the fabrication of high-quality polycrystalline and single-crystal semiconductors within the voids of MOFs by HPCVD [20]. Typically, the germanium precursor GeH_4 flows through the heated MOF at a partial pressure of 2 MPa, along with an inert carrier gas. It is worth highlighting that high pressures and toxic precursors are safe and practical because the pressure reservoir and the fibre pores have a very small volume. A smooth layer of amorphous germanium begins to deposit on the pore walls as the temperature is ramped up past 300 °C. Crystalline grains will nucleate and grow if the temperature exceeds the crystallization point of ≈ 375 °C [20]. Something similar happens with silicon as well. The losses at 1550 nm measured for an isolated silicon core correspond to a value of $\approx 7\ dB/cm$.

6.1.2.3 Crystalline compound semiconductor fibres

A typical example of crystalline compound semiconductor which can be deposited by HPCVD in a silica capillary is ZnSe, which is a good candidate to be exploited for nonlinear optical frequency conversion because it displays particularly high nonlinear 2nd-order susceptibilities (≈ 30 pm/V [199])[200]. An issue affecting the possibility of depositing ZnSe via HPCVD is the fact that typical gaseous precursors used for deposition of ZnSe in conventional CVD would prereact at room temperature due to the high pressures used in HPCVD [186]. This drawback can be overcome by adopting some organometallic precursors, such as for example $(CH_3)_2Se$ and $(CH_3)_2Zn$, which do not prereact at room temperature and allow to form ZnSe at high temperature via this series of three chemical reactions:

$$(CH_3)_2Zn(g) + H_2(g) \rightarrow Zn(g) + 2CH_4(g) \tag{6.3}$$

$$(CH_3)_2Se(g) + 2H_2(g) \rightarrow H_2Se(g) + 2CH_4(g) \tag{6.4}$$

$$Zn(g) + H_2Se(g) \rightarrow ZnSe(s) + 2H_2(g) \tag{6.5}$$

The by-product of this series of reactions is CH_4, which cannot leave by diffusion through the silica capillary walls (such it happens for H_2 in deposition of a-Si:H). For this reason, completely void-free filling of fibre pores with ZnSe appears to be a challenge. This drawback, which could be partially solved by means of post process techniques (such as for example pressure cycling techniques that successively infiltrate and remove a ZnSe precursor reaction mixture [201]), if not solved would prevent from the possibility of creating step-index ZnSe core fibres. The optical losses of ZnSe fibres are in the range of 0.5 to 1 dB/cm in correspondence of near-infrared wavelengths, with fibre cores ranging from 15 to 50 μm in diameter. The wavelength dependence of the optical loss (λ^{-3}) suggests that the dominant loss mechanism is grain-boundary or other bulk inhomogeneity scattering rather than surface scattering [201].

6.1.3 Measurement of transmission losses of semiconductor core step-index fibres

Before any attempt of exploiting the nonlinear properties of semiconductor core step-index fibres created by means of HPCVD, eventually even added to the SON induced by thermal poling, a preliminary and purely experimental study has been realized with the aim of measuring the transmission losses of the available samples. Two types of samples have been characterized, namely a-Si:H and ZnSe, both deposited inside the 9 μm core of a fused silica THF (see Fig. 3.3) by the group of Prof. J. V. Badding in Penn State University. For the characterization process our attention has been focused only onto the parts of these samples completely filled with semiconductor.

Because of the very short length of these samples (usually less than 1 cm), the technique chosen to measure linear losses of deposited semiconductor MOFs is the single pass method (see Fig. 6.2). In order to estimate transmission losses by means of this method, it is worth distinguishing the different contributions to total losses in order to isolate the contribution coming from transmission losses. These other contributions consist in losses introduced by the presence of the optical system, the Fresnel losses due to the reflection of light at the two interfaces between the fibre and the air, and the losses due to scattering phenomena of light at the interfaces.

The attenuation of the fibre due to the transmission losses is given by:

$$\alpha\left(\frac{dB}{cm}\right) = -\frac{10}{L}\log_{10}\left(\frac{P_2}{P_{in}}\right) \tag{6.6}$$

where L is the sample length, P_2 is the radiation power measured after MO_2 (see Fig. 6.2), and P_{in} is given by the following formula:

$$P_{in} = P_1\left[(1-R^2)\left(\frac{P_2'}{P_1'}\right)\right] \tag{6.7}$$

where P_1 is the power measured before MO_1, P_2' and P_1' are respectively the powers measured after MO_2 and before MO_1 when the sample is removed and MO_2 is

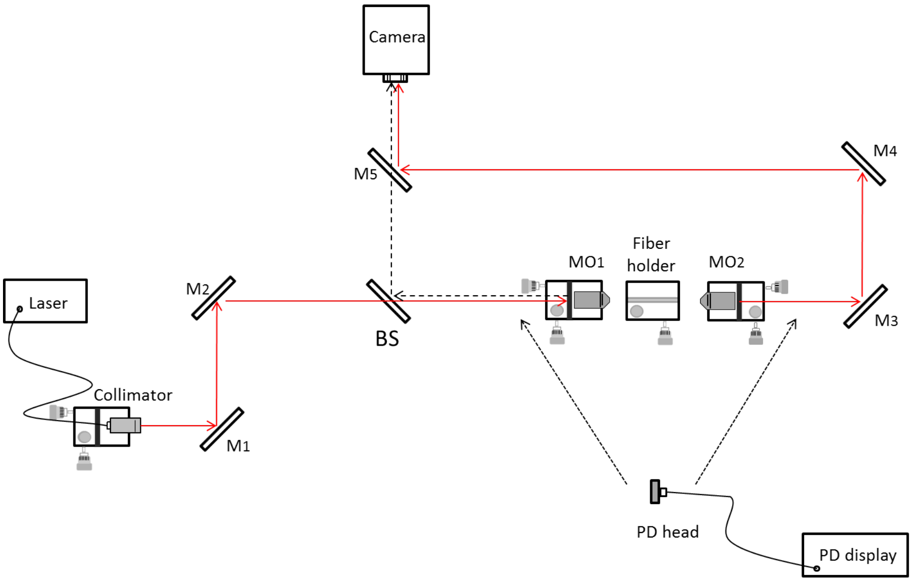

FIGURE 6.2: Schematic of the setup used to characterize deposited semiconductor samples in terms of linear transmission losses. M_i are mirrors, MO_1 is an aspheric lens (f = 1.49 mm, ⌀ = 6.25 mm, NA = 0.53, IR coating) and MO_2 is a microscope objective (5x), which are used respectively to launch light into the sample and collect it from the sample (the sample lies on top of the translation stage located between MO_1 and MO_2), BS is a beam splitter used to collect the radiation reflected by the first edge of the sample. The light which travels towards the sample is represented by the red line, the radiation back-reflected by the first surface of the sample (and collected by the camera) is identified by the dashed black line. M_5 is mounted on a flip mount to allow the alternate visualization on the camera of both the light which passes through the sample and the light reflected by its front surface. With two black dashed arrows the two positions where the IR sensor head is positioned to measure P_1 and P_2 (see equations (6.6) and (6.7)) are indicated. Two laser sources are used during the measurements, a red diode laser during the first steps of the alignment procedure and a diode laser emitting at 1550 nm during the measurements of linear losses.

positioned into the focal plane of MO_1, and R is the reflectance at the interface air/silicon, given by the expression:

$$R = \left(\frac{n_{air} - n_{sem}}{n_{air} + n_{sem}}\right)^2 \tag{6.8}$$

where n_{air} and n_{sem} are the refractive indices of respectively the air and semiconductor at the desired wavelength.

The formula 6.6 includes (in the term P_{in}) the losses due to the optical system and the unavoidable Fresnel losses due to the input/output interfaces crossed by the light, but assumes that it is possible to neglect the coupling losses due to scattering phenomena caused by the roughness of the sample ends, provided that the surface roughness is reduced as much as possible. In order to reach this target, two different techniques have been adopted and optimized, namely polishing and laser cleaving. The procedures of usage and the experimental results of these two techniques, applied to our semiconductor samples, will be presented in detail in the next two sections.

6.1.3.1 Preparation of semiconductor deposited core samples: mechanical polishing

Any surface of a solid substance is characterized by a certain roughness, and this is true even in the case of a semiconductor deposited silica optical fibre, where the roughness of the semiconductor core can be particularly pronounced and cause diffusion of the light impinging on it during for example experiments of losses measurement. It is possible to reduce this undesired roughness for example mechanically, with the help of some abrasive substance. Abrasive is a material, often a mineral, that is used to shape or finish a workpiece through rubbing which leads to part of the workpiece being worn away by friction. The process of polishing with abrasives starts with coarse ones and graduates to fine ones. Usually those abrasive substances are deposited on top of paper disks against which the surface to be polished is rubbed, either manually or by using a automated machine.

In our work the polishing process has been realized by means of a dedicated machine (Ultratec, model Ultrapol End & Edge Polisher). The sample to be polished is inserted into a capillary fibre, then immersed in liquid wax (used to fix the sample to the capillary and to fill the side holes of the three-hole deposited fibre), and finally it is fixed to the support connected to the polishing machine arm (see Fig. 6.3). Filling the fibre holes with wax avoids that fragments of glass produced during the polishing process go inside the holes, even considered how difficult can be the process of removal of these fragments afterwords.

A series of attempts of optimization of the polishing process, playing with the type of paper, the grain size of the polishing paper and the duration of the process of abrasion, has been explored. The optimized process to polish the Si deposited samples consists in 15 mins of polishing by using 8 μm (of roughness) paper, followed by 30 mins of 3 μm paper and 60 mins of 0.5 μm paper (disk rotation speed = 150 rpm). The surface of polishing paper needs to be wet (by means of

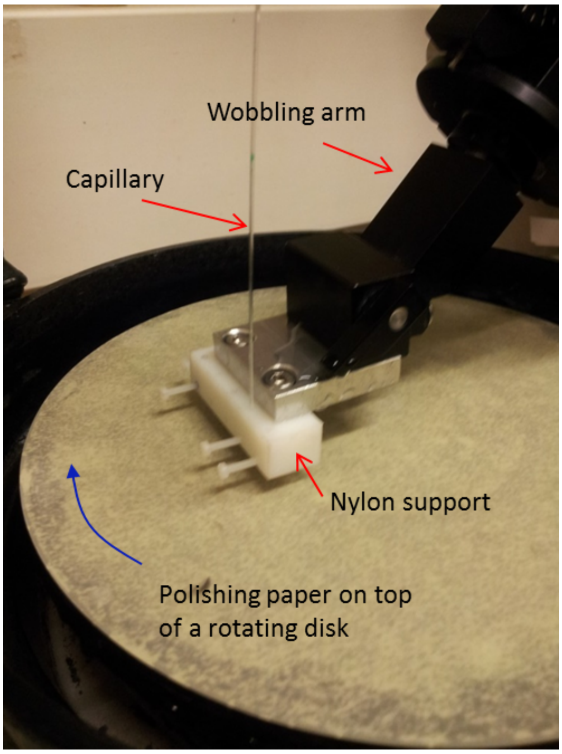

Figure 6.3: Support of the fibre to be polished. The capillary where the fibre has been previously inserted and fixed by means of some wax, is inserted inside a hole created in a nylon block and tied by means of a screw. The nylon block is then fixed to the arm (wobbling continuously from left to right in a fixed range of length) of the polishing machine, while the abrasive action is realized by means of a rotating disk on top of which the polishing paper has been adhered. The speed of rotation of the disk can be chosen according to practical considerations, related for example to the type of material to polish or the strength of the glass the fibre is made of.

distilled water) all the time during the process, otherwise deep scratches will be found on the surface after the polishing process (see Fig. 6.4). Afterwards, the sample has to be immersed in an acetone ultrasound bath for 15 mins to remove all the residual wax from its holes and surfaces. The best result of a complete polishing process of deposited Si fibre is reported in Fig. 6.4.

After being polished, some Si samples have been linearly characterized by means of the setup of Fig. 6.2 and the results of these measurements are reported in Table 6.1. It is interesting to highlight how much different the measured losses are. The reason of these quite big differences lies in the nature of those losses, which are mainly due to the quality of the deposition process of the semiconductor inside the fibre core. The presence of defects or voids in the structure of the deposited semiconductor can change significantly the scattering phenomena inside the core and so increase the transmission losses of this kind of fibres.

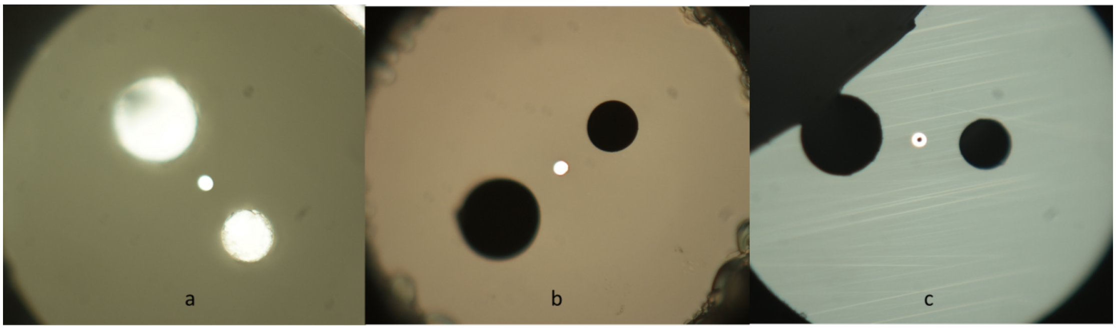

FIGURE 6.4: Cross-sections of a deposited Si sample polished by means of the method previously described; (a) shows the surface polished before acetone ultrasound bath, where it is possible to recognize the presence of wax in the holes; (b) represents the same surface after ultrasounds bath; (c) is the result of dry polishing process.

Deposited Si fibres	Sample 1	Sample 2	Sample 3
Transmission Losses (dB/cm)	13	6.5	5.6

TABLE 6.1: Transmission losses, measured by means of single pass method, of three Si deposited fibres. The average length of each sample is of ≈ 0.5 *cm*.

The same method of polishing as used for the Si samples has been applied to ZnSe samples, but the result was not as good. In Fig. 6.5 an example of a ZnSe sample polished is shown. It appears that the roughness of the core region is not reduced as expected. We believe that the reason of this difference is related to the different structural nature of the grown materials, namely the amorphous silicon and the polycrystalline ZnSe.

Another approach was attempted after the unsatisfactory results of the mechanical polishing process of the ZnSe fibres (see Fig. 6.3), which consists in a manual polishing. The semiconductor deposited core fibre, inserted into the capillary and adhered with crystalbond, is clamped inside a support which can be easily handled. The fibre is then rubbed gently against the surface of polishing papers of different grain size, always following the order from the biggest to the smallest size. The manual polishing allows for reducing the possible impact of the fibre's end surface on the rotating plate of the polishing machine (procedure which can damage the fibre's surface). The manual polishing procedure allows for a higher level of control on the number of turns which the fibre can be rubbed on the abrasive surface.

An example of these attempts of manual polishing is reported in Fig. 6.6, where it is clear that the smoothness of the semiconductor core polished manually is better than the one of the fibre via the polishing machine (see Fig. 6.5), even if there

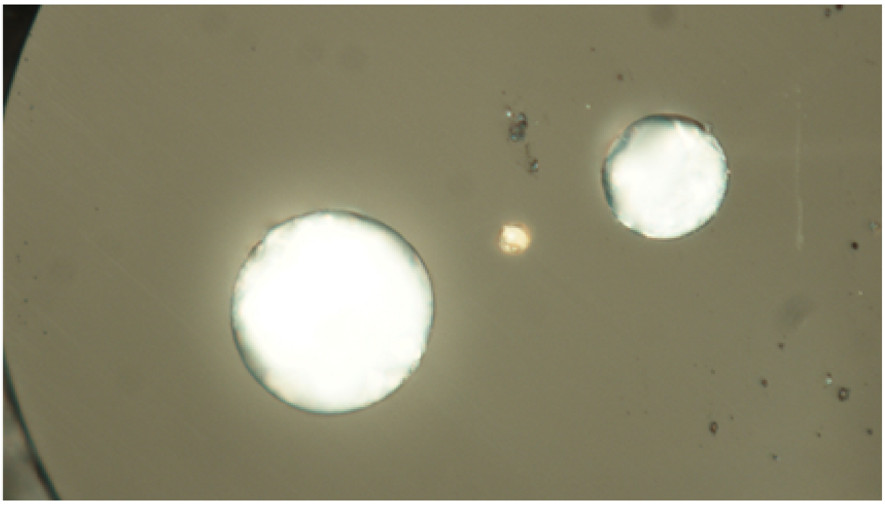

Figure 6.5: Cross-section of a deposited ZnSe fibre polished by the method described in section 6.1.3.1. The picture has been captured before the insertion of the sample in the ultrasound bath, so there are still residues of wax inside the two holes of the fibre. The colour and the roughness of the ZnSe core look like very different from the ones of the Si core as shown in Fig. 6.4 (a) and (b).

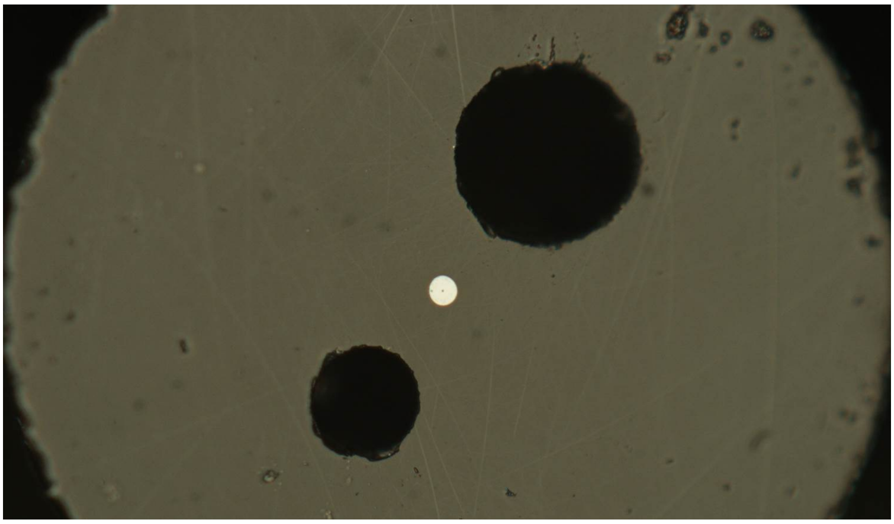

Figure 6.6: Cross-section of a deposited ZnSe fibre polished by means of the manual mechanical polishing procedure, described previously in the text. The fibre has been fixed to the capillary by means of a crystalbond. The picture has been captured after the fibre has been taken for few hours in a acetone ultrasounds bath for the removal of the residues of crystalbond from the holes of the fibre and from the top of the surface of that.

are evident scratches on the surface corresponding to the fibre's cladding. This behaviour suggests that, in order to polish the semiconductor core of the ZnSe fibre is not necessary to polish it for so long, and instead polishing the fibre for a longer time improves the quality of the fibre's cladding while the semiconductor's smoothness is worse.

None of the samples polished either via polishing machine or manually guided light at 1550 nm, possibly because of defects intrinsic in the process of deposition of ZnSe inside the core of the three-hole fibre, such as the presence of voids or cracks which of course would completely scatter the light back preventing it from traveling along any appreciable length.

6.1.3.2 Preparation of semiconductor deposited core samples: laser cleaving

The attempts of mechanical polishing of the ZnSe fibres (either manual and automatic), discussed in section 6.1.3.1, showed unreliable results, and none of the mechanically polished samples guided light at 1550 nm, another approach used to try to reduce the roughness of the ZnSe samples is represented by the laser cleaving of the fibre's end via the beam generated by a CO_2 laser (OpTek Systems).

The working principle of the laser cleaving is the so called laser ablation, a phenomenon which happens when a short-pulsed, high-peak power laser beam is focused onto any solid target, and a portion of the material instantaneously explodes into vapour [202]. The laser irradiance (power density) and the thermo-optical properties of the material are critical parameters that influence the explosive phenomena which go under the name of ablation. When the laser pulse duration is microseconds or longer and the irradiance is less then approximately $10^6\ W/cm^2$, vaporization is likely a dominant process influencing material removal from a target. Phonon relaxation rates are on the order of 0.1 ps, and absorbed optical energy is rapidly converted into heat. Heat dissipation and vaporization are fast in comparison to the laser pulse duration. The thermal and optical properties of the sample influence the amount of material removed during the laser pulse. At higher irradiance, beyond $10^9\ W/cm^2$ with nanosecond and shorter laser pulses focused onto any material, an explosion occurs, which is usually defined as ablation. Phenomenologically, the surface temperature is instantaneously heated over its vaporization temperature through linear one-photon absorption, multi-photon absorption, dielectric breakdown, and additional undefined mechanisms [203].

The features of the laser source used for our attempts of cleaving of semiconductor fibres are reported in Table 6.2. The fixed parameter is the peak power of the laser. Then the parameters which can be changed are the time duration of each pulse, which determines the energy of each pulse delivered on the fibre to be cleaved. The repetition rate, instead, defines the radiant power used every time. It is possible, of course, to deliver a defined number of pulses.

Wavelength	10400 - 10800 nm
Maximum average radiant power	100 W
Beam divergence	10 mrad
Pulse energy	5 - 200 mJ
Peak power	250 W
Pulse durations	10 μsec - 1000 μsec
Repetition rate	1 - 20 KHz

TABLE 6.2: Features of the CO_2 laser source used to cleave the ZnSe deposited fibre (OpTek Systems).

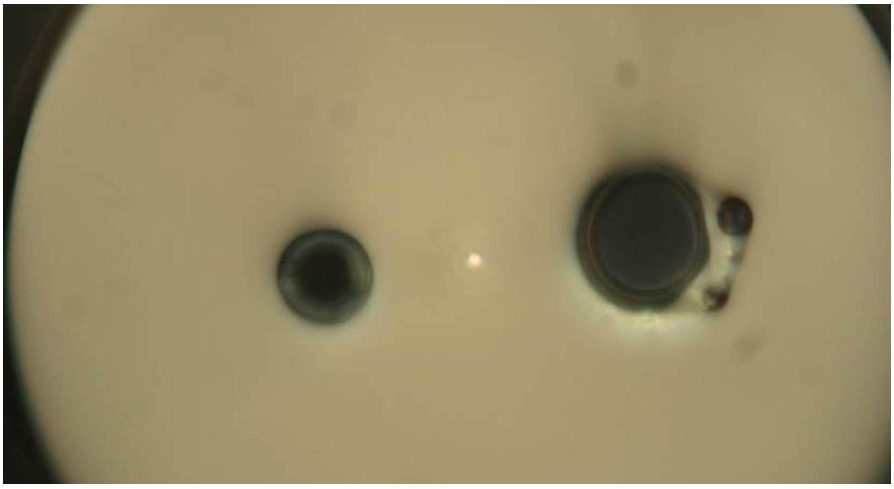

FIGURE 6.7: Cross-section of a deposited ZnSe fibre laser cleaved by means of the CO_2 laser. The parameters of the laser used for this particular cleaving process are: repetition rate of 400 Hz, pulse duration of 50 μsec. The number of pulses delivered on the fibre is 250.

During experimental optimization of the fibre's roughness via the laser radiation produced by the system described in Table. 6.2, the tailorable parameters have been changed in order to observe the effect on the quality of the surface cleaved. After every attempt the surface of the fibre laser cleaved was checked by means of an optical microscope. There was a preliminary phase of the work where the laser parameters have been optimized to cleave the three-hole fibre empty and a second part of the experimental work where the same recipe has been transferred to the fibre with the deposited semiconductor core. The best result of this series of attempts has been reported in Fig. 6.7, where it is quite clear that the process was not able to cleave perfectly both the glass and the semiconductor. Furthermore it seems that some glass, after being fused via the ablation process, re-solidified on top of the ZnSe core, creating a sort of lensing effect. None of the fibre treated with the laser cleaving process guided any light at 1550 nm.

6.1.4 Thermal poling of semiconductor core step-index fibres

Although the experimental results related to the transmission losses (quite high, or too high to observe any transmission of light through the sample) and length (too short) of the semiconductor deposited step index fibres are not very comforting, nevertheless some experiments have been realized with the aim of observing the effect of the thermal poling of this kind of devices.

A first type of experiment was realized by means of a setup similar to the one shown in Fig. 3.7. A tungsten wire was inserted inside one of the two side holes of a Si/ZnSe deposited three-hole fused silica fibre and the high electrostatic positive potential was applied to that while the fibre (located on top of a microscope slide equipped with a backplane grounded) is heated up to a temperature of $\approx$ 300 °C. The external electric field is applied for two hours and then the sample is cooled down to room temperature while the wire is still connected to the anodic potential. The result of the HF decorative etching of this poling experiment is reported in Fig. 6.8, together with the result of a poling experiment in double anode configuration (see the inductor in Fig. 3.10). In both cases $V_{app} = 4.3\ kV$. Both HF etched ends of the two fibres demonstrate that in a poling experiment with the electrodes inserted inside a THF with the core made of a semiconductor deposited via HPCVD (Si or ZnSe) it is possible to observe clearly a space-charge region, which is the sign of an electromigration process, formed even around the hole deposited with the semiconductor. In other words, in this experiment a proper electrostatic induction process happened, similar to the one realized and discussed in section 3.3, where the fibre poled by induction was equipped with an embedded

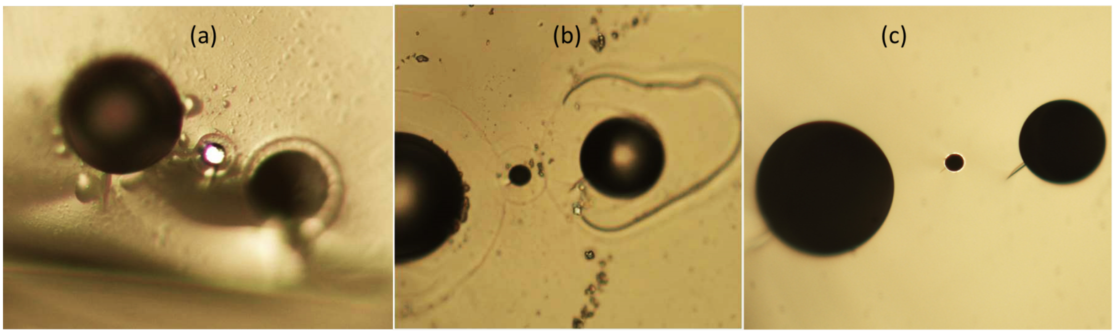

Figure 6.8: (a) HF etched cross-section of a Si deposited three-hole silica fibre poled in single anode configuration at 4.3 kV and ≈ 300 °C. The electrode inserted in the smallest of the two side holes is a piece of a tungsten wire. The total length of the sample poled is of ≈ 2 *cm*; (b) HF etched cross-section of a ZnSe deposited three-hole silica fibre poled in double anode configuration with $V_{app} = 4.3$ kV and T ≈ 300 $°C$. The total length of the sample poled is of ≈ 2 *cm*; (c) image of the ZnSe fibre before HF etching process, where the ring of ZnSe deposited is clearly shown.

floating electrode. Somehow here the semiconductor has the role of an electrode causing the creation of a space-charge region.

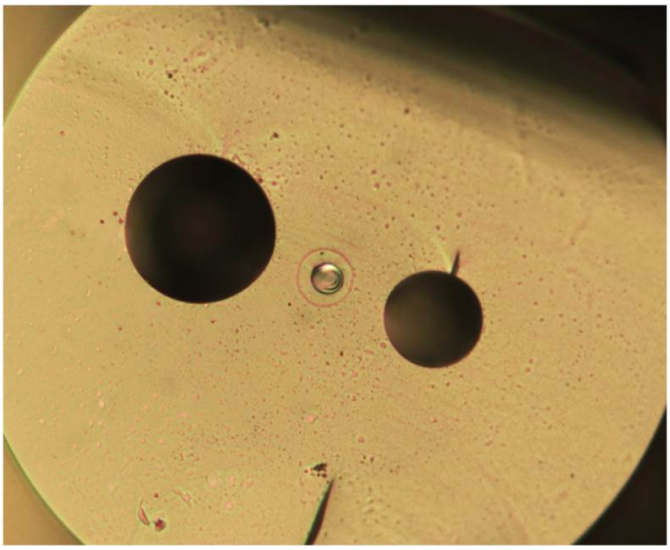

Figure 6.9: HF etched cross-section of a Si deposited three-hole silica fibre poled by means of an external inductor (see Fig. 3.10 for the exact setup adopted). The experimental conditions of the poling experiment are $V_{app} = 4.3$ kV and T ≈ 300 °.

Starting from these considerations, an induction poling experiment was attempted in a configuration similar to the one reported in Fig. 3.10, where the inductor is exactly the same and the fibre poled is a three-hole fibre deposited with a semiconductor. The experimental conditions of poling are the same previously reported in this section and the result of the decorative etching in HF solution is reported in Fig. 6.9, where it is possible to clearly see the space-charge region formed only around the semiconductor core of the three-hole fibre.

It is worth highlighting that, apart from the HF decorative etching, which anyway reveals the space-charge region, it was not possible to generate any nonlinear effect related to the presence of the semiconductor because of the very high losses affecting all the samples realized so far and even because of the very limited length of the devices, which prevented us from creating devices long enough for producing some second order nonlinear effect, such as for example a linear electro-optic effect.

6.1.5 Theoretical considerations about guidance in semiconductor core step-index fibres

Apart from the issues highlighted in the previous sections, related mainly to the high intrinsic transmission losses of the semiconductor core fibres (due mostly to defects of fabrication via HPCVD), limitations on the length of the fibres deposited, and preparation of the end surfaces of the fibres, another issue which could affect negatively the efficiency of the nonlinear behaviour of semiconductor step-index fibres consists in the fact that, with a core characterized by a refractive index of $\approx$ 2.5 (for ZnSe [204]) and of $\approx$ 3.5 (for a:Si-H [195]), the fibre operates in a multimodal regime at wavelengths around 1550 nm. This multimodal behaviour could reduce the efficiency of any effect related to the intrinsic second order nonlinearity of the semiconductor deposited in the fibre because the optical energy associated to the fundamental mode (which is the one we are interested in for generating a nonlinear effect) will be reduced by the presence of many other oscillating modes inside the fibre. However, as detailed in section 6.2.1, the potential solution to the guidance issues just reported here is not to have semiconductor core fibres but rather deposit thin layers of semiconductor in the cladding holes of twin-hole fibres, in order to exploit the effect of these intrinsically nonlinear materials on the evanescent field of the fundamental mode guided in the step-index fibre.

6.2 Functionalisation of twin-hole silica fibres and hollow-core MOFs via deposition of thin layers of intrinsically nonlinear materials

Section 6.1 reports the experimental results related to the attempt of functionalising silica optical fibres exploiting the intrinsic nonlinear properties of some materials such as semiconductors (in particular ZnSe and a-Si:H). The basic idea behind this approach consists in the creation of step-index fibres with a solid core made of a semiconductor material whose nonlinear properties should be exploited to observe some second order nonlinear phenomena due to the presence of the semiconductor or even to the superposition of both its intrinsic nonlinearity and the nonlinearity induced by means of thermal poling.

Although it was demonstrated that by poling the fibre it is possible to create a space-charge region even around the semiconductor core, which presumably should be able to enhance the global nonlinearity of these special fibres, it was impossible so far to exploit these devices to actually observe any nonlinear effect (due to the intrinsic, induced or both nonlinearities) because of some practical issues, such as high transmission losses, short length and difficulty to couple light inside the semiconductor cores.

For all the reasons just cited a new approach was chosen to try to enhance the nonlinear behaviour of different kinds of optical fibres, which should exploit the intrinsic nonlinearity of thin layers of different types of materials, deposited by means of diverse methods in the two cladding holes of a twin-hole Ge-doped silica fibre (similar to the one reported in Fig. 2.21), or in the microstructure of a hollow-core negative curvature optical fibre (such as the one reported in Fig. 2.7 (b)).

In the case of the twin-hole silica fibre the aim is the observation of an enhancement of the SON induced by periodically poling the fibre, based on the assumption that the light traveling through the fibre should "see" (at least its evanescent field) the effect of the presence of the nonlinear material deposited in one or both the cladding holes of the twin-hole fibre. In particular the SON could be increased or depositing some material already possessing a second order nonlinearity or a material possessing a high third order nonlinearity, which could be exploited to enhance the SON induced by thermal poling (see equation (2.69)). In the next section the early attempts of creating such type of fibres will be described, together with the first thermal poling experiments.

In the case of negative curvature hollow-core fibres (NC-HCFs) the deposition of thin layers of these intrinsically nonlinear materials allows them to be functionalised without changing too much their guidance properties. A recent work, which will be discussed in detail in section 6.2.2, showed the possibility of mixing successfully the tailorable characteristics of guidance of the MOFs with the nonlinearities which these materials could be able to add [205].

6.2.1 Deposition of thin semiconductor layers in twin-hole silica fibres

In section 6.2 a brief explanation is given, that the possibility of exploiting a solid semiconductor core to create any nonlinear effect is remote. The new strategy is based on the idea that, in a twin-hole Ge-doped core step-index silica fibre like in Fig. 2.20, where one of the two cladding holes is very close to the fibre's core ($\approx 5\ \mu m$), the Gaussian fundamental mode of a laser beam at 1550 nm propagating into the fibre could overlap to the thin layers of semiconductor deposited inside the hole, producing some nonlinear effect. In particular, if the deposited material possessed an intrinsic $\chi^{(3)}$ value higher than the silica one, by poling the fibre, it would be possible to exploit this higher value of the third order nonlinearity (TON) to get a higher value of induced $\chi^{(2)}$. If, however, the deposited material possessed already an intrinsic $\chi^{(2)}$, this could be directly exploited to obtain some measurable SON effect or even added to the $\chi^{(2)}$ induced by thermal poling. Fig. 6.10 shows a cross-section of the twin-hole fibre deposited with ZnSe inside one of the cladding holes via HPCVD.

Two different issues have been faced in this thesis work, namely the deposition of thin layers of semiconductor (Si and ZnSe) along the longest possible length of the twin-hole fibre, and the research of a reliable method for evaluating the eventual enhancement of the SON.

The technique chosen to deposit the semiconductor inside the cladding holes of the twin-hole fibre is the HPCVD technique, already described in section 6.1.1. Recent measurements reveal transmission losses of $\approx$ 0.5 - 0.8 dB/cm for samples with ZnSe (thickness $< 1\ \mu m$) deposited in the cladding holes. $COMSOL^{TM}$

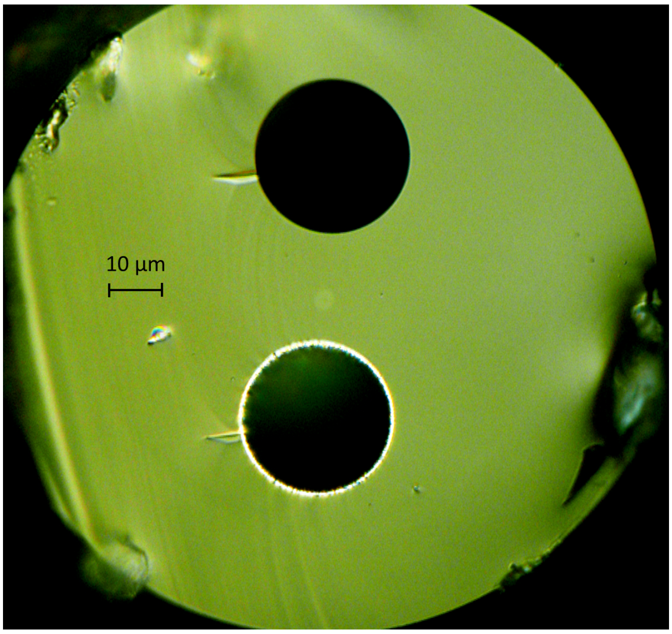

FIGURE 6.10: Cross-section of a fused silica twin-hole fibre with ZnSe deposited in one of the cladding holes via HPCVD.

Multiphysics simulations shown in Fig. 6.11 reveal that the ZnSe layer needs to be less than 1 μm to allow the mode at 1550 nm to be guided effectively.

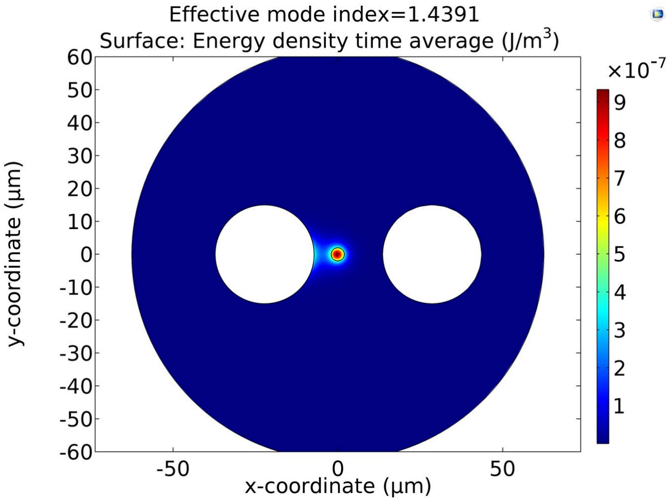

FIGURE 6.11: Energy density time average related to the fundamental mode in a step-index fibre (OD = 125 μm, core diameter = 4 μm, n_{co}(1550 nm) = 1.4457, n_{clad}(1550 nm) = 1.4378, layer of ZnSe deposited in the cladding hole closest to the core (thickness < 1 μm).

6.2.2 Deposition of semiconductor thin layers in NC-HCFs

Negative curvature hollow core fibres (NC-HCFs) are MOFs characterized by a particular geometry of their microstructured cladding, which consists in a row of silica capillaries and gives a negative curvature aspect to the core boundary (see Fig. 2.7). Their guidance mechanism is the antiresonant reflecting optical waveguide which characterizes the so-called hollow anti-resonant fibres (ARFs) and explained in detail in section 2.1.2. This category of PCFs, made of a limited number of detached glass tubes inside an outer glass jacket [206], have gained a great deal of scientific and technological interest recently due to their low attenuation in the visible [207], near [208] and mid-infrared spectral ranges [209], combined with ultra-large transmission bandwidths. Possible applications of the NC-HCFs include high power laser delivery [208], gas based laser sources [210] and telecommunications. Many variations around the basic structure of these fibres have been proposed along the years, even if always based on a single material, usually silica but not only.

For the first time we have proposed the realization of a multiple material cladding for the ARFs, which are defined “composite material anti-resonant fibres” (CM-ARFs), based on a NC-HCF, similar to the one reported in Fig. 2.7, with a thin layer of a-Si:H deposited inside the microstructure (inside and outside the cladding capillaries) via the HPCVD technique. The deposition of semiconductors with the aim of functionalising optical fibres from the nonlinear point of view is an idea already implemented in the past in solid core MOFs both guiding for modified TIR or for Bragg reflections induced by the periodic refractive index of the cladding [211]. The novelty of our proposal consists not only in the different type of MOF functionalised, but in particular in the very low attenuation (< 0.1 dB/m) of the silicon ARFs compared to the previous ones.

A theoretical study has been initially realized to see how the transmission spectrum of a NC-HCF changes by adding inside the small capillaries located around the central hole of the fibre a material of higher refractive index (with respect to the glass the cladding is made of). Fig. 6.12 shows a reproduction of a silica based ARF (n $= 1.41$ at $\lambda = 2.7$ μm), with 10 cladding tubes and an original thickness of each cladding tube of 2.4 μm. The core radius of the fibre is 47 μm. An additional internal membrane t_A is added inside each tube and is made of a material characterized by a refractive index $n_2 = 2$. The dependence of leakage loss on the additional thickness t_A shown in Fig. 6.12 at a wavelength of 2.7 μm, clearly demonstrates the anti-resonant properties of this CM-ARF. The thickness of the additional membrane of different refractive index t_A^* which corresponds to the minimum leakage loss of the single layer ARF will be referred as "antiresonant layer".

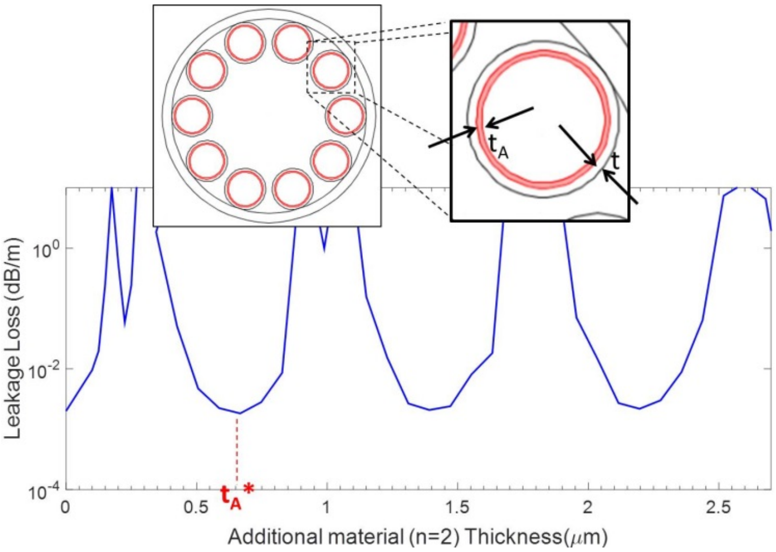

Figure 6.12: Schematic (top) of a Composite Material Hollow Anti-resonant fibre: an additional layer with thickness t_A is added to the original core boundary of thickness t. The fibre transmission spectrum at 2.7 μm shows the anti-resonant behaviour of the fibre [205]. The simulation has been performed by W. Belardi.

Fig. 6.13 (a) shows the evolution of the leakage loss when additional antiresonant glass membranes (2, 3 or 5t) are added to the basic structure. This behaviour is almost identical to that of fibre designs shown in Fig. 6.13 (b), where the thickness of the initial single silica membrane is simply increased 2, 3 or 5 times. In particular the fibre designs of (a) and (b) have the same resonant wavelengths and the same minimum leakage level. This behaviour is not surprising since the designs of Fig. 6.13 (b) can be simply seen as multiple layers (of the type (a)) with the same refractive index for the alternating layers ($n_2 = n_1$). By using the basic formulation of the resonant wavelength, it is possible to derive that the frequency spacing Δf between two resonant frequencies is [37]:

$$\Delta f = \frac{c}{2t_R\sqrt{n_1^2 - 1}} \tag{6.9}$$

where c is the speed of light in vacuum, t_R is the membrane thickness of the ARF and n_1 is the glass refractive index. Therefore when the thickness is doubled or tripled, the frequency spacing between two resonant frequencies is reduced by a factor of 2 or 3. This explains the presence in Fig. 6.13 of a different number of resonant wavelengths associated with the different number of antiresonant layers in the considered structures.

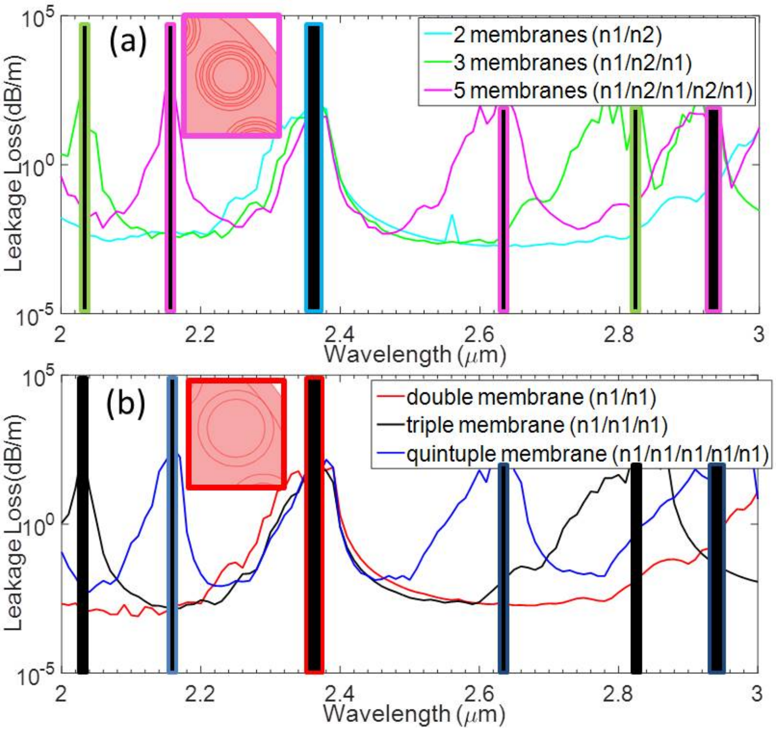

FIGURE 6.13: Top (a): Calculated leakage loss when 2 (cyan line), 3 (green line) or 5 (pink line) antiresonant layers are added to the basic structure of Fig. 6.12. Bottom (b): Calculated leakage loss when the thickness t of the basic ARF structure is increased 2 (2t, red line), 3 (3t, black line) and 5 (5t, blue line) times [205]. The simulations have been performed by W. Belardi.

It is possible to further extend the analogy between Fig. 6.13 (a) and (b) by correlating the behaviour of a CM-ARF made of two materials (with refractive index n_1 and n_2, and thickness t_1 and t_2) to that of a single material ARF with an equivalent refractive index n_{eq} and thickness t_{eq} given by:

$$n_{eq} = n_1 \frac{S_1}{S_1 + S_2} + n_2 \frac{S_2}{S_1 + S_2} \tag{6.10}$$

$$t_{eq} = t_1 + t_2 \tag{6.11}$$

where S_1 and S_2 are the surfaces occupied by the two materials, given by (see inset of Fig. 6.14):

$$S_1 = \pi(r^2 - r_1^2) \tag{6.12}$$

$$S_2 = \pi(r_1^2 - r_2^2) \tag{6.13}$$

where r_1 and r_2 are the internal radii of the two cladding tubes of thickness t_1 and t_2 respectively and r is the external radius of the composite material cladding tubes (see inset of Fig. 6.14). As an example and validation of this equivalence, we have considered the case of 2 materials with $n_1 = 1.414$ and $n_2 = 2$ ($t_1 = 0.66\ \mu m$, $t_2 = 0.99\ \mu m$, $r = 20\ \mu m$). By using equations (6.10) to (6.13) it is possible to obtain $n_{eq} = 1.7656$ and $t_{eq} = 1.65\ \mu m$. By looking at Fig. 6.14 it is clear that the leakage loss of the CM-ARF (blue line) and the equivalent ARF (red line) overlap in most of the considered spectral range. A slight difference between the two spectra is more evident at longer wavelengths where the fundamental mode interacts more strongly with the fibre cladding modes.

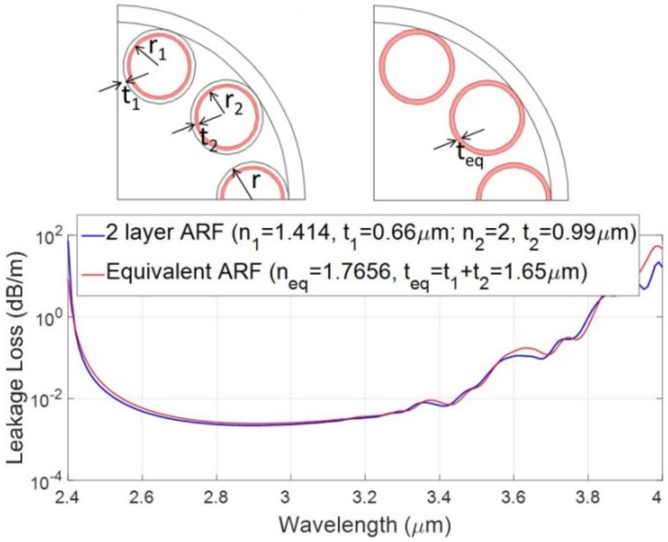

FIGURE 6.14: Equivalence between a CM-ARF with 2 antiresonant layers of thickness t_1 and t_2 (blue line) and single layer ARF with an equivalent antiresonant layer of thickness t_{eq} [205]. The simulations have been performed by W. Belardi.

The established analogy between a composite material and a conventional single material ARF suggests that only the overall optical path traveled by light at the core boundary is relevant for antiresonance guidance. This opens up the possibility to exploit the properties of additional materials deposited on the basic optical fibre matrix in order to activate and functionalise its behaviour, for example, via the free carrier plasma-dispersion effect, in which the change of refractive index and absorption resulting from a change in the concentration of free carriers by photo-excitation can be used in silicon-based all-fibre integrated modulators to achieve intensity or phase modulation [212].

From the experimental point of view, in my thesis work it was investigated the feasibility of a particular form of CM-ARF, in which the core boundary membrane is made of a composite hybrid semiconductor/glass material. Fig. 6.15 shows a typical section of a borosilicate based ARF [213] filled with a-Si:H by means of HPCVD. The CM-ARF of Fig. 6.15 (a) was obtained after a deposition of 48 hours at a temperature of 400 °C and has 3 layers of material (Silicon (white)/Borosilicate (gray)/Silicon (white). The Si layer thickness was measured using the scanning electron microscope (SEM) to be close to 300 nm. We then tested several types of ARF by using the same HPCVD technique and modifying the temperature profile along the fibre samples as well as the filling time. The fibre shown in the inset of Fig. 6.15 (b) (core diameter $d = 60\ \mu m$ and glass layer thickness of $1\ \mu m$) was coiled in a furnace at a temperature of 450 °C and filled for only 4 hours in order to obtain a very thin a-Si:H layer. A length of 35 cm of this fibre was obtained and tested.

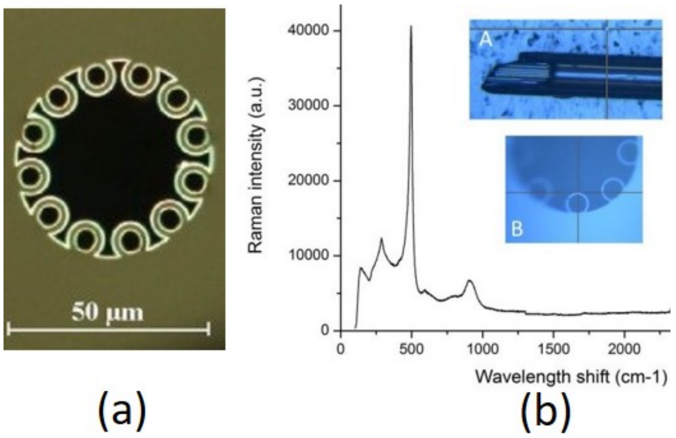

FIGURE 6.15: (a) Fabricated CM-ARF: a thin ($\approx\ 0.3\ \mu m$) layer of a:Si-H (highly reflective white material) covers the internal and external sides of the cladding tubes of a borosilicate based ARF. (b) Raman Shift spectrum of another CM-ARF shown in its longitudinal (A) and transverse (B) section. The peaks reveal the presence of a-Si:H on the external and internal surfaces of the cladding tubes. Reflective white material (a-Si:H) can also be seen in the longitudinal section (A) micrograph. [205].

We could reveal the presence of a thin layer of a-Si:H by means of Raman Spectroscopy. Fig. 6.15 (b) shows the Raman shift spectrum taken using the sample in the inset (shown in its longitudinal section (A) and transverse section (B)) and using an optical pump at a wavelength of 0.63 μm. The Raman shift at the points centred on the external and internal side of the cladding tubes confirms the presence of a-Si:H [214]. The spectrum of the signal transmitted through the considered 35 cm long sample is shown in Fig. 6.16 together with the near field intensity profile recorded by an Infrared Camera. In the considered spectral range (0.7 μm to 1.6 μm) the CM-ARF has two transmission windows (just above 0.8 μm and around 1.2 μm) and presents several peaks probably related to the coupling of the fundamental-like mode (in the inset) to the cladding modes, in both the high refractive index ($\approx$ 3.6) layers of a-Si:H.

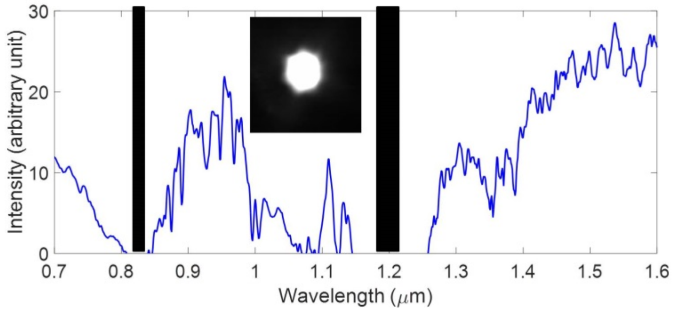

FIGURE 6.16: Transmission spectrum of the CM-ARF shown in the inset. Inset: near field intensity profile of the transmitted optical mode. [205].

In Fig. 6.17 (A) the transmission spectrum reported in Fig. 6.16 is compared with that of 7 metres of a control sample ARF that does not have any silicon. The leakage loss calculated for both the filled and unfilled ARF is also shown in Fig. 6.17 (A). The addition of the internal and external silicon layer to the original ARF results in a red-frequency shift of the entire transmission spectrum. Fig. 6.17 (B) shows what would be the effect on the leakage loss of a variation of the coating thickness of ± 10 nm, proving that the fibre attenuation levels would be kept similar but there would be a shift of the resonant wavelength (± 0.05 μm).

In order to show the impact of the optical absorption of the a-Si:H layers on the fibre performance we have compared in Fig. 6.18 the attenuation components of the CM-ARF. The fibre attenuation related to the presence of a glass and silicon material absorption are obtained as the product between the optical mode overlap on each material and their intrinsic absorption. Concerning this last quantity, we have measured the borosilicate glass absorption to be maximum 140 dB/m

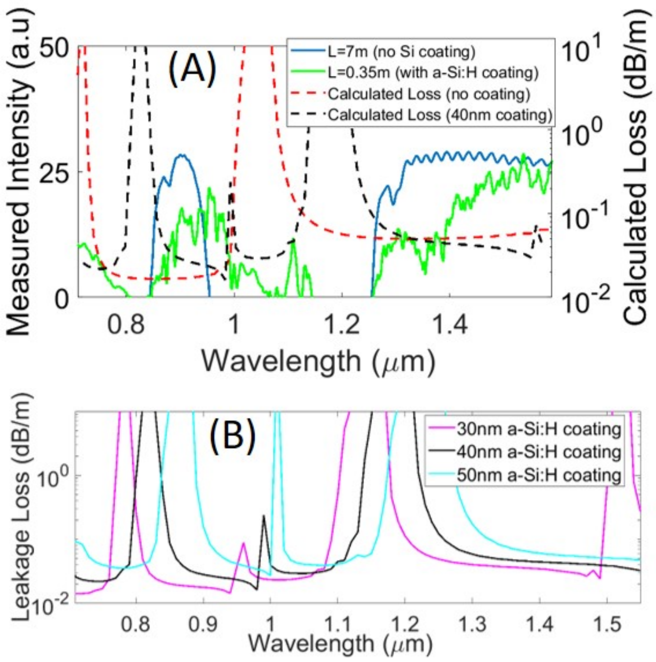

FIGURE 6.17: (A) Comparison between the transmission spectrum (left Y axis) of an unfilled control sample ARF (7 m long, green solid line) and the ARF filled with a-Si:H (0.35 m long, blue solid line) with the calculated leakage loss (right Y axis) of the unfilled control sample ARF (red dotted line) and the a-Si-H filled ARF (40 nm coating, black dotted line). (B) Calculated leakage loss for 30, 40 and 50 nm coating thickness. [205]. The simulations have been performed by W. Belardi while the loss measurements by the thesis author.

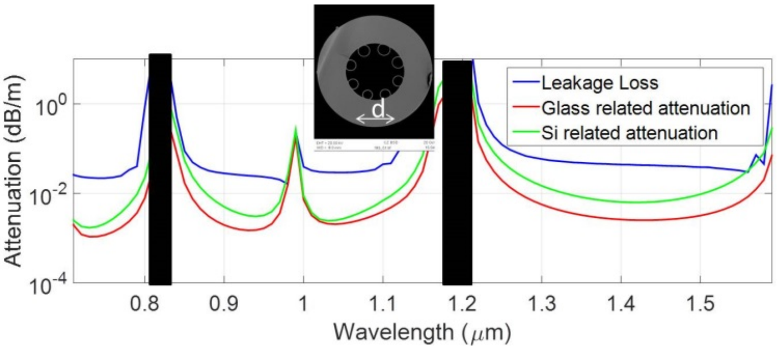

FIGURE 6.18: Different components of the total attenuation of the CM-ARF shown in the inset: leakage loss (blue line), loss related to the overlap of the optical mode on the Si layer (green line) and on the borosilicate cladding layer (red line). The material absorption has been assumed to be 10000 dB/m for a-Si:H and 140 dB/m for borosilicate. [205]. The simulations have been performed by W. Belardi.

and we have assumed a high absorption of the amorphous silicon material of 100 dB/cm. The results reported in Fig. 6.18 show that, for the considered fibre, the leakage loss (blue line) is the most important contribution to the total attenuation of the CM-ARF and demonstrates the negligible impact of the absorption of the deposited semiconductor. Levels of attenuation as low as 0.1 dB/m or less may be obtainable in long CM-ARFs.

6.3 Conclusions

This chapter presents the topic of my thesis work related to the idea of exploiting intrinsic nonlinear properties of semiconductor and 2D materials deposited inside different types of optical fibres, from twin-hole step-index silica fibres to hollow core PCFs. The possibility of using the semiconductor deposited in the fibres as electrode for thermal poling has been also demonstrated. A new approach is presented, according to which it is be possible to realize composite materials anti-resonant fibres via the deposition of materials possessing already intrinsic second or third order nonlinearity by using the HPCVD technique. This approach opens the way towards the possibility of exploiting the versatile guidance properties of a microstructured fibre together with the nonlinear properties of thin layers of some materials with the aim of producing second order nonlinear effects, such as for example wavelength tuning, or phase modulation/switch based on linear electro-optic effect.

Chapter 7

Future work

7.1 Summary

This thesis work deals with overcoming the practical limits of current state of the art thermal poling techniques, with the final aim of exploiting it to add second order nonlinear functionalities to any kind of optical fibres, from the common step-index silica fibres to the more complex MOFs of different geometries, both solid and potentially even hollow core [215]. The idea of using liquid electrodes (metallic and aqueous) together with the development of a contactless technique of thermal poling allow for thermally poling different types of optical fibres of any geometries and length. In addition, selective filling of such geometries both radially and longitudinally will allow liquid electrodes to be inserted (and then removed) in any configuration in order to optimize the $\chi^{(2)}_{eff}$ for novel device applications.

The results obtained in this thesis work include the experimental implementation of an "electrostatic induction poling technique", the development of liquid electrodes, both metallic and electrolytic and the elaboration of a model (using $COMSOL^{TM}$ Multiphysics) which allows for studying the temporal evolution of the electromigration process.

Not only does this advantageous combination allow for the poling of very long (metre scale) samples, but also within any complex geometry. This technological platform could allow for example the induction poling of solid core microstructured optical fibers where contacting multiple internal electrodes would otherwise be a prohibitive challenge. In addition, selective filling of such geometries both radially and longitudinally will allow liquid electrodes to be inserted (and then removed) in any configuration in order to optimize the $\chi^{(2)}_{eff}$ for novel device applications.

Furthermore for the first time it was conceived and partially realized the idea of exploiting the intrinsic nonlinear properties of some materials (such as for example semiconductors) deposited with a limited thickness inside a particular type of MOFs (called NC-HCFs) via a technique called HPCVD. The first demonstration of a composite material hollow antiresonant fibre with silicon deposited inside the microstructure is another key advance. This could allow for reaching results so far not conceivable in terms of efficiency. The idea for a low loss, efficient and all-fibre nonlinear device has good chances to be, as promised initially, a revolutionary idea in the topic of nonlinear photonics.

7.2 Future works

As expected for a PhD work, many topics have been opened during this research period. Part of those topics have been only briefly touched and explored. Many ideas have been generated by this thesis work, and are ready to be deeply studied in future works. The future activity will deal with the main aim of enhancing the SON of both step-index optical fibres and hollow core MOFs. Another important purpose of my future work is enlarging the range of applications of the PPSFs already realized via the integrated technological platform developed during this thesis work. In the next sections some of these topics will be briefly discussed.

7.2.1 Enhancement of SON induced in thermally poled optical fibres via deposition of semiconductor materials

The enhancement of SON induced in optical fibres thermally poled is still a main target which needs to be pursued in the near future. Early steps cited in this thesis work consist in the first deposition of semiconductor inside the cladding holes of step-index fused silica fibres, with the demonstration that it is possible to exploit the semiconductor deposited as electrode for induction poling. This result can be considered a first step towards the final purpose of measuring an enhancement of the nonlinearity induced by thermal poling in optical fibres with intrinsically nonlinear materials (semiconductors as silicon, germanium or ZnSe, but also 2D-materials, such as MoS_2 or Graphene).

7.2.2 Nonlinear functionalisation of NC-HCFs via deposition of semiconductor materials

Another topic to study and pursue is the functionalisation of NC-HCFs via deposition of semiconductors and also 2D-materials. The demonstration of electro-optic modulation or switching is the main target of this part of future work, but also the possibility of exploiting functional material for light generation and manipulation is an exciting prospect. The established analogy between a composite-material and a conventional single-material ARF suggests that only the overall optical path traveled by light at the core boundary is relevant for antiresonance guidance. This opens up the possibility to exploit the properties of additional materials deposited on the basic optical fiber matrix in order to activate and functionalise its behaviour, for example, via the free carrier plasma dispersion effect, in which the change of refractive index and absorption resulting from a change in the concentration of free carriers by photo-excitation can be used in silicon-based, all-fiber integrated modulators to achieve intensity or phase modulation. As a first step of this active hollow-core waveguide concept, we have already investigated the feasibility of a particular form of CM-ARF, in which the core-boundary membrane is made of a composite hybrid semiconductor/glass material [205].

7.2.3 Thermal poling by induction and aqueous solutions of solid core MOFs

The possibility of thermally poling solid core MOFs is still a very important target, because theoretically could allow for obtaining a η_{SH} up to 10^4 times bigger than the one induced via poling in common step-index fused silica fibres [125]. In this thesis a qualitative proof (represented by the HF etching of the poled fibre) has been presented about the possibility of exploiting induction poling and liquid electrodes embedded in the capillaries of the microstructure but of course the important proof would be the measurement of some nonlinear phenomenon related to the induced SON. The numerical simulations performed in $COMSOL^{TM}$ Multiphysics and reported in section 4.3 represent a solid base where to establish the implementation of further models of solid core MOFs equipped with liquid electrodes or even with semiconductor materials in the holes of the microstructure.

7.2.4 New applications of all-fibre, low loss, metre-long nonlinear devices

Apart from the generation of high order harmonics, already discussed in sections 5.3.1 and 5.3.2, where our PPSFs poled with liquid electrodes have been used as sources of SH and TH for cascaded four-wave mixing processes in OMFs, the number of possible applications of all-fibre, low loss, metre-long nonlinear devices characterized by an enhanced nonlinear behaviour is huge, and goes from frequency doubling for laser sources to electro-optic devices as modulators and switches, ring resonators for OPO, cavity solitons and frequency combs, fibre sensors, infrared countermeasures, quantum light sources, etc. A visual representation of most of them is reported in Fig. 7.1. In the next two sections two of these applications,

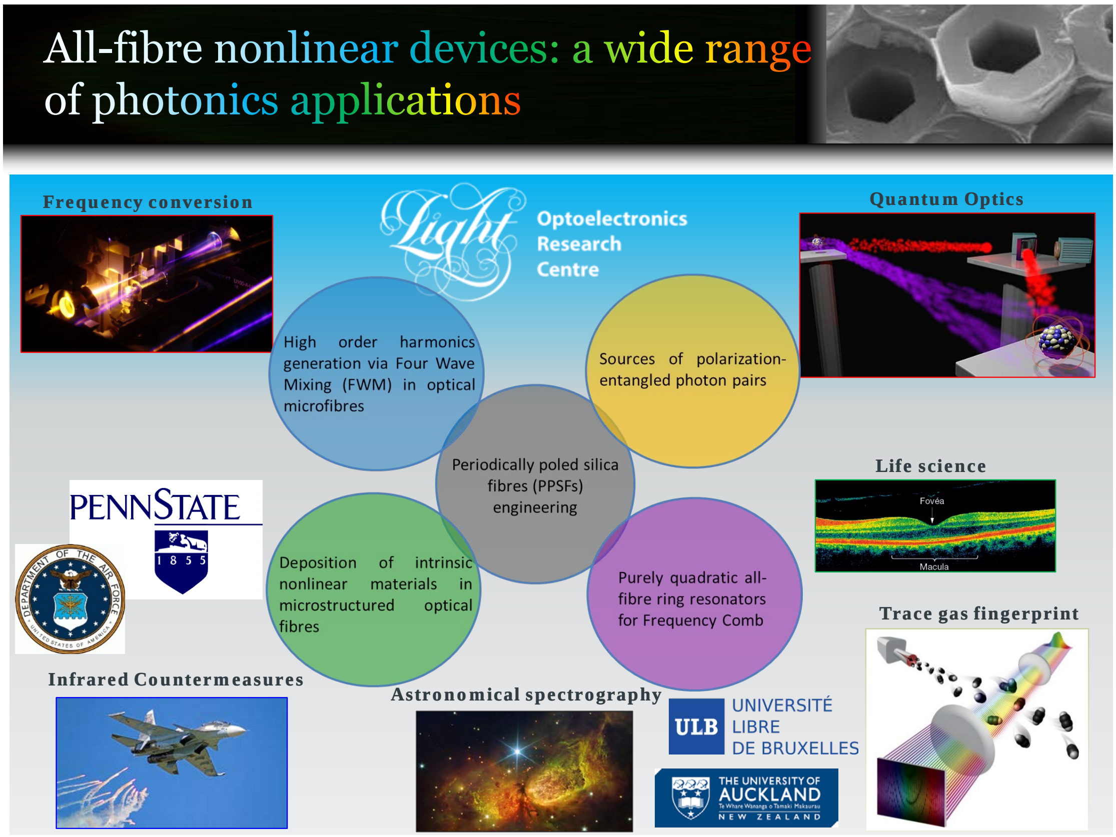

FIGURE 7.1: Principal applications of the integrated technological platform developed in this thesis work.

will be presented in detail. They represent topics of collaborations already settled up.

7.2.4.1 Purely quadratic ring resonators for frequency comb

Frequency combs (whose discovery and principles led J. L. Hall and T. W. Hänsch to the Nobel Prize in Physics in 2005) are light sources whose spectrum is composed of a sequence of equally spaced frequency components. They can be used as spectral rulers that allow for unknown optical frequencies to be measured with unprecedented precision [216]. The number of scientific fields where they have already had a relevant impact is huge, as it can be visually observed from Fig. 7.2. The origin of frequency comb generation is related to the demonstration of the first mode-locked laser [217]. As the optical field at the output of a mode locked laser consists of a train of pulses with fixed phase relationships, its optical Fourier spectrum must consist of a series of equally spaced lines. Now commercially available, stabilized frequency comb systems relying on mode-locked lasers are however bulky and expensive such that they struggle to be adopted outside of laboratories. These issues induced some research groups to work on the miniaturization of frequency comb technology. The potential portability, the ability to mass manufacture and the high power efficiency of such comb sources could open new applications to this impressive technology.

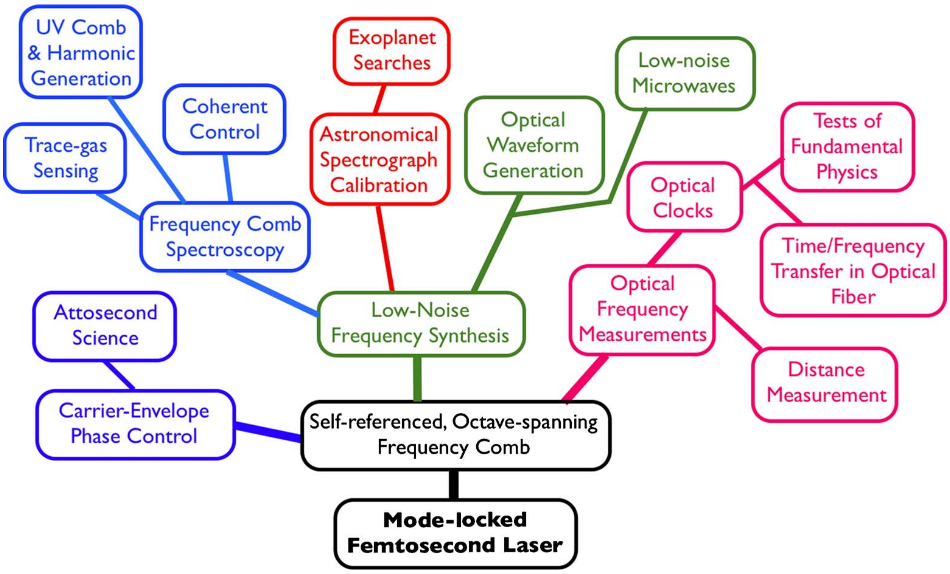

FIGURE 7.2: Applications of frequency combs [218].

In 2007 a relevant step in the direction of miniaturization was made by the first demonstration of frequency comb generation, directly from a continuous-wave laser coupled into a microresonator, a glass toroid smaller than the diameter of human hair [219]. It is now well-understood that these combs originate from the third-order optical (Kerr) nonlinearity, via a process known as modulation instability (MI). Simultaneously with the commercial development of microresonator sources, some limitations of this technology have been unveiled. In particular, existing microresonator sources are intrinsically unsuitable for the generation of frequency combs in particular key regions of the electromagnetic spectrum, such as the visible wavelengths, fundamental for applications such as Raman spectroscopy [220] and optical coherence tomography (OCT) [221], as well as the spectroscopically rich mid-infrared. In order to overcome these limits it has been conceived the idea of using the second order (quadratic) nonlinearity of materials instead of the third order (Kerr) nonlinearity.

Furthermore, recent experiments in bulky free-space resonators have demonstrated that frequency comb generation can occur entirely through quadratic effects [26]. The intrinsic features of the second order nonlinearity hold promise to deliver access to new regions of the electro-magnetic spectrum beyond conventional frequency comb technologies. Unfortunately, experimental investigations are scarce and the physics that underlie frequency comb formation in quadratic resonators is poorly understood. The main target of the project where my PPSFs are involved is to realize a complete characterization of frequency comb generation in dispersive quadratically nonlinear resonators. This work deals with the development and optimization of platforms for the experimental realization of quadratic frequency combs. The main role in this project is represented by the PPSFs poled by means of liquid metallic electrodes. The aim, at the moment, is the realization of low loss, efficient and metre-long PPSFs, to be used as all-fibre ring resonators for quadratic frequency comb generation. Improving the UV erasure technique with the aim of making it more easily feasible in a device of 1 m of length, increasing the SON by means of a process of optimization of the experimental conditions of the thermal poling experiments of fused silica step-index fibres but also the development of a technological platform to enhance the nonlinearity by means of a process of functionalisation of both the twin-hole step index PPSFs or NC-HCFs via the deposition of 2D materials or semiconductors possessing intrinsic second and third order nonlinearity, are the most important targets to be fulfilled in my future research activity.

Fig. 7.3 shows how quadratic resonators would outperform well-known Kerr resonators. The three-wave interaction inherent to the second order nonlinearity allows for generating frequency combs simultaneously in different parts of the electromagnetic spectrum. This is of paramount importance because the current trend in microresonator frequency comb generation is to reach for new spectral windows, such as the Raman efficient visible [222] and the spectroscopically rich Mid-IR [223]. Kerr combs generation in these regions is extremely challenging mainly because of the lack of efficient laser sources and the strong normal dispersion of most materials. The use of the second order nonlinearity would naturally lift those limits. Moreover, the simultaneous generation of distant combs promises to transform the way frequency combs are stabilized. However, experimental investigations are scarce and the underlying mechanisms allowing for frequency comb generation in quadratic resonators are very poorly understood.

(a) Kerr comb schematic

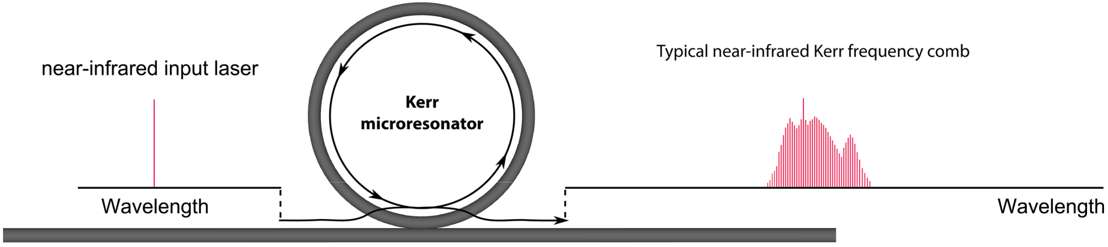

(b) Quadratic comb schematic

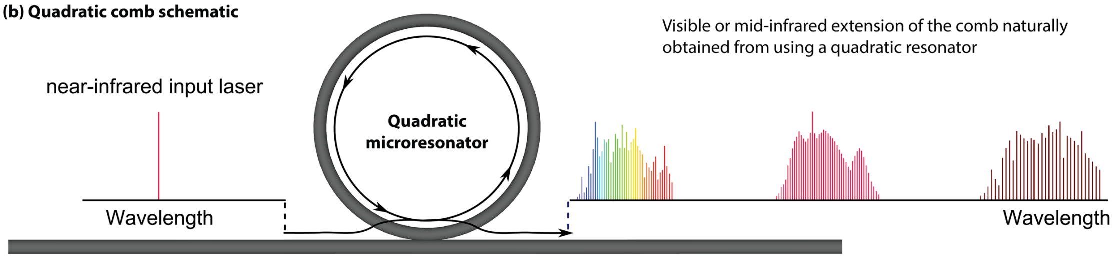

FIGURE 7.3: Schematic illustrations of frequency comb generation in (a) Kerr microresonators (adapted from [224]) and (b) quadratic microresonators (adapted from [225]). It can be envisaged that, by harnessing second order nonlinear phenomena, frequency combs can be pushed to new spectral regions.

An important step further in the comprehension of the physics of the purely quadratic ring resonators is represented by the work of Leo *et al.*, who, in 2016, developed a completely new theoretical model for quadratic frequency comb generation (in the case of cavity second harmonic generation) and obtained excellent agreement with experimental results (see Fig. 7.4), providing great insight into the physics at play [226]. Specifically, they fully grasp the role played by the dispersion (responsible for frequency dependent propagation velocities) in this system and shed light on the locking mechanism allowing distant combs to keep the same spacing, confirming the huge potential of quadratic frequency combs. This system is singly resonant, meaning that only one of the two waves was enhanced by the resonator. A further progress in the theoretical comprehension of the dynamics of the quadratic frequency comb generation is represented by the work of Leo *et al.*, published in 2016, where the dynamics of a doubly-resonant cavity (both the waves resonate) is theoretically studied [227].

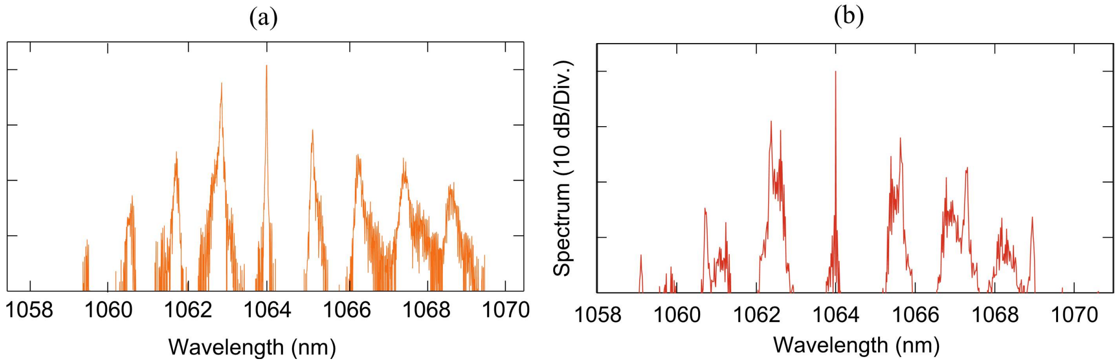

FIGURE 7.4: Comparison of (a) experimental and (b) numerically simulated spectra at the output of a free-space cavity-enhanced second-harmonic generation system. Experimental plot is adapted from [26]; Simulation is included in [226].

Besides the Cavity Second Harmonic Generation (CSHG), the other important case of intracavity conversion based on a SON is represented by the optical parametric oscillators (OPO), resonators that enhance parametric down conversion, that is the conversion of one photon to two photons at longer wavelengths [228].

The main goal of the project where I am involved is to experimentally investigate quadratic frequency combs in a fibre based setup. Fibre cavities allow for an excellent understanding of the physics at play [229]. The main component is the one providing the quadratic nonlinearity, that is my PPSF. A robust doubly (or singly) resonant dispersive quadratic cavity will allow to probe all the dynamical regimes uncovered through the extensive modeling of cavity enhanced second harmonic generation and optical parametric oscillators already developed. The main challenge lies in maintaining high finesse that is necessary for the setup to be correctly modeled by these mean field models.

These experimental results are expected to have impact beyond the field of frequency comb generation, for example offering robust and efficient frequency conversion throughout the transparency window of silica. Moreover, doubly resonant intracavity second harmonic generation was first theoretically proposed in the context of quantum optics [230]. It was shown that the nonlinear interaction leads to the generation of squeezed light, in both the singly [231] and doubly [232] resonant configurations. It is reasonable to expect that robust, fully stabilized setups hold promise to improve those results.

7.2.4.2 Sources of polarization-entangled photon pairs

In section 2.2.7.1 SPDC (also defined parametric fluorescence) has been already introduced as one of the nonlinear effects which it would be possible to produce in a medium with a non zero SON. This effect is actually a particular case of DFG, where the conversion of a photon of frequency ω_1 in two photons of frequencies ω_2 and ω_3, happens spontaneously, without the need of the incident *signal* (in this case the photon of frequency ω_2) [9]. This process occurs in accordance with conservation laws of energy and momentum:

$$\omega_1 = \omega_2 + \omega_3 \tag{7.1}$$

$$\boldsymbol{k_1} = \boldsymbol{k_2} + \boldsymbol{k_2} \tag{7.2}$$

where ω_1 and $\boldsymbol{k_1}$, ω_2 and $\boldsymbol{k_2}$, ω_3 and $\boldsymbol{k_3}$ are respectively frequency and wave vector of pump, signal and idler. If we consider a photon-crystal interaction among the three photons within a uniaxial crystal, where the pump photon is partially or fully polarized in an extraordinary direction relative to the crystals optical axis, SPDC can be implemented in two different varieties, characterized by the polarizations of the signal and idler. If both outgoing photons are ordinary in their polarization, it is called Type-I down-conversion. If one of the photons is extraordinarily polarized while the other is ordinary, it is called Type-II. In either case, the outgoing photons are correlated in their polarization.

The process of SPDC has found common application in various fields of research. More recently it found a massive application in quantum optics and quantum information technology. One of the most common quantum applications is the generation of polarization entangled photon pairs, realized either in periodically poled waveguides (such as for example periodically poled Potassium Titanyl Phosphate (PPKTP) [233] and periodically poled Lithium Niobate (PPLN) [234]) and in bulk crystals [233]). It is the correlation between the down-converted photon polarization states that makes possible the production of polarization-entangled photons. Entanglement is the quantum phenomenon where the state of a system of two or more particles is not determined by the states of the individual particles alone, and only occurs when the particles of the system share a correlation. If two photons are correlated in their polarizations, measuring the polarization state of one determines the state of the other, without having to measure it. SPDC is adequate to produce photons which are both correlated.

In optical fibres, the generation of photon pairs was initially realized by means of a four wave mixing process [235]. The first observation of SPDC in periodically poled fibres was made by Bonfrate *et al.* in 1999, even if in that work the periodically poled fibre used was a D-shape fibre [236]. In 2007 quasi-phase matched SPDC was observed inside a periodically poled twin-hole fused silica fibre [237]. Two years later, in 2009, Helt *et al.* proposed to use a straight piece of periodically poled fibre at room temperature to generate pairs of orthogonally polarized photons in a QPM-SPDC process of type II (the one related to the third peak of the tuning curve shown in Fig. 5.6). These pairs of orthogonally polarized photons can be further processed to serve as either a source of single photons, if passed through a polarization beam splitter so that one photon can herald the other, or polarization-entangled photons [238]. In 2012 for the first time it was experimentally demonstrated the generation of polarization entangled photon pairs in a periodically poled twin-hole fused silica fibre [239].

Starting from the last cited work of Zhu *et al.*, it was chosen to exploit some of the periodically poled fibres poled by means of mercury liquid electrodes to produce QPM-SPDC process of type-II, with the aim of generating orthogonally polarized photons in some experiments related to the field of gravitational quantum physics (F. Massa, University of Vienna, private communication). The future aim of this part of my work is to improve the efficiency of SPDC via the enlargement of the device length (which also contributes to the restriction of the bandwidth of the nonlinear device, highly desired in these kind of experiments) and the enhancement of the SON induced into the fibre via thermal poling and via different techniques of nonlinear functionalisation, such as those explained in more details in chapter 6.

Appendix A

List of Publications

A.1 Journal Papers

W. Belardi, **F. De Lucia**, F. Poletti, and P. J. A. Sazio, *Composite material hollow antiresonant fibers*, Optics Letters, Vol. 42, Issue 13, pp. 2535 - 2538 (2017)

F. De Lucia, D. Keefer, C. Corbari, and P. J. A. Sazio, *Thermal poling of silica optical fibers using novel liquid electrodes*, Optics Letters, Vol. 42, Issue 1, pp. 69 - 72 (2017)

M. I. M. Abdul Khudus, T. Lee, **F. De Lucia**, C. Corbari, P. J. A. Sazio, P. Horak, and G. Brambilla, *All-fiber fourth and fifth harmonic generation from a single source*, Optics Express, Vol. 24, Issue 19, pp. 21777 - 21793 (2016)

F. De Lucia, D. Huang, C. Corbari, N. Healy, and P. J. A. Sazio, *Optical fiber poling by induction: analysis by 2D numerical modeling*, Optics Letters, Vol. 41, Issue 8, pp. 1700 - 1703 (2016)

M. I. M. Abdul Khudus, **F. De Lucia**, C. Corbari, T. Lee, P. Horak, P. J. A. Sazio, and G. Brambilla, *Phase-matched parametric amplification via four-wave mixing in optical microfibers*, Optics Letters, Vol. 41, Issue 4, pp. 761 - 764 (2016)

F. De Lucia, D. Huang, C. Corbari, N. Healy, and P. J. A. Sazio, *Optical fiber poling by induction*, Optics Letters, Vol. 39, Issue 22, pp. 6513 - 6516 (2014)

A.2 Conference Papers (with abstracts)

Y. Wang, J. He, M. I. M. Abdul Khudus, R. Ismaeel, **F. De Lucia**, P. J. A. Sazio, P. Horak, N. Chiodini, M. Beresna, and G. Brambilla, *UV light generation in optical fibers*, Asia Communications and Photonics Conference (ACP) (2016)
Abstract: UV light has been generated in optical fibers using nonlinear optics (harmonic generation) and rare earth doping with Gd^{3+}.

W. Belardi, P. Sazio, **F. De Lucia**, and F. Poletti, *Composite material hollow antiresonant fibers*, Frontiers in Optics (FiO), FTu2I.3 (2016)
Abstract: We analyze air-core fiber designs with different materials in the cladding, including structures with an extended bandwidth and hybrid semiconductor/glass fibers with very low attenuation. We report on the first realization of this fiber type.

Y. Wang, M. I. M. Abdul Khudus, **F. De Lucia**, Q. Sun, J. He, P. J. A. Sazio, R. Ismaeel, M. Beresna, P. Horak, and G. Brambilla, *UV generation in silica fibres*, Frontiers in Optics (FiO), FTu1I.1 (2016)
Abstract: The generation of UV light in solid core silica fibres has been achieved using four wave mixing in optical fibre tapers or rare earth doping with Gd^{3+}.

M. Abdul Khudus, Y. Wang, **F. De Lucia**, J. He, M. Beresna, P. J. Sazio, P. Horak, N. Chiodini, and G. Brambilla, *UV generation in silica optical fibres: from rare earth doping to nonlinear optics in nanofibers*, Energy, Materials and Nanotechnology (ENM) Workshop on Optoelectronics (2016)
Abstract: UV generation in optical fibres has long been deemed challenging because of lack of suitable lasing ions in the UV and the poor transparency of germanosilicate fibres at wavelengths shorter than lambda = 400 nm. In our experiments, optical fibres with pure silica core and fluorosilicate cladding have been used, providing a loss smaller than 1dB/m at lambda < 300 nm. Two different techniques were used to achieve light generation at lambda < 400 nm: nonlinear

optics in tapered optical fibres with sub-micrometric diameter (nanofibers) and doping with rare-earths.

M. I. M. Abdul Khudus, **F. De Lucia**, C. Corbari, T. Lee, P. Horak, P. Sazio, and G. Brambilla, *Four-wave mixing UV generation in optical microfibers*, Proceedings of SPIE - The International Society for Optical Engineering, Vol. 9894, n. 98941I (2016)

Abstract: UV generation via four-wave-mixing (FWM) in optical microfibres (OMFs) was demonstrated. This was achieved by exploiting the tailorable dispersion of the OMF in order to phase match the propagation constant of the four frequencies involved in the FWM process. In order to satisfy the frequency requirement for FWM, a Master Oscillator Power Amplifier (MOPA) working at the telecom C-band was connected to a periodically poled silica fibre (PPSF), producing a fundamental frequency (FF) at 1550.3 nm and a second harmonic (SH) frequency at 775.2 nm. A by-product of this second harmonic generation is the generation of a signal at the third harmonic (TH) frequency of 516.7 nm via degenerate FWM. This then allows the generation of the fourth harmonic (FH) at 387.6 nm and the fifth harmonic (5H) at 310 nm via degenerate and nondegenerate FWM in the OMF.The output of the PPSF was connected to a pure silica core fibre which was being tapered using the modified flame brushing technique from an initial diameter of 125 μm to 0.5 μm. While no signal at any UV wavelength was initially observed, as the OMF diameter reached the correct phase matching diameters, signals at 387.6 nm appeared. Signals at 310 nm also appeared although it is not phase matched, as the small difference in the propagation constant is bridged by other nonlinear processes such as self-phase and cross phase modulation.

F. De Lucia, C. Corbari, D. Keefer, and P. J. A. Sazio, *Comparison of novel liquid electrodes for silica optica fiber thermal poling*, Conference on Lasers and Electro-Optics (CLEO), SM1P.8 (2016)

Abstract: We report experimental analysis of optical fibers thermally poled over long lengths using novel types of internal liquid electrodes to generate effective second-order nonlinearities. Our analysis includes transmission losses, depletion region formation, SHG at telecom pump wavelengths.

D. Huang, **F. De Lucia**, C. Corbari, N. Healy and P.J.A. Sazio, *Numerical analysis using 2D modeling of optical fiber poled by induction*, Proceedings of SPIE - The International Society for Optical Engineering, Vol. 9742, n. 97421O (2016)
Abstract: Thermal poling, a technique to introduce effective second-order nonlinearities in silica optical fibers, has found widespread applications in frequency conversion, electro-optic modulation, switching and polarization-entangled photon pair generation. Since its first demonstration around 25 years ago, studies into thermal poling were primarily based on anode-cathode electrode configurations. However, more recently, superior electrode configurations have been investigated that allow for robust and reliable thermally poled fibers with excellent second order nonlinear properties. Very recently, we experimentally demonstrated an electrostatic induction poling technique that creates a stable second-order nonlinearity in a twin-hole fiber without any direct physical contact to internal fiber electrodes whatsoever. This innovative technique lifts a number of restrictions on the use of complex microstructured optical fibers (MOF) for poling, as it is no longer necessary to individually contact internal electrodes and presents a general methodology for selective liquid electrode filling of complex MOF geometries. In order to systematically implement these more advanced device embodiments, it is first necessary to develop comprehensive numerical models of the induction poling mechanism itself. To this end, we have developed two-dimensional (2D) simulations of space-charge region formation using COMSOL finite element analysis, by building on current numerical models.

M. I. M. Abdul Khudus, **F. De Lucia**, C. Corbari, T. Lee, P. Sazio, P. Horak, and G. Brambilla, *Four-wave mixing enhancement in optical microfibers*, IEEE Optical Fiber Communications (OFC), Tu2E.2 (2016)
Abstract: Four-Wave-Mixing (FWM) is enhanced by tailoring the modal effective index in optical microfibers to improve the phase matching conditions. An enhancement of > 25 dB was recorded in a 6-mm-long optical microfiber.

D. Huang, **F. De Lucia**, N. Healy, C. Corbari, and P. Sazio, *Who needs contacts? Optical fiber poling by induction*, OSA Bragg Gratings, Photosensitivity, and Poling in Glass Waveguides (BGPP), BW1D-2 (2014)
Abstract: Conventional thermal poling methods require direct physical contact to internal fibers electrodes. Here, we report a novel indirect method in which

external fields are used to charge floating internal electrodes to generate depletion regions for SHG.

Bibliography

[1] J. Tyndall, “On some phenomena connected with the motion of liquids”, Proc. Roy. Inst. of Great Britain 1, pp. 446 - 448 (1854)

[2] J. L. Baird, British Patent 285,738 (1927)

[3] C. W. Hansell, U.S. Patent 1,751,584 (1930)

[4] F. P. Kapron, D. B. Keck, and R. D. Maurer, “Radiation losses in glass optical waveguides”, Appl. Phys. Lett., Vol. 17, No. 10, pp. 423 - 425 (1970)

[5] `https://www.nature.com/subjects/nonlinear-optics`

[6] P. N. Butcher, D. Cotter, “The elements of nonlinear optics”, Cambridge University Press, New York (1990)

[7] B. E. A. Saleh, M. C. Teich, “Fundamentals of photonics”, John Wiley & Sons, Inc (1991)

[8] P. A. Franken, A. E. Hill, C. W. Peters, and G. Weinreich, “Generation of optical harmonics”, Phys. Rev. Lett., Vol. 7, No. 4, pp. 118 - 119 (1961)

[9] R. W. Boyd, “Nonlinear optics”, Academic Press (1992)

[10] R. A. Myers, N. Mukherjee, and S. R. J. Brueck, “Large second-order nonlinearity in poled fused silica”, Opt. Lett., Vol. 16, No. 22, pp. 1732 - 1734 (1991)

[11] W. Xu, P. Blazkiewicz, and S. Fleming, “Silica fiber poling technology”, Adv. Mater., Vol. 13, No. 12 - 13, pp. 1014 - 1018 (2001)

[12] H. Knape, and W. Margulis, “All-fiber polarization switch”, Opt. Lett., Vol. 32, No. 6, pp. 614 - 616, (2007)

[13] W. Margulis, O. Tarasenko and N. Myrén, “Who needs a cathode? Creating a second-order nonlinearity by charging glass fiber with two anodes”, Opt. Exp., Vol. 17, No. 18, pp. 15534 - 15540 (2009)

[14] R. G. Batchko, G. D. Miller, A. Alexandrovski, M. M. Fejer, and R. L. Byer, “Limitations of high-power visible wavelength periodically poled lithium niobate devices due to green-induced infrared absorption and thermal lensing”, Proc. Lasers and Electro-Optics, CTuD6G (1998)

[15] Y. Furukawa, K. Kitamura, A. Alexandrovski, R. K. Route, M. M. Fejer, and G. Foulon, “Green-induced infrared absorption in MgO doped $LiNbO_3$”, Appl. Phys. Lett., Vol. 78, pp. 1970 - 1972 (2001)

[16] J. C. Knight, T. A. Birks, P. St. J. Russell, and D. M. Atkin, “All-silica single-mode fiber with photonic crystal cladding”, Opt. Lett., Vol. 21, No. 19, pp. 1547 - 1549 (1996)

[17] T. A. Birks, J. C. Knight, and P. St. J. Russell, “Endlessly singlemode photonic crystal fiber”, Opt. Lett., Vol. 22, No. 13, pp. 961 - 963 (1997)

[18] K. S. Novoselov, A. K. Geim, S. V. Morozov, D. Jiang, Y. Zhang, S. V. Dubonos, I. V. Grigorieva, and A. A. Firsov, “Electric field effect in atomically thin carbon films”, Science, Vol. 306, pp. 666 - 669 (2006)

[19] K. F. Mak, C. Lee, J. Hone, J. Shan, and T. F. Heinz, “Atomically thin MoS_2: a new direct gap semiconductor”, Phys. Rev. Lett., Vol. 105, 136805 (2010)

[20] P. J. A. Sazio, A. Amezcua-Correa, C. E. Finlayson, J. R. Hayes, T. J. Scheidemantel, N. F. Baril, B. R. Jackson, D. J. Won, F. Zhang, E. R. Margine, V. Gopalan, V. H. Crespi, J. V. Badding, “Microstructured optical fibers as high-pressure microfluidic reactors”, Science, Vol. 311, No. 5767, pp. 1583 - 1586 (2006)

[21] J. Yang, Y. Gu, E. Lee, H. Lee, S. H. Park, M. H. Cho, Y. H. Kim, Y.-H. Kim, and H. Kim, “Wafer-scale synthesis of thickness-controllable MoS_2 films via solution-processing using a dimethylformamide/n-butylamine/2-aminoethanol solvent system”, NANOSCALE, Vol. 7, No. 20, pp. 9311 - 9319 (2015)

[22] Y. R. Lim, W. Song, J. K. Han, Y. B. Lee, S. J. Kim, S. Myung, S. S. Lee, K.-S. An, C.-J. Choi, and J. Lim, “Wafer-Scale, homogeneous MoS_2 layers on

plastic substrates for flexible visible-light photodetectors", Advanced Materials, Vol. 28, No. 25, pp. 5025 - 5030 (2016)

[23] V. Pruneri, G. Bonfrate, P. G. Kazansky, D. J. Richardson, N. G. Broderick, and J. P. de Sandro, "Greater than 20%-efficient frequency doubling of 1532-nm nanosecond pulses in quasi-phase-matched germanosilicate optical fibers", Opt. Lett., Vol. 24, No. 4, pp. 208 - 210 (1999)

[24] E. Zhu, Z. Tang, L. Qian, L. G. Helt, M. Liscidini, J. E. Sipe, C. Corbari, A. Canagasabey, M. Ibsen, and P. G. Kazansky, "Direct generation of polarization-entangled photon pairs in a poled fiber", Phys. Rev. Lett., Vol. 108, pp. 213902-1 - 213902-5 (2012)

[25] T. Mizunami, K. Okazaki, H. Sato, and R. Kawamoto, "Second-harmonic generation and electro-optic modulation in thermally poled and unpoled twin-hole silica-glass optical fiber", Proceedings of SPIE - The International Society for Optical Engineering, Vol. 8071, No. 80710T, (2011)

[26] I. Ricciardi, S. Mosca, M. Parisi, P. Maddaloni, L. Santamaria, P. De Natale, and M. De Rosa, "Frequency comb generation in quadratic nonlinear media", Phys. Rev. A, Vol. 91, No. 063839 (2015)

[27] A. Canagasabey, M. Ibsen, K. Gallo, A. V. Gladyshev, E. M. Dianov, C. Corbari, and P. G. Kazansky, "Aperiodically poled silica fibers for bandwidth control of quasi-phase-matched second-harmonic generation", Opt. Lett., Vol. 35, No. 5, pp. 724 - 726 (2010)

[28] J. A. Armstrong, N. Bloembergen, J. Ducuing, and P. S. Pershan, "Interactions between light waves in a nonlinear dielectric", Phys. Rev., Vol. 127, No. 6, pp. 1918 - 1939 (1962)

[29] J. A. Buck, "Fundamentals of optical fibers", John Wiley & Sons, Inc (1995)

[30] P. St. J. Russell, "Photonic crystal fibers", Science, New Series, Vol. 299, No. 5605, pp. 358 - 362 (2003)

[31] P. St. J. Russell, "Photonic-crystal fibers", J. Light. Tech., Vol. 24, No. 12, pp. 4729 - 4749 (2006)

[32] J. C. Knight, J. Broeng, T. A. Birks, P. St. J. Russell, "Photonic Band Gap Guidance in Optical fibers", Science, Vol. 282, No. 5393, pp. 1476 - 1478 (1998)

[33] R. F. Cregan, B. J. Mangan, J. C. Knight, T. A. Birks, P. St. J. Russell, P. J.Roberts and D. C. Allan, “Single-Mode Photonic Band Gap Guidance of Light in Air”, Science, New Series, Vol. 285, No. 5433, pp. 1537 - 1539 (1999)

[34] E. Yablonovitch, “Photonic band-gap structures”, J. Opt. Soc. Am. B, Vol. 10, No. 2, pp. 283 - 205 (1993)

[35] P. St. J. Russell, T. A. Birks, F. D. Lloyd-Lucas, “Photonic Bloch waves and photonic band gaps”, Confined Electrons and Photons: New Physics and Applications, E. Burstein and C. Weisbuch, Eds. (Plenum, New York), Vol. 340, pp. 585 - 633 (1995)

[36] T. A. Birks, P. J. Roberts, P. St. J. Russell, D. M. Atkin, and T. J. Shepherd, “Full 2D photonic band gaps in silica/air structures”, Electron. Lett., Vol. 31, No. 22, p. 1941 - 1943 (1995)

[37] N. M. Litchinitser, A. K. Abeeluck, C. Headley, and B. J. Eggleton, “Antiresonant reflecting photonic crystal optical waveguides”, Opt. Lett., Vol. 27, No. 18, p. 1592 - 1594 (2002)

[38] M. A. Duguay, Y. Kokubun, T. L. Koch and Loren Pfeiffer, “Antiresonant reflecting optical waveguides in SiO_2Si multilayer structures”, Appl. Phys. Lett., Vol. 49, No. 1, p. 13 - 15 (1986)

[39] F. Luan, A. K. George, T. D. Hedley, G. J. Pearce, D. M. Bird, J. C. Knight, and P. St. J. Russell, “All-solid photonic bandgap fiber”, Opt. Lett., Vol. 29, No. 20, p. 2369 - 2371 (2004)

[40] G. Bouwmans, L. Bigot, Y. Quiquempois, F. Lopez, L. Provino, and M. Douay, “Fabrication and characterization of an allsolid 2D photonic bandgap fiber with a low-loss region ($<$ 20 dB/km) around 1550 nm”, Opt. Exp., Vol. 13, No. 21, pp. 8452 - 8459 (2005)

[41] A. D. Pryamikov, A. S. Biriukov, A. F. Kosolapov, V. G. Plotnichenko, S. L. Semjonov, and E. M. Dianov, “Demonstration of a waveguide regime for a silica hollow-core microstructured optical fiber with a negative curvature of the core boundary in the spectral region $> 3.5\ \mu m$”, Opt. Exp., Vol. 19, No. 2, pp. 1441 - 1448 (2011)

[42] F. Yu, and J. C. Knight, “Negative curvature hollow-core optical fiber”, IEEE J. Sel. Top. Quantum Electron., Vol. 22, No. 2, 4400610-1 - 4400610-11 (2016)

[43] C. C. Davis, “Lasers and electro-optics”, Cambridge University Press, New York (1996)

[44] E. Y. Zhu, L. Qian, L. G. Helt, M. Liscidini, J. E. Sipe, C. Corbari, A. Canagasabey, M. Ibsen, and P. G. Kazansky, “Measurement of $\chi^{(2)}$ symmetry in a poled fiber”, Opt. Lett., Vol. 35, No. 10, pp. 1530 - 1532 (2010)

[45] M. Born, and E. Wolf, “Principle of optics”, Pergamon press, London (1959)

[46] D. Gloge, “Weakly guiding fibers”, Appl. Opt., Vol. 10, No. 10, pp. 2252 - 2258 (1971)

[47] D. Marcuse, “Light transmission optics”, Van Nostrand, Princeton (1982)

[48] D. Marcuse, “Theory of dielectric optical waveguides”, Academic Press, New York (1991)

[49] A. W. Snyder, and J. D. Love, “Optical waveguide theory”, Chapman and Hall, New York (1983)

[50] P. G. Kazansky, and V. Pruneri, “Electric-field poling of quasi-phase-matched optical fibers”, J. Opt. Soc. Am. B, Vol. 14, No. 11, pp. 3170 - 3179 (1997)

[51] M. M. Fejer, G. A. Magel, D. H. Jundt, and R. L. Byer, “Quasi-phase matched second-harmonic generation: tuning and tolerances”, IEEE Journal of Quantum Electronics, Vol. 28, No. 11, pp. 2631 - 2653 (1992)

[52] G. P. Agrawal, “Nonlinear fiber Optics”, Optics and Photonics, Academic Press, (1995)

[53] P. P. Ho, D. Ji, Q. Z. Wang, and R. R. Alfano, “Temporal behaviour of cross-phase-modulated second-harmonic generation of ultrashort laser pulses in nonlinear-optical media”, J. Opt. Soc. Am. B, Vol. 7, No. 3, pp. 276 - 284 (1990)

[54] J. Comley, and E. Garmire, “Second harmonic generation from short pulses”, Appl. Phys. Lett., Vol. 12, No. 1, pp. 7 - 9 (1968)

[55] M. I. A. Khudus, T. Lee, F. De Lucia, C. Corbari, P. Sazio, P. Horak, and G. Brambilla, “All-fiber fourth and fifth harmonic generation from a single source”, Opt. Exp., Vol. 24, No. 19, pp. 21777 - 21793 (2016)

[56] “ASTM Standards on Glass and Glass Products ”, ASTM Committee C14, American Society for Testing Materials (1955)

[57] W. H. Zachariasen, “The atomic arrangement in glass”, J. Am. Chem. Soc., Vol. 54, No. 10, pp. 3841 - 3851 (1932)

[58] B. E. Warren, “The basic principles involved in the glassy state”, J. Appl. Phys., Vol. 13, No. 10, pp. 602 - 610 (1942)

[59] S. R. Elliott, “Physics of amorphous materials”, Longman, London and New York (1983)

[60] B. E. Warren, and J. Biscoe, “Fourier Analysis of X-ray patterns of soda-silica glass”, J. Am. Ceram. Soc., Vol. 21, No. 7, pp. 259 - 265 (1938)

[61] M. Yamane, and Y. Asahara, “Glasses for photonics”, Cambridge University Press (2000)

[62] Y. Fujii, B. S. Kawasaki, K. O. Hill, and D. C. Johnson, “Sum-frequency light generation in optical fibers”, Opt. Lett., Vol. 5, No. 2, pp. 48 - 50 (1980)

[63] Y. Sasaki and Y. Ohmori, “Phasematched sumfrequency light generation in optical fibers”, Appl. Phys. Lett., Vol. 39, No. 6, pp. 466 - 468 (1981)

[64] Y. Ohmori, and Y. Sasaki, “Two-wave sum-frequency light generation in optical fibers”, IEEE Transactions on Microwave theory and techniques, Vol. MTT-30, No. 4, pp. 604 - 608 (1982)

[65] J. M. Gabriagues and L. Fersing, “Second and third harmonic generation in optical fibers”, OSA Technical Digest of Conference on Lasers and Electro-Optics, paper THI33 (1984)

[66] U. Osterberg and W. Margulis, “Dye laser pumped by Nd:YAG laser pulses frequency doubled in a glass optical fibers”, Opt. Lett., Vol. 11, No. 8, pp. 516 - 518 (1986)

[67] U. Osterberg and W. Margulis, “Experimental studies on efficient frequency doubling in glass optical fibers”, Opt. Lett., Vol. 12, No. 1, pp. 57 - 59 (1987)

[68] R. H. Stolen, and H. W. K. Tom, “Self-organized phase-matched harmonic generation in optical fibers”, Opt. Lett., Vol. 12, No. 8, pp. 585 - 587 (1987)

[69] D. S. Bethune, “Quadrupole second-harmonic generation for a focused beam of arbitrary transverse structure and polarization”, Opt. Lett., Vol. 6, No. 6, pp. 287 - 289 (1981)

[70] M. C. Farries, P. St. J. Russell, M. E. Fermann, D. N. Payne, “Second-harmonic generation in an optical fiber by self-written $\chi^{(2)}$ grating”, Electron. Lett., Vol. 23, No. 7, pp. 322 - 324 (1987)

[71] R. W. Terhune and D. A. Weinberger, “Second-harmonic generation in fibers”, J. Opt. Soc. Am. B, Vol. 4, No.5, pp. 661 - 674 (1987)

[72] D. M. Krol, D. J. DiGiovanni, W. Pleibel, and R. H. Stolen, “Observation of resonant enhancement of photoinduced second-harmonic generation in Tm-doped aluminosilicate glass fibers”, Opt. Lett., Vol. 18, No. 15, pp. 1220 - 1222 (1993)

[73] R. Kashyap, “Phase-matched periodic electric-field-induced second-harmonic generation in optical fibers”, J. Opt. Soc. Am. B, Vol. 6, No. 3, pp. 313 - 328 (1989)

[74] Quartz glass for optical data and properties, Heraeus Amersil Inc, 3473 Satellite Boulevard, Duluth, GA, 30136-5821

[75] N. Mukherjee, R. A. Myers, and S. R. J. Brueck, “Dynamics of second-harmonic generation in fused silica”, J. Opt. Soc. Am. B, Vol. 11, No. 4, pp. 665 - 669 (1994)

[76] A. von Hippel, E. P. Gross, J. G. Jelatis, and M. Geller, “”Photocurrent, space-charge buildup, and field emission in alkali halide crystals”, Phys. Rev., Vol. 91, No. 3, pp. 568 - 579 (1953)

[77] T. G. Alley, S. R. J. Brueck, and R. Myers, “Space charge dynamics in thermally poled fused silica”, J. of Non-Crystalline Solids, Vol. 242, No. 2 - 3, pp. 165 - 176 (1998)

[78] A. von Hippel, “C. Breakdown. Electric breakdown of solid dielectrics”, Trans. Faraday Soc., Vol. 42, A078 - A087 (1946)

[79] U. K. Krieger, and W. A. Lanford, “Field assisted transport of Na^{+} ions, Ca^{2+} ions and electrons in commercial soda-lime glass I: Experimental”, J. Non-Cryst. Solids, Vol. 159, No. 1 - 3, pp. 50 - 61 (1988)

[80] C. M. Lepienski, J. A. Giacometti, G. F. Leal Ferreira, F. L. Freire Jr., and C. A. Achete, "Electric field distribution and near-surface modifications in soda-lime glass submitted to a dc potential", J. Non-Cryst. Solids, Vol. 159, No. 3, pp. 204 - 212 (1993)

[81] Z. He, G. Borchardt, and W. Wegener, "Ionic space charge phenomena during SIMS analysis of ceramic materials", Fresenius' J. Anal. Chem., Vol. 348, No. 4, pp. 264 - 268 (1994)

[82] P. G. Kazansky, A. R. Smith, and P. St. J. Russell, G. M. Yang and G. M. Sessler, "Thermally poled silica glass: Laser induced pressure pulse probe of charge distribution", Appl. Phys. Lett., Vol. 68, No. 2, pp. 269 - 271 (1996)

[83] D. Pureur, A. C. Liu, M. J. F. Digonnet, and G. S. Kino, "Absolute measurement of the second-order nonlinearity profile in poled silica", Opt. Lett., Vol. 23, No. 8, pp. 588 - 590 (1998)

[84] K. Yamamoto, and H. Namikawa, "The irreversible and reversible changes in silica glasses observed by electrical-properties .1. Synthetic silica glass by flame fusion", J. of Ceram. Soc. Jpn (Int. Ed), Vol. 102, No. 7, pp. 658 - 664 (1994)

[85] K. Yamamoto, and H. Namikawa, "The irreversible and reversible changes in silica glasses observed by electrical-properties .2. Quartz glass by flame fusion", J. of Ceram. Soc. Jpn (Int. Ed), Vol. 103, No. 9, pp. 910 - 916 (1995)

[86] T. G. Alley, S. R. J. Brueck, and M. Wiedenbeck, "Secondary ion mass spectrometry study of space-charge formation in thermally poled fused silica", J. Appl. Phys., Vol. 86, No. 12, pp. 6634 - 6640 (1999)

[87] T. G. Alley, and S. R. J. Brueck, "Visualization of the nonlinear optical space-charge region of bulk thermally poled fused-silica glass", Opt. Lett., Vol. 23, No. 15, pp. 1170 - 1172 (1998)

[88] W. Margulis, and F. Laurell, "Interferometric study of poled glass under etching", Opt. Lett., Vol. 21, No. 21, pp. 1786 - 1788 (1996)

[89] B. Lesche, F. C. Garcia, E. N. Hering, W. Margulis, I. C. S. Carvalho, and F. Laurell, "Etching of silica glass under electric fields", Phys. Rev. Lett., Vol. 78, No. 11, pp. 2172 - 2175 (1997)

[90] A. L. C. Triques, C. M. B. Cordeiro, V. Balestrieri, B. Lesche, W. Margulis, and I. C. S. Carvalho, “Depletion region in thermally poled fused silica”, Appl. Phys. Lett., Vol. 76, No. 18, pp. 2496 - 2498 (2000)

[91] A. L. C. Triques, I. C. S. Carvalho, M. F. Moreira, H. R. Carvalho, R. Fischer, B. Lesche, and W. Margulis, “Time evolution of depletion region in poled silica”, Appl. Phys. Lett., Vol. 82, No. 18, pp. 2948 - 2950 (2003)

[92] H. An, G. Cox, and S. Fleming, “Visualization of second-order nonlinear layer in thermally poled fused silica glass”, Appl. Phys. Lett., Vol. 85, No. 24, pp. 5819 - 5821 (2004)

[93] M. Qiu, S. Egawa, K. Horimoto, and T. Mizunami, “The thickness evolution of the second-order nonlinear layer in thermally poled fused silica”, Opt. Comm., Vol. 189, No. 1 - 3, pp. 161 - 166 (2001)

[94] D. Faccio, V. Pruneri, and P. G. Kazansky, “Dynamics of the second-order nonlinearity in thermally poled silica glass”, Appl. Phys. Lett., Vol. 79, No. 17, pp. 2687 - 2689 (2001)

[95] C. S. Franco, G. A. Quintero, N. Myrn, A. Kudlinski, H. Zeghlache, H. R. Carvalho, A. L. C. Triques, D. M. Gonzlez, P. M. P. Gouva, G. Martinelli, Y. Quiquempois, B. Lesche, W. Margulis, and I. C. S. Carvalho, “Measurement of depletion region width in poled silica”, Appl. Opt, Vol. 44, No. 27, pp. 5793 - 5796 (2005)

[96] A. Kudlinski, Y. Quiquempois, and G. Martinelli, “Modeling of the $\chi^{(2)}$ susceptibility time-evolution in thermally poled fused silica”, Opt. Exp., Vol. 13, No. 20, pp. 8015 - 8024 (2005)

[97] A. Kudlinski, Y. Quiquempois, and G. Martinelli, “Time evolution of the second-order nonlinear profile within thermally-poled silica samples”, Opt. Lett., Vol. 30, No. 9, pp. 1039 - 1041 (2005)

[98] X. Liu, X. Sun, and M. Zhang, “Theoretical analysis of thermal/electric field poling fused silica with multiple carrier model”, Jpn. J. Appl. Phys., Vol. 39, Part. 1, No. 8, pp. 4881 - 4883 (2000)

[99] A. Kudlinski, G. Martinelli, Y. Quiquempois, and H. Zeghlache, “Microscopic model for the second order nonlinearity creation in thermally poled bulk silica glasses samples”, Proc. of OSA BGPP, Vol. 93, paper n. TUC3 (2003)

[100] A. Kudlinski, Y. Quiquempois, M. Lelek, H. Zeghlache, and G. Martinelli, "Complete characterization of the nonlinear spatial distribution induced in poled silica glass with a submicron resolution", Appl. Phys. Lett., Vol. 83, No. 17, pp. 3623 - 3625 (2003)

[101] P. G. Kazansky, L. Dong, and P. St. J. Russell, "High second-order nonlinearities in poled silicate fibers", Opt. Lett., Vol. 19, No. 10, pp. 701 - 703 (1994)

[102] P. G. Kazansky, P. St. J. Russell, L. Dong and C. N. Pannell, "Pockels effect in thermally poled silica optical fibers", Elect. Lett., Vol. 31, No. 1, pp. 62 - 63 (1995)

[103] V. Pruneri, and P. G. Kazansky, "Electric-field thermally poled optical fibers for quasi-phase-matched second-harmonic generation", IEEE Phot. Tech. Lett., Vol. 9, No. 2, pp. 185 - 187 (1997)

[104] T. Fujiwara, D. Wong, and S. Fleming, "Large electrooptic modulation in a thermally-poled germanosilicate fiber", IEEE Phot. Tech. Lett., Vol. 7, No. 10, pp. 1177 - 1179 (1995)

[105] D. Wong, W. Xu, S. Fleming, M. Janos, and K.-M. Lo, "Frozen-in electrical field in thermally poled fibers", Opt. Fib. Tech., Vol. 5, pp. 235 - 241 (1999)

[106] P. Blazkiewicz, W. Xu, D. Wong, S. Fleming, and T. Ryan, "Modification of thermal poling evolution using novel twin-hole fibers", J. Light. Tech., Vol. 19, No. 8, pp. 1149 - 1154 (2001)

[107] P. Blazkiewicz, W. Xu, D. Wong, and S. Fleming, "Mechanism for thermal poling in twin-hole silicate fibers", J. Opt. Soc. Am. B, Vol. 19, No. 4, pp. 870 - 874 (2002)

[108] N. Myrén, H. Olsson, L. Norin, N. Sjödin, P. Helander, J. Svennebrink and W. Margulis, "Wide wedge-shaped depletion region in thermally poled fiber with alloy electrodes", Opt. Exp., Vol. 12, No. 25, pp. 6093 - 6099 (2004)

[109] H. An, and S. Fleming, "Investigating the effectiveness of thermally poling optical fibers with various internal electrode configurations", Opt. Exp., Vol. 20, No. 7, pp. 7436 - 7444 (2012)

[110] W. M. Moreau, "Semiconductor Lithography", Plenum Press, New York and London (1988)

[111] G. A. C. M. Spierings, “Wet chemical etching of silicate glasses in hydrofluoric acid based solutions”, J. Mater. Sci., Vol. 28, No. 23, pp. 6261 - 6273 (1993)

[112] M. Prokopowicz-Prigogine, “Reactivity of a silica network of glass: molecular mechanism of the dissolution of a silica network in aqueous HF-HCl solutions”, Glastech. Ber., Vol. 62, No. 7, pp. 249 - 255 (1989)

[113] D. E. Carlson, “Ion depletion of glass at a blocking anode: I. Theory and experimental results for alkali silicate glasses”, J. Am. Cer. Soc., Vol. 57, No. 7, pp. 291 - 294 (1974)

[114] A. J. Ikushima, T. Fujiwara, and K. Saito, “Silica glass: A material for photonics”, J. Appl. Phys., Vol. 88, No. 3, pp. 1201 - 1213 (2000)

[115] T. Fujiwara, D. Wong, Y. Zhao, S. Fleming, S. Poole, and M. Sceats, “Electro-optic modulation in germanosilicate fiber with UV-excited poling”, Electr. Lett., Vol. 31, No. 7, pp. 573 - 575 (1995)

[116] P. G. Kazansky, A. Kamal, and P. St. J. Russell, “High second-order nonlinearities induced in lead silicate glass by electron-beam irradiation”, Opt. Lett., Vol. 18, No. 9, pp. 693 - 695 (1993)

[117] L. J. Henry, B. V. McGrath, T. G. Alley, and J. J. Kester, “Optical nonlinearity in fused silica by proton implantation”, J. Opt. Soc. Am. B, Vol. 13, No. 5, pp. 827 - 836 (1996)

[118] A. Okada, K. Ishii, K. Mito, and K. Sasaki, “Phasematched secondharmonic generation in novel corona poled glass waveguides”, Appl. Phys. Lett., Vol. 60, No.23, pp. 2853 - 2855 (1992)

[119] Z. Xu, L. Liu, Z. Hou, P. Yang, X. Liu, L. Xu, W. Wang, M. Affatigato, and S. Feller, “Influence of different poling methods on the second-order nonlinearity in fused silica glasses”, Opt. Comm., Vol. 174, No. 5-6, pp. 475 - 479 (2000)

[120] Y. Quiquempois, P. Niay, M. Douay, and B. Poumellec, “Advances in poling and permanently induced phenomena in silica-based glasses”, Current Opinion in Solid State and Material Science, Vol. 7, No. 2, pp. 89 - 95 (2003)

[121] L. Canioni, M. O. Martin, B. Bousquet, and L. Sarger, “Precise measurements and analysis of linear and nonlinear optical properties of glass materials near 1.5 μm”, Opt. Comm., Vol. 151, No. 4 - 6, pp. 241 - 246 (1998)

[122] C. J. Marckmann, G. Genty, Y. Ren, J. Arentoft, and M. Kristensen, “Bragg gratings as probes to determine nonlinearities induced by thermal poling”, Bragg Gratings, Photosensitivity, and Poling in Glass Waveguides, OSA Technical Digest Series, paper BFC3 (2001)

[123] A. C. Liu, M. J. F. Digonnet, and G. S. Kino, “DC Kerr coefficient of silica: theory and experiment”, Proc. SPIE, Vol. 3542, pp. 102 - 107 (1998)

[124] A. Boskovic, S. V. Chernikov, J. R. Taylor, L. Gruner-Nielsen, and O. A. Levring, “Direct continuous-wave measurement of $n2$ in various types of telecommunication fiber at 1.55 μm”, Opt. Lett., Vol. 21, No. 24, pp. 1966 - 1968 (1996)

[125] T. M. Monro, V. Pruneri, N. G. R. Broderick, D. Faccio, P. G. Kazansky, and D. J. Richardson, “Broad-band second-harmonic generation in holey optical fibers”, IEEE Phot. Tech. Lett., Vol. 13, No. 9, pp. 981 - 983 (2001)

[126] D. Faccio, A. Busacca, W. Belardi, V. Pruneri, P. G. Kazansky, T. M. Monro, D. J. Richardson, B. Grappe, M. Cooper and C. N. Pannell, “Demonstration of thermal poling in holey fibres”, Electron. Lett., Vol. 37, No. 2, pp. 107 - 108 (2001)

[127] M. Bache, H. Nielsen, J. Lgsgaard, and O. Bang, “Tuning quadratic nonlinear photonic crystal fibers for zero group-velocity mismatch”, Opt. Lett., Vol. 31, No. 11, pp. 1612 - 1614 (2006)

[128] M. Fokine, L. E. Nilsson, A. A. Claesson, D. Berlemont, L. Kjellberg, L. Krummenacher, and W. Margulis, “Integrated fiber MachZehnder interferometer for electro-optic switching”, Opt. Lett., Vol. 27, No. 18, pp. 1643 - 1645 (2002)

[129] J. R. Sparks, J. L. Esbenshade, R. He, N. Healy, T. D. Day, D. W. Keefer, P. J. A. Sazio, A. C. Peacock, and J. V. Badding, “Selective semiconductor filling of microstructured optical fibers”, J. Light. Tech., Vol. 29, No. 13, pp. 2005 - 2008 (2011)

[130] F. De Lucia, D. Huang, C. Corbari, N. Healy, and P. J. A. Sazio, "Optical fiber poling by induction: analysis by 2D numerical modeling", Opt. Lett., Vol. 41, No. 8, pp. 1700 - 1703 (2016)

[131] F. De Lucia, D. Huang, C. Corbari, N. Healy, and P. J. A. Sazio, "Optical fiber poling by induction", Opt. Lett., Vol. 39, No. 22, pp. 6513 - 6516 (2014)

[132] D. L. Logan, "A first course in the finite element method", Cengage Learning (2011)

[133] A. Camara, O. Tarasenko, and W. Margulis, "Study of thermally poled fibers with a twodimensional model", Opt. Exp., Vol. 22, No. 15, pp. 17700 - 17715 (2014)

[134] S. Fleming and H. An, "Poled glasses and poled fiber devices", J. Ceram. Soc. Jpn., Vol. 116, No. 1358, pp. 1007 - 1023 (2008)

[135] M. I. Petrov, Ya. A. Lepen'kin, and A. A. Lipovskii, "Polarization of glass containing fast and slow ions", J. Appl. Phys., Vol. 112, No. 4, pp. 043101-1 - 043101-8 (2012)

[136] A. A. Lipovskii, V. G. Melehin, Y. P. Svirko, and V. V. Zhurikhina, "Bleaching versus poling: Comparison of electric field induced phenomena in glasses and in glass-metal nanocomposites", J. Appl. Phys., Vol. 109, No. 1, pp. 011101-1 - 011101-11 (2011)

[137] A. De Francesco and G. E. Town, "Modeling the electrooptic evolution in thermally poled germanosilicate fibers", IEEE J. Quantum Electron., Vol. 37, No. 10, pp. 1312 - 1320 (2001)

[138] G. Frischat, "Sodium diffusion in SiO_2 glass", J. Am. Ceram. Soc., Vol. 51, No. 9, pp. 528 - 530 (1968)

[139] T. Drury and J. P. Roberts, "Diffusion in silica glass following reaction with tritiated water vapor", Phys. Chem. Glasses, Vol. 4, pp. 79 - 90 (1963)

[140] M. Fokine, L. Kjellberg, P. Helander, N. Myren, L. Norin, H. Olsson, N. Sjodin, and W. Margulis, "A fiber-based kerr switch and modulator", Proc. of ECOC, Vol. 1, pp. 43 - 44 (2004)

[141] D. Halliday, J. Walker, and R. Resnick, "Fundamentals of Physics", John Wiley & Sons. (2010)

[142] H. Semat, and R. Katz, “Physics”, Rinehart & Company, Inc, New York (1958)

[143] T. W. Richards, and S. Boyer, “FURTHER STUDIES CONCERNING GALLIUM. Its Electrolytic Behavior, Purification, Melting Point, Density, Coefficient of Expansion, Compressibility, Surface Tension, and Latent Heat of Fusion”, J. Am. Chem. Soc., Vol. 43, No. 2, pp. 274 - 294 (1921)

[144] Atomic Energy Commission, “Liquid metals handbook”, R. N. Lyon, Government Printing Office, Washington (1952)

[145] A. Defrain, “Metastable states of Ga–Supercooling and Polymorphism”, J. Chim. Phys., Vol. 74, No. 7, pp. 851 - 862 (1977)

[146] H. Y. Park, and M. S. Jhon, “Thermodynamic and transport properties of liquid Gallium”, J. Kor. Nucl. Soc., Vol. 14, No. 1, pp. 10 - 16 (1982)

[147] P. Ascarelli, “Atomic radial distributions and ion-ion potential in liquid gallium”, Phys. Rev., Vol. 143, No. 1, pp. 36 - 47 (1966)

[148] H. Richter, “Solid amorphous Bi, Ga, and Fe as examples of liquid-like amorphous substances”, J. Vac. Sci. Tech., Vol. 6, No. 5, pp. 855 - 858 (1969)

[149] A. D. McNaught and A. Wilkinson, “IUPAC. Compendium of Chemical Terminology”, Oxford: Blackwell Scientific Publications (1997)

[150] R. L. David, “The Elements”, CRC Handbook of Chemistry and Physics, Internet Version 2007, 87th ed.; Taylor and Francis: Boca Raton, FL.

[151] M. Shepherd, S. Schuhmann, R. H. Flinn, J. W. Hough, and P. A. Neal, “Hazard of mercury vapor in scientific laboratories”, J. Research Nat. Bur. Stand., Vol. 26, pp. 357 - 375 (1941)

[152] D. A. Skoog, D. M. West, J. F. Holler, and S. R. Crouch, “Fundamentals of analytical chemistry”, Thomson Brooks/Cole (8th ed.) (2004)

[153] F. Ouellette, K. O. Hill, and D. C. Johnson, “Light induced erasure of self-organized $\chi^{(2)}$ gratings in optical fibers”, Opt. Lett., Vol. 13, No. 6, pp. 515 - 517 (1988)

[154] I. C. S. Carvalho, W. Margulis, and B. Leshe, “Erasure of frequency doubling gratings in optical fibers by ultraviolet light excitation”, Elect. Lett., Vol. 27, No. 17, pp. 1497 - 1498 (1991)

[155] A. Kameyama, A. Yokotani, and K. Kurosawa, “Identification of defects associated with second-order optical nonlinearity in thermally poled high-purity silica glasses”, J. Appl. Phys., Vol. 89, No. 9, pp. 4707 - 4713 (2001)

[156] H.-Y. Chen, J.-S. Sue, Y.-H. Lin, and S. Chao, “Quasi-phase-matched second harmonic generation in ultraviolet-assisted periodically poled planar fused silica”, Opt. Lett., Vol. 28, No. 11, pp. 917 - 919 (2003)

[157] G. Bonfrate, V. Pruneri, and P. G. Kazansky, “Periodic UV erasure of the nonlinearity for quasi-phase-matching in optical fibers”, CLEO2000, paper CMO5 (2000)

[158] A. Canagasabey, C. Corbari, A. V. Gladyshev, F. Liegeois, S. Guillemet, Y. Hernandez, M. V. Yashkov, A. Kosolapov, E. M. Dianov, M. Ibsen, and P. G. Kazansky, “High-average-power second-harmonic generation from periodically poled silica fibers”, Opt. Lett., Vol. 34, No. 16, pp. 2483 - 2485 (2009)

[159] C. Corbari, A. V. Gladyshev, L. Lago, M. Ibsen, Y. Hernandez, and P. G. Kazansky, “All-fiber frequency-doubled visible laser”, Opt. Lett., Vol. 39, No. 22, pp. 6505 - 6508 (2014)

[160] A. Canagasabey, C. Corbari, Z. Zhang, P. G. Kazansky, and M. Ibsen, “Broadly tunable second-harmonic generation in periodically poled silica fibers”, Opt. Lett., Vol. 32, No. 13, pp. 1863 - 1865 (2007)

[161] A. Canagasabey, M. Ibsen, K. Gallo, A. V. Gladyshev, E. M. Dianov, C. Corbari, and P. G. Kazansky, “Aperiodically poled silica fibers for bandwidth control of quasi-phase-matched second-harmonic generation”, Opt. Lett., Vol. 35, No. 5, pp. 724 - 726 (2010)

[162] E. Y. Zhu, Z. Tang, L. Qian, L. G. Helt, M. Liscidini, J. E. Sipe, C. Corbari, A. Canagasabey, M. Ibsen, and P. G. Kazansky, “Poled-fiber source of broadband polarization-entangled photon pairs”, Opt. Lett., Vol. 38, No. 21, pp. 4397 - 4400 (2013)

[163] C. Corbari, “Development of non-linear waveguide devices for optical signal processing”, University of Southampton, PhD Thesis, (2005)

[164] F. De Lucia, D. Keefer, C. Corbari, and P. J. A. Sazio, “Thermal poling of silica optical fibers using liquid electrodes”, Opt. Lett., Vol. 42, No. 1, pp. 69 - 72 (2017)

[165] W. L. Marshall, “Electrical conductance of liquid and supercritical water evaluated from 0 °C and 0.1 MPa to high temperatures and pressures. Reduced-state relationships”, J. Chem. Eng. Data, Vol. 32, No. 2, pp. 221 - 226 (1987)

[166] D. A. Masten, B. R. Foy, D. M. Harradine, and R. B. Dyer, “In situ Raman spectroscopy of reactions in supercritical water”, J. Phys. Chem., Vol. 97, No. 33, pp. 8557 - 8559 (1993)

[167] M. I. A. Khudus, F. De Lucia, C. Corbari, T. Lee, P. Horak, P. Sazio, and G. Brambilla, “Phase matched parametric amplification via four-wave mixing in optical microfibers”, Opt. Lett., Vol. 41, No. 4, pp. 761 - 764 (2016)

[168] G. Brambilla, “Optical fiber nanowires and microwires: a review”, J. Opt., Vol. 12, 043001 (2010)

[169] E. C. Mägi, L. B. Fu, H. C. Nguyen, M. R. E. Lamont, D. I. Yeom, and B. J. Eggleton, “Enhanced Kerr nonlinearity in sub-wavelength diameter As_2Se_3 chalcogenide fiber tapers”, Opt. Exp., Vol. 15, No. 16, pp. 10324 - 10329 (2007)

[170] A. C. Sodré, J. C. Boggio, A. A. Rieznik, H. E. Hernandez-Figueroa, and J. C. Knight, “Highly efficient generation of broadband cascaded four-wave mixing products”, Opt. Exp., Vol. 16, No. 4, pp. 2816 - 2828 (2008)

[171] P. P. Baveja, D. N. Maywar, and G. P. Agrawal, “Interband four-wave mixing in semiconductor optical amplifiers with ASE-enhanced gain recovery ”, IEEE J. Sel. Top. Quantum Electron., Vol. 18, No. 2, pp. 899 - 908 (2012)

[172] D. A. V. Klinera, F. Di Teodorob, J. P. Koplowb, S. W. Mooreb, and A. V. Smith, “Efficient second, third, fourth, and fifth harmonic generation of a Yb-doped fiber amplifier”, Opt. Commun., Vol. 210, No. 3, pp. 393 - 398 (2002)

[173] S. A. Slattery, D. N. Nikogosyan, and G. Brambilla, “fiber Bragg grating inscription by high-intensity femtosecond UV laser light: comparison with other existing methods of fabrication”, J. Opt. Soc. Am. B, Vol. 22, No. 2, pp. 354 - 361 (2005)

[174] P. J. Campagnola and C.-Y. Dong, “Second harmonic generation microscopy: principles and applications to disease diagnosis”, Laser Photonics Rev., Vol. 5, No. 1, pp. 13 - 26 (2011)

[175] R. del Coso, and J. Solis, "Relation between nonlinear refractive index and third-order susceptibility in absorbing media", J. Opt. Soc. Am. B, Vol. 21, No. 3, pp. 640 - 644 (2004)

[176] T. Wang, X. Gai, W. Wei, R. Wang, Z. Yang, X. Shen, S. Madden, and B. Luther-Davies, "Systematic z-scan measurements of the third order nonlinearity of chalcogenide glasses", Opt. Mat. Exp., Vol. 4, No. 5, pp. 1011 - 1022 (2014)

[177] F. Eroni. P. dos Santos, F. C. Favero, A. S. L. Gomes, J. Xing, Q. Chen, M. Fokine, and I. C. S. Carvalho, "Evaluation of the third-order nonlinear optical properties of tellurite glasses by thermally managed eclipse Z-scan", J. Appl. Phys., Vol. 105, No. 2, 024512 (2009)

[178] H. Tichá, and L. Tichý, "Semiempirical relation between non-linear susceptibility (refractive index), linear refractive index and optical gap and its application to amorphous chalcogenides", J. Optoelectron. Adv. Mater., Vol. 4, No. 2, pp. 381 - 386 (2002)

[179] D. E. Carlson, K. W. Hang, and G. F. Stockdale, "Electrode "polarization" in alkali-containing glasses", J. Am. Cer. Soc., Vol. 55, No. 7, pp. 337 - 341 (1972)

[180] M. Dussauze, T. Cremoux, F. Adamietz, V. Rodriguez, E. Fargin, G. Yang, and T. Cardinal, "Thermal poling of optical glasses: mechanisms and second-order optical properties", Int. J. Appl. Glass Science, Vol. 3, No. 4, pp. 309 - 320 (2012)

[181] F. C. Garcia, I. C. S. Carvalho, E. Hering, W. Margulis, and B. Lesche, "Inducing a large second-order optical nonlinearity in soft glasses by poling", Appl. Phys. Lett., Vol. 72, No. 25, pp. 3252 - 3254 (1998)

[182] M. Guignard, Virginie Nazabal, F. Smektala, H. Zeghlache, A. Kudlinski, Y. Quiquempois, and G. Martinelli, "High second-order nonlinear susceptibility induced in chalcogenide glasses by thermal poling ", Opt. Exp., Vol. 14, No. 4, pp. 1524 - 1532 (2006)

[183] M. Dussauze, X. Zheng, V. Rodriguez, E. Fargin, T. Cardinal, and F. Smektala, "Photosensitivity and second harmonic generation in chalcogenide arsenic sulfide poled glasses", Opt. Mat. Exp., Vol. 2, No. 1, pp. 45 - 54 (2012)

[184] H. Zeghlache, M. Guignard, A. Kudlinski, Y. Quiquempois, G. Martinelli, V. Nazabal, and F. Smektala, “Stabilization of the second-order susceptibility induced in a sulfide chalcogenide glass by thermal poling”, J. Appl. Phys., Vol. 101, No. 8, 084905 (2007)

[185] C. R. Kurkjian, J. T. Krause, and M. J. Matthewson, “Strength and fatigue of silica optical fibers”, J. of Light. Tech., Vol. 7, No. 9, pp. 1360 - 1370 (1989)

[186] J. R. Sparks, P. J. Sazio, V. Gopalan, and J. V. Badding, “Templated chemically deposited semiconductor optical fiber materials”, Annual Review of Materials Research, Vol. 43, pp. 527 - 557 (2013)

[187] R. He, T. D. Day, M. Krishnamurthi, J. R. Sparks, P. J. A. Sazio, V. Gopalan, and J. V. Badding, “Silicon p-i-n junction fibers”, Adv. Mater., Vol. 25, No. 10, pp. 1461 - 1467 (2013)

[188] J. M. Jasinski, and S. M. Gates, “Silicon chemical vapor deposition one step at a time: fundamental studies of silicon hydride chemistry”, Acc. Chem. Res., Vol. 24, No. 1, pp. 9 - 15 (1991)

[189] C. J. Giunta, R. J. McCurdy, J. D. Chapple-Sokol, and R. G. Gordon, “Gas-phase kinetics in the atmospheric pressure chemical vapor deposition of silicon from silane and disilane”, J. Appl. Phys., Vol. 67, No. 2, pp. 1062 - 1075 (1990)

[190] N. F. Baril, R. He, T. D. Day, J. R. Sparks, B. Keshavarzi, M. Krishnamurthi, A. Borhan, V. Gopalan, A. C. Peacock, N. Healy, P. J. Sazio, and J. V. Badding, “Confined high-pressure chemical deposition of hydrogenated amorphous silicon”, J. Am. Chem. Soc., Vol. 134, No. 1, pp. 174 - 179 (2012)

[191] N. F. Baril, B. Keshavarzi, J. R. Sparks, M. Krishnamurthi, I. Temnykh, P. J. A. Sazio, A. C. Peacock, A. Borhan, V. Gopalan, and J. V. Badding, “High-pressure chemical deposition for void-free filling of extreme aspect ratio templates”, Adv. Mater., Vol. 22, No. 41, pp. 4605 - 4611 (2010)

[192] R. A. Street, “Hydrogenated amorphous silicon”, Cambridge Univ. Press, Cambridge, UK (1991)

[193] P. Mehta, M. Krishnamurthi, N. Healy, N. F. Baril, J. R. Sparks, P. J. A. Sazio, V. Gopalan, J. V. Badding, and A. C. Peacock, “Mid-infrared transmission properties of amorphous germanium optical fibers”, Appl. Phys. Lett., Vol. 97, 071117 (2010)

[194] P. Mehta, N. Healy, N. F. Baril, P. J. A. Sazio, J. V. Badding, and A. C. Peacock, “Nonlinear transmission properties of hydrogenated amorphous silicon core optical fibers”, Opt. Exp., Vol. 18, No. 16, pp. 16826 - 16831 (2010)

[195] K. Narayanan and S. F. Preble, “Optical nonlinearities in hydrogenated amorphous silicon waveguides”, Opt. Exp., Vol. 18, No. 9, pp. 8998 - 9005 (2010)

[196] A. C. Liu, M. J. Digonnet, and G. S. Kino, “DC Kerr coefficient of silica: theory and experiment”, Proc. of Photonics East (ISAM, VVDC, IEMB), pp. 102 - 107 (1998)

[197] M. Zelikson, J. Salzman, K. Weiser, and J. Kanicki, “Enhanced electro-optic effect in amorphous hydrogenated silicon based waveguides”, Appl. Phys. Lett., Vol. 61, No. 14, pp. 1664 - 1666 (1992)

[198] P. Mehta, N. Healy, T. D. Day, J. R. Sparks, P. J. A. Sazio, J. V. Badding, and A. C. Peacock, “All-optical modulation using two-photon absorption in silicon core optical fibers”, Opt. Exp., Vol. 19, No. 20, pp. 19078 - 19083 (2011)

[199] I. T. Sorokina, “Solid-state mid-infrared laser Sources”, Springer Science & Business Media, (2003)

[200] M. Baudrier-Raybaut, R. Haïdar, P. Kupecek, P. Lemasson, and E. Rosencher, “Random quasi-phase-matching in bulk polycrystalline isotropic nonlinear materials”, Nature, Vol. 432, No. 7015, pp. 374 - 376 (2004)

[201] J. R. Sparks, R. He, N. Healy, M. Krishnamurthi, A. C. Peacock, P. J. A. Sazio, V. Gopalan, and J. V. Badding, “Zinc selenide optical fibers”, Adv. Mater., Vol. 23, No. 14, pp. 1647 - 1651 (2011)

[202] R. E. Russo, “Laser ablation”, Applied Spectroscopy, Vol. 49, No. 9, pp. 14A - 28A (1995)

[203] J. F. Ready, “Effects due to absorption of laser radiation”, J. Appl. Phys., Vol. 36, No. 2, pp. 462 - 468 (1965)

[204] D. T. F. Marple, “Refractive index of ZnSe, ZnTe, and CdTe”, J. Appl. Phys., Vol. 35, No. 3, pp. 539 - 542 (1964)

[205] W. Belardi, F. De Lucia, F. Poletti, and P. J. A. Sazio "Composite material hollow antiresonant fibers", Opt. Lett., Vol. 42, No. 13, pp. 2535 - 2538 (2017)

[206] A. N. Kolyadin, A. F. Kosolapov, A. D. Pryamikov, A. S. Biriukov, V. G. Plotnichenko and E. M. Dianov, "Light transmission in negative curvature hollow core fiber in extremely high material loss region", Opt. Exp., Vol. 21, No. 8, pp. 9514 - 9519 (2013)

[207] W. Belardi, "Design and properties of hollow antiresonant fibers for the visible and near infrared spectral range", J. Light. Tech., Vol. 33, No. 21, pp. 4497 - 4503 (2015)

[208] M. Michieletto, J. K. Lyngsø, C. Jakobsen, J. Lægsgaard, O. Bang, and T. T. Alkeskjold, "Hollow-core fibers for high power pulse delivery", Opt. Exp., Vol. 24, No. 7, pp. 7103 - 7119 (2016)

[209] W. Belardi, and J. C. Knight "Hollow antiresonant fibers with low bending loss ", Opt. Exp., Vol. 22, No. 8, pp. 10091 - 10096 (2014)

[210] Z. Wang, W. Belardi, F. Yu, W. J. Wadsworth, and J. C. Knight "Efficient diode-pumped mid-infrared emission from acetylene-filled hollow-core fiber", Opt. Exp., Vol. 22, No. 18, pp. 21872 - 21878 (2014)

[211] N. Healy, J. R. Sparks, R. R. He, P. J. A. Sazio, J. V. Badding, and A. C. Peacock "High index contrast semiconductor ARROW and hybrid ARROW fibers", Opt. Exp., Vol. 19, No. 11, pp. 10979 - 10985 (2011)

[212] D.-J. Won, M. O. Ramirez, H. Kang, V. Gopalan, N. F. Baril, J. Calkins, J. V. Badding, and P. J. A. Sazio, "All-optical modulation of laser light in amorphous silicon-filled microstructured optical fibers", Appl. Phys. Lett., Vol. 91, No. 16, 161112 (2007)

[213] W. Belardi, N. White, J. Lousteau, X. Feng, and F. Poletti, "Hollow core antiresonant fibers in borosilicate glass", Proceedings of WSOF, WW4A.4 (2015)

[214] V. A. Volodin and D. I. Koshelev, "Quantitative analysis of hydrogen in amorphous silicon using Raman scattering spectroscopy", J. Raman Spectrosc., Vol. 44, No. 12, pp. 1760 - 1764 (2013)

[215] J.-M. Ménard, F. Köttig, and P. St. J. Russell, "Broadband electric-field-induced LP_{01} and LP_{02} second harmonic generation in Xe-filled hollow-core PCF", Opt. Lett., Vol. 41, No. 16, pp. 3795 - 3798 (2016)

[216] T. Udem, R. Holzwarth, and T. W. Haënsch, "Optical frequency metrology", Nature, Vol. 416, No. 6877, pp. 233 - 237 (2002)

[217] L. E. Hargrove, R. L. Fork, and M. A. Pollack, "Locking of HeNe laser modes induced by synchronous intracavity modulation", Appl. Phys. Lett., Vol. 5, No. 1, pp. 4 - 5 (1964).

[218] S. A. Diddams, "The evolving optical frequency comb [Invited]", J. Opt. Soc. Am. B, Vol. 27, No. 11, pp. B51 - B62 (2010)

[219] P. Del'Haye, A. Schliesser, O. Arcizet, T. Wilken, R. Holzwarth, and T. J. Kippenberg, "Optical frequency comb generation from a monolithic microresonator", Nature, Vol. 450, No. 7173, pp. 1214 - 1217 (2007)

[220] H. Mikami, M. Shiozawa, M. Shirai, and K. Watanabe, "Compact light source for ultrabroadband coherent anti-Stoke Raman scattering (CARS) microscopy", Opt. Exp., Vol. 23, No. 3, pp. 2872 - 2878 (2015)

[221] J. Yi, Q. Wei, W. Liu, V. Backman, and H. F. Zhang, "Visible-light optical coherence tomography for retinal oximetry", Opt. Lett., Vol. 38, No. 11, pp. 1796 - 1798 (2013)

[222] H. Zhao, B. Kuyken, S. Clemmen, F. Leo, A. Subramanian, A. Dhakal, P. Helin, S. Severi, E. Brainis, G. Roelkens, and R. Baets, "Visible-to-near-infrared octave spanning supercontinuum generation in a silicon nitride waveguide", Opt. Lett., Vol. 40, No. 10, pp. 2177 - 2180 (2015)

[223] A. G. Griffith, R. K. W. Lau, J. Cardenas, Y. Okawachi, A. Mohanty, R. Fain, Y. H. D. Lee, M. Yu, C. T. Phare, C. B. Poitras, A. L. Gaeta, and M. Lipson, "Silicon-chip mid-infrared frequency comb generation", Nat. Commun., Vol. 6, 6299 (2015)

[224] S. Coen, H. G. Randle, T. Sylvestre, and M. Erkintalo, "Modeling of octave-spanning Kerr frequency combs using a generalized mean-field LugiatoLefever model", Opt. Lett., Vol. 38, No. 1, pp. 37 - 39 (2013)

[225] T. Hansson, F. Leo, M. Erkintalo, S. Coen, I. Ricciardi, M. De Rosa, and S. Wabnitz, "Theory of quadratic optical frequency combs", IEEE Transparent Optical Networks (ICTON), We.C1.3, pp. 1 - 4 (2016)

[226] F. Leo, T. Hansson, I. Ricciardi, M. De Rosa, S. Coen, S. Wabnitz, and M. Erkintalo, "Walk-off-induced modulation instability, temporal pattern formation, and frequency comb generation in cavity-enhanced second-harmonic generation", Phys. Rev. Lett., Vol. 116, No. 3, 33901 (2016)

[227] F. Leo, S. Coen, T. Hansson, I. Ricciardi, M. De Rosa, S. Wabnitz and M. Erkintalo, "Frequency-comb formation in doubly resonant second-harmonic generation", Phys. Rev. A, Vol. 93, No. 4, 43831 (2016)

[228] J. A. Giordmaine and R. C. Miller, "Tunable coherent parametric oscillation in $LiNbO_3$ at optical frequencies", Phys. Rev. Lett., Vol. 14, No. 24, pp. 973 - 976 (1965)

[229] H. Jung, R. Stoll, X. Guo, D. Fischer, and H. X. Tang, "Green, red, and IR frequency comb line generation from single IR pump in AlN microring resonator", Optica, Vol. 1, No. 6, pp. 396 - 399 (2014)

[230] P. D. Drummond, K. J. McNeil, and D. F. Walls, "Non-equilibrium transitions in sub/second harmonic generation", Optica Acta: International Journal of Optics, Vol. 27, No. 3, pp. 321 335 (1980)

[231] T. Paschotta, M. Collett, P. Krz, K. Fiedler, H. A. Bachor, and J. Mlynek, "Bright squeezed light from a singly resonant frequency doubler", Phys. Rev. Lett., Vol. 72, No. 24, pp. 3807 - 3810 (1994)

[232] P. Kürz, R. Paschotta, K. Fiedler, A. Sizmann, G. Leuchs, and J. Mlynek, "Squeezing by second-harmonic generation in a monolithic resonator", Appl. Phys. B, Vol. 55, No. 3, pp. 216 - 225 (1992)

[233] M. Fiorentino, S. M. Spillane, R. G. Beausoleil, T. D. Roberts, P. Battle, and M. W. Munro, "Spontaneous parametric down-conversion in periodically poled KTP waveguides and bulk crystals", Appl. Phys. B, Vol. 55, No. 3, pp. 216 - 225 (1992)

[234] S. Tanzilli, W. Tittel, H. De Riedmatten, H. Zbinden, P. Baldi, M. De Micheli, D. B. Ostrowsky, and N. Gisin, "PPLN waveguide for quantum communication", Eur. Phys. J. D, Vol. 18, No. 2, pp. 155 - 160 (2002)

[235] H. Takesue and K. Inoue, "Generation of polarization-entangled photon pairs and violation of Bell's inequality using spontaneous four-wave mixing in a fiber loop", Phys. Rev. A, Vol. 70, 031802(R) (2004)

[236] G. Bonfrate, V. Pruneri, P. G. Kazansky, P. Tapster, and J. G. Rarity, "Parametric fluorescence in periodically poled silica fibers", Appl. Phys. Lett., Vol. 75, No. 16, pp. 2356 - 2358 (1999)

[237] P. K. Huy, A. T. Nguyen, E. Brainis, M. Haelterman, P. Emplit, C. Corbari, A. Canagasabey, P. G. Kazansky, O. Deparis, A. Fotiadi, P. Mgret, and S. Massar, "Photon pair source based on parametric fluorescence in periodically poled twin-hole silica fiber", Opt. Exp., Vol. 15, No. 8, pp. 4419 - 4426 (2007)

[238] L. G. Helt, E. Y. Zhu, M. Liscidini, L. Qian, and J. E. Sipe, "Proposal for in-fiber generation of telecom-band polarization-entangled photon pairs using a periodically poled fiber", Opt. Lett., Vol. 34, No. 14, pp. 2138 - 2140 (2009)

[239] E. Y. Zhu, Z. Tang, L. Qian, L. G. Helt, M. Liscidini, J. E. Sipe, C. Corbari, A. Canagasabey, M. Ibsen, and P. G. Kazansky, "Direct generation of polarization-entangled photon pairs in a poled fiber", Phys. Rev. Lett., Vol. 108, 213902 (2012)

Optical fiber poling by induction

F. De Lucia,[1] D. Huang,[2] C. Corbari,[1] N. Healy,[1] and P. J. A. Sazio[1,*]
[1]*Optoelectronics Research Centre, University of Southampton, SO17 1BJ, UK*
[2]*Department of Electrical and Electronic Engineering, Imperial College London, SW7 2AZ, UK*
**Corresponding author: pjas@soton.ac.uk*

Received August 11, 2014; revised October 14, 2014; accepted October 19, 2014;
posted October 20, 2014 (Doc. ID 220697); published November 12, 2014

Conventional thermal poling methods require direct physical contact to internal fiber electrodes. Here, we report an indirect electrostatic induction technique using electrically floating wires inside the fiber combined with external electric fields that can allow for facile poling of complex microstructured fibers (MOFs) of arbitrarily long lengths. In combination with our unique ability to use liquid gallium electrodes, inducing second-order nonlinearities inside otherwise difficult to access multi-core or multi-hole MOFs now becomes entirely feasible and practical. The formation of a permanent second-order nonlinearity is unequivocally demonstrated by realizing quasi-phase-matched frequency doublers using periodic UV erasure methods in the induction-poled fibers. The second-order susceptibility created inside the fiber is driven by the potential difference established between the floating electrodes, which we calculate via numerical simulations.

OCIS codes: (190.4370) Nonlinear optics, fibers; (230.4320) Nonlinear optical devices; (190.2620) Harmonic generation and mixing; (230.1150) All-optical devices.
http://dx.doi.org/10.1364/OL.39.006513

Optical fiber-based photonic devices have a number of compelling advantages compared with conventional bulk components, as they allow for robust, environmentally rugged, lightweight, and compact systems that do not require careful alignment of free-space optics and have excellent thermal management capabilities due to very high surface to volume ratios. In addition, the highly extended electromagnetic interaction length and optical mode confinement/engineering realizable with these waveguides allow for a variety of nonlinear device functionality such as $\chi^{(3)}$-based frequency conversion [1]. Nevertheless, glass optical fibers, like all centrosymmetric media, lack the second-order nonlinearity $\chi^{(2)}$ unless they are poled. The thermal poling technique, introduced by Myers *et al.* [2] in 1991 is used to break the centrosymmetry via the application of high DC voltages to glass samples (bulk or fibers) at elevated temperatures (~200°C–300°C) to create a space-charge region near the anodic surface of the sample [3]. In conventional optical fiber poling, high DC voltages are typically applied by inserting electrodes (usually tungsten wires or a low-temperature molten metal alloy) into capillary holes adjacent to the fiber core, and connecting them separately to the anode and cathode of a HV power supply. However, due to the small distance between the internal electrodes (~20–30 μm), electrical breakdown can occur if the high electric field exceeds the dielectric strength of glass. As a result, alternative electrode configurations have been investigated. In particular, Margulis *et al.* [4] demonstrated that it is possible to improve both the strength and stability of the effective $\chi^{(2)}$ if both the electrodes inside the fiber are connected to the same anodic potential, without requiring any cathode electrodes. This somewhat counterintuitive result prompted An and Fleming [5] to explore alternative electrode configurations more systematically, including single anode, double anode, single cathode and double cathode in order to optimize the $\chi^{(2)}$ response. Here, we report an indirect fiber poling method in which it is possible to not only dispense with the cathodes, but also with any direct physical contact to the internal anodes themselves. This technique can therefore potentially overcome many issues commonly encountered with manufacturing electrodes inside fibers. This includes the length limitations and $\chi^{(2)}$ inhomogeneities that plague manual wire insertion methods: direct contacts to molten metal-filled fibers require extra processing steps in order to side polish and access the wires inside, resulting in significantly weakened structures. More fundamentally, considering the well known relation $\chi^{(2)} \sim 3\chi^{(3)} E_{\text{rec}}$ in a glass [2], conventional device structures will always be limited in $\chi^{(2)}$ efficiency to about 1 pm/V. This is because the maximum E-field recordable in silica will be limited by its dielectric strength to $\sim 10^8$ V/m, while the inherent $\chi^{(3)}$ properties of silica are of order $\sim 10^{-22}$ m^2/V^2. In order to move beyond this limitation, it will be necessary to explore for example, photonic crystal fiber poling to allow for exquisite control over optical mode confinement, effective group index, dispersion, etc., thus potentially generating very high second-order nonlinearities. However, conventional poling methods are completely impractical to use on such complex and intricate fibers but may very well become viable using the induction poling process reported here.

The waveguides used for the experiments were sourced from Fibercore Ltd., Southampton UK. It is important to note that the use of commercial fibers was motivated purely by their availability and simplicity, i.e., a convenient test bed to verify our understanding of the physical processes involved in induction poling. These pure silica optical fibers have an OD of 125 μm (not including polymer coating) and a 4.3-μm diameter, 0.17 numerical aperture (NA) Germania-doped glass core. For the initial experiments, a pressure filling technique similar to the one described by Fokine *et al.* [6] was used to fill the internal holes with liquid metal as can be seen in Fig. 1. The indirect electrostatic induction poling setup itself is shown in Fig. 2 and consists of two separate fibers with embedded electrodes, namely the "inductor" (colored blue in Fig. 2) and the metal-filled sample (colored red). The inductor is a multi-hole silica capillary 6 cm in length, with two 18-μm-diameter tungsten wires

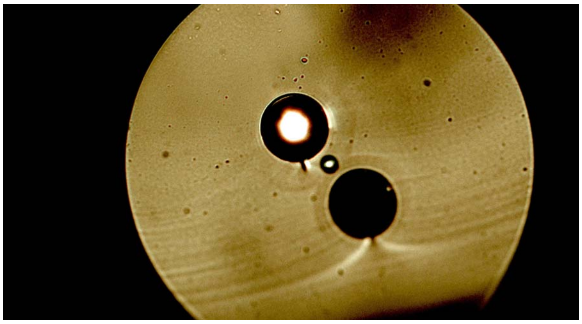

Fig. 1. Twin 19-μm holes in silica fiber with Germania-doped core. The depletion regions generated via electrostatic induction poling are visible after etching. A gallium electrode has been selectively purged, highlighting the versatility of the technique.

manually inserted inside. Both wires are looped and connected to the positive terminal of a HV source, typically operated at +4300 V. The liquid metal filling was used as the internal floating electrodes of the sample. As thermal poling requires elevated temperatures (~300°C), the polymer coating of both fibers is removed beforehand to prevent burning. During the experiment, the sample was mounted immediately adjacent to the inductor, and both were adhered to the surface of a standard microscope slide with an evaporated gold layer on the opposite face, used as the grounding backplane. The ground plane function is described in the numerical simulations section. The inductor, sample, and slide were then placed in good thermal contact into a glass Petri dish placed on the surface of a hotplate as shown in Fig. 2. Note that the sample used in this experiment was more than 3× the length of the inductor, and in fact as far as we can ascertain, there is no sample length restriction provided the correct poling temperature is maintained.

After reaching the poling temperature, +4300 V was applied to the inductor, and the sample was left to pole for 120 min before the hotplate is switched off and allowed to cool with the high voltage continually applied for a further 60 min or more. At this point, the HV power supply was also switched off. The second-order nonlinearity induced in glasses by thermal poling is associated with the creation of a depletion region, generated by the electromigration of impurity ions at elevated temperatures. A useful method of directly visualizing this depletion region is by using HF acid decorative etching [7] as can be seen in Fig. 1. Here, the regions surrounding the liquid metal electrodes are typical and representative of those observed throughout the entire 20-cm length of the induction poled sample after (destructive) sectioning and etching, thus providing strong evidence that depletion was induced along the entire sample.

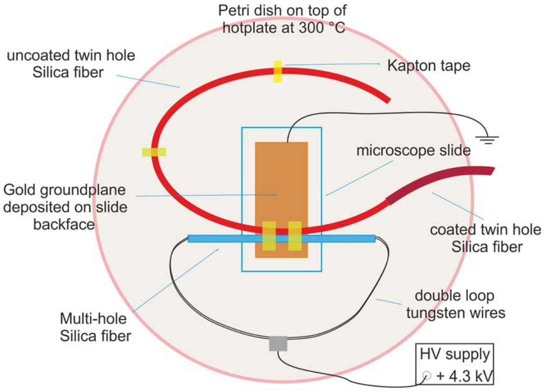

Fig. 2. Electrostatic induction poling setup with inductor and sample in close proximity. The sample remains attached to the original polymer coated section outside the hot zone. The silica fiber containing the inductor wires serves as a dielectric barrier to prevent unwanted electrical breakdown in air.

Nevertheless, in of itself, depletion formation is not necessarily indicative of useful $\chi^{(2)}$ device functionality, but this can be verified by measuring the second harmonic generation (SHG) response, which we realized by periodically poling the samples via UV erasure [8]. However, prior to the $\chi^{(2)}$-grating writing process, correct sample preparation is key to efficient SHG operation. In particular, we observed that leaving electrodes embedded *in situ* resulted in very high linear optical absorption losses (approx. 4 dB/cm at 1550 nm). It is therefore necessary to remove the electrodes after poling, and pure Gallium was found to be an ideal liquid metal in this respect as both pressurized filling [6] and subsequent removal of the liquid metal could be conveniently carried out at room temperature. Furthermore, to the authors' knowledge, this is also the first reported example of successfully using liquid gallium as electrodes for thermal optical fiber poling. After gallium removal, the sample was spliced with two pieces of SM980 fiber on each end (Fibercore Ltd., OD 125 μm, 5.4-μm mode field diameter, NA = 0.15) to facilitate optical pumping.

In 1962 Armstrong *et al.* [9] proposed the quasi-phase matching (QPM) method to overcome the drawback of mismatch in dispersive media, in which the wave-vector mismatch is compensated by modulating the nonlinearity previously induced by poling. If the nonlinear coefficient is a periodic function in z, of period Λ, the mismatch between the pump and second harmonic is ΔK_q, where q is an integer that defines the order of QPM. To first order, the condition of QPM is given by the following equation:

$$\Delta K = \frac{4\pi}{\lambda} n_{\mathrm{eff}}^{2\omega} - 2\frac{2\pi}{\lambda} n_{\mathrm{eff}}^{\omega} - \frac{2\pi}{\Lambda_{\mathrm{QPM}}} = 0. \qquad (1)$$

Starting from Eq. (1), where $n_{\mathrm{eff}} = n_{\mathrm{eff}}(\lambda, \mathrm{NA}, a)$ is the effective refractive index of the propagating modes and depends on the wavelength of the fundamental mode, the NA of the fiber and the diameter of the fiber core (a), we can obtain the expression of the QPM period, which is

$$\Lambda_{\mathrm{QPM}} = \frac{\lambda}{2(n_{\mathrm{eff}}^{2\omega} - n_{\mathrm{eff}}^{\omega})}. \qquad (2)$$

The first grating was written with a 57-μm period. The modulation in $\chi^{(2)}$ nonlinearity is achieved by periodic UV erasure of the poling field by local exposure to 355 nm radiation delivered as a 200-kHz train of 8-ps pulses, focused to a 10 μm × 100 μm spot size with a total fluence of 200 J/cm^2. The setup used both for optical characterization and UV erasure of the periodically poled fibers is shown in Fig. 3, including a high power pulsed pump laser source (second harmonic of a mode-locked

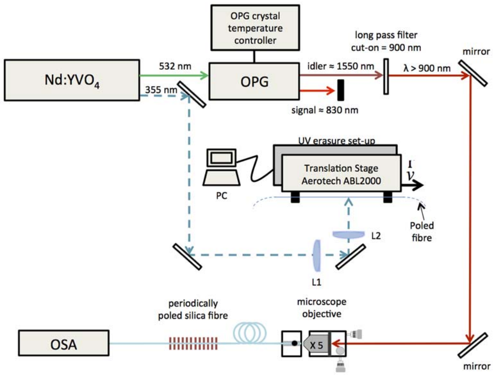

Fig. 3. Experimental setup for the inscription of the QPM-grating in the induction-poled fiber by 355 nm erasure. L1 and L2 are cylindrical lenses of focal length $f = 500$ and 85 mm, respectively, used to produce a spot size on the fiber of 10 μm × 100 μm. The optical setup used for the SHG nonlinear characterization of the periodically poled fiber is also shown.

amplified Nd:YVO$_4$ solid state laser, pulse duration 8 ps, repetition rate 250 kHz, average power 2.5 W), pumping an optical parametric generator (OPG), to produce a broadband infrared idler output (3 dB bandwidth approx. 80 nm, average power of 50 mW) that is temperature tunable between 1100 and 2500 nm. The long-wave pass filter in the optical setup rejects all radiation below the cut-on wavelength (900 nm) associated with the source. This ensures that any spectra observed at wavelengths shorter than 900 nm will be due only to nonlinear processes occurring within the periodically poled fiber. The black trace in Fig. 4 shows the output spectrum of the first 57-μm period grating. The tunable broadband laser pump launched into the fiber generates a frequency-doubled response centered at the QPM wavelength of 1666 nm. Deviations from the theoretically expected Sinc^2 profile of the SHG are mainly attributed to grating fabrication errors resulting from the incomplete removal of the fiber polymer coating and gallium residues left inside the fiber after purging. A second sample was prepared under identical experimental conditions but written with a period of 55.5 μm in order to shift the QPM wavelength to ~1550 nm as determined from numerical simulations of the fiber dispersion. The shorter wavelength output (red trace in Fig. 4) clearly demonstrates that the SHG output is due to induction poling. In order to provide a quantitative value for $\chi^{(2)}$, we launched 50 mW of tunable narrow linewidth NIR laser radiation, tuned around this 1550-nm QPM wavelength. The resulting SHG was measured using a silicon detector with sensitivity in the 200-pW range. From the analysis of Pruneri *et al.* [10] for a periodically poled silica fiber, given a device length of 17.83 mm and a modal overlap area of 40.3 μm at 1586 nm wavelength, splice losses of 0.76 dB plus residual liquid metal loss of 0.03 dB/cm after purging, we estimate a $\chi^{(2)}$ value of ≤ 0.0011 pm/V. This is close to the expected value for pure Suprasil grade silica [2]. Furthermore, as the QPM grating phase matches the LP01 pump to the LP01 second harmonic, the SHG is generated in the diffraction limited fundamental mode.

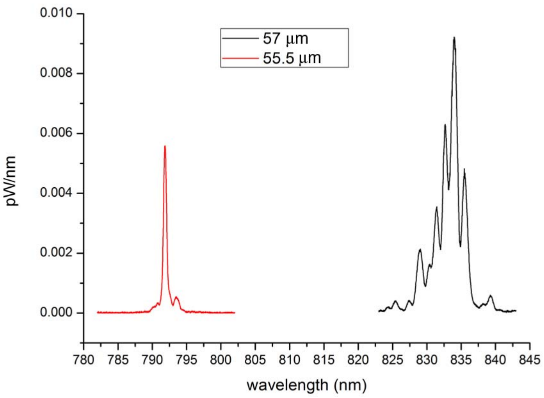

Fig. 4. SHG spectra of induction poled samples with different QPM grating periods written via UV erasure.

The indirect electrostatic induction mechanism operates by charging up the embedded, electrically floating gallium wires created inside the sample. We have modeled this behavior using COMSOL multiphysics numerical simulations of the electric potential distributions between the inductor, the sample, and the ground plane. Figure 5 (Top) shows a 2D map of the equipotentials

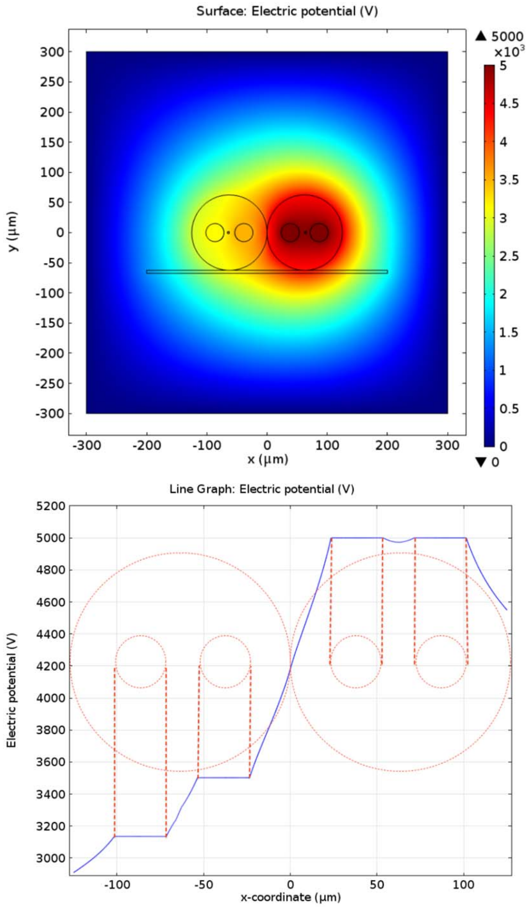

Fig. 5. (Top) Simulated 2D electric potential distribution presenting the initial conditions before poling begins. In the model, +5 kV is applied to both anodes of the inductor, while both wires inside the sample are left floating. Here, the only well defined ground is the air box enclosing the entire structure. (Bottom) A line scan through the geometric centers of the fibers reveals large potential variations in the sample that can drive impurity ion migration for depletion formation.

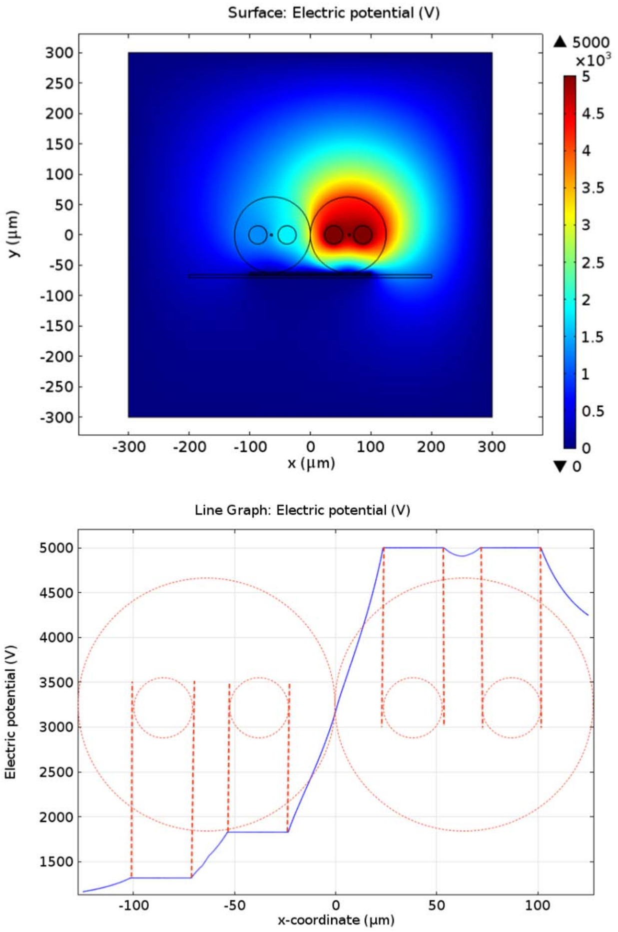

Fig. 6. (Top) Simulated initial 2D electric potential distribution before poling begins with both grounded air box and incorporated ground plane. (Bottom) A line scan through the geometric centers of the fibers shows lower absolute electric potential values compared with Fig. 5, but higher relative internal potential differences between the sample electrodes to drive ion migration/depletion formation.

calculated using Gauss' law before charged ion migration begins to generate the depletion regions. Note that in this first model, only the virtual "air box" that encloses the entire structure is grounded. A line scan of the electric potential along $y = 0$ through the common geometric centers of the two fibers shown in Fig. 5 (Bottom) demonstrates that a potential difference of ~375 V develops between the floating sample electrodes, strongly suggesting that an enhanced "avalanche-like" positive feedback mechanism similar to that described by Margulis *et al.* [4] initiates the formation of the depletion region. In addition, the electric field distribution can be tailored to optimize the potential difference between the sample electrodes. In the second model, as well as the grounded air box, the ground plane on which the fibers are placed has also been "switched on" (Fig. 6, top) and the potential differences again recorded by a line scan through the common geometric fiber centers (Fig. 6, bottom). Here it can be observed that the relative potential difference between the floating sample electrodes has now increased to ~500 V, although the absolute value of the electric potential has reduced (~3500 to ~3125 V in the first model compared with ~1825 to ~1325 V in the second). Simulations also reveal that the relative azimuth rotation angle of the sample with respect to the inductor fiber can further enhance the internal potential difference, demonstrating that induction poling can be engineered and optimized with many different parameters. A full numerical analysis of this parameter space including charge migration and depletion region formation will be addressed in future work.

In conclusion, we have both numerically simulated and experimentally demonstrated an indirect electrostatic induction technique for thermally poling silica fibers with embedded electrodes. QPM via periodic UV erasure confirms that a second-order nonlinearity has been generated by induction, using easily removable liquid gallium electrodes. This innovative technique lifts a number of restrictions on the use of complex microstructured optical fibers (MOF) for poling, as it is no longer necessary to individually contact internal electrodes. This discovery also presents a general methodology for selective liquid metal filling both radially and longitudinally, allowing for indirect poling inside any complex geometry, as well as over arbitrarily long MOF sample lengths. The optical mode confinement, dispersion, and effective group index engineering possible using MOFs poled via this method could open up completely new areas of highly efficient $\chi^{(2)}$-based fiber device applications.

The authors acknowledge EPSRC EP/I035307/1 and C. Corbari acknowledges the EU project CHARMING (contract no. FP7-288786) for financial support. We also thank P. G. Kazansky for access to scientific and technical facilities.

References

1. Y. Q. Xu and S. G. Murdoch, Opt. Lett. **36**, 4266 (2011).
2. R. A. Myers, N. Mukherjee, and S. R. J. Brueck, Opt. Lett. **16**, 1732 (1991).
3. N. Mukherjee, R. A. Myers, and S. R. J. Brueck, J. Opt. Soc. Am. B **11**, 665 (1994).
4. W. Margulis, O. Tarasenko, and N. Myrén, Opt. Express **17**, 15534 (2009).
5. H. An and S. Fleming, Opt. Express **20**, 7436 (2012).
6. M. Fokine, L. E. Nilsson, A. A. Claesson, D. Berlemont, L. Kjellberg, L. Krummenacher, and W. Margulis, Opt. Lett. **27**, 1643 (2002).
7. T. G. Alley and S. R. J. Brueck, Opt. Lett. **23**, 1170 (1998).
8. A. Canagasabey, M. Ibsen, K. Gallo, A. V. Gladishev, E. M. Dianov, C. Corbari, and P. G. Kazansky, Opt. Lett. **35**, 724 (2010).
9. J. A. Armstrong, N. Bloembergen, J. Ducuing, and P. S. Pershan, Phys. Rev. **127**, 1918 (1962).
10. V. Pruneri, G. Bonfrate, P. G. Kazansky, D. J. Richardson, N. G. Broderick, J. P. de Sandro, C. Simonneau, P. Vidakovic, and J. A. Levenson, Opt. Lett. **24**, 208 (1999).

Letter Vol. 41, No. 4 / February 15 2016 / *Optics Letters* 761

Optics Letters

Phase matched parametric amplification via four-wave mixing in optical microfibers

Muhammad I. M. Abdul Khudus,[1,2,*] **Francesco De Lucia,**[1] **Costantino Corbari,**[1,3] **Timothy Lee,**[1] **Peter Horak,**[1] **Pier Sazio,**[1] **and Gilberto Brambilla**[1]

[1]*Optoelectronics Research Center, University of Southampton, Southampton SO17 1BJ, UK*
[2]*Photonics Research Centre, Department of Physics, Faculty of Science, University of Malaya, 50603 Kuala Lumpur, Malaysia*
[3]*Renishaw plc, New Mills, Wotton-under-Edge, Gloucestershire GL12 8JR, UK*
**Corresponding author: miak2g12@soton.ac.uk*

Received 13 November 2015; revised 7 January 2016; accepted 8 January 2016; posted 11 January 2016 (Doc. ID 253837); published 5 February 2016

Four-wave mixing (FWM) based parametric amplification in optical microfibers (OMFs) is demonstrated over a wavelength range of over 1000 nm by exploiting their tailorable dispersion characteristics to achieve phase matching. Simulations indicate that for any set of wavelengths satisfying the FWM energy conservation condition there are two diameters at which phase matching in the fundamental mode can occur. Experiments with a high-power pulsed source working in conjunction with a periodically poled silica fiber (PPSF), producing both fundamental and second harmonic signals, are undertaken to investigate the possibility of FWM parametric amplification in OMFs. Large increases of idler output power at the third harmonic wavelength were recorded for diameters close to the two phase matching diameters. A total amplification of more than 25 dB from the initial signal was observed in a 6 mm long optical microfiber, after accounting for the thermal drift of the PPSF and other losses in the system. © 2016 Optical Society of America

OCIS codes: (190.4370) Nonlinear optics, fibers; (190.4410) Nonlinear optics, parametric processes; (190.4380) Nonlinear optics, four-wave mixing.

http://dx.doi.org/10.1364/OL.41.000761

Four-wave mixing (FWM) is a process in which four waves interact via the optical Kerr nonlinearity of a medium, where two photons from one or two 'pump' waves (for instance at frequencies ω_1, ω_2) are annihilated, and two new photons, called the signal (ω_3) and idler (ω_4), are created [1]. One application of FWM is parametric amplification, where the power from one wavelength is transferred to another wavelength, and has been demonstrated in a variety of optical fibers, with the highest recorded conversion being 70 dB [1–4]. However, parametric amplification via FWM requires phase matching for efficient energy conversion in order to compensate for material and waveguide dispersion as well as nonlinear effects, often limiting the bandwidth of the process [5]. A number of schemes were proposed which allowed for a broader bandwidth, but the largest realized bandwidth is 900 and 300 nm for solid core and microstructured optical fibers, respectively [6,7]. In this Letter, we demonstrate the possibility of using optical microfibers (OMFs) for FWM parametric amplification over a wavelength band of over 1000 nm by exploiting the tailorable dispersion characteristics of the OMF to optimize the diameter for phase matching. The technique theoretically allows for the amplification and generation of an almost arbitrary set of wavelengths, as well as the possibility of building fully fiberized light sources in the ultraviolet (UV) and mid-infrared (mid-IR) wavelength ranges.

OMFs are typically drawn from conventional fibers, most commonly by the flame brushing technique, where a section of the fiber is heated to the softening point and pulled to reduce the diameter. By doing so, the optical core of the fiber gradually disappears, and the erstwhile cladding becomes the core, with air being the cladding. This allows for higher mode confinement, translating into an increased nonlinearity of up to 100 times the original value, as well as, relatively low losses of typically <1 dB [8]. The relatively high nonlinearity and tailorable dispersion has been previously exploited to achieve intermodal third harmonic generation in optical microfibers [9,10], as well as an efficient means to achieve parametric conversion [11]. The phase matching and energy conservation conditions for efficient FWM, respectively, can be written as [5]:

$$\beta(\omega_4) + \beta(\omega_3) = \beta(\omega_1) + \beta(\omega_2), \quad \textbf{(1)}$$

$$\omega_1 + \omega_2 = \omega_3 + \omega_4, \quad \textbf{(2)}$$

where the subscripts 1, 2, 3, and 4 refer to the four interacting wavelengths and $\beta(\omega)$ is the propagation constant for frequency ω. Here, we will assume that light at all wavelengths is propagating in the fundamental mode of the OMF as this would be the most efficient mode for FWM.

In order to find the OMF diameter required to achieve phase matching in Eq. (1), the rigorous eigenvalue equations for a step index refractive index profile were solved for a silica OMF. The wavelengths employed are harmonics of the fundamental wavelength at 1550 nm, such that they automatically satisfy Eq. (2). To account for both degenerate $\omega_1 = \omega_2$ and non-degenerate $\omega_1 \neq \omega_2$ FWM, the wavelengths of the fundamental frequency (FF), second harmonic (SH), third harmonic (TH), and fourth harmonic (FH) were taken into consideration, as shown in Fig. 1(a).

Three different FWM schemes were theoretically investigated, namely, FWM between (A) FF, SH, and TH (degenerate); (B) FF, SH, TH, and FH (non-degenerate); and (C) SH, TH, and FH (degenerate). The sum of the propagation constants on each side of Eq. (1) was plotted for each FWM scheme in Fig. 1(b). The raw data used in this Letter can be obtained from [12]. This yields the predicted phase matching diameters for the fundamental modes of the three FWM schemes discussed above. It is clear that for each FWM scheme, there are two phase matching diameters at which Eq. (1) is satisfied, denoted d_1 and d_2, as detailed in Table 1. Experimentally, this translates into two different diameters at which FWM amplification is expected to occur in an OMF. Here, we shall only consider scheme (A), with schemes (B) and (C) being studied in a future work. These wavelengths are chosen primarily for experimental reasons, but the technique can be easily extended to any number of wavelength combinations satisfying Eq. (2), as illustrated in Fig. 1(c) for the degenerate FWM. It can be seen that phase matching can be achieved with a wide range of pump wavelengths (λ_1 and λ_2). A plot of the dispersion of the microfiber is shown in Fig. 2 to indicate the change of the dispersion with OMF diameter.

Table 1. Phase Matching Diameters for the Three Different FWM Schemes Considered[a]

FWM Scheme and Type	Phase Matching Diameter (μm)	
	d_1	d_2
(A) degenerate	2.886	0.800
(B) non-degenerate	1.719	0.790
(C) degenerate	0.872	0.530

[a] d_1 and d_2 Denote the first and second phase matching diameters, respectively.

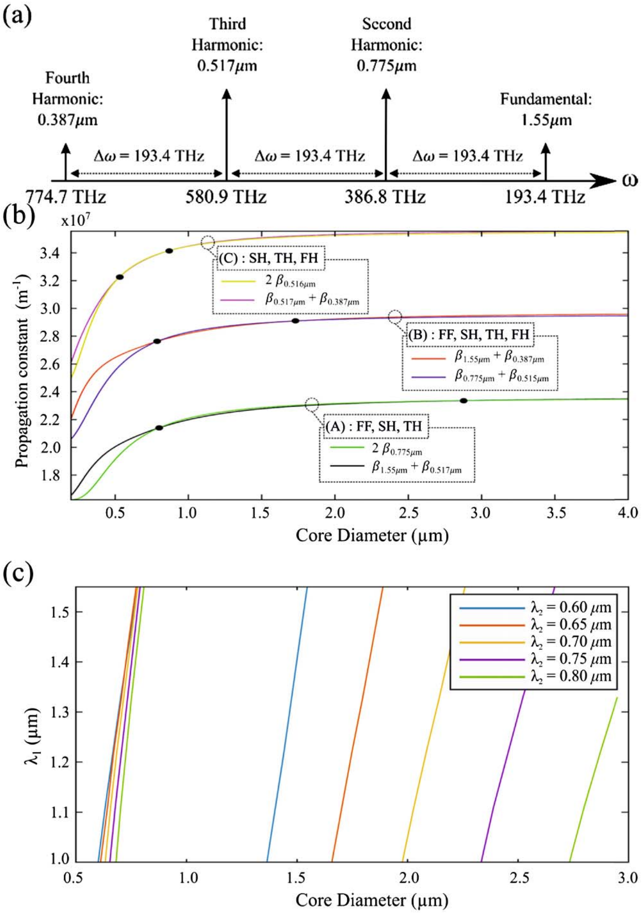

Fig. 1. (a) Frequencies investigated for FWM. The frequencies denoting pump, idler, and signal vary with the scheme for FWM, as detailed in Table 1. (b) Relation between the OMF diameter and mode propagation constants for three different FWM schemes; black dots represent phase matching diameters satisfying Eq. (1). (c) Degenerate FWM phase matched diameter for a set first pump wavelength, λ_1, (left) and five different signal wavelengths, λ_2. The idler wavelength λ_3 can be calculated from $1/\lambda_3 = 2/\lambda_2 - 1/\lambda_1$. Two distinct sets of phase matching diameters can be discerned from the figure.

To investigate this, a master oscillator power amplifier (MOPA) seeded by a narrowband continuous wave (CW) seed laser (Photonetics Tunics BT) working in the telecom C-band wavelength region (1530–1565 nm) was employed. The MOPA system (shown in Fig. 3) produced an output at a central wavelength of 1550.3 nm with a pulse width of 5 ns, repetition rate of 200 kHz, and average powers of between 300 and 800 mW, which translated into peak powers of between 300 and 800 W. The pulses were generated using an electro-optic modulator

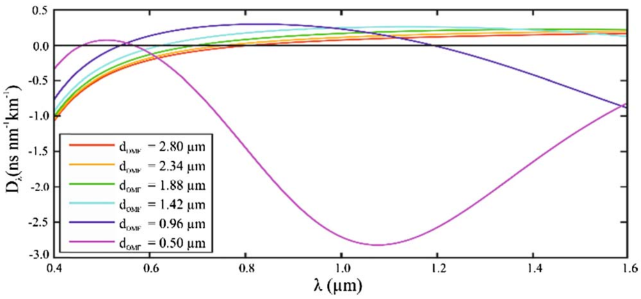

Fig. 2. Variation in the dispersion of the OMF (D_λ) with wavelength λ for different OMF diameter (d_{OMF}), where it can be observed that the dispersion changes significantly for diameters $0.5\ \mu\text{m} < d_{\text{OMF}} < 1\ \mu\text{m}$.

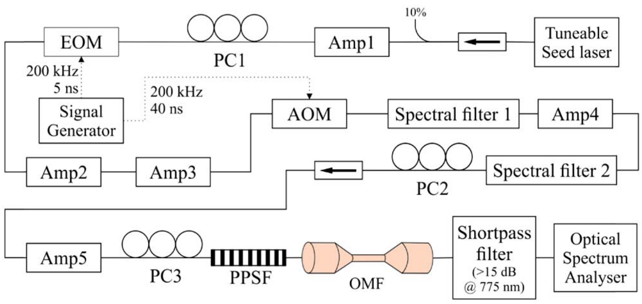

Fig. 3. Schematic of the experimental setup used to investigate enhancement of the idler signal due to phase matching in the OMFs. A total of five amplifiers (Amp#) were employed in conjunction with two spectral filters in order to minimize OSNR and inter-pulse ASE. Here, PPSF is a periodically poled silica fiber; PC# is a polarization controller.

(EOM), which is then followed by an acousto-optic modulator (AOM) further along the chain to remove any inter-pulse amplified spontaneous emission (ASE) in the system to ensure that the majority of the power is contained in the pulse. Two fiberized thin film spectral filters operating in the C-band were also employed in order to improve the optical signal-to-noise ratio (OSNR) at the final output, required for an efficient SH generation. Polarization is managed by the use of two polarization controllers (PC) in the MOPA chain.

The output of the MOPA was then connected to a periodically poled silica fiber (PPSF) designed to be quasi-phase matched (QPM) for efficient conversion of the FF at 1550.3 nm into the SH at 775.15 nm via the SH generation (SHG), which has a total insertion loss of <0.5 dB. The PPSF was fabricated from a twin-hole Germania doped fused silica fiber manufactured by Acreo Fiberlab. The two holes were first fully filled with Gallium liquid electrodes by means of a pressure filling technique similar to the one described in [13]. Tungsten wires were then inserted at each end of the two holes before the entire ensemble was sealed with superglue. The fiber was then thermally poled by applying a positive voltage of 7.5 kV on both the electrodes whilst being heated at 250°C on a hotplate [14]. The sample was left to pole for 120 min before the hotplate was switched off and allowed to cool with the high voltage continually applied for a further 60 min. This procedure induces an effective second order susceptibility $\chi^{(2)}_{\mathrm{eff}}$ uniformly across the silica fiber core by means of a third order rectification process expressed by the relationship $\chi^{(2)}_{\mathrm{eff}} \approx 3\chi^{(3)} E_{\mathrm{rec}}$, where $\chi^{(3)}$ is the third order susceptibility of silica and E_{rec} is the static frozen-in electric field due to poling [15,16]. QPM allows the wavevector mismatch between the FF and SHs to be compensated by modulating the nonlinearity induced by poling. This modulation is achieved by a periodic UV erasure of the poling field by local exposure to 355 nm radiation delivered as a 200 kHz train of 8 ps pulses, focused to a 10 μm × 100 μm spot size with a total fluence of 200 J/cm^2 [17]. After exposing the poled fiber to this focused high-energy UV radiation, the resulting free carrier generation inside the fiber locally nullifies the frozen-in electric field E_{rec} [18]. A spatially periodic exposure of the uniformly poled fiber, therefore, produces a modulation of $\chi^{(2)}_{\mathrm{eff}}$. The period of this $\chi^{(2)}_{\mathrm{eff}}$ grating is chosen to allow for QPM at the desired wavelength. The use of PPSF allows for the adoption of an all-fiber nonlinear device and does not suffer from some constraints of the more common nonlinear devices such as relatively short interaction lengths, high costs, relatively low damage threshold, diffraction losses, and walk-off effects.

As the PPSF is highly sensitive to polarization, the incoming polarization was controlled by two PCs before and after the fifth amplifier (Amp5 in Fig. 3). To ensure efficient SHG, the PPSF was first directly connected to the first amplifier (Amp1) operating at a CW power of 30 mW and the wavelength from the tunable seed laser was changed gradually to see the change in the PPSF output. Once the wavelength which produces the highest SH signal is determined, the central wavelengths of both spectral filters were adjusted accordingly and the MOPA chain was reconnected. A pump power of 300 mW was employed at the MOPA output in order to avoid pump depletion and any other undesirable nonlinear effects. At this power level, the OSNR of the MOPA output is more than 50 dB, suitable for a relatively efficient SHG, producing an average output power of more than 3 mW at 775 nm. This resulted in both the FF and SH wavelengths existing at the output end of the PPSF. A by-product of the SHG process, however, is the generation of a signal at the TH wavelength via non-phase-matched sum frequency generation (SFG), where $\omega_3 = \omega_1 + \omega_2$. This is similar to the results in [19] and is due to slight variations in the PPSF grating. The efficiency of this process is exceedingly small ($\eta \sim 10^{-9}$), as the PPSF was optimized for SHG and not for the TH wavelength, but it provides a "seed" laser with which parametric amplification can occur.

The simultaneous generation of the SH and TH wavelengths, in addition to the FF wavelength, allows the frequency requirement for parametric amplification via degenerate FWM as detailed in scheme (A) of Table 1 to be automatically satisfied. This is enhanced as the FF, SH, and TH are co-polarized and overlap spatially, both of which are a consequence of the SHG and SFG processes in the PPSF. Very long pulses were employed in order to eliminate walk-off effects. The resulting output spectrum from the PPSF which has been passed through a shortpass filter before tapering is given in Fig. 4.

The output from the PPSF was then spliced to a length of Z Fiber (Sumitomo Electric) before being connected with a shortpass filter, designed to have a loss of more than 15 dB at 775 nm, and a broadband optical spectrum analyzer (OSA) (Yokogawa AQ6315A). The Z Fiber is then tapered by using the modified flame brushing technique, which employs a microheater, with the tapering profile being carefully controlled in order to satisfy the adiabaticity criteria thereby minimizing loss [7,8]. A length of 6 mm of the Z Fiber was tapered, from an initial diameter of 125 μm to a final diameter of 0.5 μm, in order to fully explore the entire range of the predicted phase matching diameters. At the end of the tapering process, the OMF has a full length of approximately 29 mm, with a waist length of 6 mm and a waist diameter of 0.5 μm. The 1.55 μm MOPA source, connected to the PPSF, was launched into the fiber whist being tapered. The temporal evolution of the output spectra at the peak of the idler wavelength (516.7 nm) was recorded with the OSA as shown in Fig. 5. A resolution of 10 nm was employed to capture all the generated signal power.

Initially, there is a very small signal at the idler wavelength, as explained above. This signal does not vary significantly as tapering takes place initially, with the small variation being ac-

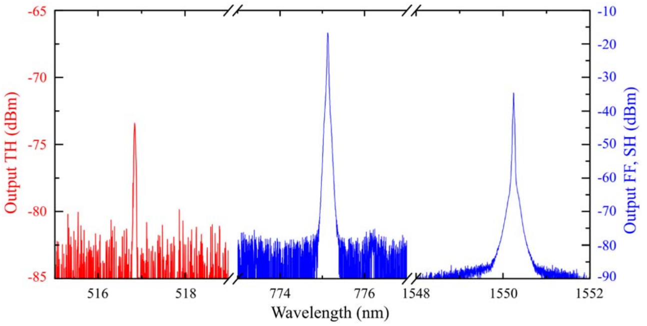

Fig. 4. Initial output signal from the PPSF after a shortpass filter. The loss of the filter is wavelength dependent, with longer wavelengths registering higher losses, causing the signal at FF (1550.3 nm) to appear smaller than the SH (755.15 nm), both shown here in blue. The idler signal (516.75 nm), shown in red, is relatively small and is just above the noise level. This is the signal that will be amplified by the OMF, as shown in Fig. 5.

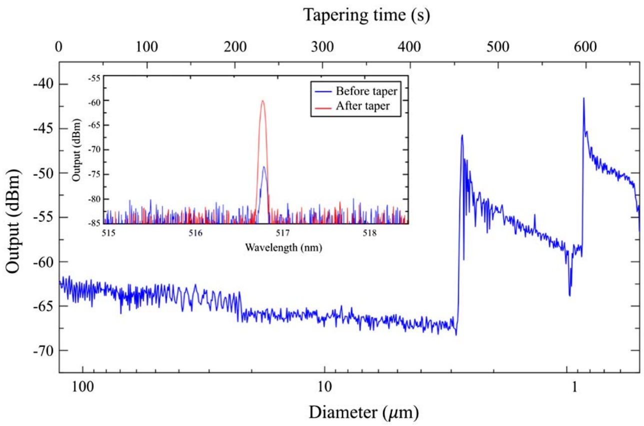

Fig. 5. Evolution of the idler signal at 516.75 nm with respect to the diameter (logarithmic) and the processing time (linear) during tapering. Inset: the idler signal before and after the tapering process. The data in the inset was measured with a resolution of 0.05 nm and a higher sensitivity, as compared to 10 nm and a lower sensitivity for the main figure, resulting in the apparent discrepancy in the initial power measurement.

counted for by the tapering process itself as well as the thermal drift of the PPSF. As the OMF diameter reaches the first phase matching diameter ($d_1 \approx 2.89$ μm), the output intensity increases by more than 22 dB. The signal then decreases as the fiber is tapered further, as the tapering process reduces the OMF length at which the phase matching diameter occurs, although, due to the increasing overall length of the microfiber there is a time-varying range of diameters in the OMF transition region which are phase matched and nearly phase matched, resulting in a gradual decrease in the signal. This downward trend is observed until the fiber reaches the second phase matching diameter ($d_1 \approx 0.80$ μm), where the signal increases dramatically by approximately 15 dB, reaching the highest recorded output power. As the fiber is tapered even more, the signal monotonically decreases until the tapering process stops at a diameter of 0.5 μm. The slight drop in intensity observed at $t = 580$ s and at the end of the tapering process is due to the OMF moving inside the microheater and approaching its walls. Additionally, at the end of processing, there are changes in the effective refractive index associated with temperature changes as the taper is taken out of the microheater. The inset in Fig. 5 shows the 12 dB increase in idler output between the untapered fiber and the OMF with the 0.5 μm diameter. Figure 5 indicates that if the tapering process is stopped at an OMF with a length of 6 mm and waist of approximately 800 nm, a total maximum enhancement of more than 20 dB from the original signal can be achieved, with the figure being closer to 25 dB if we use the output intensity at 5 μm as a baseline.

The final efficiency was increased from $\eta \sim 10^{-9}$ to $\eta \sim 10^{-7}$, corresponding to a parametric gain of 25 dB or 4.17 dB/mm, by using this method. This is very low compared to devices such as semiconductor optical amplifiers, where FWM efficiencies in excess of 20 dB are possible [20], but is comparable to other parametric amplifiers and is able to potentially operate across the entire optical bandwidth [1–7]. The final efficiency can be improved by increasing the pump-to-signal ratio, while the overall parametric gain can be improved by the fabrication of a longer OMF and by increasing the efficiency of the SHG, where an efficiency of 45% has been shown to be achievable [21].

In summary, we have demonstrated parametric amplification via FWM in optical microfibers, achieved by changing the diameter of the OMF to satisfy the phase matching requirement. After accounting for thermal drift, an amplification of more than 25 dB in the idler signal over a wavelength range of > 1000 nm was achieved by using an OMF with a waist length of 6 mm seeded by a MOPA operating in the telecom C-band in conjunction with a PPSF that generates the required FWM wavelengths. In principle, this technique can be extended to any wavelength, allowing for the relatively efficient generation and amplification of arbitrary wavelengths, assuming that other nonlinear effects such as SPM and XPM do not dominate.

Funding. Engineering and Physical Sciences Research Council (EPSRC) (EP/L01243X/1).

Acknowledgment. The authors thank Oleksandr Tarasenko and Walter Margulis from Acreo Fiberlab, who manufactured the fiber used for the PPSF as well as Peter Kazansky, Francesca Parmigiani, James Wilkinson, and Senthil Ganapathy at the Optoelectronics Research Centre of the University of Southampton for access to the necessary technical facilities.

REFERENCES

1. J. Hansryd, P. Andrekson, M. Westlund, J. Li, and P. Hedekvist, IEEE J. Sel. Top. Quantum Electron. **8**, 506 (2002).
2. L. Provino, A. Mussot, E. Lantz, T. Sylvestre, and H. Maillotte, J. Opt. Soc. Am. B **20**, 1532 (2003).
3. J. E. Sharping, J. Lightwave Technol. **26**, 2184 (2008).
4. T. Torounidis, P. A. Andrekson, and B. Olsson, IEEE Photon. Technol. Lett. **18**, 1194 (2006).
5. G. P. Agrawal, *Nonlinear Fiber Optics* (Academic, 2013), pp. 397–456.
6. J. C. Boggio, S. Moro, B. P. P. Kuo, N. Alic, B. Stossel, and S. Radic, J. Lightwave Technol. **28**, 443 (2010).
7. A. C. Sodré, J. M. Chavez Boggio, A. A. Rieznik, H. E. Hernandez-Figueroa, H. L. Fragnito, and J. C. Knight, Opt. Express **16**, 2816 (2008).
8. G. Brambilla, J. Opt. **12**, 043001 (2010).
9. T. Lee, Y. Jung, C. A. Codemard, M. Ding, N. G. R. Broderick, and G. Brambilla, Opt. Express **20**, 8503 (2012).
10. V. Grubsky and A. Savchenko, Opt. Express **13**, 6798 (2005).
11. M. I. M. Abdul Khudus, T. Lee, T. Huang, X. Shao, P. Shum, and G. Brambilla, Fiber Integr. Opt. **34**, 53 (2015).
12. M. Abdul Khudus, F. De Lucia, C. Corbari, T. Lee, P. Horak, P. Sazio, and G. Brambilla, "Enhancement of four-wave mixing frequency generation in optical microfibers [dataset]" (University of Southampton, 2015), http://dx.doi.org/10.5258/SOTON/383708.
13. M. Fokine, L. E. Nilsson, Å. Claesson, D. Berlemont, L. Kjellberg, L. Krummenacher, and W. Margulis, Opt. Lett **27**, 1643 (2002).
14. W. Margulis, O. Tarasenko, and N. Myrén, Opt. Express **17**, 15534 (2009).
15. R. A. Myers, N. Mukherjee, and S. R. J. Brueck, Opt. Lett. **16**, 1732 (1991).
16. P. G. Kazansky and P. St J. Russel, Opt. Commun. **110**, 611 (1994).
17. F. De Lucia, D. Huang, C. Corbari, N. Healy, and P. J. A. Sazio, Opt. Lett. **39**, 6513 (2014).
18. C. Corbari, A. V. Gladyshev, L. Lago, M. Ibsen, Y. Hernandez, and P. G. Kazansky, Opt. Lett. **39**, 6505 (2014).
19. M. Robles-Agudo, R. S. Cudney, and L. A. Ríos, Opt. Express **14**, 10663 (2006).
20. P. P. Baveja, D. N. Maywar, and G. P. Agrawal, IEEE J. Sel. Top. Quantum Electron. **18**, 899 (2012).
21. E. L. Lim, C. Corbari, A. V. Gladyshev, S. U. Alam, M. Ibsen, and D. J. Richardson, *Specialty Optical Fibers* (Optical Society of America, 2014), paper JTu6A-5.

Optics Letters

Optical fiber poling by induction: analysis by 2D numerical modeling

F. De Lucia,[1,†] D. Huang,[2,†] C. Corbari,[1] N. Healy,[3] and P. J. A. Sazio[1,*]

[1]*Optoelectronics Research Centre, University of Southampton, Southampton SO17 1BJ, UK*
[2]*Institute of High Performance Computing, A*STAR, 1 Fusionopolis Way, 138632 Singapore, Singapore*
[3]*Emerging Technology and Materials Group, Newcastle University, Merz Court, Newcastle NE1 7RU, UK*
Corresponding author: pjas@soton.ac.uk

Received 16 February 2016; revised 8 March 2016; accepted 10 March 2016; posted 16 March 2016 (Doc. ID 259214); published 5 April 2016

Since their first demonstration some 25 years ago, thermally poled silica fibers have been used to realize device functions such as electro-optic modulation, switching, polarization-entangled photons, and optical frequency conversion with a number of advantages over bulk free-space components. We have recently developed an innovative induction poling technique that could allow for the development of complex microstructured fiber geometries for highly efficient $\chi^{(2)}$-based device applications. To systematically implement these more advanced poled fiber designs, we report here the development of comprehensive numerical models of the induction poling mechanism itself via two-dimensional (2D) simulations of ion migration and space-charge region formation using finite element analysis.

OCIS codes: (190.4370) Nonlinear optics, fibers; (230.4320) Nonlinear optical devices; (190.2620) Harmonic generation and mixing; (230.1150) All-optical devices; (000.4430) Numerical approximation and analysis.

http://dx.doi.org/10.1364/OL.41.001700

The development of thermal poling, a technique to generate effective second-order nonlinearities in silica optical fibers [1], has found widespread applications in parametric frequency conversion [2], electro-optic modulation, switching [3], and polarization-entangled photon pair generation [4]. During thermal poling, the optical fiber is heated to increase the mobility of the impurity charge carriers (typically Na^+, Li^+, and K^+), while a high voltage is applied for a certain time between two electrodes embedded into the fiber [5]. The static electric field due to the application of the high voltage causes the impurity charges to drift from regions at high potential toward regions at lower potential, creating a space-charge region located near the anode. When the sample is cooled down, while the voltage is still applied, an electric field is frozen into the depleted region, and an effective nonlinear susceptibility $\chi^{(2)}_{\text{eff}}$ is induced into the sample due to a process of third-order nonlinear optical rectification. The early issues mainly related to the high risk of breakdown between the two electrodes (typically separated by a few tens of microns) were addressed by Margulis *et al.* [6], who demonstrated that it is possible to induce a value of $\chi^{(2)}_{\text{eff}}$ higher than the one obtained in the conventional case [5] by means of a poling configuration in which the two embedded electrodes are connected to the same positive potential of the anode. The method for "charging" optical fibers has been recently further developed by De Lucia *et al.* [7], who discovered that it is possible to create a space-charge region using electrostatic induction between an external inductor and the floating electrodes embedded inside a fused silica twin-hole fiber. As this novel technique avoids any physical contact to the internally embedded electrodes, it automatically lifts a number of restrictions on the use of microstructured optical fibers for poling, where the multiple contacting of individual electrodes becomes a prohibitive challenge. Thus, the induction poling technique, together with the use of embedded liquid electrodes such as Gallium [7], could, for example, allow for the poling of complex photonic crystal fibers (PCF), with the aim of realizing devices that fully exploit the inherently desirable PCF properties of strong optical mode confinement, dispersion, effective group index engineering, etc., for highly efficient nonlinear functionality.

To systematically implement these advanced device concepts, it is first necessary to develop comprehensive numerical models of the induction poling mechanism itself. To this end, we report here the development of two-dimensional (2D) simulations of induced space-charge region formation using COMSOL finite element analysis. This builds on current numerical models by Camara *et al.* [8] who developed a 2D analysis that accurately describes the specific geometry of poled fibers with internal electrodes, thus highlighting the role of various cations and the time evolution of second-order nonlinear profile within the fiber geometry. However, our recent experimental demonstration of electrostatic induction poling suggests that substantial modifications to the boundary conditions of these current 2D models are required to fully elucidate this novel poling mechanism. In the first instance, this arises due to the inherent assumption [8] that the outer surface of the fiber is always at ground potential. While this is a reasonable assumption when considering the experimental setup described by Margulis *et al.* [6], an external field applied by an inductor to floating electrodes inside fibers would, by definition, be fully shielded by this grounded surface, thus completely inhibiting the induction poling process. Furthermore, the model of Camara *et al.* [8] concludes that field-dependent H_3O^+ ion injection, which only becomes significant for longer poling times, does not differ significantly from constant rate injection conditions, given that the electric field at the anode-glass boundary reaches a value of $\sim 10^9$ V/m over a short time period and then remains constant. However, in the induction poling geometry, the variable floating potentials inherent in this process require a field-dependent charge injection scheme. Finally, it is also necessary to modify the field dependency to take into account ion recombination at the cladding-air interface. We show that mapping the salient features of the induction poling experimental geometry allows us to draw a more appropriate set of boundary conditions, and the modified 2D model can then be used to describe the dynamics of the second-order nonlinearity created inside the fiber when it is both close to and far away from the external inductor (as shown in Fig. 1).

As described in [8,9], sodium (Na^+) is the cation of highest mobility in silica, and its displacement results in a cation-depleted region of high electrical resistivity near the floating electrodes embedded inside a fused silica twin-hole fiber waveguide. The negatively charged, nonbridging oxygen sites left behind (uncompensated negative charges) have very low mobility at 300°C, and it is this charge separation that gives rise to the recorded field. The ions reaching the electrode-cladding surface or the air-cladding surface are assumed to recombine on these surfaces, rather than accumulate. If poling continues long enough, the width of the depletion region increases, but other slower cations are also driven into the glass (e.g., H_3O^+), which begin to neutralize the uncompensated negative charges. When both migration and diffusion are taken into account, the local equation of continuity and Poisson's equation leads to the following partial differential equation solved in x, y, and t:

$$\frac{\partial \boldsymbol{c}_i}{\partial \boldsymbol{t}} + \nabla \cdot (-\boldsymbol{D}_i \nabla \boldsymbol{c}_i - \boldsymbol{z}_i \boldsymbol{\mu}_i \boldsymbol{F} \boldsymbol{c}_i \nabla \boldsymbol{V}) = \boldsymbol{R}_i, \tag{1}$$

where the index i represents one of the positive ionic species ($i = 1$ for sodium ions and $i = 2$ for the injected charges), the first term in brackets accounts for diffusion, and the other term corresponds to drift in the electric field. In Eq. (1), c is the concentration, D is the diffusivity, z is the charge, μ is the ion mobility, F is Faraday's constant, V is the electric potential, and R is the consumption or production rate. The electric field and potential distribution as a function of poling duration are derived from Maxwell's equations in the electrostatic regime, from which it is possible to deduce the second-order nonlinearity spatial distribution within the fiber.

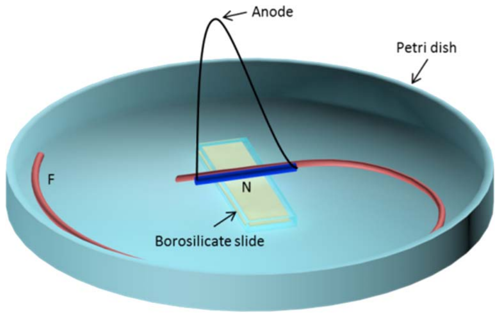

Fig. 1. Schematic of the experimental setup for induction poling of optical fibers. The inductor is colored blue (equipped with two electrodes connected to the same anodic potential) with the sample colored red (with two embedded floating electrodes) to be poled by induction. Both are adhered to a glass slide and held in close proximity. N identifies a region of the sample near the inductor, F, a section of the same sample located far away from the inductor. The entire Petri dish is heated with a (electrically earthed) hotplate at 300°C.

For the implementation of the COMSOL model, a twin-hole fiber with dimensions identical to our experimentally relevant samples described in [7] (i.e., OD = 125 μm, core diameter 4.3 μm, NA = 0.17) is enclosed by a virtual "air box," as shown in Fig. 2. An inductor placed adjacent to the fiber provides the external electric field that charges up the floating electrodes inside (see Fig. 1). The uniformly distributed Na^+ ions are assumed to have an initial concentration of 1 ppm at $t = 0$ s. It is also assumed that there is up to 1 ppm of H_3O^+ ions injectable at the holes, with none present within the fiber at $t = 0$ s. To achieve initial charge neutrality, negatively charged, nonbridging oxygen sites (i.e., NBO^-) with extremely low mobility are uniformly distributed inside the fiber with a concentration of 1 ppm at $t = 0$ s.

The holes are also assumed to be entirely filled with metal electrodes and present an equipotential. Only the outer boundaries of the "air box" (a cube with side 10 cm) and the ground plane (presented by the metallic heater) located 10 μm underneath the inductor and fiber sample in Fig. 2 are assumed to be electrically earthed. Furthermore, H_3O^+ ions can be injected through the electrode-cladding surface when located at electric potentials higher than the surrounding cladding. An adjustable parameter σ_2 (whose value was chosen to be the same as the well established thermal poling model reported in [9]) is used to describe the charge injection into the fiber. We also need to consider the special case where the electric field is less than zero. In this case, H_3O^+ ions in the nearby cladding (either previously injected or diffused from other parts of the fiber) will have a negative injection rate, thus implying an outflow of

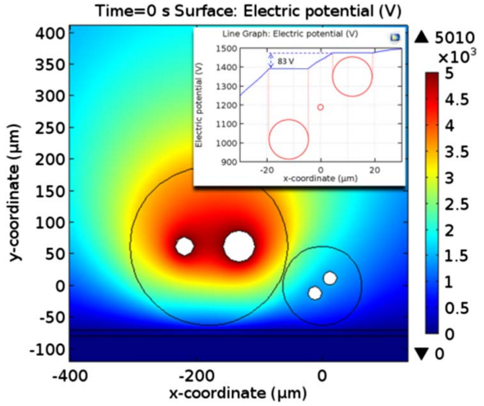

Fig. 2. 2D representation of the initial ($t = 0$ s) electric potential distribution developed within the electrostatic induction poling mechanism. The setup consists of the external inductor on the LHS, composed of twin electrodes at +5 kV running through a 6 cm long silica fiber dielectric sheath, as shown in Fig. 1, to prevent unwanted electrical breakdown to a grounded heater underneath. The sample being poled on the RHS is described in [7] and is rotated at an arbitrary angle with respect to the inductor to replicate realistic experimental conditions. The inset shows the electric potential values recorded along a line scan through the geometric centers of the sample, exhibiting a potential difference of around 83 V.

H_3O^+ ions. However, if there are not any H_3O^+ ions (i.e., $c(H_3O^+) = 0$) at the electrode-cladding boundary, the injection rate will be zero, even with an electric field less than zero. Therefore, the variation of the injected H_3O^+ ions density per unit of time at the electrode-cladding surface can be written as [9]

$$\left(\frac{\partial c_2}{\partial t}\right)\bigg|_{surface} = \sigma_2 E, \qquad E \geq 0 \quad or \quad E < 0 \; and \; c_2 > 0, \tag{2}$$

$$\left(\frac{\partial c_2}{\partial t}\right)\bigg|_{surface} = 0, \textbf{ otherwise}, \tag{3}$$

where E is the electric field magnitude at the electrode surface.

The avalanche-like, positive feedback depletion region formation as described by Margulis *et al.* [6] in "cathode-free" fibers is also considered to operate in an enhanced form within the electrostatic induction poling mechanism [7]. However, within this configuration, it is important to note that there are two distinct and separate spatial regimes. First, we can examine the evolution of the depletion region formation when the fiber sample is immediately adjacent to the external inductor, as shown in Fig. 3, where the electric field from the inductor penetrates inside the fiber sample as it lacks a grounded outer surface in contrast to existing thermal poling models. As can be seen, after 100 min, the electric potential distribution developed inside the fiber sample, and subsequent cation migration leads to an asymmetry in comparing both the size and shape of the depletion regions formed around the internal floating electrodes. This disparity reflects the inhomogeneity of the electric field distribution close to the inductor and the strong influence of the nearby ground plane defined by the heater (and the relatively low series resistance of the borosilicate glass slide and Petri dish at elevated temperatures in Fig. 1). The summation of sodium and hydronium ion depletion regions, where H_3O^+ ions occupy the negatively charged sites left by migrating Na^+ ions, results in a circular negative net charge distribution layer [8] surrounding the floating electrodes that will be asymmetric, as detailed above.

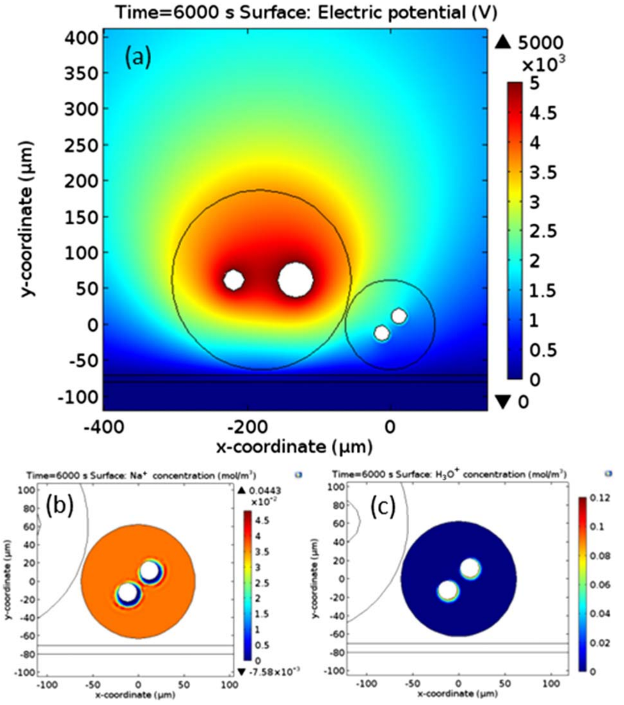

Fig. 3. Distribution of (a) electric potential, (b) Na^+, and (c) H_3O^+ mobile cations after 100 min of poling near the inductor (position N in Fig. 1).

As well as this specific behavior close to the (6 cm long) inductor, it is also possible to model the poling mechanism some distance from this region as, typically, the sample being poled is many times longer than the inductor itself (see [7] and Fig. 1). In this spatially separated scenario, it is valid to assume that the electric field due to the inductor no longer has any direct influence on the cation migration within the remainder of the sample. Nevertheless, due to the fact that during induction poling, there is very little, if any, current flow through the fiber; therefore, virtually no voltage drop due to metallic series resistance, the internal floating electrodes will present a well-characterized equipotential surface throughout the entire sample. This means that any electric potential picked up by the floating electrodes close to the inductor will be effectively transferred to any remote location throughout the fiber. In addition, this electric potential will constantly evolve due to the temporal evolution of the induction poling dynamics. In other words, the model used to describe the induction poling mechanism far from the inductor can be considered as similar to that developed by Camara *et al.* [8]. Important differences remain, however, such as the position of the ground potential which, rather than being the outer surface of the fiber sample, is defined instead as the outer boundaries of a virtual "air box," as well as the electrically earthed heater (combined with the low borosilicate glass series resistance), as shown in Fig. 4. Furthermore, the electric potential of each internal electrode is not a value fixed at $t = 0$ as in [8], but rather varies continuously as defined by the electric potential distribution close to the inductor.

It is interesting to note how the model both close to (Fig. 2) and far from (Fig. 5) the inductor exhibits a strong inhomogeneity of the electric field distribution around the floating electrodes, as well as a strong influence due to the earthed heater. This suggests that an enhanced "avalanche-like" positive feedback [6,7] drives the formation of the depletion region. Furthermore, it is worth noting that, even if the electric equipotential surfaces of the floating electrodes near and far from the inductor evolve in time in the same way, the two depletion regions develop differently in the two different locations. This is due to the presence of the external electric field of the inductor, which modifies the total electric field distribution around each electrode, compared to the situation far from the inductor. A different distribution of the electric field in the space around the electrodes will determine a different evolution of the depletion region in these positions. As shown in Fig. 6, our simulations also reveal that the relative azimuth rotation angle of the sample (with respect to the inductor fiber and underlying heater), as well as the position of the core with respect to the electrodes, can further enhance the internal potential difference, demonstrating that induction poling can be engineered and optimized with many different parameters.

In summary, we have presented the results of 2D simulations [10] developed using COMSOL Multiphysics finite element analysis of space-charge region formation generated via electrostatic induction poling. Substantial modifications to the boundary conditions of current numerical models were

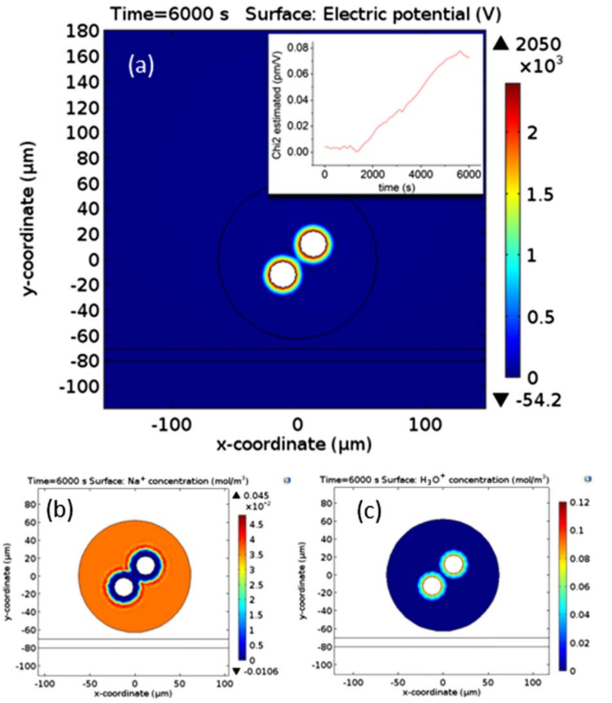

Fig. 4. Distribution of (a) electric potential, (b) Na^+, and (c) H_3O^+ mobile cations after 100 min of poling far from the inductor (position F in Fig. 1). The inset of (a) shows the evolution of the second-order nonlinearity as derived from the magnitude of the electric field at the center of the fiber where the 4.3 µm diameter, NA = 0.17, Germania doped core is located, as described in [7].

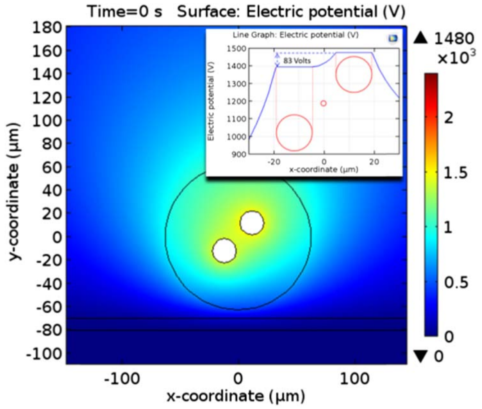

Fig. 5. Distribution of the initial ($t = 0$ s) electric potential far from the inductor. The inset shows the electric potential values recorded along a line scan through the geometric centers of the sample, exhibiting a potential difference value of around 83 V, as in the inset of Fig. 2.

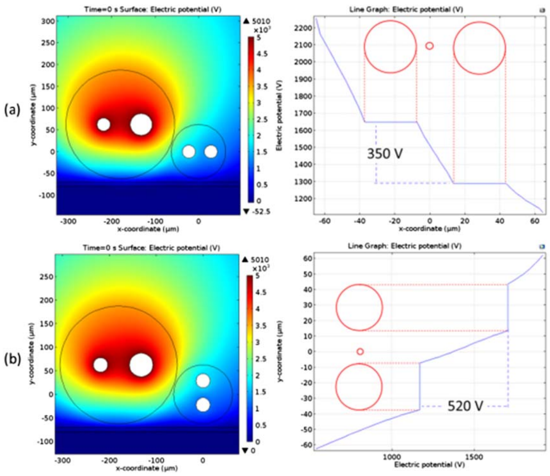

Fig. 6. (a) (Left) Simulated initial 2D electric potential distribution before charged ion migration begins to generate the depletion region. The external inductor and adjacent sample fiber are shown with zero relative azimuthal rotation. (Right) A line scan through the geometric centers of the sample reveals large potential variations (350 V) that drives impurity ion migration during electrostatic induction poling. (b) (Left) 2D electric potential distribution for a 90 deg relative azimuthal rotation of the sample. (Right) A line scan through the geometric centers of this sample orientation exhibits an even larger (520 V) potential difference between the internal electrodes compared with the sample in (a), resulting in faster depletion region dynamics.

required to fully elucidate this novel poling mechanism. This modified 2D model can be used to understand the dynamics of the second-order nonlinearity created inside the fiber sample due to depletion region formation when it is both close to and far from the inductor. Our numerical analysis presents us with a powerful general method to develop models of induction poling within any complex geometry such as, for example, microstructured optical fibers that potentially allow up to improvements of four orders of magnitude in second-harmonic generation efficiency relative to conventionally poled step-index optical fibers [11].

[†] These authors contributed equally to this work.

Funding. Engineering and Physical Sciences Research Council (EPSRC) (EP/I035307/1).

REFERENCES

1. R. A. Myers, N. Mukherjee, and S. R. J. Brueck, Opt. Lett. **16**, 1732 (1991).
2. A. Canagasabey, C. Corbari, A. V. Gladyshev, F. Liegeois, S. Guillemet, Y. Hernandez, M. V. Yashkov, A. Kosolapov, E. M. Dianov, M. Ibsen, and P. G. Kazansky, Opt. Lett. **34**, 2483 (2009).
3. M. Malmstrom, O. Tarasenko, and W. Margulis, Opt. Express **20**, 9465 (2012).
4. E. Y. Zhu, Z. Tang, L. Qian, L. G. Helt, M. Liscidini, J. E. Sipe, C. Corbari, A. Canagasabey, M. Ibsen, and P. G. Kazansky, Opt. Lett. **38**, 4397 (2013).
5. D. Wong, W. Xu, S. Fleming, M. Janos, and K.-M. Lo, Opt. Fiber Technol. **5**, 235 (1999).
6. W. Margulis, O. Tarasenko, and N. Myrén, Opt. Express **17**, 15534 (2009).
7. F. De Lucia, D. Huang, C. Corbari, N. Healy, and P. Sazio, Opt. Lett. **39**, 6513 (2014).
8. A. Camara, O. Tarasenko, and W. Margulis, Opt. Express **22**, 17700 (2014).
9. A. Kudlinski, Y. Quiquempois, and G. Martinelli, Opt. Express **13**, 8015 (2005).
10. F. De Lucia, D. Huang, C. Corbari, N. Healy, and P. J. A. Sazio, *Optical Fiber Poling by Induction: Analysis by 2D Numerical Modelling [Dataset]* (University of Southampton, 2016).
11. T. M. Monro, V. Pruneri, N. G. R. Broderick, D. Faccio, P. G. Kazansky, and D. J. Richardson, IEEE Photon. Technol. Lett. **13**, 981 (2001).

All-fiber fourth and fifth harmonic generation from a single source

MUHAMMAD I.M. ABDUL KHUDUS,[1,2,*] TIMOTHY LEE,[1] FRANCESCO DE LUCIA,[1] COSTANTINO CORBARI,[1,3] PIER SAZIO,[1] PETER HORAK,[1] AND GILBERTO BRAMBILLA[1]

[1] *Optoelectronics Research Center, University of Southampton, Southampton, SO17 1BJ, UK*
[2] *Photonics Research Centre, Department of Physics, Faculty of Science, University of Malaya, 50603 Kuala Lumpur, Malaysia*
[3] *Renishaw plc, New Mills, Wotton-under-Edge, Gloucestershire, GL12 8JR, UK*
[*] *miak2g12@soton.ac.uk*

Abstract: All-fiber fourth and fifth harmonic generation from a single source is demonstrated experimentally and analyzed theoretically. Light from a fully fiberized high power master oscillator power amplifier is launched into a periodically poled silica fiber generating the second harmonic. The output is then sent through two optical microfibers that generate the third and fourth harmonic, respectively, via four wave mixing (FWM). For a large range of pump wavelengths in the silica optical transmission window, phase matched FWM can be achieved in the microfibers at two different diameters with relatively wide fabrication tolerances of up to +/-5 nm. Our simulations indicate that by optimizing the second harmonic generation efficiency and the diameters and lengths of the two microfibers, conversion efficiencies to the fourth harmonic in excess of 25% are theoretically achievable.

OCIS codes: (190.2620) Harmonic generation and mixing; 190.4160) Multiharmonic generation; (190.4370) Nonlinear optics, fibers; (190.4410) Nonlinear optics, parametric processes; (190.4380) Nonlinear optics, four-wave mixing

---

References and links

1. D. N. Nikogosyan, *Nonlinear Optical Crystals: A Complete Survey* (Springer Science+Business Media, Inc, 2005).
2. V. P. Gapontsev, V. A. Tyrtyshnyy, O. I. Vershinin, B. L. Davydov, and D. A. Oulianov, “Third harmonic frequency generation by Type-I critically phase-matched LiB_3O_5 crystal by means of optically active quartz crystal,” Opt. Express **21**(3), 3715–3720 (2013).
3. Y. Kaneda, J. M. Yarborough, L. Li, N. Peyghambarian, L. Fan, C. Hessenius, M. Fallahi, J. Hader, J. V. Moloney, Y. Honda, M. Nishioka, Y. Shimizu, K. Miyazono, H. Shimatani, M. Yoshimura, Y. Mori, Y. Kitaoka, and T. Sasaki, “Continuous-wave all-solid-state 244 nm deep-ultraviolet laser source by fourth-harmonic generation of an optically pumped semiconductor laser using $CsLiB_6O_{10}$ in an external resonator,” Opt. Lett. **33**(15), 1705–1707 (2008).
4. D. A. V. Klinera, F. Di Teodorob, J. P. Koplowb, S. W. Mooreb, and A. V. Smith, “Efficient second, third, fourth, and fifth harmonic generation of a Yb-doped fiber amplifier," Opt. Commun. **210**(3), 393–398 (2002).
5. S. A. Slattery, D. N. Nikogosyan, and G. Brambilla, “Fiber Bragg grating inscription by high-intensity femtosecond UV laser light: comparison with other existing methods of fabrication,” J. Opt. Soc. Am. B **22**(2), 354–361 (2005).
6. P.J. Campagnola and C.-Y. Dong, “Second harmonic generation microscopy: principles and applications to disease diagnosis,” Laser Photonics Rev. **5**(1), 13–26 (2011).
7. P. A. Champert, S. V. Popov, J. R. Taylor, and J. P. Meyn, “Efficient second-harmonic generation at 384 nm in periodically poled lithium tantalate by use of a visible Yb–Er-seeded fiber source,” Opt. Lett. **25**(17), 1252–1254 (2000).
8. G.K. Samanta, S. Chaitanya Kumar, M. Mathew, C. Canalias, V. Pasiskevicius, F. Laurell, and M. Ebrahim-Zadeh, “High-power, continuous-wave, second-harmonic generation at 532 nm in periodically poled $KTiOPO_4$,” Opt. Lett. **33**(24), 2955–2957 (2008).
9. S.V. Popov, S.V. Chernikov and J.R. Taylor “6-W Average power green light generation using seeded high power ytterbium fiber amplifier and periodically poled KTP,” Opt. Commun. **174**(1) 231–234 (2000).
10. S. Chaitanya Kumar, G. K. Samanta, and M. Ebrahim-Zadeh “High-power, single-frequency, continuous-wave second-harmonic-generation of ytterbium fiber laser in PPKTP and MgO:sPPLT,” Opt. Express **17**(16), 13711–13726 (2009).
11. W. Margulis and U. Österberg, “Second-harmonic generation in optical glass fibers,” J. Opt. Soc. Am. B **5**(2), 312–316 (1988).

12. N. Myrén, H. Olsson, L. Norin, N. Sjödin, P. Helander, J. Svennebrink, and W. Margulis, "Wide wedge-shaped depletion region in thermally poled fiber with alloy electrodes," Opt. Express **12**(25), 6093–6099 (2004).
13. V. Pruneri, G. Bonfrate, P. G. Kazansky, D. J. Richardson, N. G. Broderick, J. P. De Sandro, C. Simonneau, P. Vidakovic, and J. A. Levenson "Greater than 20%-efficient frequency doubling of 1532-nm nanosecond pulses in quasi-phase-matched germanosilicate optical fibers," Opt. Lett. **24**(4), 208–210 (1999).
14. W. Margulis, O. Tarasenko, and N. Myrén "Who needs a cathode? Creating a second-order nonlinearity by charging glass fiber with two anodes," Opt. Express **17**(18), 15534–15540 (2009).
15. R. A. Myers, N. Mukherjee, and S. R. J. Brueck "Large second-order nonlinearity in poled fused silica," Opt. Lett. **16**(22), 1732–1734 (1991).
16. A. Canagasabey, C. Corbari, Z. Zhang, P.G. Kazansky, and M. Ibsen. "Broadly tunable second-harmonic generation in periodically poled silica fibers," Opt. Lett. **32**(13), 1863–1865 (2007).
17. A. Canagasabey, M. Ibsen, K. Gallo, A. V. Gladishev, E. M. Dianov, C. Corbari, and P. G. Kazansky "Aperiodically poled silica fibers for bandwidth control of quasi-phase-matched second-harmonic generation," Opt. Lett. **35**(5), 724–726 (2010)
18. C. Corbari, A. V. Gladishev, L. Lago, M. Ibsen, Y. Hernandez, and P. G. Kazansky "All-fiber frequency-doubled visible laser," Opt. Lett. **39**(22), 6505–6508 (2014).
19. E. L. Lim, C. Corbari, A V. Gladyshev, S. U. Alam, M. Ibsen, D. J. Richardson, and P. G. Kazansky, "Multi-watt all-fiber frequency doubled laser," in *Advanced Photonics*, OSA Technical Digest (Optical Society of America, 2014), paper JTu6A.5.
20. V. Grubsky and A. Savchenko, "Glass micro-fibers for efficient third harmonic generation," Opt. Express **13**(18), 6798–6806 (2005).
21. T. Lee, Y. Jung, C.A. Codemard, M. Ding, N.G.R. Broderick, and G. Brambilla, "Broadband third harmonic generation in tapered silica fibers," Opt. Lett. **20**(8), 8503–8511 (2012).
22. A. Coillet and P. Grelu "Third-harmonic generation in optical microfibers: from silica experiments to highly nonlinear glass prospects," Opt. Commun. **285**(16), 3493–3497 (2012).
23. M.I.M Abdul Khudus, T. Lee, P. Horak, and G. Brambilla, "Effect of intrinsic surface roughness on the efficiency of intermodal phase matching in silica optical nanofibers," Opt. Lett. **40**(7), 1318–1321 (2015).
24. M. I. M. Abdul Khudus, F. De Lucia, C. Corbari, T. Lee, P. Horak, P. Sazio, and G. Brambilla, "Phase matched parametric amplification via four-wave mixing in optical microfibers," Opt. Lett. **41**(4), 761–764 (2015).
25. A. C. Sodre, J. C. Boggio, A. Rieznik, H. Hernandez-Figueroa, H. Fragnito, and J. C. Knight, "Highly efficient generation of broadband cascaded four-wave mixing products," Opt. Express **16**(4), 2816–2828 (2008).
26. A. V. Husakou and J. Herrmann, "Supercontinuum generation, four-wave mixing, and fission of higher-order solitons in photonic-crystal fibers," J. Opt. Soc. Am. B **19**(9), 2171–2182 (2002).
27. J.C. Boggio, S. Moro, B.P.-P. Kuo, N. Alic, B. Stossel, and S. Radic, "Tunable parametric all-fiber short-wavelength ir transmitter," J. Lightwave Technol. **28**(4), 443–447 (2010).
28. Y.H. Li, Y.Y. Zhao, and L.J. Wang, "Demonstration of almost octave-spanning cascaded four-wave mixing in optical microfibers," Opt. Lett. **37**(16) 3441–3443 (2012).
29. N.I. Nikolov, T. Sørensen, O. Bang, and A. Bjarklev, "Improving efficiency of supercontinuum generation in photonic crystal fibers by direct degenerate four-wave mixing," J. Opt. Soc. Am. B **20**(11), 2329–2337 (2003).
30. G. Brambilla, "Optical fiber nanowires and microwires: a review," J. Opt. **12**, 043001 (2010).
31. V. Neustruev, "Colour centres in germanosilicate glass and optical fibers," J. Phys. : Condens. Matter **6**(35), 6901 (1994).
32. R. Kitamura, L. Pilon, and M. Jonasz, "Optical constants of silica glass from extreme ultraviolet to far infrared at near room temperature," Appl. Opt. **46**(33), 8118–8133 (2007).
33. L. Skuja, "Optically active oxygen-deficiency-related centers in amorphous silicon dioxide," J. Non-Cryst. Solids **239**(1), 16–48 (1998).
34. Y. Jung, G. Brambilla, and D.J. Richardson, "Optical microfiber coupler for broadband single-mode operation," Opt. Express **17**(7), 5273–5278 (2009).
35. T. Birks and Y.W. Li, "The shape of fiber tapers," J. Lightwave Technol. **10**(4), 432–438 (1992).
36. T. Sudmeyer, Y. Imai, H. Masuda, N. Eguchi, M. Saito, and S. Kubota, "Efficient 2nd and 4th harmonic generation of a single-frequency, continuous-wave fiber amplifier," Opt. Express **16**(3), 1546–1551 (2008).
37. G. Agrawal, *Nonlinear Fiber Optics*, 5th ed. (Academic Press, 2012).
38. S. Afshar and T.M. Monro, "A full vectorial model for pulse propagation in emerging waveguides with subwavelength structures part I: Kerr nonlinearity," Opt. Express **17**(4), 2298–2318 (2009).
39. D. Milam, "Review and assessment of measured values of the nonlinear refractive-index coefficient of fused silica," Appl. Opt. **37**(3), 546–550 (1998).
40. M.I.M. Abdul Khudus, T. Lee, T. Huang, X. Shao, P. Shum, and G. Brambilla, "Harmonic generation via χ^3 intermodal phase matching in microfibers," Fiber Integr. Opt. **34**(1), 53–65 (2015).

---

1. Introduction

Harmonic generation involves the generation of new frequencies which are multiples of a fundamental frequency (FF) via nonlinear processes. Typically, harmonic generation is achieved with the use of a variety of nonlinear crystals [1], where second/fourth harmonic generation (SHG/FHG) is typically done by employing one/two second-harmonic-generating nonlinear crystals and third/fifth harmonic generation (THG/5HG) is obtained by sum frequency generation between the fundamental/third harmonic frequency and the second harmonic frequency [2–4]. These methods allow for the generation of wavelengths inaccessible by conventional laser technology, and have widespread applications such as fiber Bragg grating inscription and microscopy [5, 6].

Fiber lasers, while providing the possibility of high peak powers, good modal properties and long interaction lengths, have generally only been employed as pump sources for harmonic generation [7–10]. Due to the lack of inversion symmetry in silica, efficient SHG cannot be observed in glass optical fibers, and it is only by using periodically poled silica fibers (PPSF) that broadband and high average power SHG conversion processes have been demonstrated [11–18]. Indeed, SHG via PPSF with efficiencies of up to 45% have been observed recently, opening the possibility of an all-fiber harmonic generation laser system [19]. The high nonlinearity of optical microfibers (OMF) has been proposed for intermodal third harmonic generation [20–22], but this experiences fundamental limitations imposed by detunings resulting from the intrinsic roughness of the OMF surface [23]. PPSF have also been used in conjunction with OMFs to achieve parametric amplification of ~25 dB at the third harmonic (TH) wavelength [24].

Here, all-fiberized FHG and 5HG from a single fiberized Erbium doped fiber source is demonstrated via a combination of quasi-phase-matched SHG and phase-matched four wave mixing (FWM).

2. Fourth and fifth harmonic generation via four wave mixing

Previous schemes for broadband generation in optical fiber primarily relied on higher order cascaded FWM, often working in conjunction with other nonlinear effects such as supercontinuum generation or soliton fission [25–27]. In OMFs, FWM over a bandwidth of nearly an octave has been demonstrated by pumping at the anomolous dispersion region with high power pulses [28]. Moreover, the dispersion of a photonic crystal fiber (PCF) can be tailored to achieve three seperate zero dispersion wavelengths (ZDWs) allowing for FWM to occur [29]. This effect has also been observed in OMFs, where a small signal at the third harmonic (TH) frequency was parametrically amplified by tailoring the OMF dispersion to allow for phase matched FWM to occur [24]. This same technique is exploited here in order to demonstrate FHG and 5HG.

All-fiberized FHG and 5HG is achieved using cascaded nonlinear processes including SHG, THG and FWM. First, a high power pulsed near-IR Master Oscillator Power Amplifier (MOPA) source is employed in conjunction with a PPSF for SHG. The TH wavelength generated as a non-phase matched by-product of the SHG is parametrically amplified by an OMF with a specific phase matching diameter (PMD) [24]. These three wavelengths are then employed in another OMF to allow for FHG and 5HG via FWM.

2.1. Phase matching in OMFs

Efficient FWM requires the energy conservation and phase matching conditions to be satisfied. The general FWM process with pumps at frequencies ω_2 and ω_3 generate signal and idler frequencies at ω_1 and ω_4, respectively, as shown in Fig. 1.

The energy conservation and phase matching condition can be written as:

$$\omega_2 + \omega_3 = \omega_1 + \omega_4 \tag{1}$$

$$\beta_2 + \beta_3 = \beta_1 + \beta_4 \tag{2}$$

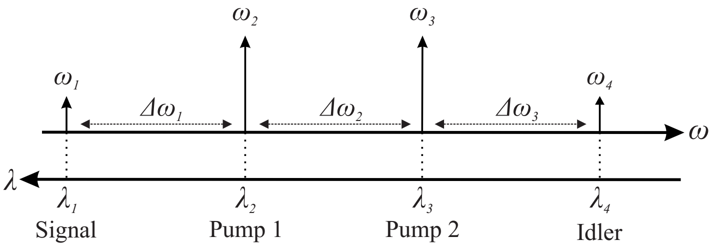

Fig. 1. Schematic of FWM. In general, $\Delta\omega_1 = \Delta\omega_3 \neq \Delta\omega_2$.

where β_i is the propagation constant of the mode at frequency i. Equation (2) can also be equivalently written as,

$$\Delta\beta = \beta_2 + \beta_3 - \beta_1 - \beta_4 = 0 \tag{3}$$

where $\Delta\beta$ is the FWM detuning due to phase mismatch. While this applies to any combination of optical fiber modes of the interacting wavelengths, only the fundamental HE_{11} mode is considered here as it has the largest modal overlap.

Two basic classifications are typically employed, depending on the configuration of the pump wavelength. Degenerate FWM (DFWM) occurs when the two pump wavelengths are equal ($\omega_l = \omega_m$), while non-degenerate FWM (NDFWM) occurs when the two pumps are not equal ($\omega_l \neq \omega_m$). In both cases, the energy conservation condition in Eq. (1) can be easily satisfied as any combination of pump wavelengths yields specific idler and signal wavelengths. The phase matching condition in Eq. (2), on the other hand, may only be achieved by tailoring the dispersion of the waveguide in order to compensate for the material dispersion of the interacting modes at different wavelengths, achieved by varying the diameter in OMFs.

In the experiments, a FF wavelength of $\lambda_{FF} = 1.55$ μm is employed to generate a SH wavelength at $\lambda_{SH} = 0.775$ μm, which is then employed to generate the TH, FH and 5H wavelengths ($\lambda_{TH} = 0.517$ μm, $\lambda_{FH} = 0.387$ μm and $\lambda_{5HF} = 0.31$ μm, respectively). Setting $\lambda_1 = \lambda_{FF}$, $\lambda_2 = \lambda_{SH}$, $\lambda_3 = \lambda_{TH}$, $\lambda_4 = \lambda_{FH}$, and $\lambda_5 = \lambda_{5H}$, the detuning condition in Eq. (3) can then be applied to these five interacting wavelengths for various DFWM and NDFWM schemes satisfying the energy conservation condition in Eq. (1), depicted in Fig. 2. The PMD for a particular FWM scheme occurs when $\Delta\beta = 0$, as shown in Fig. 2(a) for the three FWM schemes involving the generation of the FH wavelength and detailed in Table 1. From Fig. 2(b), no phase matching diameter was found to exist for the 5H wavelength. An analysis of the wavelengths employed in [28] shows that while the OMFs were not operating at the PMD, the phase mismatch is relatively small, thus could be ‘bridged’ by nonlinear phase shifts and result in relatively broad cascaded FWM.

The phase matching calculation can then be generalized for FWM in OMFs with any set of interacting wavelengths within the silica optical window ($\lambda = 0.2-2.0$ μm). The PMD for both DFWM and NDFWM for various interacting wavelengths can then be calculated, as shown in Fig. 3.

Interestingly, for both DFWM and NDFWM, there are nearly always at least one diameter for which FWM phase matching occurs for any set of interacting wavelengths, potentially allowing near arbitrary generation of wavelength. Therefore, Fig. 3(a) is a generalized result of those recorded in [24]. Note, however, that as NDFWM has an unlimited combination of wavelengths that satisfy Eqs. (1) and (2), Fig. 3(b) shows only the signal satisfying $\Delta\omega_1 = \Delta\omega_2 = \Delta\omega_3$.

2.2. Experiments

The experimental demonstration was undertaken using the setup shown in Fig. 4(a). A fully fiberized MOPA seeded by a continuous wave laser (Photonetics Tunics BT) operating in the

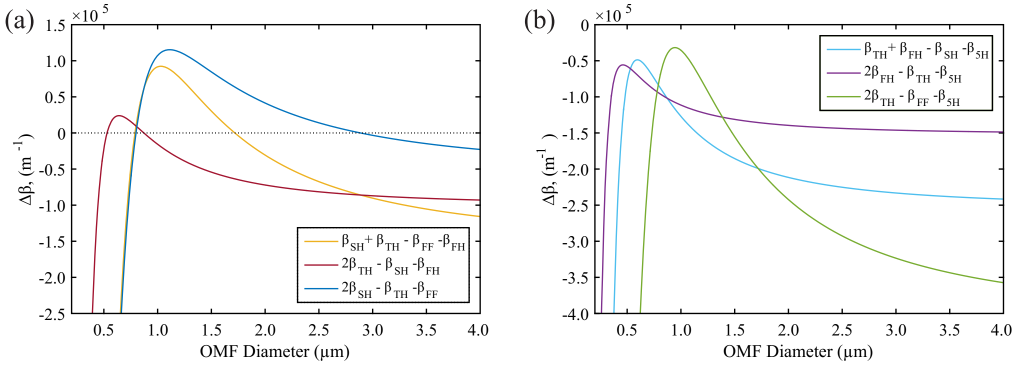

Fig. 2. Evolution of detuning $\Delta\beta$ with OMF diameter for different FWM schemes for (a) FHG and (b) 5HG for the wavelengths which are considered. The diameters at which $\Delta\beta = 0$ are the phase matching diameters for a particular FWM scheme.

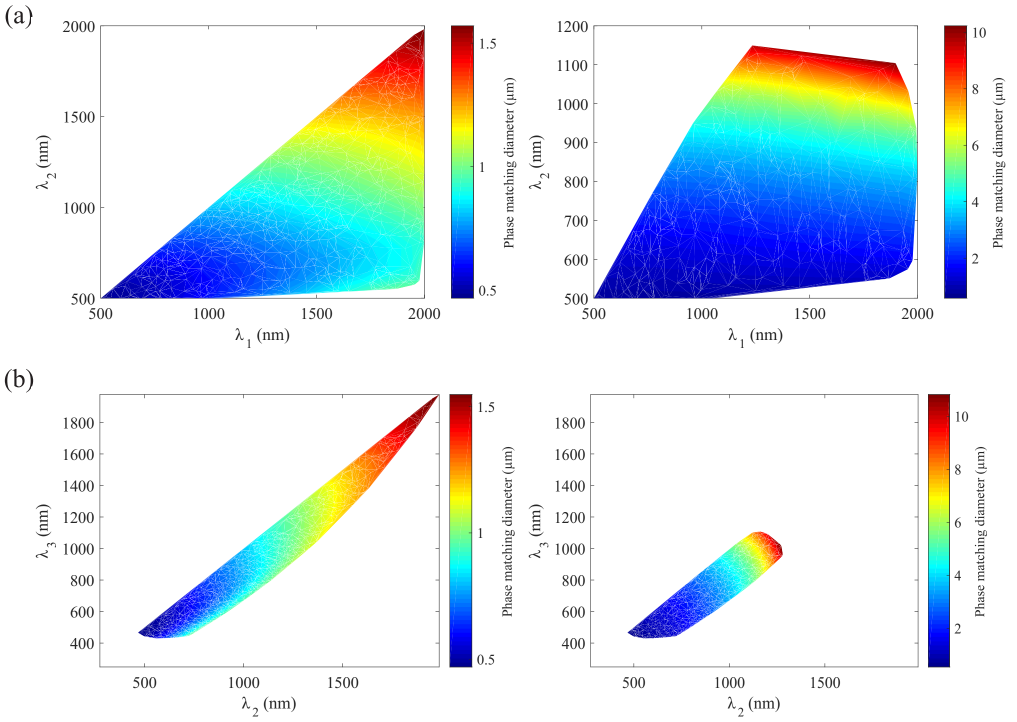

Fig. 3. FWM PMD in OMFs within the optical transmission window of silica for (a) degenerate FWM ($\lambda_2 = \lambda_3$), where λ_2 is the pump wavelength and λ_1 is the signal wavelength; and (b) non-degenerate FWM for a range of pumps λ_2 and λ_3. Here, the frequency difference is equal ($\Delta\omega_1 = \Delta\omega_2 = \Delta\omega_3$). As the OMF nonlinearity decreases significantly with increasing the OMF size, $d < 10$ μm was chosen in order to achieve relatively high nonlinearity [30]. The left and right plots in (a) and (b) show the two possible PMDs.

telecom C-band wavelength region (1530 – 1565 nm) was used as the FF pump source, and generated pulses with duration $\tau = 5$ ns, repetition rate $f = 200$ kHz and an average power $P_{av} = 300 - 800$ mW, corresponding to a peak power $P_{peak} = 300 - 800$ W. The pulses were generated by an electro-optic modulator (EOM), with any inter-pulse amplified spontaneous emission (ASE) being reduced by an acousto-optic modulator further along the MOPA chain.

Table 1. Phase matching diameters (PMDs) for three different FWM schemes. d_1 and d_2 denote two separate phase diameters

FWM type	Pump Wavelength(s) (μm)	Generated Wavelengths (μm)		PMD (μm)	
		Signal	Idler	d_1	d_2
(I) Degenerate	0.775	1.55	0.517	2.89	0.80
(II) Non-degenerate	0.775 0.517	1.55	0.387	1.72	0.79
(III) Degenerate	0.517	0.775	0.387	0.87	0.53

The use of the AOM in conjunction with two tunable spectral filters minimizes inter-pulse ASE in both the temporal domain and the spectral domain, allowing the pump signal at the FF wavelength to have an optical signal-to-noise ratio (OSNR) in excess of 40 dB at a pump power of 300 mW [19]. A SH wavelength was generated by splicing the MOPA output to a PPSF with a total insertion loss of 1.7 dB. The PPSF, a twin-hole Germania doped fused silica fiber manufactured by Acreo Fiberlab and poled via the application of a positive voltage of 7.5 kV to both liquid electrodes embedded in the two holes of the fiber for 120 minutes at a temperature of 300 °C, was then spliced to a pure silica fiber that was tapered to provide two OMFs. However, as the final amplifier (Amp5 in Fig. 4(a)) is noisy, the maximum average output power of the MOPA was also limited to approximately 380 mW corresponding to an initial average power of approximately 4 mW at the SH wavelength as it was found that the power at the SH wavelength decreases with any additional increase in pump power. The typical output spectrum from the PPSF after the SHG process is shown in Fig. 4(b).

A 6 mm-long, 2.5 μm-diameter OMF (OMF1) was fabricated from the pure silica fibre using the modified flame brushing method [30] to amplify the signal at the TH wavelength, generated in the PPSF as a non-phase matched by-product of the SHG process. OMF1 had a diameter close to the first PMD ($d = 2.89$ μm) and was fabricated whilst the MOPA source was turned on to check the parametric amplification efficiency in real time. A pure silica core fiber (Z-fiber, Sumitomo Electric) was chosen because standard telecom SMF-28 optical fibers exhibit a significant absorption in the UV region [31, 32]. However, the Z fibre still exhibited large losses at wavelengths shorter than 300 nm, attributed to the oxygen-silica deficiency center, thereby limiting the application to the near UV wavelength region [33].

In order to ensure that the PMD was achieved, OMF1 was spliced with a short pass filter designed to have high losses (> 80 dB) only at the FF, and the output at the TH wavelength was monitored whilst tapering. The tapering process was then stopped shortly after the PMD was achieved as detailed in [24]. However, the OMF1 diameter was kept smaller than the optimum PMD in order to ensure that the high power at the SH wavelength was not depleted. Table 1 shows that there are three PMDs near $d \sim 0.8$ μm: d_2 in schemes (I) and (II), and d_1 in scheme (III). The OMF diameter fluctuations related to fabrication imprecisions can be $> \pm 50$ nm, thus OMF1 has a large range of diameters along its length which comprise both PMDs and thus involve both generation of the FH and TH wavelengths. As the purpose of the OMF1 was to boost the power of the TH wavelength, any energy transfer to the FH was undesirable. Furthermore, initial experiments showed that no FH signal could be observed at $d \sim 0.8$ μm at the OMF1 output. The first PMD at $d \sim 2.89$ μm was therefore chosen as the diameter of OMF1. The output from the OMF1 is shown in Fig. 5.

The short pass filter was then removed and replaced with a filter with high losses at the FF, SH and TH wavelengths (>45 dB, >35 dB and >15 dB, respectively) which was then spliced to a broadband 3dB OMF coupler as described in [34], with one output connected to an UV spectrometer (Ocean Optics USB4000) and the other output connected to a power meter recording the power at 775 nm (Thorlabs S130C). This is to monitor any background signal

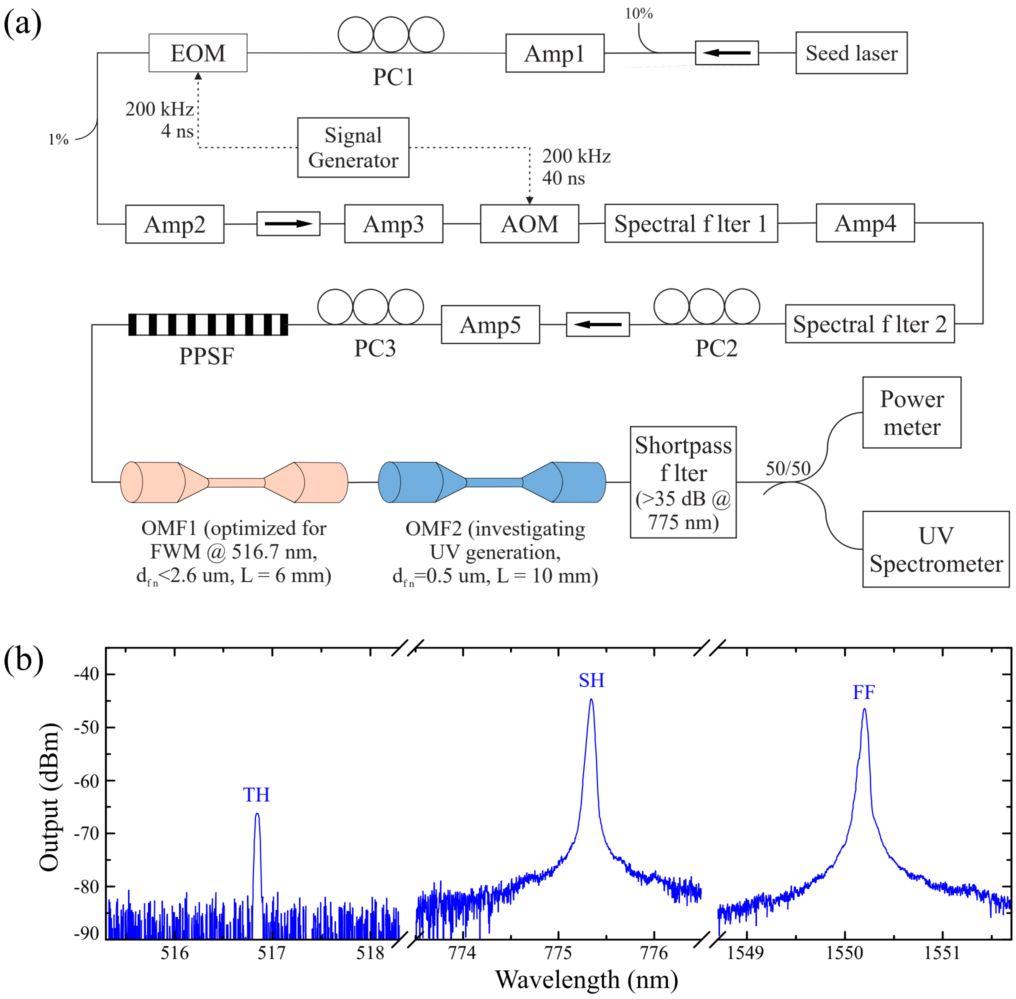

Fig. 4. (a) Experimental setup for UV generation in OMFs. Five amplifiers (Amp#) were employed in the MOPA chain with the pulses carved by an electro-optic modulator (EOM) and an acoustic optical modulator (AOM). Two spectral filters were employed in order to allow for an OSNR of more than 40 dB at the output. The polarization in the chain is managed by three polarization controllers (PC). PPSF designates the periodically poled silica fiber. (b) Typical output spectrum after SHG from the PPSF which is spliced to a shortpass filter with losses of > 40 dB and > 70 dB at the SH and FF wavelengths, respectively.

during the tapering process as the UV spectrometer is sensitive to visible light and therefore would register both the TH and SH signals.

A section of the Z-fiber between OMF1 and the shortpass filter was then tapered to fabricate a second OMF (OMF2) from an initial diameter $d_{in} = 125\ \mu$m to a final diameter $d_{fin} = 500$ nm whilst being pumped by the MOPA source. The power at both the SH and the UV spectrum was continuously monitored, and the polarization controllers (PCs) in the MOPA chain were adjusted occasionally to compensate for thermal drifts. In order to ensure that the actual diameter closely followed the predicted diameter of OMF2 over a significant distance, a length of 10 mm was selected, with the OMF2 profile carefully controlled to satisfy the adiabaticity criteria in order to minimize losses [35]. The evolution of the UV spectrum with the OMF2 diameter is shown in Fig. 6, where both the FH and the 5H wavelengths are presented.

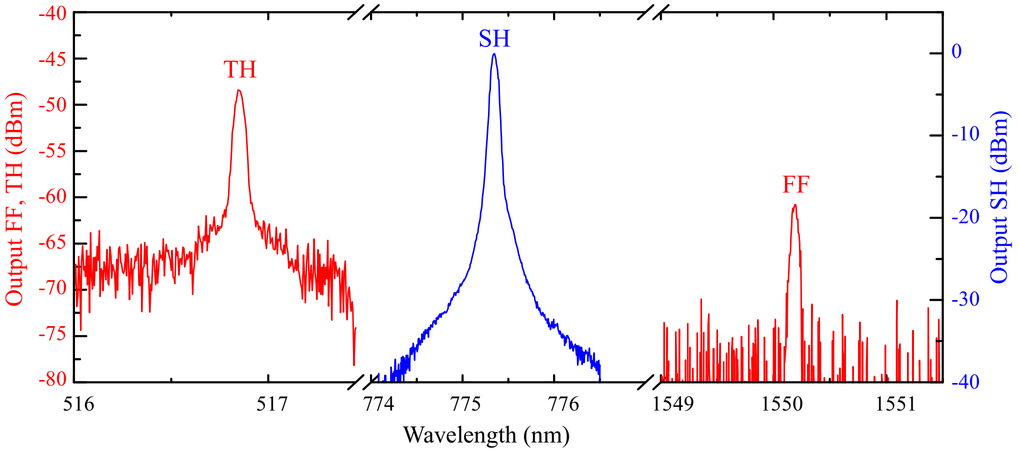

Fig. 5. Output spectrum from the OMF1 after a shortpass filter designed to remove radiation at 1.55 μm. The signal at the third harmonic wavelength (0.517 μm) has been enhanced by the parametric amplification in OMF1 to more than -50 dBm from an initial signal of approximately -65 dBm.

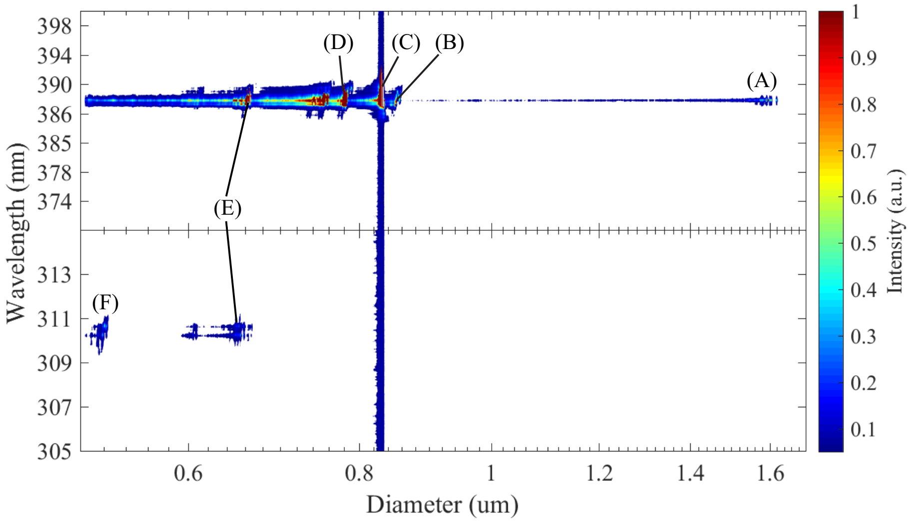

Fig. 6. Output spectrum from the OMF2 after a shortpass filter designed to attenuate the FF, SH and TH wavelengths. The detector is sensitive to visible light, which manifests as a broadband background signal which varies slightly as the OMF is tapered. Tests with higher powers at the SH and TH indicate that the signals at the SH and TH do not appear as narrowband radiation. (A)-(F) represent the FH and 5H signals.

Figure 6 shows that initially, i.e. for large fiber diameters, there is no signal at neither the FH nor the 5H wavelength. As the OMF2 diameter was reduced, a signal at the FH wavelength appeared at the diameter of $d_{(A)} \sim 1.64$ μm. This diameter is smaller than the first predicted PMD and was not associated to any significant energy transfer in simulations using the same parameters. It is thought, therefore, that the observed signal might have been due to a combination of slight changes in the polarization state of the system and relatively low efficiencies. This relatively weak signal first grew slightly before reducing in intensity as the OMF was tapered, since the segment of OMF2 at the PMD decreases as the tapering process evolves. This is shown schematically in Fig. 7, and is due to the fact that the conversion process is dependent on the interaction length. As shown in Fig. 7(a), no signal is discernible at the FH wavelength before the OMF waist reaches the PMD. At the PMD, the efficiency increases dramatically as the dispersion requirement 2 for efficient FWM is achieved, as shown in Fig. 7(b). As the fiber is tapered further, diameter decreases, although due to the increase overall length of the OMF, there is always a range of diameters in the transition region which are phase matched or nearly phase matched, as shown in Fig. 7(c). However, as the process continues, an increasingly larger proportion of the OMF becomes smaller than the phase matching diameter, causing the observed gradual drop in the efficiency.

At $d_{(B)} \sim 850$ nm, however, a large increase in the signal at the FH wavelength was recorded, corresponding to the first PMD from the second DWFM process (d_1 in scheme (III) of Table 1) with the difference attributable to the detuning from self-phase modulation (SPM) and cross phase modulation (XPM), as well as experimental errors in diameter estimation. Another large spike was then observed at $d_{(C)} \sim 830$ nm. Here, there is an increase in the overall background across the entire wavelength range, suggesting that the PMD corresponding to the generation of the TH is reached (d_2 in scheme (I) of Table 1), as the CCD array of the spectrometer is sensitive to visible light, scattered by the grating inside the spectrometer. This generation of the TH wavelength simultaneously increasing the efficiency of FWM at the FH wavelength as energy is transferred from both the FF and SH to the TH and then to the FH.

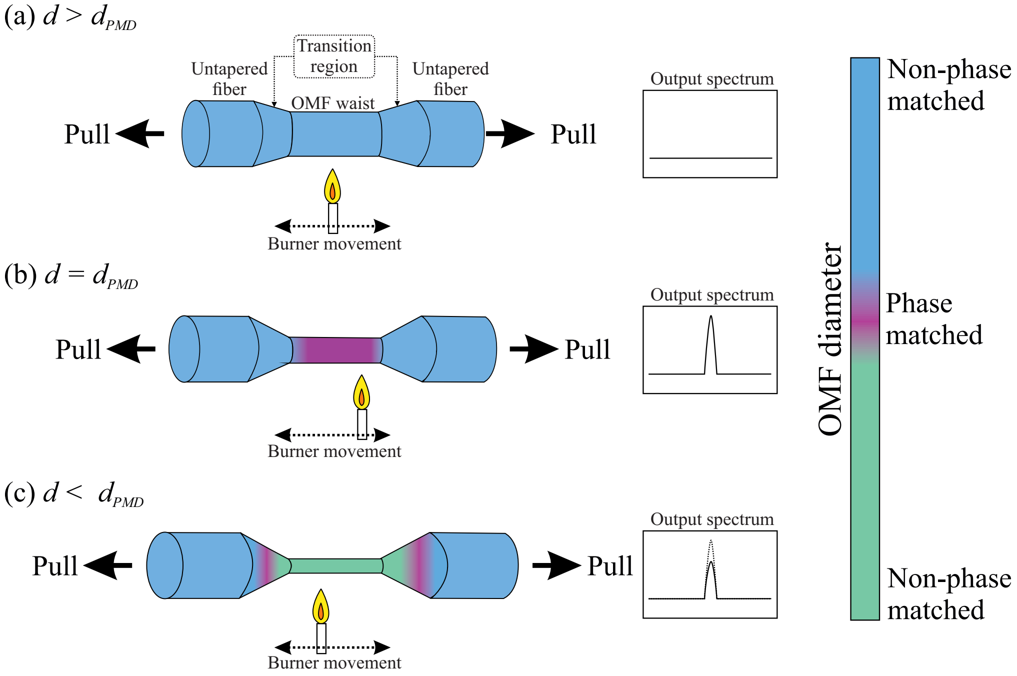

Fig. 7. Schematic of the tapering process in the experiment. Here, d is the diameter of the OMF, and d_{PMD} is the phase matching diameter for FWM.

The next significant increase in the signal at the FH was recorded at $d_{(D)} \sim 780$ nm, probably associated to the second PMD originating from the NDWFM process (d_2 in scheme (II) of Table 1). The signal then gradually decreased before abruptly increasing again at $d_{(E)} \sim 670$ nm, at which point a small signal at the 5H ($\lambda = 0.31$ μm) was observed. This diameter does not correspond to any PMD for either the FH or the 5H. In the case of the FH, however, simulations indicate that energy transfer occurs at approximately this diameter, probably due to the fact that condition in Eq. (2) for the DFWM which produces the FH is nearly fulfilled and the small phase mismatch may easily be bridged by nonlinear phase shifts due to SPM and XPM. The fact that a signal could be observed at the 5H despite the detuning is not near the optimum diameter (i.e. when $\Delta\beta$ is closest to 0) for any of the three FWM schemes shown in Fig. 2(b) is due to the combination of relatively small phase mismatch and a relatively high power at the FH wavelength, allowing NDFWM between the SH, TH, FH and 5H wavelengths to occur. This is supported by the fact that as the OMF diameter is reduced, the signal at the 5H is also reduced significantly. The next 5H signal observed at a diameter $d_{(F)} \sim 0.525$ μm can similarly be attributed to NDWFM between the SH, TH, FH and 5H as the $\Delta\beta$ is closest to 0 at this diameter. However, there was no corresponding spike at the FH despite being close to the PMD.

The approximate maximum average output power at the FH, after accounting for transmission losses, was $P_{FH_{max}} \sim 8 - 10$ nW at $d \sim 0.8$ μm, corresponding to an efficiency of $\sim\ 2 \times 10^{-8}$. The low efficiency may be attributed to the low power at the SH and TH wavelengths as well as the fact that the OMF waist was not uniform, which therefore limited energy transfer. This is extremely low when compared to the state-of-the-art technology, where FHG efficiency in excess of 50% has been shown to be achievable by employing cavity-enhanced SHG and FHG with nonlinear crystals [36]. Indeed, commercially available single-pass FHG devices typically have conversion efficiencies in excess of 10%. Therefore, in order to ascertain whether it is possible to achieve reasonable efficiencies with this method, a full theoretical treatment of FWM energy transfer for harmonic generation is undertaken, which shall also allow an investigation on the any fundamental limitations of FWM in OMFs.

3. Theory and simulation

The greatest issue in the experimental demonstration above is the power of the pump wavelengths at the SH and TH wavelengths. The low SHG efficiency limited the amount of power which can be transferred to the TH wavelength, thereby limiting the overall UV generation efficiency. However, SHG with PPSF has been shown to be very efficient, with the highest conversion efficiency being 45% [19]. Therefore, this section investigates the theoretical efficiency of the THG and FHG processes in OMFs.

3.1. Efficiency calculations

The equations governing the transfer of energy in FWM processes are well known and have been widely employed [37]. A fully vectorial description of FWM in high contrast waveguides such as OMFs has been derived by employing the Lorentz reciprocity theorem [38]. Following this, the sum of the electric and magnetic fields of four interacting wavelengths of k, l, m and n can be expressed as,

$$\widetilde{\mathbf{E}}(\mathbf{r}, \omega) = \sum_{\nu=k,l,m,n} A_\nu \frac{\mathbf{F}_\nu(\mathbf{r}, \omega_\nu)}{\sqrt{N_\nu}} e^{i(\beta_\nu z - \omega_\nu t)} + c.c. \tag{4}$$

$$\widetilde{\mathbf{H}}(\mathbf{r}, \omega) = \sum_{\nu=k,l,m,n} B_\nu \frac{\mathbf{G}_\nu(\mathbf{r}, \omega_\nu)}{\sqrt{N_\nu}} e^{i(\beta_\nu z - \omega_\nu t)} + c.c. \tag{5}$$

where ω_ν is the frequency, β_ν is the propagation constant, A_ν and B_ν are the amplitude of the electric and magnetic fields, and $\mathbf{F}_\nu(\mathbf{r}, \omega_\nu)$ and $\mathbf{G}_\nu(\mathbf{r}, \omega_\nu)$ are the electric and magnetic modal field distributions which satisfy the normalization relation,

$$N_\mu = \frac{1}{4} \int [\mathbf{F}_\mu(\mathbf{r}, \omega) \times \mathbf{G}^*_\mu(\mathbf{r}, \omega) + \mathbf{F}_\mu(\mathbf{r}, \omega) \times \mathbf{G}^*_\mu(\mathbf{r}, \omega)] \cdot \hat{z} dA \tag{6}$$

Only terms which are energy conserving (Eq. (1)) are considered, with terms corresponding to phase matching (Eq. (2)) retained as they are dependent on the geometry of the waveguide. Any fast rotating terms (e.g. $e^{i(\beta_\alpha-\beta_\sigma)z}$, $e^{-i(\omega_\alpha-\omega_\sigma)t}$) are neglected as the coupling is assumed to be small. The vectorial FWM equation for wavelength l can then be written as,

$$\begin{aligned}\frac{\partial A_l(z,t)}{\partial z} = -\frac{\alpha_l}{2}A_l + \gamma_l \Bigg\{ & \Theta_l |A_l|^2 A_l + \sum_{p=m,n,k} \Theta_{lp}(2|A_p|^2 A_l) \\ & + \Theta_{klmn}[2(A_k A_n A_m^*)]e^{-i(\beta_l+\beta_m-\beta_k-\beta_n)z} \Bigg\}\end{aligned} \tag{7}$$

where,

$$\gamma_l = i\left(\frac{\epsilon_0}{\mu_0}\right)\frac{2\pi n_{(2)}(\omega_l)n^2(\omega_l)}{3\lambda_l} \tag{8a}$$

$$\Theta_l = \int \frac{2|\mathbf{F}_l|^4 + |\mathbf{F}_l^2|^2}{\sqrt{N_l^4}} dS \tag{8b}$$

$$\Theta_{lp} = \int \frac{|\mathbf{F}_l \cdot \mathbf{F}_p^*|^2 + |\mathbf{F}_p|^2|\mathbf{F}_l|^2 + |\mathbf{F}_l \cdot \mathbf{F}_p|^2}{\sqrt{N_l^2 N_p^2}} dS \tag{8c}$$

$$\Theta_{klmn} = \int \frac{(\mathbf{F}_k \cdot \mathbf{F}_n)(\mathbf{F}_l^* \cdot \mathbf{F}_m^*)}{\sqrt{N_k N_l N_m N_n}} dS \tag{8d}$$

α_l is the loss, λ_l is the wavelength at frequency ω_l, $n(\omega_l)$ is the linear refractive index, $n_{(2)}(\omega_l)$ is the nonlinear refractive index, and ϵ_0 and μ_0 are the permittivity and permeability of free space, respectively. For generality, $n(\omega_l)$ and $n_{(2)}(\omega_l)$ have been left with an explicit dependence on the frequency. Note that the modal integrals in Eq. (8) are calculated only over the region where the nonlinear material is present. This takes account of the fact that significant fractions of the mode may propagate beyond the core region and therefore do not contribute to the conversion process.

Equation 7 is the general vectorial equation describing FWM with continuous wave (CW) or quasi-CW pump sources. Here, the first and second terms correspond to SPM and XPM, respectively. The third term is the energy transfer term corresponding to NDFWM between ω_k, ω_l, ω_m and ω_n. This equation may therefore be applied for any set of wavelengths satisfying Eq. (1) by selecting and adding the relevant terms. For instance, in the specific case where $\Delta\omega_1 = \Delta\omega_2 = \Delta\omega_3$, two additional terms corresponding to two DFWM scenarios may be introduced for when ω_l is the pump (Θ_{kllm}) and the signal (Θ_{lmmn}). As there are no assumptions made on the modal distribution of the interacting wavelengths, this set of equations may also be applied for intermodal FWM. However, only the fundamental HE_{11} mode will be considered here for the four interacting waves, as it gives the highest overlap between their respective field distributions.

The efficiency of the conversion process is theoretically calculated for the SH, TH and FH wavelengths in sections 3.2 and 3.3, excluding the 5H wavelength to simplify the analysis. Therefore, the pump wavelengths for the FWM process are chosen to be at the SH and TH wavelengths (0.775 μm and 0.517 μm, respectively), with the idler and signal at the FH wavelength (0.387 μm) and at the FF wavelength (1.55 μm), respectively. The OMF losses are assumed to be negligible [30].

3.2. Degenerate FWM for third harmonic generation

Equation 7 is employed to estimate the efficiency of the conversion process for OMFs with diameters close to the PMD. Simulations were undertaken with parameters similar to a MOPA source operating at 1.55 μm working in conjunction with a PPSF, generating the SH wavelength at 0.775 μm with parameters given in [19] in order to achieve the best theoretical efficiency from realistic sources. Calculations were done with a quasi-CW pulsed laser with a peak power of approximately $P_{peak_{\mathrm{FF}}} = 1$ kW at the MOPA output. The power is limited to 1 kW in order to allow for comparison with the theoretical results of intermodal THG in OMFs [20]. Assuming a loss of 0.5 dB at the FF after the conversion process, this translated to a peak power of approximately $P_{peak_{\mathrm{FF}}} = 534$ W at the FF and $P_{peak_{\mathrm{SH}}} = 400$ W at the SH wavelength after the PPSF. A small signal at the TH wavelength with a peak power of $P_{peak_{\mathrm{TH}}} = 1 \times 10^{-9}$ W generated from non-phase matched sum frequency generation was also included. This was then propagated through a straight ideal OMF with a diameter close to the PMD for scheme (I) in Table 1, and the fraction of power in each wavelength ($\Upsilon_l = P_l/P_{total}$, where l is the wavelength) was calculated. Note that the final value of Υ_l may be interpreted as the overall efficiency (η) of the energy transfer from the FF to wavelength l. Figure 8 shows the calculated Υ_l of the DFWM scheme (I) in Table 1 for an OMF with a length of 10 cm around the two PMDs, $d \simeq 2.89$ μm and $d \simeq 0.80$ μm. The variation in the nonlinear refractive index $n_{(2)}$ was extrapolated from [39] with the UV resonance set at 1.45×10^5 cm^{-1}.

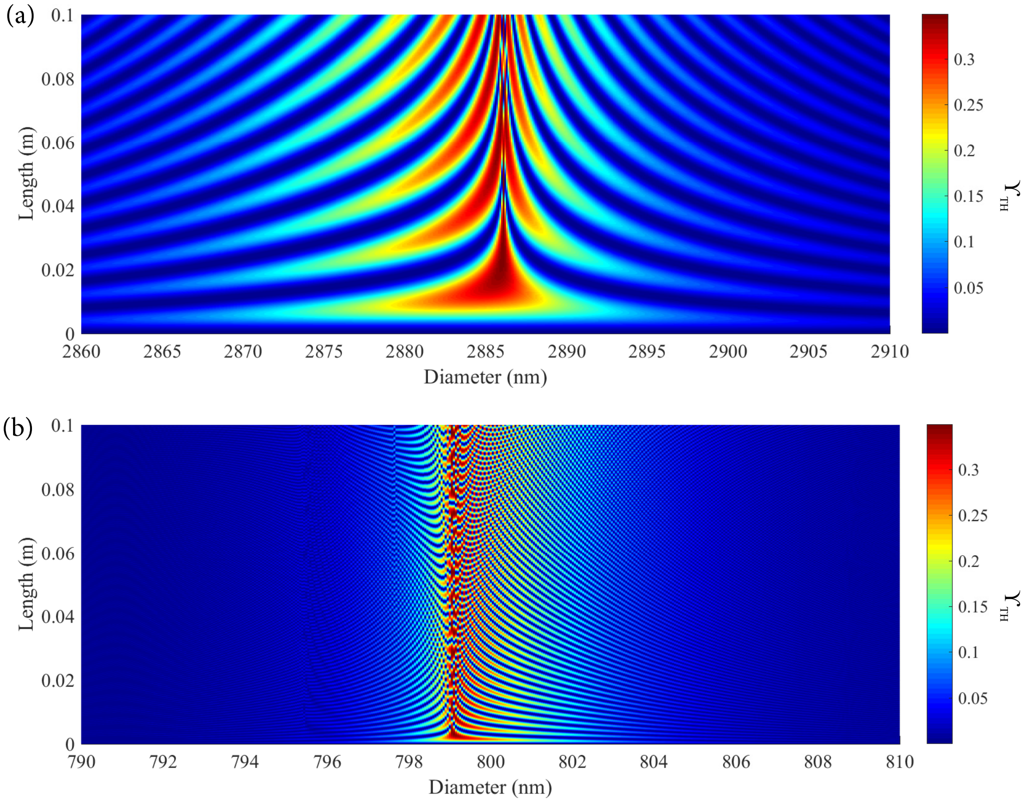

Fig. 8. Calculated fraction of total power, Υ_{TH}, at the idler (TH) wavelength ($\lambda_{\mathrm{TH}} = 0.517$ μm) for the DFWM detailed by scheme (I) in Table 1. The power at the signal ($\lambda_{\mathrm{FF}} = 1.55$ μm) and pump wavelengths ($\lambda_{\mathrm{SH}} = 0.775$ μm) is set at $P_{\mathrm{FF}} = 534$ W and $P_{\mathrm{SH}} = 400$ W, respectively. Two PMDs around (a) $d_1 = 2.886\mu$m and (b) $d_2 = 0.799$ μm are used.

Efficiencies in excess of 30% are predicted with a 2-3 cm long OMF, lower than the value (> 80%) calculated for ideal intermodal THG in OMFs [20]. This is because the power transfer is limited by the fraction of power in the SH wavelength, and therefore cannot exceed 35% here as there is also a small transfer of power back to the FF. However, the range of diameters at which efficient FWM occurs is relatively large. For instance, it is possible to achieve theoretical efficiencies in excess of 15% with a 1 cm OMF at $d_1 \pm 5$ nm, while the same efficiency can be achieved with a 3 mm OMF at $d_2 \pm 3$ nm. This relatively large tolerance in the PMD is due to the rate at which dephasing from the ideal phase matching condition occurs as described by Eq. (2). The dephasing rate is dependent on the slope of the change in the normalized propagation constant of the interacting wavelength as exemplified by Fig. 2(a). A consequence of this is the dephasing rate is much less pronounced at larger diameters, increasing the diameter range at which phase matching can occur. Notably, this large diameter range at which efficient energy transfer occurs theoretically overcomes fundamental limitations imposed by frozen-in surface waves - whose variation in the diameter is of the order of 1 nm - which limits the efficiency of THG in OMFs to $\eta < 1\%$ [23]. The oscillating behaviour of Υ_{TH} around the PMD is similar to that observed in [40], and can be explained from the fact that the small phase mismatch limits total energy transfer though relatively high efficiencies can still be achieved for diameters slightly above or below the PMD.

It should be noted, however, that while the diameter range for phase matching is larger at d_1, the rate of energy transfer is much higher at d_2, as the effective nonlinearity at d_2 is significantly higher as a result of a smaller diameter. Therefore, there is a trade-off between the PMD tolerance and the rate at which energy transfer occurs.

3.3. Non-degenerate FWM for fourth harmonic generation

The generated signal from the DFWM described above in section 3.2 is then employed for NDFWM, where the signal and idler wavelengths are given by the FF and FH wavelengths at 1.55 μm and 0.387 μm, respectively, and the pump wavelengths are given by the SH and TH wavelengths at 0.775 μm and 0.517 μm, respectively.

As the FWM process transfers energy from the two pump wavelengths to the signal and idler wavelengths, the pump wavelengths need to contain significant fractions of the total power. Therefore, the scheme employed in section 2.2 whereby two OMFs are used for efficient FWM is employed, OMF1 being used to boost the power at the TH wavelength as described above and OMF2 to investigate FHG. First, the power at the TH wavelength was amplified by OMF1 at $d \sim 2.89$ μm at a length of 7 mm to produce similar levels of power at the SH and TH. This produces output powers at the FF, SH, TH and FH, of $P_{\mathrm{FF}} = 588.1$ W, $P_{\mathrm{SH}} = 168.0$ W, $P_{\mathrm{TH}} = 189.1$ W and $P_{\mathrm{FH}} = 0.8$ mW, respectively. The small signal at the FH is due to non-phase matched transfer of energy from the TH to the FH which has a power fraction of $\Upsilon_{\mathrm{FH}} \sim 10^{-7}$. This is propagated through OMF2 which has a length of 10 cm and a diameter close to the PMD at $d_1 = 1.72$ μm and $d_2 = 0.79$ μm, as specified by scheme (II) in Table 1. The evolution of Υ_{FF}, Υ_{TH} and Υ_{FH} at the PMD $d \simeq 1.72$ μm is shown in Fig. 9.

Final efficiencies over 25% at the FH wavelength are theoretically possible with short OMFs ($\sim$ 1 cm) over a relatively broad diameter range of $d \geq 4$nm, though due to the transfer of power between the four interacting wavelengths, the final efficiency cannot exceed 28% and the fraction of power in the FH oscillates significantly. Substantial energy transfer in the TH at $d \sim 1.726 - 1.730$ μm can also be observed in Fig. 9(b), where the energy is not transferred to the FH but to and from the SH via DFWM between the FF, SH and TH as evidenced by the same behaviour in Υ_{FF} in Fig. 9(c). This is not predicted by Eq. (2), but is a result of the interaction between the SPM, XPM and transfer terms in Eq. (7). Interestingly, the total change in Υ_{FF} is relatively small ($\sim$ 0.06) as compared to the FH and TH. Physically, this can be explained by the fact that the photons at the TH and FH wavelengths have three and four times the energy of the photons at the FF wavelength, respectively. Therefore, in the generation of the idler and signal photons during the FWM process, more energy is transferred to the shorter wavelengths as a result of energy conservation, resulting in the difference in Υ_{FF}, Υ_{TH} and Υ_{FH}.

The evolution of Υ_{FH} at OMF diameters around $d \sim 0.79$ μm with the same input power is

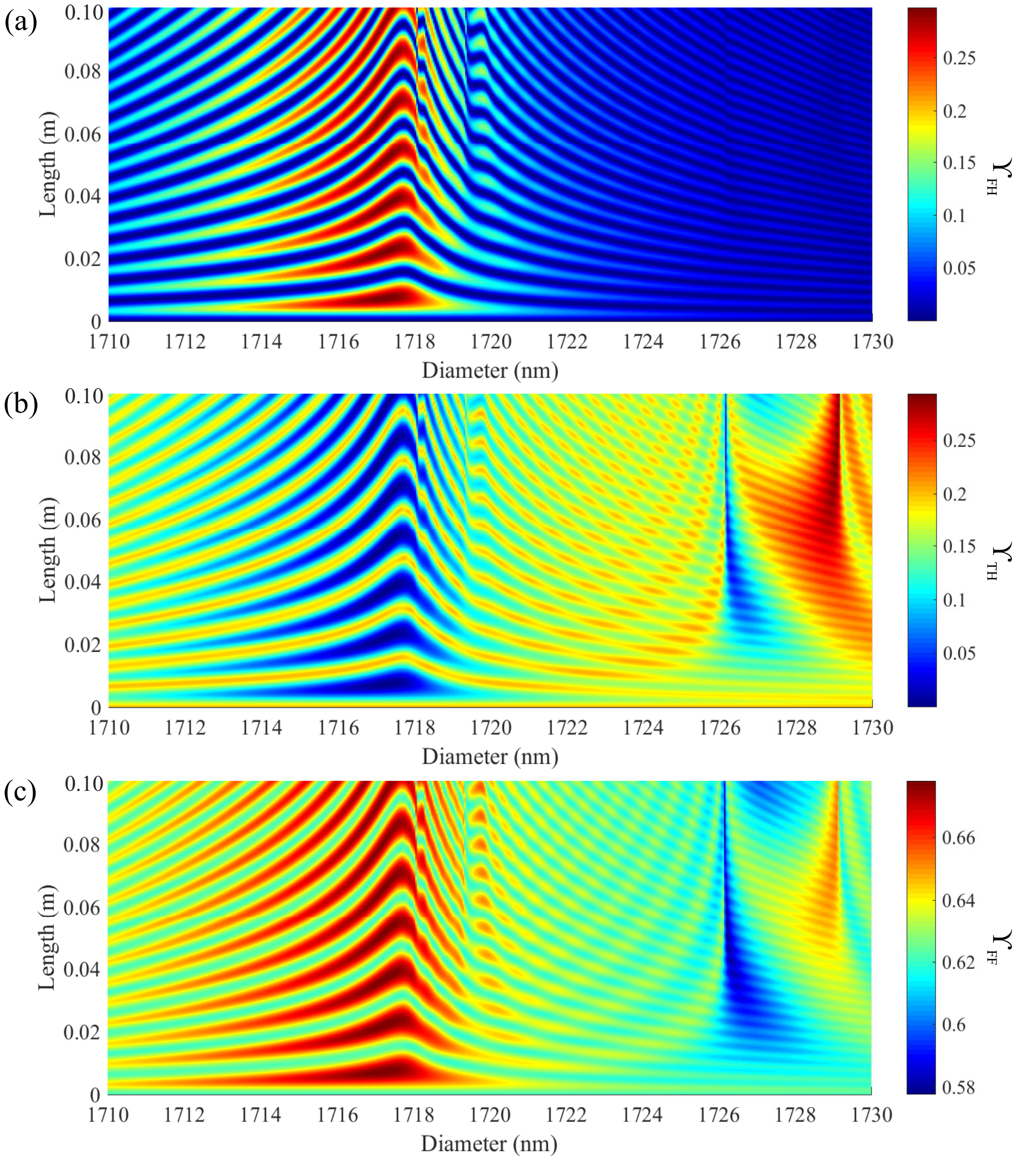

Fig. 9. Evolution of the fraction of total power (Υ_I) in the (a) FH wavelength (0.387 μm), (b) TH wavelength (0.517 μm) and (c) FF wavelength (1.550 μm) around the PMD $d \simeq 1.72$ μm. The total peak power (including loss) is approximately 1 kW.

shown in Fig. 10(a). The final efficiency can be seen to be $> 30\%$, but the range of diameters at which phase matching occurs is relatively small, as DFWM between the FF, SH and TH occurs at $d \sim 0.795$ μm. To investigate the effect that the proportion of power in each pump wavelength has on efficiency, the output power of the OMF 1 is varied by selecting a length of 2 mm. This short length did not allow for large transfers of energy between the interacting wavelengths, therefore the fraction of power in the TH is quite small, producing approximately $\Upsilon_{SH} \sim 39\%$ and $\Upsilon_{TH} \sim 3\%$. Using this as an input for OMF2, the evolution of Υ_{FH} is calculated for diameters around $d \sim 0.79$ μm, as shown in Fig. 10(b). It is immediately apparent that while the overall efficiency has decreased to $\sim 17\%$, the most efficient energy transfer occurs at $d \sim 0.795\ \mu$m, which is near the PMD for DFWM between the FF, SH and TH wavelength. This is due to the fact that the TH wavelength is quite weak, and at this diameter, there is considerable transfer of energy from the SH to the TH, which is then further transferred to the FH, as the phase mismatch is relatively small. This is significant as in practice OMF fabrication error is typically $> \pm 6$ nm and it might be more practical to have a large mismatch in the input pump powers in order to have higher overall efficiency at this PMD. Finally, the proportion of

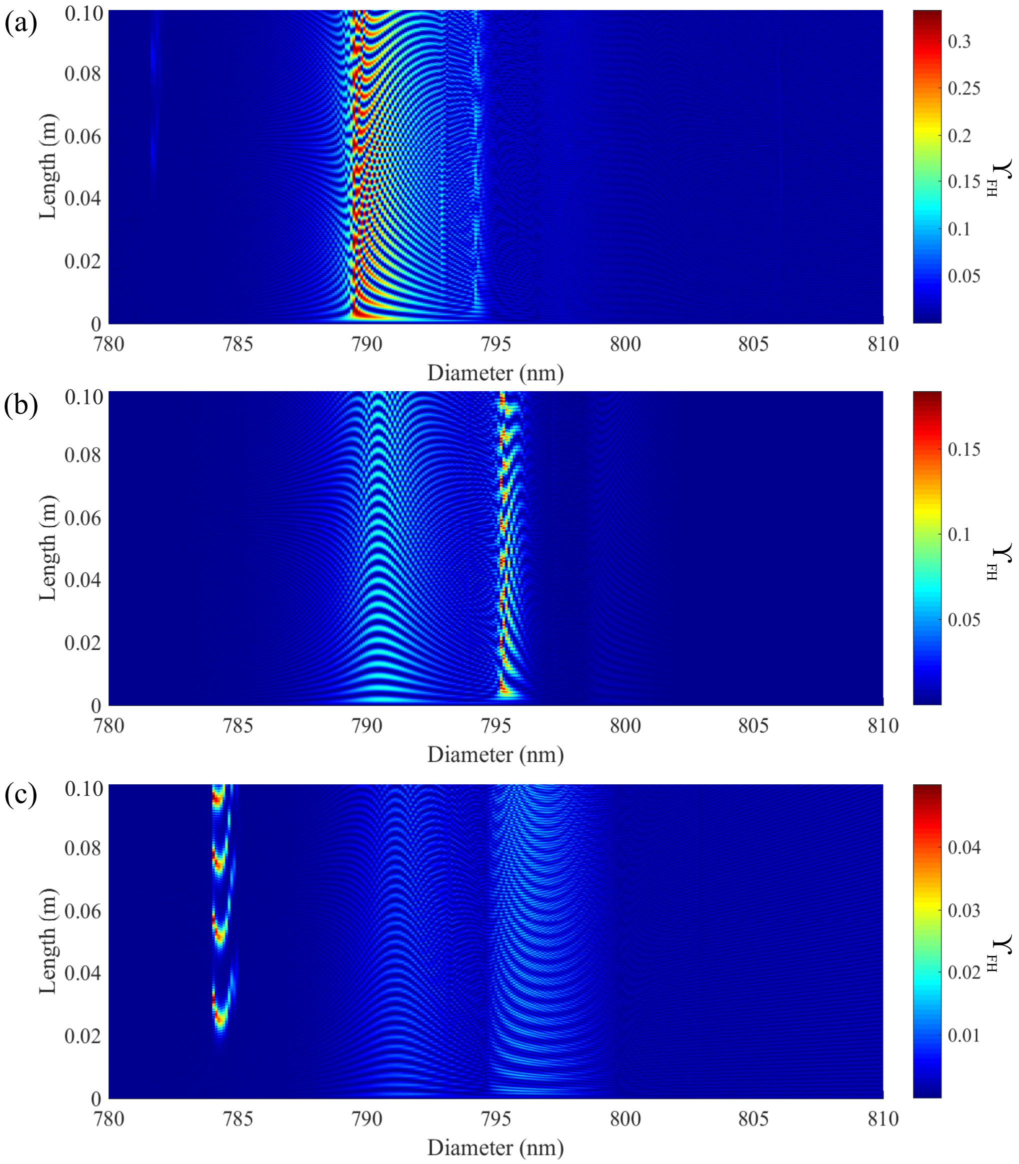

Fig. 10. Evolution of the fraction of total power (Υ_l) in the FH wavelength ($0.387\ \mu$m) around the phase matching diameter $d \sim 0.79\mu$m for three initial power fractions, $\Upsilon_{SH} : \Upsilon_{FH}$, of (a) 17% : 20%, (b) 39% : 3.0% and (c) 0.6% : 33%. The total peak power (including loss) is approximately 1 kW.

the power in the TH wavelength is increased such that the proportion of power of the SH and TH wavelengths are $\Upsilon_{SH} \sim 3\%$ and $\Upsilon_{TH} \sim 34\%$, respectively, by selecting a length of 20 mm for OMF1. The evolution Υ_{TH} in OMF2 over a length of 10 cm is shown in Fig. 10(c). In this scheme, the final efficiency at the FH is the lowest ($\leq$ 5%), as most of the energy transfer is from the TH back to the SH. Therefore, this scheme is not preferred for transferring energy from the FF to the FH wavelength.

The evolution of the energy transfer is therefore significantly dependent on the fraction of power in each wavelength, and for large imbalances in the fraction of power, the main movement of energy transfer is typically from wavelengths with higher powers to those with lower powers. However, the multiharmonic generation process is potentially efficient, if fabrication errors can be kept smaller than 6 nm.

This model is then employed to estimate the efficiency of the FWM FH wavelength generation with the input power given by the output of OMF1. It was discovered that the maximum efficiency possible was $\Upsilon_{FH} \sim 1.8 \times 10^{-6}$, corresponding to a maximum output power of $P_{FH} \sim$ 460 nW. This large discrepancy is likely due to the large fabrication error, which in this case was possibly $> \pm$ 50 nm, thereby significantly reducing the power transfer to the FH. The fact that the diameter range at which efficiency phase matching occurs is quite small may also contribute to the relatively low efficiency. This may be improved by optimizing both the pump parameters and the fabrication methods to reduce fabrication error. Furthermore, due to the relatively small diameter tolerance of the FWM process at $d_{PMD} \sim 0.8$ μm, it may be more advantageous to fabricate long OMFs at the other wider PMD $d \sim 1.7$ μm despite the lower effective nonlinearity to allow for better conversion to the FH wavelength. Finally, efficiency of this process can be significantly increased by improving the efficiency of the SHG process or by employing more powerful coherent sources at the pump wavelengths.

4. Conclusion

In conclusion, all-fiberized fourth and fifth harmonic generation from a single source is demonstrated by employing a high power MOPA source working in the telecom C-band in conjunction with a PPSF and two OMFs. Phase matching in the two OMFs was achieved by exploiting the tailorable dispersion characteristics of OMFs to compensate for material dispersion of the interacting wavelengths. Calculations indicate that there are two PMDs for FHG, though there are no diameters at which 5HG will be phase matched. An experimental demonstration was undertaken, where it was shown that the FH wavelength is generated near the theoretical PMD, while the 5H wavelength appears at diameters for which the ‘gap’ in phase matching between the interacting wavelengths is small enough to be bridged by other nonlinear effects.

Simulations with a high power pulsed source at 1.55 μm working in conjunction with a PPSF to generate a SH wavelength at 0.775 μm with an efficiency of 40% indicate the efficiency of parametric amplification at the TH can be in excess of 15% for a relatively broad range of OMF diameter. This broad diameter at which energy transfer occurs transcends the limitation imposed by random dephasing due to frozen-in surface waves, which have been suggested to limit the efficiency of intermodal THG in OMFs to $\eta \sim< 1\%$. Using two OMFs, FWM over a wavelength range of over 1200 nm with efficiencies of more than 25% were theoretically predicted. In practice, the PMD will need to be considered carefully, as the fraction of power in each wavelength is crucial in determining the direction of energy transfer, and relatively inefficient transfer of energy is possible if the phase matching points between different FWM schemes overlap with one another. Notably, these simulations show that all-fiber multiharmonic generation may be efficient if the fabrication error is not too large.

Funding

Engineering and Physical Sciences Research Council (EPSRC)(EP/L01243X/1, EP/I035307/1).

Acknowledgments

The authors would like to thank Oleksandr Tarasenko and Walter Margulis from Acreo Fiberlab who manufactured the fiber used for the PPSF as well as Peter Kazansky, Francesca Parmigiani, James Wilkinson, Senthil Ganapathy, Kyle Bottrill and Arthur Degen-Knifton at the Optoelectronics Research Centre of the University of Southampton for access to the necessary technical facilities and insightful discussions. All data supporting this study are openly available from the University of Southampton repository at http://dx.doi.org/10.5258/SOTON/387990.

Optics Letters

Thermal poling of silica optical fibers using liquid electrodes

F. De Lucia,[1] D. W. Keefer,[2] C. Corbari,[3] and P. J. A. Sazio[1,*]

[1]Optoelectronics Research Centre, University of Southampton, Southampton SO17 1BJ, UK
[2]Department of Chemistry, Pennsylvania State University, University Park, Pennsylvania 16802, USA
[3]Renishaw plc, New Mills, Wotton-under-Edge, Gloucestershire GL12 8JR, UK
*Corresponding author: pjas@soton.ac.uk

Received 16 September 2016; revised 20 October 2016; accepted 25 October 2016; posted 27 October 2016 (Doc. ID 276032); published 21 December 2016

Thermal poling is a well-known technique for inducing second-order nonlinearities in centrosymmetric silica optical fibers. However, some 25 years since its discovery, there still remain a number of issues that prevent the realization of very long length, highly efficient all-fiber nonlinear device applications that include frequency conversion or sources of polarization-entangled photon pairs. In this Letter, we report a thermal poling method that utilizes a novel range of liquid metal and aqueous electrodes embedded into the optical fibers. We demonstrate that it is possible to pole samples that are potentially meters in length, characterized by very low losses for efficient second-harmonic generation processes. The maximum estimated effective value of $\chi^{(2)}$ (0.12 pm/V) obtained using mercury electrodes is the highest reported in periodically poled silica fibers.

OCIS codes: (190.4370) Nonlinear optics, fibers; (230.4320) Nonlinear optical devices; (190.2620) Harmonic generation and mixing; (230.1150) All-optical devices.

http://dx.doi.org/10.1364/OL.42.000069

Thermal poling is a well-established technique [1] used to generate effective second-order susceptibility in centrosymmetric materials such as bulk glasses by freezing a static electric field inside. The technique has been used in silica optical fibers [2] and improved in terms of nonlinear performance by Margulis *et al.* [3], who developed a cathode-less configuration to pole the samples. Despite these efforts, the thermal poling is still compromised by issues that prevent the realization of long, low-loss and efficient all-fiber nonlinear devices [4,5]. Recently, however, De Lucia *et al.* [6] developed a new technique to pole optical fibers by means of an electrostatic induction mechanism. This innovation overcomes some of the otherwise intractable fabrication issues encountered with creating electrodes inside silica fibers. Simple manual wire insertion methods for example are both length restricted and unreliable, whereas molten-metal-filled fibers require a number of processing steps in order to establish direct electrical contact to the internal electrodes which, if left *in-situ* after the poling, can result in very large optical absorption losses. In contrast, the poling by induction [6] avoids any physical contact to the electrodes; these are typically composed of conductive liquids for facile removal after the poling has been completed to minimize optical loss. Not only does this advantageous combination allow for the poling of very long (meter scale) samples, but also within any complex geometry. This could include, for example, the induction poling of microstructured optical fibers where contacting multiple internal electrodes would otherwise be a prohibitive challenge. In addition, selective filling of such geometries both radially and longitudinally will allow liquid electrodes to be inserted (and then removed) in any configuration in order to optimize the effective $\chi^{(2)}$ for novel device applications.

In this Letter, we employ the cathode-less [3] poling configuration in order to examine the performance of a number of different liquid electrodes. The resulting fiber devices were initially characterized in terms of their linear transmission losses and tested for evidence of depletion region formation. The effective second-order nonlinearities were then evaluated by quasi-phase matching (QPM) a 1550 nm laser pump wavelength via the UV erasure technique [7] and measuring the second-harmonic generation (SHG) output power. By comparing these different electrode types and their respective optical fiber device performance parameters, we can identify new routes toward the realization of highly efficient and robust $\chi^{(2)}$ fiber waveguides.

In order to ensure reproducibility, four identical, twin-hole germania-doped, fused silica fibers sourced from Acreo Fiberlab ($\mathrm{OD} = 125\ \mu\mathrm{m}$, $\mathrm{NA} = 0.17$, electrodes holes diameter $= 30\ \mu\mathrm{m}$, core diameter $= 4\ \mu\mathrm{m}$) were used. The schematic in Fig. 1 shows the experimental setup consisting of a metallic heater (which also acts as the electrical ground plane for this poling configuration) on top of which is placed a 10 mm thick borosilicate glass strip in order to ensure adequate electrical insulation between the electrodes embedded into the sample and the grounded surface of the hotplate, while simultaneously maintaining a good thermal contact. This particular setup

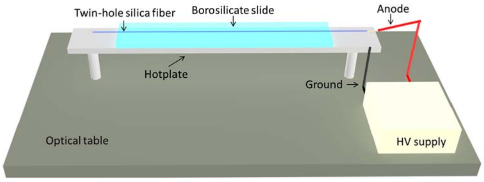

Fig. 1. Schematic of setup used for the thermal poling of optical fibers with internal liquid electrodes.

allows for the thermal poling of samples up to 60 cm in length, but much longer lengths can easily be accommodated using the Petri dish setup previously used in [6], provided the optimum poling temperature is maintained along the entire sample. The electrode liquids used to fill the twin-hole fiber samples were gallium, mercury, a HCl solution diluted at 20% in DI water and, finally, ordinary tap water. The liquid metals were introduced into the samples using pressurization techniques [4], whereas the aqueous solutions could be inserted via normal capillary action. After filling, tungsten wires were inserted into the twin holes at one end of the samples, ensuring electrical contact with the liquid. Both ends were then sealed with epoxy or superglue, and all four samples were poled under the same experimental conditions, with an applied voltage of $+5$ kV, a hotplate temperature of 300°C, a heating time of 120 min followed by a cooling time of 45 min to room temperature with the HV constantly applied. The second-order nonlinearity induced by thermal poling is defined by the following equation [1]:

$$\chi^{(2)} = 3\chi^{(3)}E_{\mathrm{rec}}, \tag{1}$$

where $\chi^{(3)}$ is the third-order susceptibility, which is a property of the glass used to make the fiber and E_{rec} is the electric field frozen into the optical fiber due to the space charge region formation. This effect arises due to the electromigration of impurity ions already present in the glass, due to an applied electric field at elevated (~300°C) temperatures [8]. This depletion region formation is strong evidence of an electric field frozen into the glass and, thus, of an effective second-order nonlinearity created in the fiber. A very useful method for direct visualization of the space charge region formation is the HF acid decorative etching technique [9]. In Fig. 2, micrograph cross sections of the samples poled using these four different electrode types are shown after being etched for 1 min in a HF buffered solution. These etched sections are taken from a region halfway along the length of each fiber. As expected, under the large applied bias and temperature of 300°C, the non-volatile liquid metal electrodes generated depletion regions throughout the fiber samples, as shown in Fig. 2. Remarkably, given these extreme conditions, the embedded aqueous electrodes also yielded well-defined depletion regions (shown in Fig. 2) throughout the entire 60 cm length of the test devices; to the best of our knowledge, this is the first time that optical fibers have been thermally poled using aqueous electrolytic electrodes. This highly counterintuitive result is currently under further investigation, as it is not yet fully understood how electrical continuity is maintained during poling, while the fiber is held well above the boiling points of these aqueous solutions for extended periods. Depletion region formation throughout the entire sample is unequivocal evidence that electrical continuity was not compromised during the experiment.

Some insight can be gained into this unusual phenomenon by observing the fiber using a stereomicroscope during the heating phase of the poling, but before the application of the high voltage. The fiber was monitored both in the center and on each of the of the end caps created to seal the fiber. Each cap consists of a piece of silica capillary with an internal diameter larger than the OD of the fiber sample into which the end of the fiber is partially inserted and filled with an epoxy resin. Once it had reached ~100°C, some bubbles were observed in the center of the fiber which push the aqueous solution toward the ends. At 300°C, before applying the external voltage, the fiber sample appears to be completely empty in the 60 cm of length placed on top of the hotplate, with some liquid remaining in the parts of the fiber located close to the end caps. We hypothesize that at high temperatures, the aqueous solution is close to its supercritical fluid point (which, for water, is at 374°C and 221.1 bars). Under these conditions, it is expected that the conductance of the fluid will rapidly increase [11] and, indeed, can exhibit conductance values that are orders of magnitude higher than those of standard temperature and pressure values. This near-critical operating point, therefore, could allow the high pressure/temperature/conductance fluid created within the twin-hole fiber to act as an efficient electrode. Electrical continuity is completed via the liquid regions located at the end caps and the tungsten wires inserted inside. Further investigations to confirm this hypothesis will be addressed in future work, focusing on in-*situ* optical spectroscopic studies [12] for which the optical fiber platform is inherently well suited.

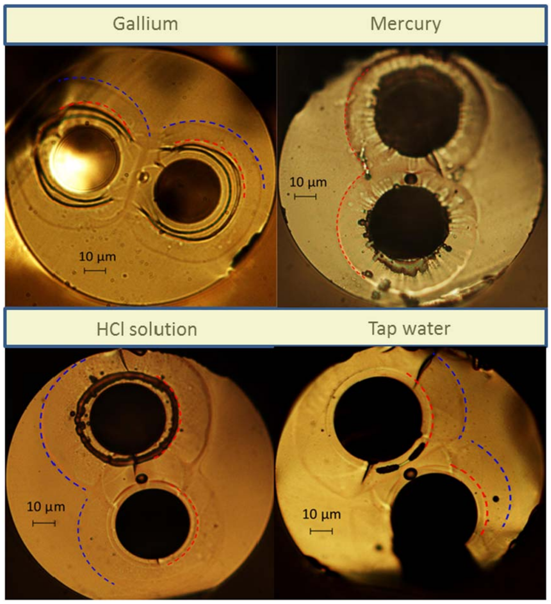

Fig. 2. Cross-sectional micrographs of the HF etched samples poled using novel liquid electrode types. The HF decorative etching process reveals the presence of depletion regions in all four twin-hole Ge-doped core, fused silica fibers. The observed dual concentric depletion region formation (highlighted by means of the red and blue dotted lines as a guide for the eye) is likely to be due to the Na^+ and Li^+ impurity charges involved in the electromigration process, typically characterized by differing ion mobilities in the glass [10].

As previously described, the HF decorative etching procedure [9] is strongly indicative, but not a rigorously quantitative measurement of the induced nonlinearity. In order to obtain a comprehensive evaluation of the induced $\chi^{(2)}$ value, the SHG response can be measured by modulating the nonlinearity via

UV erasure techniques [7] which allows for QPM [13] the phase velocity disparity in dispersive media present between the pump wavelength and the SHG. The relationship between the period of the grating written by UV erasure and the wavelength of the pump where the second harmonic is phase-matched (to the first order of approximation) is expressed in Eq. (2):

$$\Lambda_{\mathrm{QPM}} = \frac{\lambda}{2(n_{\mathrm{eff}}^{2\omega} - n_{\mathrm{eff}}^{\omega})}, \tag{2}$$

where $n_{\mathrm{eff}} = n_{\mathrm{eff}}(\lambda, \mathrm{NA}, a)$ is the effective refractive index of the propagating modes and depends on the wavelength of the fundamental mode, the NA of the fiber, and the diameter of the fiber core a.

Prior to the grating writing process, it is necessary to completely remove the electrodes from the fiber samples in order to minimize linear loss. This is particularly true for the liquid metal electrodes, as these exhibit very high optical absorption losses [6]. These metals (i.e., gallium and mercury) can be removed by using the same pressurization system initially used to fill the fibers [4]. However, we note that the samples poled by means of electrolytic solutions do not need to be purged and emptied, as the aqueous electrodes at 300°C in the part of the fibers located on top of the heater are already completely void once the thermal poling is completed.

The experimental setup used to write the QPM gratings is the same as reported in [6], in which 355 nm of laser radiation is delivered as a 200 kHz train of 8 ps pulses, focused to a 10 × 100 μm spot size onto the fiber with a total fluence of 200 J/cm^2. The periodically poled samples were then characterized using the setup shown schematically in Fig. 3, and the resultant tuning curves of the fibers poled with metallic liquid electrodes are shown in Fig. 4, demonstrating the expected Sinc^2 transfer function, i.e., the Fourier transform of the square QPM grating. In order to provide a quantitative value for the $\chi^{(2)}$ values according to the analysis of Pruneri *et al.* [14] for a periodically poled fiber, the sample shown in Fig. 4(a), i.e., using Gallium electrodes, has a fabricated device length of 28.5 cm and a modal overlap area of 49.43 μm^2 at a 1550 nm CW pump wavelength. In Fig. 4(b), the sample using mercury electrodes has a device length of 20 cm and a modal overlap area of 49.43 μm^2 at a 1550 nm CW pump wavelength.

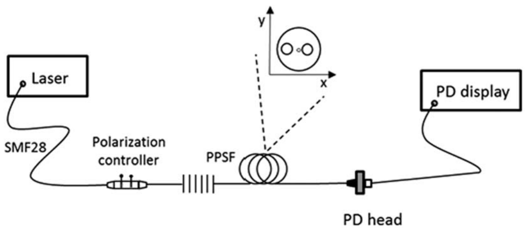

Fig. 3. Setup for SHG measurements for PPSF. The source is a tunable diode laser emitting at 1550 nm [Photonetics, model 3542 HE CL, linewidth (FWHM) = 100 kHz), CW power of 6 mW]. The polarization controller allows for changing the polarization state of the pump radiation, and a low-power calibrated photodiode sensor (Newport, model 918D-UV-OD3) is used to measure the SHG optical power. The inset shows the cross section of the twin-hole silica fiber. The principal polarization axes of the fiber are assumed to be aligned along the two orthogonal axes x and y, where x is the direction of the frozen-in electric field.

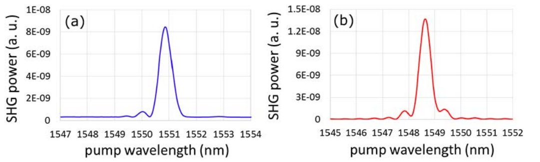

Fig. 4. Tuning curves of the two samples poled by means of metallic electrodes for (a) gallium (insertion loss at 1550 nm = 1.8 dB, $\chi^{(2)}$ estimated at 0.056 pm/V, $\Lambda_{\mathrm{QPM}} = 57.3072$ μm) and (b) mercury (insertion loss at 1550 nm = 1 dB, $\chi^{(2)}$ estimated at 0.12 pm/V, $\Lambda_{\mathrm{QPM}} = 57.1937$ μm) and characterized using the setup shown in Fig. 3. The curves represent the SHG power measured by a photodiode, while the wavelength of the pump light emitted by the tunable narrowband CW source is changed step by step over a range centered at 1550 nm.

The periodically poled silica fiber (PPSF) device consists of two SM980 Thorlabs fibers (manufacturer datasheet parameters; OD 125 μm, 5.3–6.4 μm mode field diameter at 980 nm, NA = 0.13–0.15) spliced to either end of a PPSF to act as buffers that facilitate the optical launch and pumping. An important aspect of the measured $\chi^{(2)}$ values which, as well as being dependent on the thermal poling conditions and the quality and accuracy of the QPM grating writing process, is the strong influence of the overall device insertion losses, which include the splice and transmission losses. Mercury electrodes tend to be superior to gallium in this respect as they leave few residues after poling and purging, resulting in overall losses of the entire device of approximately 1 dB. To the best of our knowledge, the effective $\chi^{(2)}$ of 0.12 pm/V shown in Fig. 4(b) is the highest value for a PPSF published to date. As a direct comparison, the two samples poled using aqueous electrodes which, as shown in Fig. 2, also yielded the well-defined depletion regions indicative of induced second-order nonlinearity, were optically characterized with exactly the same setup used for the metallic electrode samples. In contrast, however, the SHG power measured by the photodiode in Fig. 3 was too low to be accurately quantified in these samples using the low power CW pumping setup, as it could not be resolved from the noise floor of the photodiode sensor. In order to find conclusive evidence of SHG in these samples and exclude the possibility that the etched regions shown in Fig. 2 were due to some other unknown effect, the SHG of the aqueous electrode samples were characterized using the setup shown schematically in Fig. 5. Here, a high-power laser (the second harmonic of a mode-locked amplified Nd:YVO4 solid state laser, pulse duration 8 ps, repetition rate 250 kHz, average power 2.5 W), is used to pump an optical parametric generator, thus producing a high peak power broadband infrared idler output (3 dB bandwidth approximately 80 nm, average power of 50 mW) that is temperature tunable between 1100 and 2500 nm. A long-wave pass filter in the optical setup rejects all radiation below the cut-on wavelength (900 nm) associated with the source. This ensures that any spectra observed at wavelengths shorter than 900 nm are due only to nonlinear processes occurring within the PPSF. Figure 6 shows the SHG spectra obtained for two samples poled under identical experimental conditions using HCl aqueous electrodes with different grating

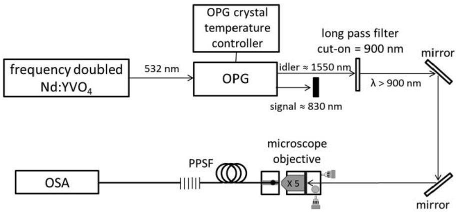

Fig. 5. High-power pulsed laser pump setup for the nonlinear characterization of PPSF devices poled using aqueous electrodes.

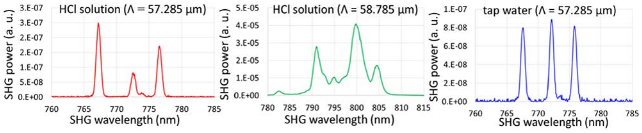

Fig. 6. SHG output spectra of optical fibers poled using a HCl solution, as well as ordinary tap water, characterized using the setup shown in Fig. 5. Insertion loss at 1550 nm = 0.7 dB for water and 0.5 dB for HCl solution. The induced $\chi^{(2)}$ for both aqueous solutions is estimated [14] at ≤ 0.001 pm/V, assuming a fabricated device length of 20 cm and a modal overlap area of 49.43 $\mu\mathrm{m}^2$ at 1550 nm pump wavelength.

periods. The spectrum of a sample poled using tap water electrodes is also shown. Here, each SHG spectrum consists of three peaks, corresponding to different combinations of the polarization states of the two pump photons producing the SHG. This degeneracy of the polarization is due to the birefringence of the fiber along the x and y axes [15]. The presence of the three peaks instead of just one observed in the SHG tuning curves shown in Fig. 4 is due to the fact that, for the setup in Fig. 3, the CW pump output is linearly polarized and can be adjusted by means of a polarization controller to produce QPM of type I (XX → X). In contrast, the pulsed high-power pump used to characterize the samples poled using aqueous electrodes is not linearly polarized, so it always contains both components of polarization along the x and y axes. Nevertheless, the observation of distinct peaks at second-harmonic wavelengths corresponding to two different QPM grating periods that accurately follow the linear relationship expressed in Eq. (2) provide convincing evidence of the formation of an effective $\chi^{(2)}$ in these novel aqueous electrode PPSFs, which exhibit very low optical insertion losses compared with the metallic liquid electrode samples. However, despite the potential improvement in nonlinear process efficiency conferred by this desirable characteristic, it comes at a cost, as the effective $\chi^{(2)}$ values in the aqueous electrode samples is clearly inferior to those with gallium and mercury. We believe this is due to higher resistivity of the electrolytic solutions compared with pure metals, thus potentially reducing the magnitude of electric field that can be frozen into the glass fiber which, in turn, leads to a decrease in induced $\chi^{(2)}$ nonlinearity.

In summary, this Letter presents, to the best of our knowledge, the first successful attempt at optical fiber thermal poling using non-metallic internal electrodes. This result, in combination with our induction poling technique demonstrated in [6], offers a significant advance toward the implementation of a generalized method for the thermal poling of any complex fiber geometry and length. This could include microstructured optical fibers that potentially allow up to four orders of magnitude in improvements of second-order nonlinear processes, compared with conventional twin-hole, step-index germania-doped fused silica fibers [16].

Funding. Engineering and Physical Sciences Research Council (EPSRC) (EP/I035307/1).

Acknowledgment. The authors thank Oleksandr Tarasenko and Walter Margulis from Acreo Fiberlab who manufactured the fiber periodically poled and Peter Kazansky for access to the necessary technical facilities. F. De Lucia thanks Andrea Ravagli for interesting discussions about the chemistry of superfluids. Under the EPSRC research data management scheme, the datasets of the figures in this Letter can be found at http://dx.doi.org/10.5258/SOTON/386825.

REFERENCES

1. R. A. Myers, N. Mukherjee, and S. R. J. Brueck, Opt. Lett. **16**, 1732 (1991).
2. D. Wong, W. Xu, S. Fleming, M. Janos, and K.-M. Lo, Opt. Fiber Technol. **5**, 235 (1999).
3. W. Margulis, O. Tarasenko, and N. Myrén, Opt. Express **17**, 15534 (2009).
4. M. Fokine, L. E. Nilsson, A. A. Claesson, D. Berlemont, L. Kjellberg, L. Krummenacher, and W. Margulis, Opt. Lett. **27**, 1643 (2002).
5. A. Canagasabey, C. Corbari, A. V. Gladyshev, F. Liegeois, S. Guillemet, Y. Hernandez, M. V. Yashkov, A. Kosolapov, E. M. Dianov, M. Ibsen, and P. G. Kazansky, Opt. Lett. **34**, 2483 (2009).
6. F. De Lucia, D. Huang, C. Corbari, N. Healy, and P. Sazio, Opt. Lett. **39**, 6513 (2014).
7. A. Canagasabey, M. Ibsen, K. Gallo, A. V. Gladishev, E. M. Dianov, C. Corbari, and P. G. Kazansky, Opt. Lett. **35**, 724 (2010).
8. N. Mukherjee, R. A. Myers, and S. R. J. Brueck, J. Opt. Soc. Am. B **11**, 665 (1994).
9. T. G. Alley and S. R. J. Brueck, Opt. Lett. **23**, 1170 (1998).
10. T. G. Alley, S. R. J. Brueck, and M. Wiedenbeck, J. Appl. Phys. **86**, 6634 (1999).
11. W. L. Marshall, J. Chem. Eng. Data **32**, 221 (1987).
12. D. A. Masten, B. R. Foy, D. M. Harradine, and R. B. Dyer, J. Phys. Chem. **97**, 8557 (1993).
13. J. A. Armstrong, N. Bloembergen, J. Ducuing, and P. S. Pershan, Phys. Rev. **127**, 1918 (1962).
14. V. Pruneri, G. Bonfrate, P. G. Kazansky, D. J. Richardson, N. G. Broderick, J. P. de Sandro, C. Simonneau, P. Vidakovic, and J. A. Levenson, Opt. Lett. **24**, 208 (1999).
15. E. Y. Zhu, L. Qian, L. G. Helt, M. Liscidini, J. E. Sipe, C. Corbari, A. Canagasabey, M. Ibsen, and P. G. Kazansky, Opt. Lett. **35**, 1530 (2010).
16. T. M. Monro, V. Pruneri, N. G. R. Broderick, D. Faccio, P. G. Kazansky, and D. J. Richardson, IEEE Photon. Technol. Lett. **13**, 981 (2001).

Optics Letters

Composite material hollow antiresonant fibers

Walter Belardi,* Francesco De Lucia, Francesco Poletti, and Pier J. Sazio

Optoelectronics Research Centre, University of Southampton, Highfield, Southampton, Hampshire SO17 1BJ, UK
**Corresponding author: w.belardi@soton.ac.uk*

Received 9 May 2017; revised 24 May 2017; accepted 24 May 2017; posted 25 May 2017 (Doc. ID 295709); published 26 June 2017

We study novel designs of hollow-core antiresonant fibers comprising multiple materials in their core-boundary membrane. We show that these types of fibers still satisfy an antiresonance condition and compare their properties to those of an ideal single-material fiber with an equivalent thickness and refractive index. As a practical consequence of this concept, we discuss the first realization and characterization of a composite silicon/glass-based hollow antiresonant fiber.

OCIS codes: (060.2280) Fiber design and fabrication; (060.2400) Fiber properties; (060.4005) Microstructured fibers.

https://doi.org/10.1364/OL.42.002535

After almost two decades of improvement in fiber technology, the development of hollow-core optical fibers (HCs) [1,2] is still very active. In particular, the use of hollow fiber structures comprising only a limited number of detached glass tubes within an outer glass jacket is gaining significant interest [3,4]. The use of this fiber type has resulted in HCs with relatively low attenuation in the visible [5,6], near [7–9], and mid-infrared spectral ranges [4], combined with ultra-large transmission bandwidths [5,8,9]. Possible applications of these hollow antiresonant fibers (ARFs) range from high-power laser delivery [7] to gas-based laser sources [10] and telecommunications [9].

Several modifications of this basic fiber design have been proposed [5,11–15] in order to further reduce their level of leakage loss or increase their birefringence. However, all of the previous designs and fabrication proposals have concerned ARFs made of a single material (typically silica, even though other glass materials have also been considered [16,17]). In this Letter, we seek to explore a novel form of this ARF type by using, for the first time (to our knowledge), multiple materials for the fiber cladding. We numerically study the transmission properties of these composite-material antiresonant fibers (CM-ARFs) by correlating the composite-material membrane properties to that of a "single equivalent membrane," with an identical effective thickness and refractive index. We apply this concept to the design of a novel form of ARF by adopting a hybrid semiconductor/glass-core-boundary membrane. As in previous works on semiconductor optical fibers [18,19], the inclusion of a semiconductor is desirable in order to realize functionalized devices. For example, a light induced refractive index change may be adopted for all optical fiber modulation [20]. We numerically demonstrate that, in contrast to previous structures with silicon in the cladding area [18], this novel type of silicon antiresonant fiber is predicted to have very low attenuation (<0.1 dB/m). Finally, we report on the first fabrication and characterization of a silicon/borosilicate based ARF.

Figure 1 shows a reproduction of a silica-based ARF ($n = 1.41$ at $\lambda = 2.7$ μm) already fabricated in Ref. [4] with 10 cladding tubes and an original thickness of the cladding tubes $t = 2.4$ μm (in white). The core radius is 47 μm. An additional internal membrane t_A (in red) is added corresponding to a material with refractive index $n_2 = 2$.

The dependence of leakage loss on the additional thickness t_A, shown in Fig. 1 at a wavelength of 2.7 μm, clearly demonstrates the antiresonant properties of this CM-ARF. In the following, we will refer to an "antiresonant layer" as that additional membrane with a thickness t_A^* corresponding to the minimum leakage loss of the single-layer ARF (see Fig. 1).

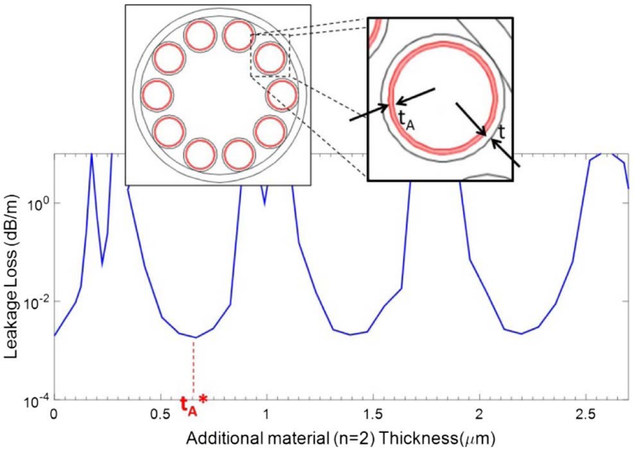

Fig. 1. Sketch (top) of a composite-material hollow antiresonant fiber: an additional layer with thickness t_A is added to the original core boundary of thickness t. The fiber transmission spectrum at 2.7 μm shows the antiresonant behavior of the fiber.

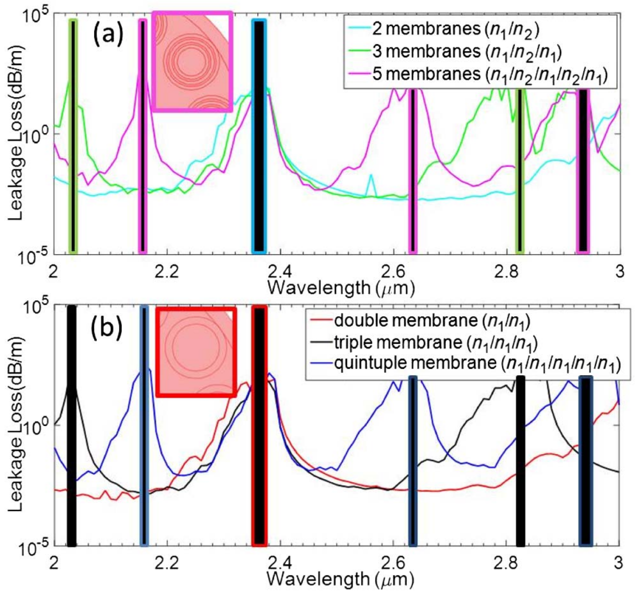

Fig. 2. Top (a): calculated leakage loss when 2 (cyan line), 3 (green line), or 5 (pink line) antiresonant layers are added to the basic structure of Fig. 1. Bottom (b): calculated leakage loss when the thickness t of the basic ARF structure is increased 2 ($2t$, red line), 3 ($3t$, black line), and 5 ($5t$, blue line) times.

Figure 2(a) shows the evolution of the leakage loss when additional antiresonant glass membranes ($2t$, $3t$, or $5t$) are added to the basic structure. This behavior is almost identical to that of fiber designs shown in Fig. 2(b) where the thickness of the initial single-silica membrane is simply increased 2, 3, or 5 times (red, black, and blue curves). In particular, the fiber designs of (a) and (b) have the same resonant wavelengths and the same minimum leakage level. This is not surprising since the designs of Fig. 2(b) can be simply seen as multiple layers [of the type (a)] with the same refractive index for the alternating layers ($n_2 = n_1$). By using the basic formulation of the resonant wavelength [21], it is possible to derive that the frequency spacing Δf between two resonant frequencies is

$$\Delta f = \frac{c}{2t_R\sqrt{n_1^2 - 1}}, \tag{1}$$

where c is the speed of light in vacuum, t_R is the membrane thickness of the ARF, and n_1 is the glass refractive index. Therefore, when the thickness is doubled or tripled, the frequency spacing between two resonant frequencies is reduced by a factor of 2 or 3. This explains the presence in Fig. 2 of a different number of resonant wavelengths associated with the different number of antiresonant layers in the considered structures. The small differences between the spectra of Figs. 2(a) and 2(b) are associated only with the different optical couplings between the fundamental-like modes transmitted in the fiber core and the different cladding modes present in the two structures [8].

We can further extend the analogy between Figs. 2(a) and 2(b) by correlating the behavior of a CM-ARF made of two materials (with refractive index n_1 and n_2, and thickness t_1 and t_2) to that of a single-material ARF with an equivalent refractive index n_{eq} and thickness t_{eq}. We define

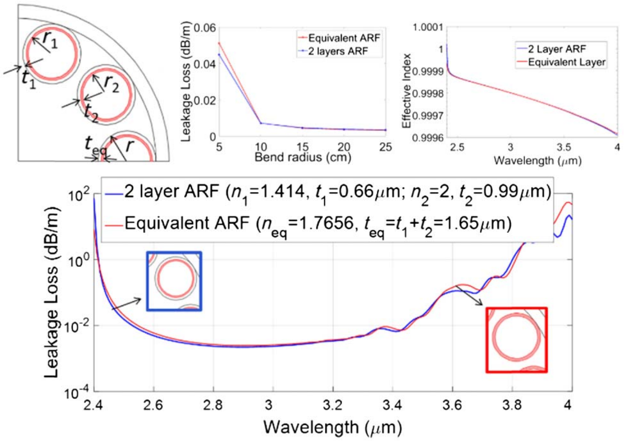

Fig. 3. Equivalence between a CM-ARF with two antiresonant layers of thickness t_1 and t_2 (blue line) and single-layer ARF with an equivalent antiresonant layer of thickness t_{eq}.

$$n_{\mathrm{eq}} = n_1\frac{S_1}{S_1 + S_2} + n_2\frac{S_2}{S_1 + S_2}, \tag{2}$$

and

$$t_{\mathrm{eq}} = t_1 + t_2, \tag{3}$$

where S_1 and S_2 are the surfaces occupied by the two materials and are given by (see inset of Fig. 3):

$$S_1 = \pi(r^2 - r_1^2), \tag{4}$$

$$S_2 = \pi(r_1^2 - r_2^2), \tag{5}$$

where r_1 and r_2 are the internal radii of the two cladding tubes of thickness t_1 and t_2, respectively, and r is the external radius of the composite-material cladding tubes (see inset of Fig. 3). As an example and validation of this equivalence, we have considered the case of two materials with $n_1 = 1.414$ and $n_2 = 2$ ($t_1 = 0.66$ μm, $t_2 = 0.99$ μm, $r = 20$ μm). By using Eqs. (2)–(5), it is possible to obtain $n_{\mathrm{eq}} = 1.7656$ and $t_{\mathrm{eq}} = 1.65$ μm. By looking at Fig. 3, we can see that the leakage loss of the CM-ARF (blue line) and the equivalent ARF (red line) overlap in most of the considered spectral range. A slight difference between the two spectra is more evident at longer wavelengths where the fundamental mode interacts more strongly with the fiber-cladding modes. The behavior of the equivalent structure is the same even when the fiber is bent with a bend radius greater than 10 cm.

The established analogy between a composite-material and a conventional single-material ARF suggests that only the overall optical path travelled by light at the core boundary is relevant for antiresonance guidance. This opens up the possibility to exploit the properties of additional materials deposited on the basic optical fiber matrix in order to activate and functionalize its behavior, for example, via the free carrier plasma-dispersion effect, in which the change of refractive index and absorption resulting from a change in the concentration of free carriers by photo-excitation can be used in silicon-based, all-fiber integrated modulators to achieve intensity or phase modulation [20]. As a first step of this "active hollow-core waveguide" concept, we have investigated the feasibility of a

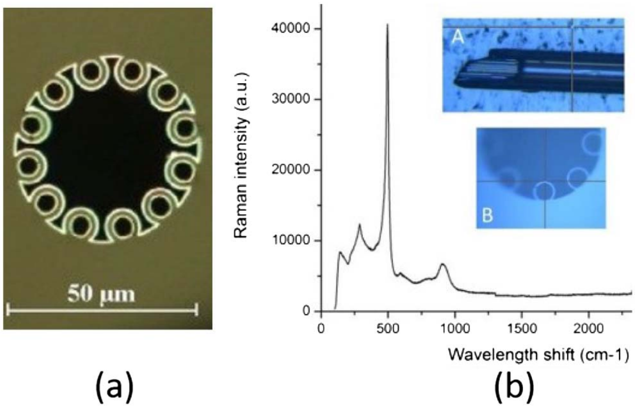

Fig. 4. (a) Fabricated CM-ARF: a thin (~0.3 μm) layer of a:Si-H (highly reflective white material) covers the internal and external sides of the cladding tubes of a borosilicate-based ARF. (b) Raman shift spectrum of another CM-ARF shown in its longitudinal (A) and transversal (B) sections. The peaks reveal the presence of a-Si:H on the external and internal surfaces of the cladding tubes. Reflective white material (a-Si:H) can also be seen in the longitudinal section (A) micrograph.

particular form of CM-ARF, in which the core-boundary membrane is made of a composite hybrid semiconductor/glass material. Semiconductor optical fibers [19] have received great attention in recent years because of the prospect for integration of the existing optical fiber infrastructure with the novel silicon photonics platform [22]. Since the first inclusions of semiconductors within optical fibers [23], progress in the area has seen some demonstrations of optical devices [19]. Although potentially these structures may provide unique characteristics, their use is currently limited by the very high attenuation observed to date in these fibers (of order 1 dB/cm). Here we show that this problem can be mitigated by filling semiconductors within ARFs. Figure 4 shows a typical section of a borosilicate-based ARF [17] filled with amorphous hydrogenated silicon (a-Si:H) by using a high-pressure chemical vapor deposition (HPCVD) method [23].

The CM-ARF of Fig. 4(a) was obtained after a deposition of 48 h at a temperature of 400°C and has three layers of material [silicon (white)/borosilicate (gray)/silicon (white)]. The Si layer thickness was measured using the SEM to be close to 300 nm.

We then tested several types of ARFs by using the same HPCVD technique and modifying the temperature profile along the fiber samples, as well as the filling time. The fiber shown in the inset of Fig. 4(b) (core diameter $d = 60$ μm and glass layer thickness of 1 μm) was coiled in a furnace at a temperature of 450°C and filled for only 4 h in order to obtain a very thin a-Si:H layer thickness. A length of 35 cm of this fiber was obtained and tested.

We could reveal the presence of a thin layer of a-Si:H by means of Raman spectroscopy. Figure 4(b) shows the Raman shift spectrum taken using the sample in the inset [shown in its longitudinal section (A) and transversal section (B)] and using an optical pump at a wavelength of 0.63 μm. The Raman shifts at the points centered on the external and internal sides of the cladding tubes confirm the presence of a-Si:H [24].

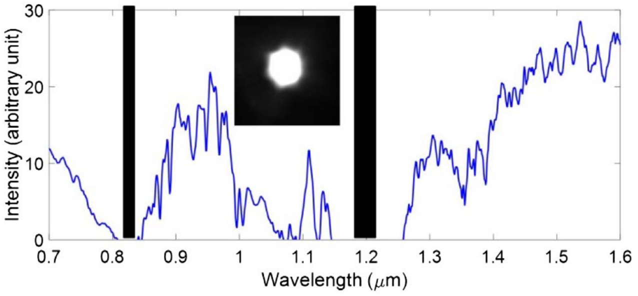

Fig. 5. Transmission spectrum of the CM-ARF shown in the inset of Figs. 4(b) and 7. Inset: near-field intensity profile of the transmitted optical mode.

The spectrum of the signal transmitted through the considered 35-cm-long sample is shown in Fig. 5 together with the near-field intensity profile recorded by an infrared camera. In the considered spectral range (0.7–1.6 μm), the CM-ARF has two transmission windows (just above 0.8 μm and around 1.2 μm) and presents several peaks probably related to the coupling of the fundamental-like mode (in the inset) to the cladding modes, in both the two high refractive index (~3.6) layers.

In Fig. 6(a), we have compared this measured transmission spectrum (blue solid line) with that of 7 meters of the same ARF without any silicon filling (green solid line; glass thickness is 1 μm, and glass dispersion is taken into account) and the calculation of the leakage loss for both the filled CM-ARF (black dotted line) and the unfilled ARF (red dotted line). Our simulations show how the addition of the internal and external silicon layers to the original ARF results in a

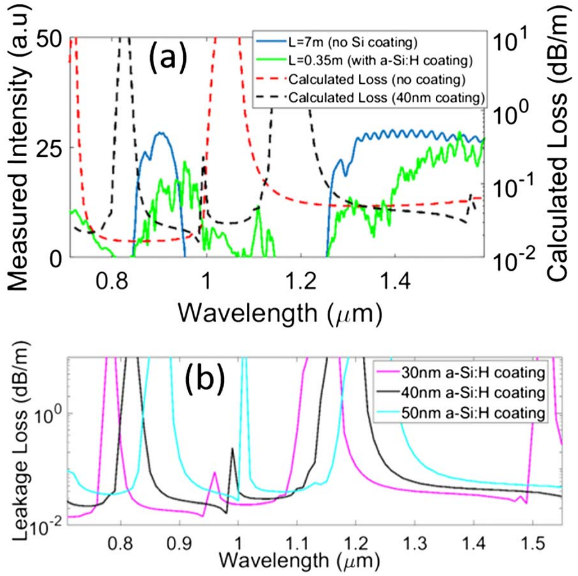

Fig. 6. (a) Comparison between the transmission spectrum (left *y* axis) of an unfilled ARF (7 m long, green solid line) and the same ARF filled with a-SI:H (0.35 m long, blue solid line) with the calculated leakage loss (right *y* axis) of the unfilled ARF (red dotted line) and the a-Si-H filled ARF (40 nm coating, black dotted line). (b) Calculated leakage loss for 30, 40, and 50 nm coating thickness.

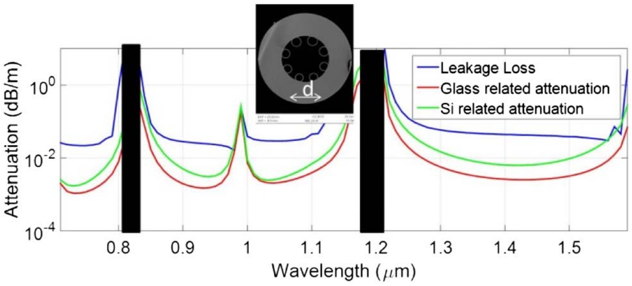

Fig. 7. Different components of the total attenuation of the CM-ARF shown in the inset: leakage loss (blue line), and loss related to the overlap of the optical mode on the Si layer (green line) and on the borosilicate cladding layer (red line). The material absorption has been assumed to be 10,000 dB/m for a-Si:H and 140 dB/m for borosilicate.

red-frequency shift of the entire transmission spectrum. Figure 6(b) shows what would be the effect on the leakage loss of a variation of the coating thickness of ±10 nm, proving that the fiber attenuation levels would be kept similar, but there would be a shift of the resonant wavelength (±0.05 μm).

In order to show the impact of the optical absorption of the a-Si:H layers on the fiber performance, we have compared in Fig. 7 the attenuation components of the CM-ARF. The fiber attenuation related to the presence of a glass (red line) and silicon (green line) material absorption is obtained as the product between the optical mode overlap on each material and their intrinsic absorption. Concerning this last quantity, we have measured the borosilicate glass absorption to be maximum 140 dB/m, and we have assumed a high absorption of the amorphous silicon material of 100 dB/cm.

The results show that, for the considered fiber, the leakage loss (blue line) is the most important contribution to the total attenuation of the CM-ARF and demonstrates the negligible impact of the absorption of the deposited semiconductor. As shown in Fig. 7, levels of attenuation as low as 0.1 dB/m or less may be obtainable in long CM-ARFs.

In conclusion, in this work we have demonstrated that CM-ARFs have the same characteristics of single-layer ARFs. We have formulated an equivalence between single-layer and CM-ARFs. By using this concept, we have fabricated and characterized the first silicon-based ARF, showing the potential of this platform for the realization of semiconductor-based devices with low attenuation. The exploration of this new avenue of research may lead to the implementations of novel forms of composite (glass/semiconductor) devices based on HC optical fiber technology with intriguing prospects in the broad fields of optical sensing, communications, light, generation and manipulation. (Datasets at http://doi.org/10.5258/SOTON/D0046.)

Funding. Engineering and Physical Sciences Research Council (EPSRC) (EP/I01196X/1, EP/I035307/1).

REFERENCES

1. R. F. Cregan, B. J. Mangan, J. C. Knight, T. A. Birks, and P. St.J. Russell, Science **285**, 1537 (1999).
2. P. J. Roberts, F. Couny, H. Sabert, B. J. Mangan, D. P. Williams, L. Farr, M. W. Mason, A. Tomlinson, T. A. Birks, J. C. Knight, and P. St.J. Russell, Opt. Express **13**, 236 (2005).
3. A. N. Kolyadin, A. F. Kosolapov, A. D. Pryamikov, A. S. Biriukov, V. G. Plotnichenko, and E. M. Dianov, Opt. Express **21**, 9514 (2013).
4. W. Belardi and J. C. Knight, Opt. Express **22**, 10091 (2014).
5. W. Belardi, J. Lightwave Technol. **33**, 4497 (2015).
6. S. Gao, Y. Wang, X. Liu, C. Hong, S. Gu, and P. Wang, Opt. Lett. **42**, 61 (2017).
7. M. Michieletto, J. K. Lyngsø, C. Jakobsen, J. Lægsgaard, O. Bang, and T. T. Alkeskjold, Opt. Express **24**, 7103 (2016).
8. B. Debord, A. Amsanpally, M. Chafer, A. Baz, M. Maurel, J. M. Blondy, E. Hugonnot, F. Scol, L. Vincetti, F. Gérôme, and F. Benabid, Optica **4**, 209 (2017).
9. J. R. Hayes, S. R. Sandoghchi, T. D. Bradley, Z. Liu, R. Slavik, M. A. Gouveia, N. V. Wheeler, G. T. Jasion, Y. Chen, E. Numkam-Fokoua, M. N. Petrovich, D. J. Richardson, and F. Poletti, in *Optical Fiber Communications Conference and Exhibition (OFC)* (2016), paper Th5A.3.
10. Z. Wang, W. Belardi, F. Yu, W. J. Wadsworth, and J. C. Knight, Opt. Express **22**, 21872 (2014).
11. W. Belardi and J. C. Knight, in *Optical Fiber Communication Conference* (Optical Society of America, 2014), paper Th2A.45, Supplementary Material.
12. Md. S. Habib, O. Bang, and M. Bache, Opt. Express **24**, 8429 (2016).
13. X. Huang, W. Qi, D. Ho, K. Yong, F. Luan, and S. Yoo, Opt. Express **24**, 7670 (2016).
14. Md. I. Hasan, N. Akhmediev, and W. Chang, Opt. Lett. **42**, 703 (2017).
15. W. Ding and Y. Wang, Opt. Express **23**, 21165 (2015).
16. A. F. Kosolapov, A. D. Pryamikov, A. S. Biriukov, V. S. Shiryaev, M. S. Astapovich, G. E. Snopatin, V. G. Plotnichenko, M. F. Churbanov, and E. M. Dianov, Opt. Express **19**, 25723 (2011).
17. W. Belardi, N. White, J. Lousteau, X. Feng, and F. Poletti, *Workshop on Specialty Optical Fibers and their Applications* (Optical Society of America, 2015), paper WW4A.4.
18. N. Healy, J. R. Sparks, R. R. He, P. J. A. Sazio, J. V. Badding, and A. C. Peacock, Opt. Express **19**, 10979 (2011).
19. J. R. Sparks, P. J. A. Sazio, V. Gopalan, and J. V. Badding, Annu. Rev. Mater. Res. **43**, 527 (2013).
20. D. Won, M. O. Ramirez, H. Kang, V. G. F. Baril, J. Calkins, J. V. Badding, and P. J. A. Sazio, Appl. Phys. Lett. **91**, 161112 (2007).
21. N. M. Litchinitser, A. K. Abeeluck, C. Headley, and B. J. Eggleton, Opt. Lett. **27**, 1592 (2002).
22. D. Thomson, A. Zilkie, J. E. Bowers, T. Komljenovic, G. T. Reed, L. Vivien, D. Marris-Morini, E. Cassan, L. Virot, J. Fédéli, J. Hartmann, J. H. Schmid, D. Xu, F. Boeuf, P. O'Brien, G. Z. Mashanovich, and M. Nedeljkovic, J. Opt. **18**, 073003 (2016).
23. P. J. Sazio, A. Amezcua-Correa, C. E. Finlayson, J. R. Hayes, T. J. Scheidemantel, N. F. Baril, B. R. Jackson, D. J. Won, F. Zhang, E. R. Margine, V. Gopalan, V. H. Crespi, and J. V. Badding, Science **311**, 1583 (2006).
24. V. A. Volodin and D. I. Koshelev, J. Raman Spectrosc. **44**, 1760 (2013).